University of Sussex

The XMM Cluster Survey: Optical to X-ray Scaling Relations.

Alberto Bermeo-Hernandez

Submitted for the degree of Doctor of Philosophy

University of Sussex

April 2017

UNIVERSITY OF SUSSEX

Alberto Bermeo-Hernandez, Doctor of Philosophy

The XMM Cluster Survey: Optical to X-ray Scaling Relations

In this thesis. we present the optical to X-ray scaling relations from the XMM Cluster Survey (XCS) and the red-sequence Matched-filter Probabilistic Percolation cluster finding algorithm (redMaPPer) cluster catalogs. XCS finds galaxy clusters in the XMM-Newton public archive and redMaPPer uses optical data from the Sloan Digital Sky Survey eighth data release (SDSS-DR8) and the Dark Energy Survey first year data release (DES Y1). redMaPPer catalogs provide reliable photometric redshift estimations that have been calibrated with spectroscopic redshifts. The XCS temperature and luminosity pipelines need redshift information to calculate the X-ray observables.

We introduced third generation of the XCS Post Processing Pipeline (XCS3P). A description of the previous versions is given, highlighting the modifications made for XCS3P-v3. This methodology was validated by comparing the $L_{\rm X}-T_{\rm X}$ relation obtained from XCS3P-v1, XCS3P-v2 and the current version, the results are similar to XCS3P-v2 finding a self similar evolution.

Samples of clusters are defined after several control filters, each cluster has optical and X-ray follow up, the sample has 327 unique clusters that span a redshift range of $0.08 < z < 0.8$. Optical to X-ray scaling relations are obtained for the samples XCS-RM (SDSS DR8), XCS-RM (DES Y1) and XCS-RM (SDSS+DES Y1). Obtaining as a result, the most comprehensive examination of the $T_{\rm X} - \lambda$ and $L_{\rm X} - \lambda$ relations up to date, showing a clear correlation between the observables. This work confirms that it is possible to relate optical properties with the underlying mass. Cluster observables like the X-ray temperature, X-ray luminosity and the optical richness are well known mass tracers.

The XCS3P-v3 methodology and the process followed to obtain the scaling relations are validated using four non-redMaPPer cluster catalogs, two from the optical (CAMIRA and GMBCG) and two from the millimiter (SPT and Planck). The results show a clear correlation between X-ray and optical and millimeter observables. This analysis is not a robust as for redMaPPer, thus further work is needed to present this results to the scientific community.

Contents

List of Tables

List of Figures

Chapter 1

Introduction

1.1 Introduction to Galaxy Clusters

Galaxy clusters are the largest gravitationally bound structures in the Universe. Early studies by Zwicky, 1933a on the Coma cluster found that masses inferred from the measured velocity dispersion exceeds the mass of the stars in the cluster by a factor of $\sim 200-400$, with this evidence Zwicky postulated the existence of an extra none visible component, dark matter.

Clusters are multi-component systems consisting of baryons, in the form of a hot intracluster medium (ICM) (12%) and stars (1.3%), and dark matter (87%) (Loewenstein, 2003). The ICM is mostly composed of ionized hydrogen and helium, it also contains heavy elements such as iron, nickel, silicon, sulfur, argon, and calcium. Rich clusters can contain hundreds or even thousands of galaxies.

Galaxy clusters are cosmological and astrophysical laboratories for testing models of structure formation, galaxy evolution, and the thermodynamics of the ICM. Their large masses make them a useful probe of the growth of structure over cosmological time, thus providing cosmological constraints that are complementary to other probes (Kravtsov and Borgani, 2012).

The temperature of the ionized gas that compounds the majority of the intra cluster media scales with the total mass of the cluster (Vikhlinin et al., 2009, **Mantz2010 Mantz2016**). Thus, knowing the cluster mass at different periods allows to study the evolution of clusters and lastly, the evolution of matter in the Universe.

1.1.1 Cluster Observables

Clusters offer multiple observable signals across the electromagnetic spectrum. At X-ray wavelengths, the hot ICM emits thermal Bremsstrahlung radiation[1]. Stellar emission from galaxies and intracluster light dominates the optical near-IR. At millimeter wavelengths, clusters are visible due to inverse Compton scattering of photons from the cosmic microwave background. Figure 1.1 taken from Allen, Evrard and Mantz, 2011 shows the cluster Abell 1835 observed in the X-ray (Chandra X-ray Observatory), optical (CFHT) and millimeter wavelengths (WMAP).

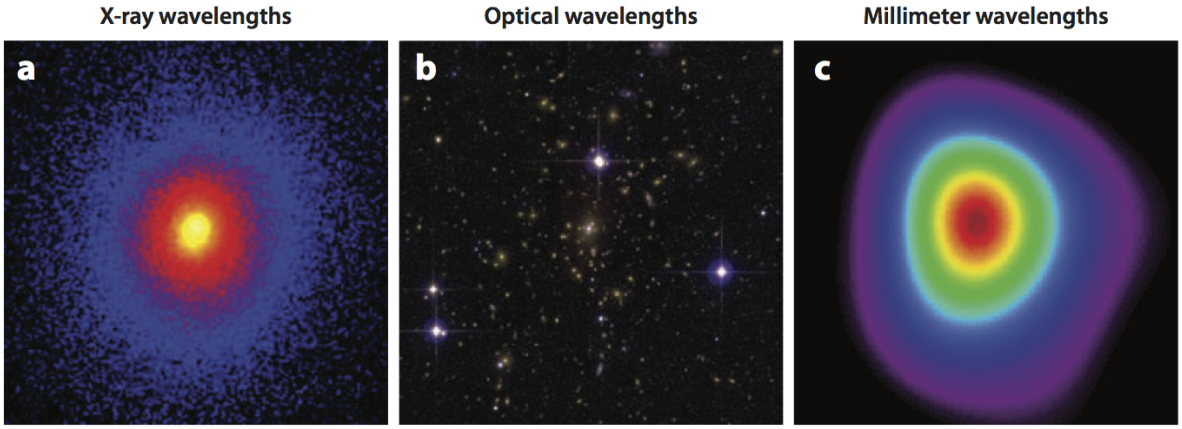

Figure 1.1: Figure and caption taken from Allen, Evrard and Mantz, 2011: Images of Abell 1835 at (a) X-ray, (b) optical, and (c) millimeter wavelengths, exemplifying the regular multiwavelength morphology of a massive, dynamically relaxed cluster.

X-ray Emission Mechanism

The following description of X-ray emission mechanisms is based on Sarazin, 1986. The Bremsstrahlung emissivity at a frequency ν of an ion of charge Z in a plasma with an electron temperature T_g is given by:

$$\epsilon_\nu^{ff} = \frac{2^5\pi e^6}{3m_e c^3}\left(\frac{2\pi}{3m_e k}\right)^{1/2} Z^2 n_e n_i g_{ff}(Z, T_g, \nu) T_g^{-1/2} \exp(-h\nu/kT_g), \tag{1.1}$$

where n_e and n_i are the number density of electrons and ions, respectively. g_{ff} is the Gaunt factor that corrects for quantum mechanical effects and for the effect of distant collisions. If the ICM is mainly at a single temperature, then Equation 1.1 indicates that the X-ray spectrum should be close to an exponential of the frequency.

[1] In a ionized gas (plasma), free electrons are continually accelerated by the slow moving ions, thus producing radiation.

At the high temperatures which predominate in clusters, thermal bremsstrahlung is the dominant X-ray emission process, this emission is mainly from hydrogen and helium. The X-ray line emission is mainly the result of electron collisions and it is given by

$$\int \epsilon_{\nu}^{line} = n(X^i) n_e \frac{h^3 \nu \Omega(T_g) B}{4\omega_{gs}(X^i)} \left[\frac{2}{\pi^3 m_e^3 k T_g}\right]^{1/2} \exp(-\Delta E/kT_g), \tag{1.2}$$

where $h\nu$ is the energy of the transition, ΔE is difference between the ground state and excitation energy, B is the probability that the upper state decays, and Ω is the transition strength (it is not a cosmological density parameter), and $\omega_{gs}(X^i)$ is the statistical weight of the energy levels of the ion.

When a cluster reaches equilibrium, the intracluster medium is in collisional equilibrium as well. From equation 1.2 we conclude that the X-ray emission is proportional to the density of protons and electrons. Luminosity is then defined as:

$$L_{\nu} \equiv \Lambda_{\nu}(T, Z) \int n_e n_p dV, \tag{1.3}$$

and the X-ray surface brightness is

$$I_{\nu} \equiv \Lambda_{\nu}(T, Z) \int n_e n_p dl, \tag{1.4}$$

here Λ_{ν} is the cooling function, it encodes the emitted energy per volume for a plasma, given its temperature and emissivity.

Cluster Observables in the Optical Band

Galaxy clusters were first found and studied using optical observations. Influential early catalogues of nearby ($z < 0.2$) clusters include Zwicky, 1933b, and Abell, Corwin, Harold G. and Olowin, 1989. The optical and near-infrared emission from galaxy clusters is predominantly starlight, the galaxy population of clusters are dominated by ellipticals and lenticulars galaxies. It is well known that galaxies in rich environments tend to be passive, i.e. have little or no ongoing star formation. This means that galaxies in clusters gather into a tight locus on colour-magnitude relations, known as the red sequence (Visvanathan and Sandage, 1977). In this thesis we make extensive use of the red sequence Matched filter Probabilistic Percolation (redMaPPer) (Rykoff et al., 2013) cluster catalogs (described in detail in Chapter 2).

The most important optical observables for a cluster are its richness (i.e. the number of galaxies within a defined aperture), the total optical/near-IR luminosity, the galaxy velocity dispersion, and the colour-magnitude relation. For an in-depth review of these observables, the reader is referred to Stott et al., 2009; Voit, 2005.

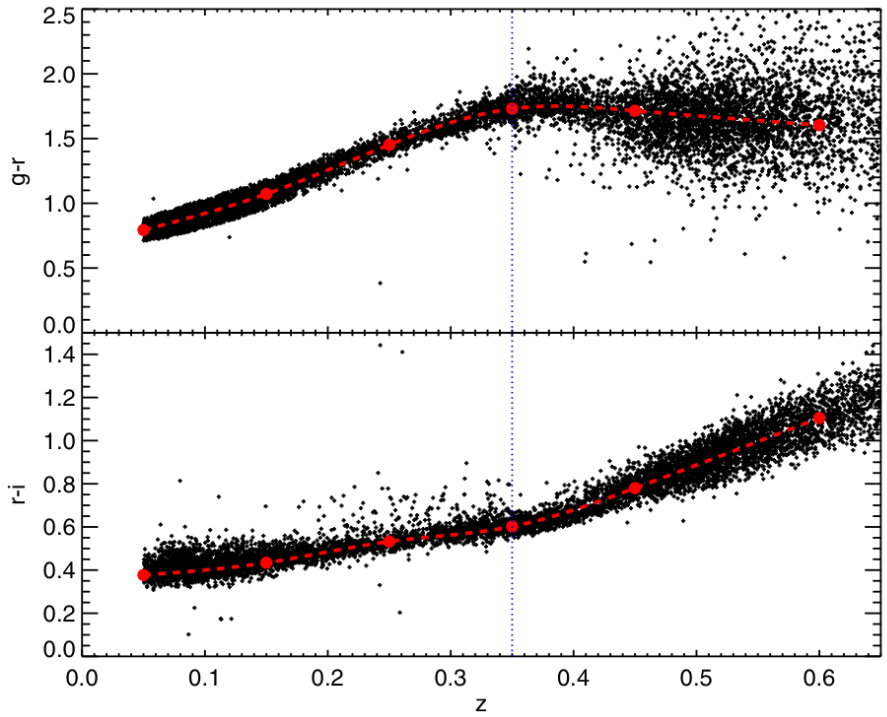

Figure 1.2: Figure taken from Rykoff et al., 2013: Sample of red sequence spectroscopic galaxies selected from SDSS DR8. Top panel shows $g - r$ color and bottom panel $r - i$ color.

Clusters Observables in the Millimeter Band

Hot gas in clusters can also be observed through its effect on the cosmic microwave background (CMB). Sunyaev and Zeldovich, 1970, predicted that hot gas in galaxy clusters will distort observations of CMB photons due to inverse Compton scattering with the hot ICM, this is called the thermal Sunyaev-Zeldovich (SZ) effect. The motion of a cluster with respect to the CMB produces an additional distortion, known as the kinetic Sunyaev-Zeldovich effect. The SZ effect is distance independent, unlike optical and X-ray brightness. Thus, a dedicated SZ cluster survey efficiently finds clusters out to arbitrarily high redshifts (Voit, 2005). The magnitude of the effect is proportional to the line-of-sight integral of the product of the gas density and temperature:

$$Y_{SZ} \propto \int n_e T dV, \tag{1.5}$$

The so-called Compton-Y parameter provides information of the total thermal energy of the electrons from which it is possible to derive the total gas mass within a certain volume, if the gases mass is proportional to the total cluster mass for any particular region, then Y_{SZ} can be used to calculate cluster masses.

Gravitational Lensing by Clusters

One of the predictions from general relativity is that massive objects curve space-time, so that the path of photons passing near these objects will bend, this phenomenon is known as gravitational lensing. This effect can both magnify and distort the images of background galaxies. Gravitational lensing can be detected in the statistical appearance of background galaxies observed through clusters and in the open field. Given that the space time is modified by all the mass of all the cluster components, gravitational lensing can be used to calculate not only the mass associated with galaxies and the ICM but also the mass correspondent to dark matter, and therefore the total mass of a cluster.

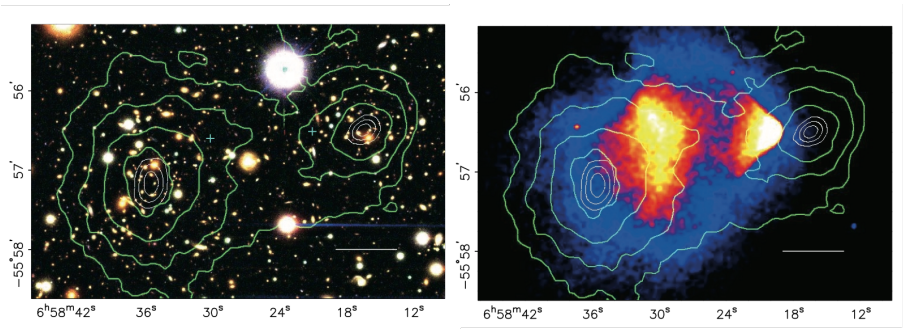

Figure 1.3: Figure and caption taken from Clowe et al., 2006: (Left) Color image from the Magellan images of the merging cluster $1E\ 0657-558$, with the white bar indicating 200 kpc at the distance of the cluster. (Right) Chandra image of the cluster. Shown in green contours are the weak lensing reconstructions. The blue plus signs show the locations of the centres used to measure the mass of the hot gas.

1.2 Basic Concepts in Cosmology

ΛCDM is the standard model of Cosmology adopted by the community. It assumes the components of the universe are dark energy (in the form of a cosmological constant), dark matter and baryonic matter. It further assumes the cosmological principle, i.e. that the universe is homogeneous and isotropic on large scales. The metric that describes a universe that follows the cosmological principle is the Friedmann-Robertson-Walker (FRW) metric,

$$ds^2 = -dt^2 + a^2(t)\left[\frac{dr^2}{1-kr^2} + r^2 d\theta^2 + r^2 \sin^2\phi^2\right], \tag{1.6}$$

where r, θ, ϕ are comoving spatial coordinates, t is time, and the expansion is described by the cosmic scale factor $a(t)$. The quantity k is the curvature of 3-dimensional space: $k = 0$ corresponds to a spatially flat, Euclidean universe, $k > 0$ to positive curvature and

$k < 0$ to negative curvature. By solving the field equations of General Relativity with the FRW metric, it is possible to obtain the Friedmann equations,

$$H^2 = \frac{8\pi G\rho}{3} - \frac{k}{a^2} + \frac{\Lambda}{3}, \tag{1.7}$$

$$\frac{\ddot{a}}{a} = -\frac{4\pi G}{3}(\rho + 3p) + \frac{\Lambda}{3}, \tag{1.8}$$

$$\dot{\rho} = -3H(\rho + p), \tag{1.9}$$

where $H \equiv \dot{a}/a$ is the Hubble parameter, an overdot denotes a time derivative, ρ is the total density of the universe (sum of matter, radiation, dark energy) and p is the total pressure (sum of pressures of each component), Λ is the cosmological constant. Equation 1.9 describes the conservation of energy, thus the evolution of energy density is controlled by the ratio of the pressure to the energy density $\omega_i \equiv p_i/\rho_i$.

Some of the cosmological quantities used in this thesis are described below.

The wavelength λ of moving photons though the universe scale with $a(t)$, and the redshift of light emitted from a distance source at time t_e,

$$1 + z = \frac{\lambda_o}{\lambda_e} = \frac{1}{a(t_e)}, \tag{1.10}$$

λ_o is the observed wavelength.

The Friedmann equation 1.7 can be rewritten as

$$\left(\frac{\dot{a}}{a}\right)^2 = H(z)^2 = H_0^2 E(z)^2, \tag{1.11}$$

where H_0 is the Hubble constant and takes measured values between (67−72) [(km/s)/Mpc] (Bonvin et al., 2017, Alam et al., 2016, Ade et al., 2016). In this thesis, where needed, we assume a value of $H_0 = 70$ (km/s)/Mpc. $E(z)$ depends on the assumed cosmological model, for ΛCDM it is,

$$E(z) = \sqrt{\Omega_m(1+z)^3 + \Omega_\Lambda}, \tag{1.12}$$

the density of a universal component is expressed as $\Omega_i = \rho_i/\rho_c$, the critical density of the universe is defined as $\rho_c \equiv 3H_0^2/8\pi G$. Thus, Ω_m is the matter density (both baryonic and dark matter) and Ω_Λ is the dark energy density. The density of the radiation and relativistic particles (Ω_R) is small enough to not be considered in the present epoch of the universe.

The universe has three main distinct eras: radiation dominated ($z \gtrsim 3000$), matter dominated ($300 \gtrsim z \gtrsim 0.5$), and dark energy dominated ($z \lesssim 0.5$). Figure 1.4 taken from Frieman, Turner and Huterer, 2008, illustrates the evolution of each component through cosmic time.

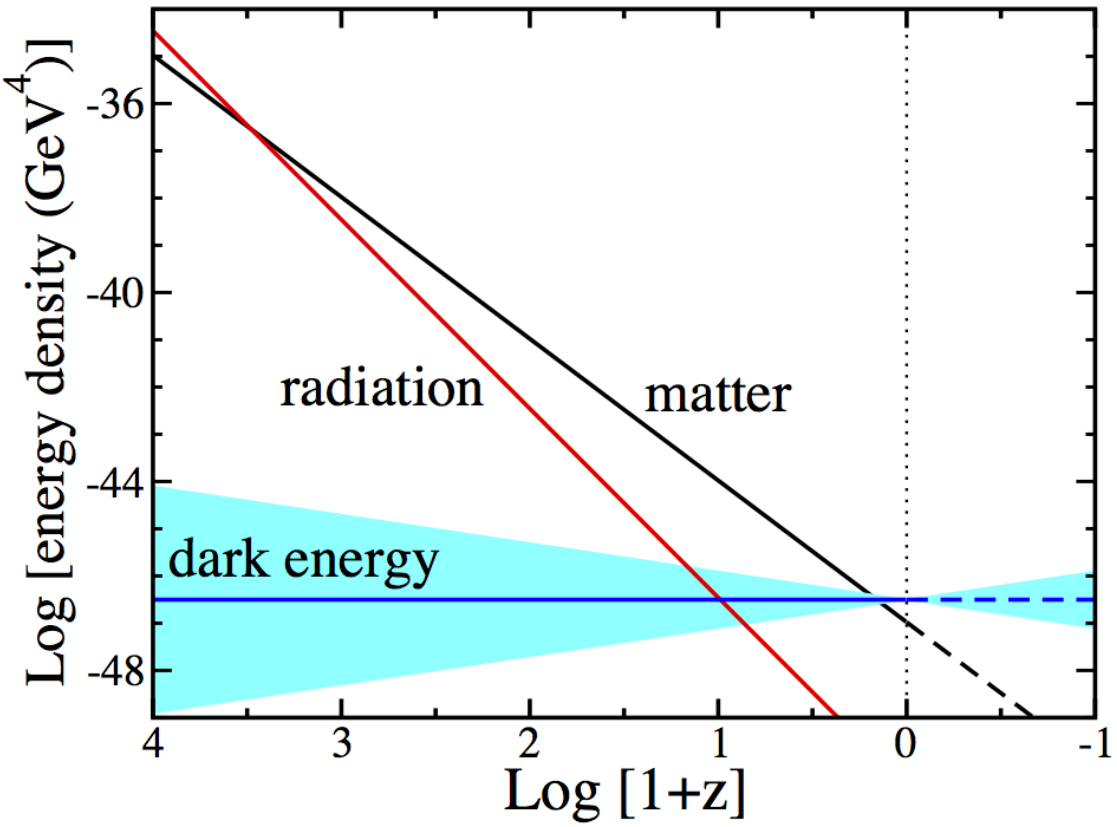

Figure 1.4: Figure and caption taken from Frieman, Turner and Huterer, 2008: Evolution of radiation, matter, and dark energy densities with redshift. For dark energy, the band represents $\omega = -1 \pm 0.2$.

For an object with intrinsic luminosity L and measured flux F, the luminosity distance d_L is given by:

$$d_L \equiv \sqrt{\frac{L}{4\pi F}} = (1+z)r(z), \tag{1.13}$$

where $r(z)$ is the comoving distance to an object at redshift z, this quantity is defined as

$$r(z) = \int_0^z \frac{dz'}{H(z')} = \int_{1/(1+z)}^1 \frac{da}{a^2 H(a)}. \tag{1.14}$$

The angular-diameter distance d_A, is the distance inferred from the angular size $\delta\theta$ of a distant object of a fixed diameter D, is defined by

$$d_A \equiv \frac{D}{\delta\theta} = \frac{r(z)}{1+z} = \frac{d_L}{(1+z)^2}. \tag{1.15}$$

The comoving volume element per unit solid angle $d\Omega$ is given by

$$\frac{d^2V}{dz d\Omega} = r^2 \frac{dr}{dz} \frac{1}{\sqrt{1-kr^2}} = \frac{r^2(z)}{H(z)}. \tag{1.16}$$

Dark energy has an equation of state, that could be defined simply as

$$\omega = \frac{p_\lambda}{\rho_\lambda} \tag{1.17}$$

where p_λ and ρ_λ are the dark energy pressure and energy density respectively. For ΛCDM, dark energy is described by the cosmological constant and $\omega = 1$.

1.3 The Self-similar model

The self-similar model was proposed by Kaiser, 1986. It states that spherical dark matter halos of fixed mass and redshift are identical, and their properties scale according to simple power-laws. In general an object is said to be self-similar when each portion of itself can be considered a reduce-scale image of the whole. From the mathematical point of view, a self-similar function is invariant under dilatation.
The self-similar model makes three general assumptions:

1. Dark matter halos form via gravitational collapse from peaks in the initial density field in the Einstein-de Sitter universe ($\Omega_m = 1$). Gravitational collapse is scale free.

2. The amplitude of density fluctuations is a power-law function of their size, $P(k) \propto k^n$ (k is the wavevector.)

3. Physical processes effecting baryons within the halos do not introduce new scales in the problem.

The argument of self-similarity holds for collisionless particles, such as dark matter where gravity is the only force acting on the particles. However, from numerical simulations (e.g. Navarro, Frenk and White, 1995) there is evidence that self-similarity holds for the gas component if the effects of gravity and shock heating are included.

1.4 Cluster Scaling Relations

Scaling relations are functions that relate cluster observables (e.g. X-ray temperature, luminosity, optical richness) with the total cluster mass and redshift (Giodini et al., 2013; Allen, Evrard and Mantz, 2011; Mantz et al., 2014a). These functions are important for obtaining cosmological constraints. They also provide useful astrophysical information because they are the result of physics of cluster formation and evolution. If gravity is the dominant process in clusters, then we can use the self-similar model to predict simple

scaling relations between cluster properties and the total mass (Kaiser, 1986). In this scenario, the scaling of cluster observables with mass and redshift follow power laws.
Following Allen, Evrard and Mantz, 2011 notation, let $s_i = \ln(S_i)$ for each of the N observables S_i and let $\mu = \ln M$ where M is the total mass of the cluster, the power-law assumption transforms to log-linear scaling

$$\bar{s}(\mu, z) = \mathbf{m}\mu + \mathbf{b}(z), \tag{1.18}$$

$\bar{s}$ denotes the average of parameter s over a large cosmic volume. the elements of $\mathbf{m}$ are the slopes of the individual observable-mass relations, and the intercepts $\mathbf{b}(z)$ reflects the evolution at fixed mass.
Several simple relations between X-ray observables can be predicted. Consider the mass contained in a sphere with radius T_Δ with a overdensity that is defined in terms of the critical density $\Delta(\rho_c)$ (see Section 1.2):

$$M_\Delta = \frac{4\pi}{3}\Delta R_\Delta^3. \tag{1.19}$$

Galaxy clusters are considered to be in hydrostatic equilibrium when the pressure gradient balances the gravitational force, under this equilibrium the virial relation holds,

$$MT_{gas} \propto \frac{GM}{R_{vir}}, \tag{1.20}$$

if we consider the virial radius R_{vir} similar to R_Δ then it is possible to combine Equations 1.19 and 1.20 to obtain a relation between the temperature and mass,

$$\begin{aligned} T_{gas} &\propto M^{2/3}\rho_c^{1/3}, \\ T_{gas} &\propto M^{2/3}H^{2/3}, \\ M &\propto T_{gas}^{3/2}E^{-1}(z), \end{aligned} \tag{1.21}$$

where $E(z)$ and H (from Equations 1.7, 1.12) has been used. $T_{\rm gas}$ is not the same as the spectroscopic temperature $T_{\rm X}$ derived from the X-ray spectrum, although, in practice, deviations from $T_{\rm X}$ and $T_{\rm gas}$ are small (Kravtsov and Borgani, 2012).

The most studied X-ray scaling relation is $L_{\rm X} - T$ and it remains as the best studied one (Mitchell et al., 1979; Mushotzky, 1984; Allen, Schmidt and Fabian, 2001; Reichert et al., 2011; Mantz et al., 2016).
The bolometric luminosity of a cluster is given by:

$$L_{\rm X} = \int \epsilon(T, n) dV, \tag{1.22}$$

if the particles only interact collisionally (as expected by self-similarity):

$$\epsilon(T,n) = n_i n_e \Lambda(T,Z) \propto n_i n_e \Lambda_0 T^{1/2}, \tag{1.23}$$

when the cluster is isothermal, the luminosity can be written as

$$L_{\rm X} = \Lambda_0 T_g^{1/2} \int n_i n_e dV, \tag{1.24}$$

The number density of ions and electrons is proportional to the total density of the cluster $n_i, n_e \propto \rho$, thus,

$$\begin{aligned} L_{\rm X} &\propto \rho^2 T_g^{1/2} R^3 \\ L_{\rm X} &\propto \rho T_g^{1/2} M \end{aligned} \tag{1.25}$$

then for a particular overdensity $\Delta = n\rho/\rho_c$, then

$$\begin{aligned} L_{\rm X} &\propto \Delta \rho_c T_g^{1/2} M \\ L_{\rm X} &\propto E(z)^2 T_g^{1/2} M, \end{aligned} \tag{1.26}$$

finally from equation 1.21 we write the relation of $L_{\rm X}$ and T_g under self similarity:

$$L_{\rm X} \propto E(z) T_g^2. \tag{1.27}$$

In this model, clusters with the same temperature are more luminous at higher redshift. From equation 1.26, it is possible to obtain the relation between $L_{\rm X}$ and the total mass, clearing T_g from equation 1.21 and subtituting

$$\begin{aligned} L_{\rm X} &\propto E(z) \left(M^{2/3} E(z)^{2/3} \right)^2 \\ L_{\rm X} &\propto E(z)^{7/3} M^{4/3} \end{aligned} \tag{1.28}$$

1.5 Cosmology Constraints from Galaxy Clusters

1.5.1 Cluster Counts and Clustering

A wide characterization of the number of cluster and its properties at certain position and redshift, can provide a tool to constrain cosmological parameters. For a given survey, the expected number of clusters N_{ai} within a mass bin a and redshift bin i can be defined as (Allen, Evrard and Mantz, 2011):

$$N_{ai} = \frac{\Delta\Omega_i}{4\pi} \int_{z_i}^{z_{i+1}} dz \frac{dV}{dz} \int_{\ln M_a}^{\ln M_{a+1}} d\ln M \frac{dn}{d\ln M}, \tag{1.29}$$

where Ω is the solid angle (not a cosmology density parameter). Cosmology information is included through the mass function and the volume element dV/dz.

The mass function of a cluster is a description of the number of clusters with a given mass in a unit of comoving volume. This function can be predicted analytically (Press and Schechter, 1974). In order to apply this approach to constrain cosmology, it is necessary to consider that equation 1.29 needs to be corrected to add information from redshift uncertainties and possible counting errors from incompleteness and impurities on the survey.

Modeling the cluster counts numerically, Borgani, 2006 calculated the cluster mass function showing its relation with the assumed cosmological parameters, see Figure 1.5.

Observational studies have measured the cluster mass function, Vikhlinin et al., 2009 analyzed a sample of 85 bright clusters detected from Chandra and the ROSAT all sky survey, this study constrained the dark energy equation of state (equation 1.17) and the total matter density parameter, finding $\omega_0 = -1.14 \pm 0.21$ and $\Omega_m = 0.38 \pm 0.08$.

1.5.2 f_{gas} Test

Galaxy clusters are bounded structures, massive enough to be provide an almost fair sample of the matter content of the universe. The ratio of baryonic to total mass in clusters should closely match the ratio of the cosmological parameters Ω_b/Ω_m. Allen et al., 2008 defined the mass fraction of hot gas as

$$f_{gas} = \left(\frac{\Omega_b}{\Omega_m}\right), \tag{1.30}$$

where Ω_b is the baryon density parameter and Ω_m is the total matter density parameter, a sum of baryon and dark energy matter.

Measurements of the apparent evolution of the cluster X-ray gas mass fraction can also be used to probe the acceleration of the universe. f_{gas} is derived from the observed X-ray gas temperature and density profiles. Hydrodynamical simulations of large and relaxed clusters have shown that f_{gas} should be approximate constant with redshift (Crain et al., 2007).

Any inaccuracies in instrument calibration, as well as any bias in measured masses or in the X-ray temperature and density profiles, will cause the measured values of f_{gas} to be different from the true values. Mantz et al., 2014b incorporate total mass measurements from gravitational lensing into the f_{gas} model, defining a complete model for f_{gas}

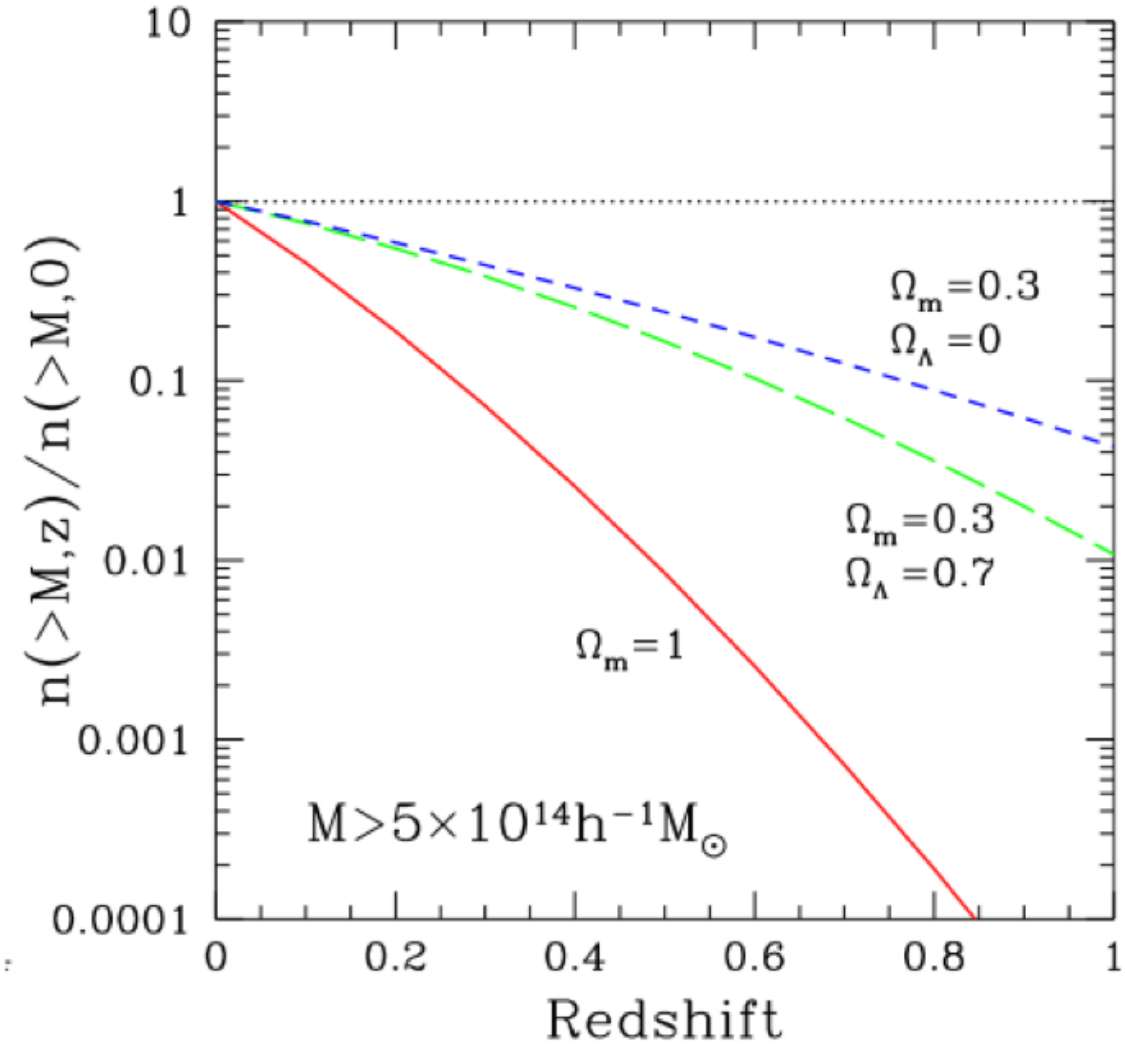

Figure 1.5: Figure taken from Borgani, 2006: Cluster mass function dependence on the assumed cosmology, each line represent a particular choice on the Ω_m and Ω_Λ density parameters.

calculation:

$$f_{gas}^{ref} = K(z) A \Upsilon_0 (1 + \Upsilon_1 z) \left(\frac{\Omega_b}{\Omega_m}\right) \left[\frac{d_a^{ref}}{d_a(z)}\right]^{3/2} \tag{1.31}$$

where $d_a(z)$ and d_a^{ref} are the angular diameter distances to the clusters for the test and reference cosmology (which is equation 1.15 assuming ΛCDM cosmology). The factor A accounts for the change in the angle subtended by r_{2500} as the underlying cosmology is varied, it has the form:

$$A = \left(\frac{\theta_{2500}^{\lambda\mathrm{CDM}}}{\theta_{2500}}\right)^{\eta} \approx \left(\frac{H(z) d_a(z)}{[H(z) d_a(z)]^{\Lambda\mathrm{CDM}}}\right)^{\eta}, \tag{1.32}$$

here, $\eta = 0.442 \pm 0.035$ defined as the slope of the f_{gas} profile at a relevant radius as

measured for the reference cosmology. The $K(z)$ function on equation 1.31 models the mean ratio of lensig to X-ray mass, and $\Upsilon_0(1 + \Upsilon_1 z)$ describes the depletion of X-ray emitting gas in the $0.8 - 1.2r_{2500}$ shell.

Analysis from Allen et al., 2004; Allen, Evrard and Mantz, 2011; Mantz et al., 2014a being the latest Mantz et al., 2014b where f_{gas} is used to constrain cosmological parameters were results from CMB (Planck, ACT and SPT), supernova and BAO data are combined with results from clusters. Figure 1.6 (top) presents the constrains on the dark energy equation of state and the total mass density, and (below) the constrains of dark energy and total mass densities. The best fitting values from the combined analysis are $\Omega_m = 0.304 \pm 0.016$ and $\Omega_{\rm DE} = 0.703 \pm 0.016$.

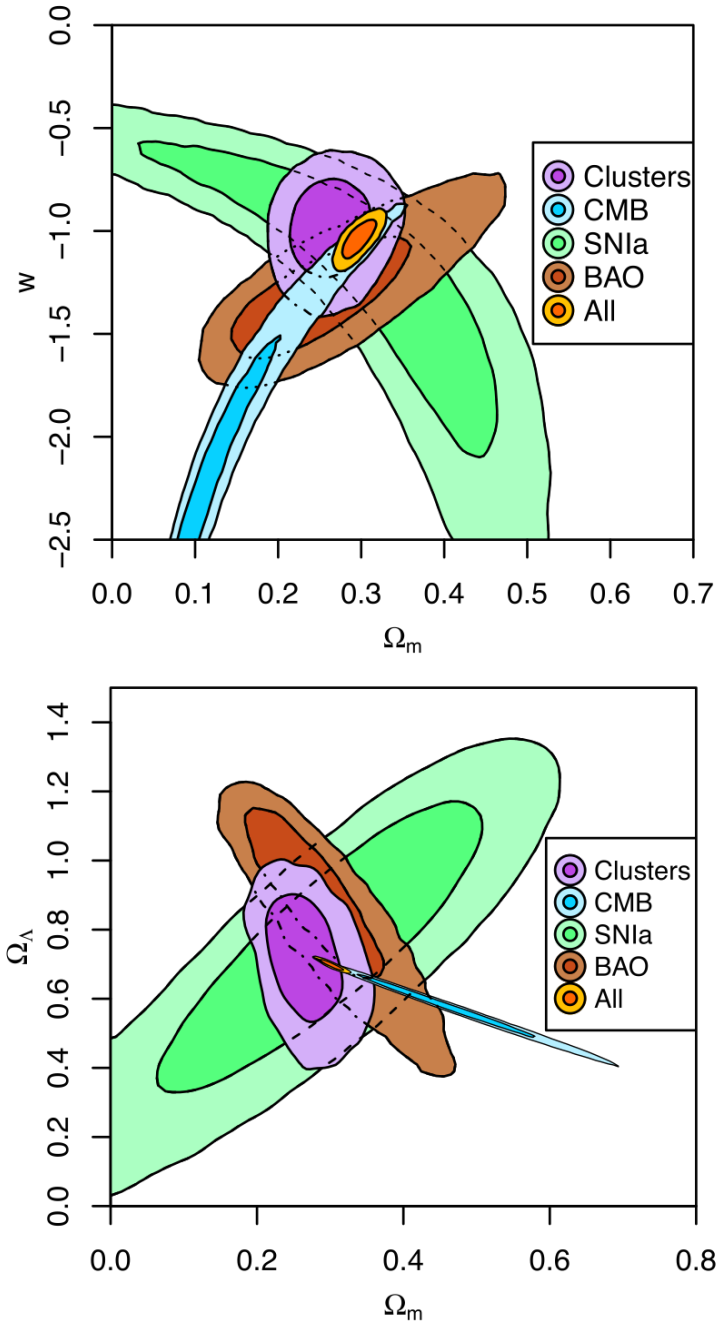

Figure 1.6: Figure taken from Mantz et al., 2014b: (Top) Cosmological constraints on the dark energy equation of state w and the matter density parameter Ω_m. Cluster constraints from the f_{gas} test are compared with results from CMB (Planck, ACT and SPT), supernova and BAO data. (Below) Constraints on dark energy and total mass densities. Dark and light shading, indicate the 68.3 and 95.4 per cent confidence regions.

1.6 XMM-Newton Space Observatory

The X-ray Multi Mirror Telescope (XMM-Newton) was launched on 1999. The 4 tonne, 10 meter long XMM-Newton spacecraft comprises two large payload modules connected by a long carbon fibre tube which form the optical telescope optical bench (Jansen et al., 2001, Figure 1.7.

The spacecraft has three degrees of stabilization, which allow it to aim at a target with an accuracy of 0.25 to 1 arcseconds. The instruments on board XMM-Newton are three European Photon Imaging Cameras (EPIC), two Reflection Grating Spectrometers (RGS), and an Optical Monitor.

The orbit of the telescope is highly eccentric, with a $\sim$ 48 hour period. The perigee is 7000 km and apogee of 114 000 km, while the inclination is $\sim -40°$. This orbit was chosen to allow all the cameras to be cooled to between $-80°$C and $-100°$C using only passive radiators.

1.6.1 XMM Instrumentation

European Photon Imaging Camera (EPIC)

The main focal plane instrument on XMM-Newton is the European Photon Imaging Camera (EPIC). The two MOS and the PN cameras offer the possibility to perform sensitive imaging observations over the field of view (30 arcmin), in the energy range from 0.15 to 15 keV with an angular resolution of 6.6 arcsec.

Two of the cameras employ Metal Oxide Semi-conductor (MOS) charged couple devices (CCD) (Turner, Abbey and Arnaud, 2000), the third camera used a new type of CCD (PN) (Strüder et al., 2001). All EPIC CCDs operate in photon counting mode with a fixed, mode dependent frame read-out frequency, producing tables with one entry per received event (event lists). These entries list properties such as the position at which photons are registered, their arrival time and their energies.

There are seven EEV type 22 front-illuminated CCDs in the focal plane of each MOS camera. The CCDs are buttable with a dead region of less than 300 microns wide on three sides; to minimise the dead space, adjacent CCDs are stepped about 1 mm to overlap by 300 microns. The imaging area is $\sim 2.5 \times 2.5$cm per CCD, the mosaic of seven covers 62mm in diameter, equivalent to 28.4 arcmin. Figure 1.8 illustrates the CCD arrange on the MOS cameras.

The PN camera has four individual quadrants each having three plane PN-CCD subunits

with a format 200×64 pixels are operated in parallel. The PN array was especially designed for the XMM-Newton FOV and mirror PSF having an imaging area of 6×6 cm, covering about 97% FOV. About 6 cm^2 of the sensible area of the CCD is outside the FOV and is used for background studies. Figure 1.9 illustrates the CCD array of the PN camera.

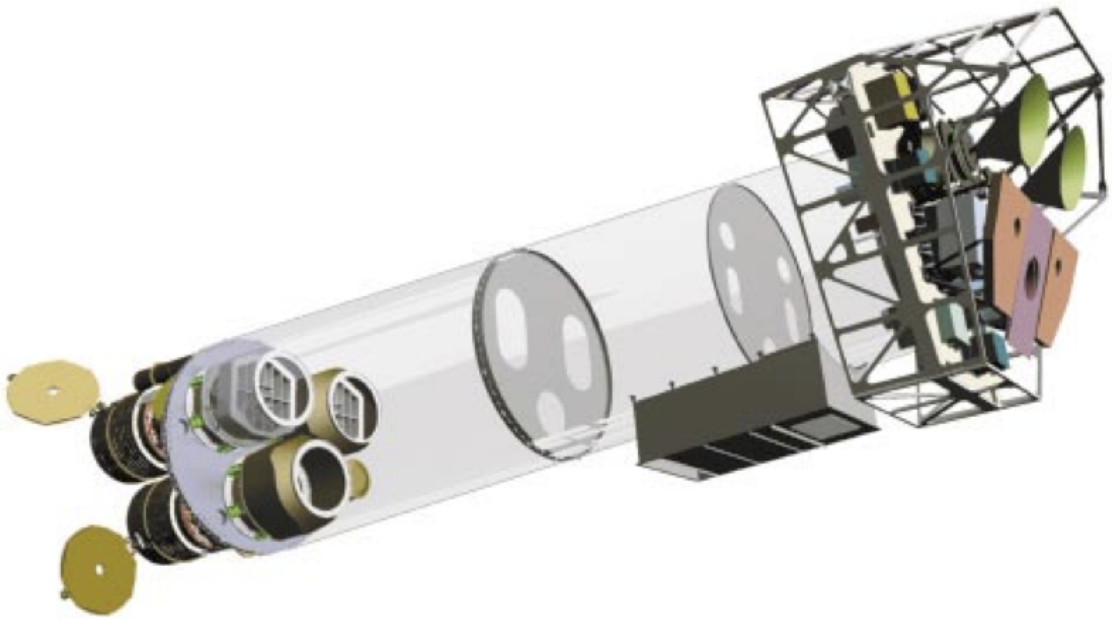

Figure 1.7: Figure and caption taken from Jansen et al., 2001: View of the XMM-Newton observatory, to the left the three mirrors modules (with RGA units mounted behind two of them) can be seen, while at the right the back-end of the instrument plataform with all the radiators is visible.

The quantum efficiency of a CCD is governed by the ability of incident photons to be absorbed in the depletion region of the sensor. It is the quantum efficiency of the EPIC-MOS chips that limits the energy passband at its hard energy end, while the PN camera can detect photons with high efficiency up to 15 keV. Figure 1.10 shows the behavior of the quantum efficiency for MOS and PN.

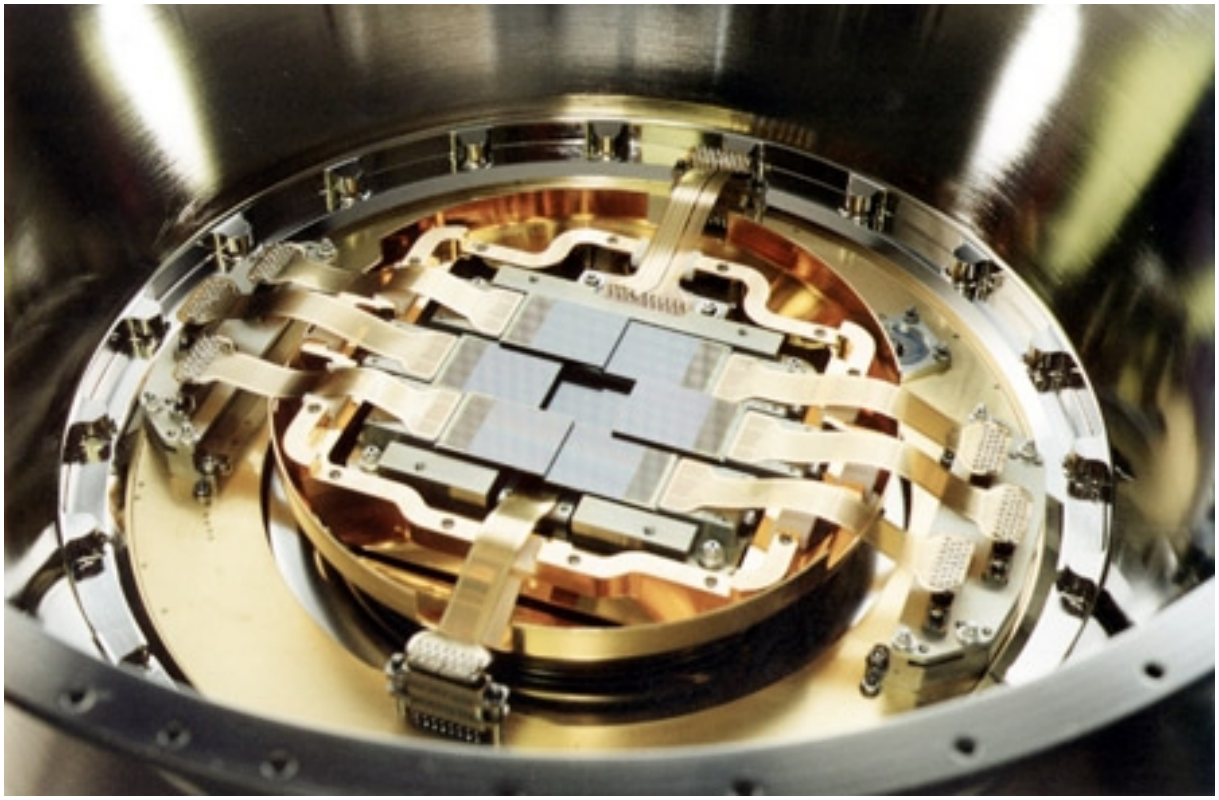

Figure 1.8: Figure and caption taken from Turner, Abbey and Arnaud, 2000: CCD array of the MOS cameras.

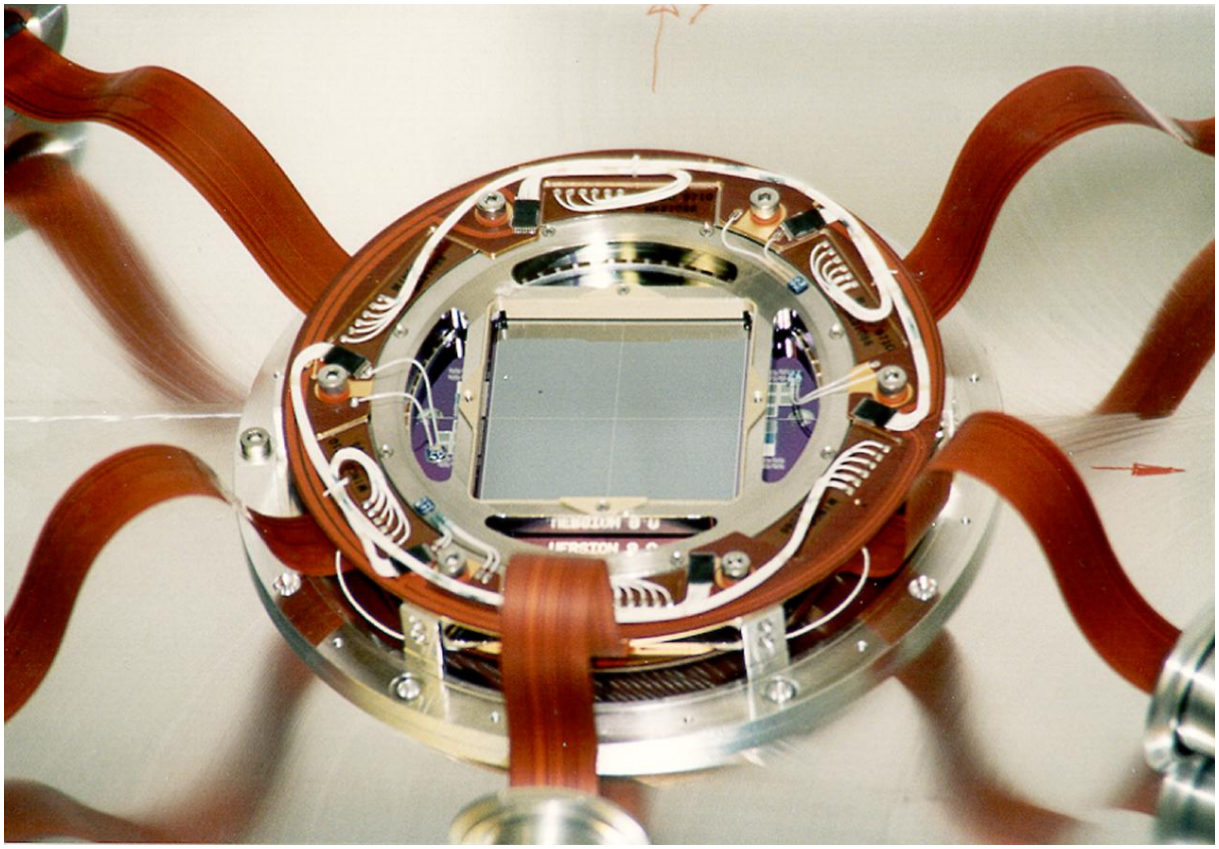

Figure 1.9: Figure and caption taken from Strüder et al., 2001: CCD array of the PN camera: The picture shows the twelve chips mounted and the connections to the integrated preamplifiers.

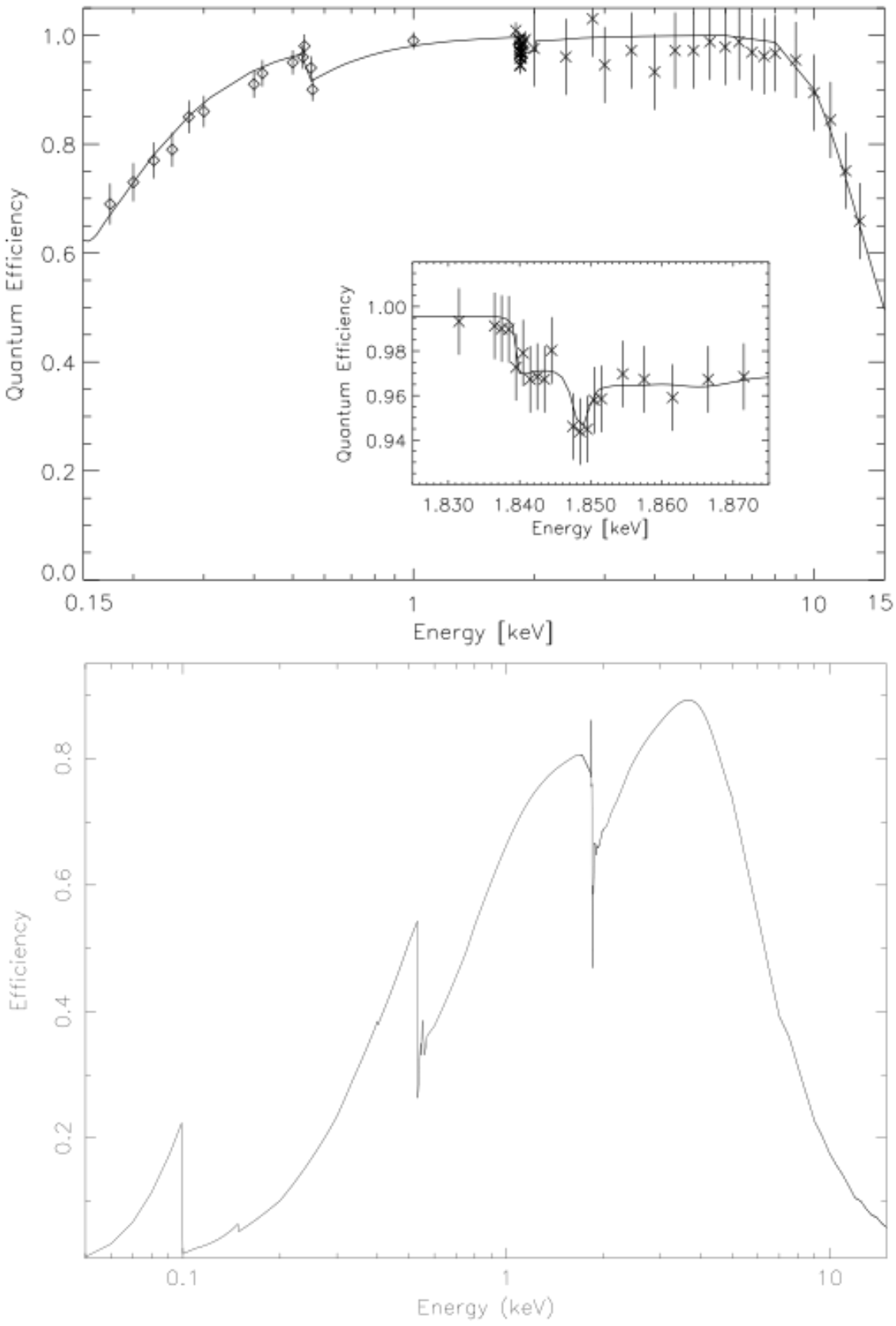

Figure 1.10: Figure taken from Turner, Abbey and Arnaud, 2000 and Strüder et al., 2001: Quantum efficiency for PN (top) and MOS (below).

The XMM-Newton Optical Monitor

The Optical/UV Monitor Telescope (XMM-OM) is mounted on the mirror support platform of XMM-Newton alongside the X-ray mirror modules. It provides coverage between 170 nm and 650 nm of the central 17 arcmin square region of the X-ray FOV, permitting routine multiwavelength observations of XMM targets simultaneously in the X-ray and ultraviolet/optical band (Mason et al., 2001).

The telescope module consists of a modified 30 cm Ritchey-Chretien telescope with focal ratio of $f/12.7$. The incoming light is reflected by a mirror inclined at an angle of 45° to one of two redundant detectors. The light falls onto the primary mirror, which reflects it onto the secondary, from where it goes to the inclined mirror that reflects it onto the detector, Figure 1.11 illustrates the schematic of XMM-OM. (Note that XMM-OM data are not used in this thesis.)

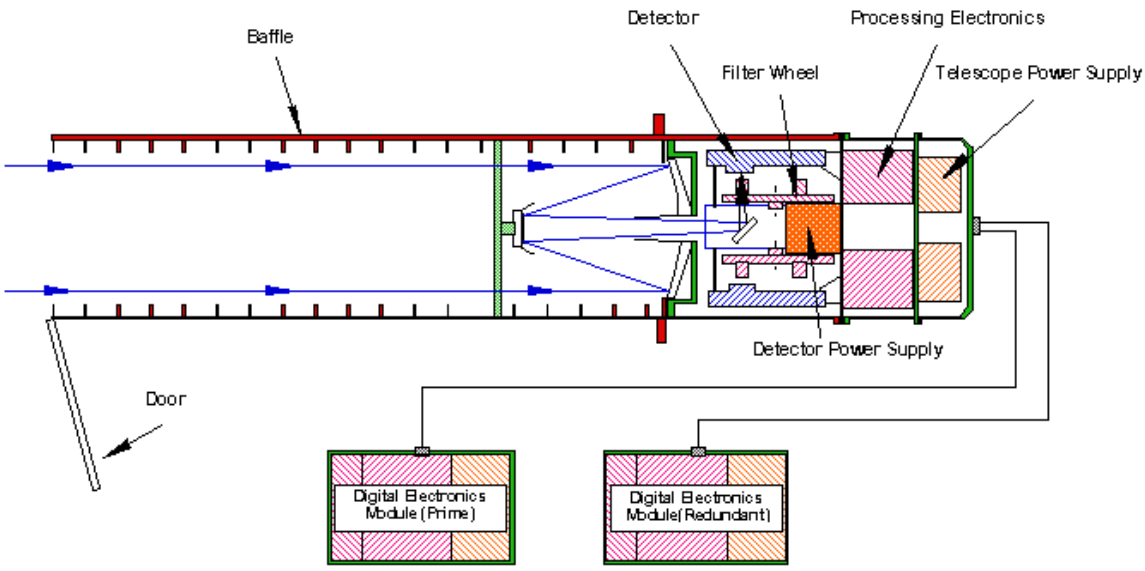

Figure 1.11: Figure taken from Mason et al., 2001: Schematic of XMM-OM telescope.

The Reflection Grating Spectrometer (RGS)

The RGS design incorporates an array of reflection gratings placed in the converging beam at the exit from the X-ray telescope. The grating stack intercepts roughly half of the X-ray light and deflects it a strip of CCD detectors offset from the telescope focal plane. The grating stack consists of 182 identical gratings, mounted at grazing incidence to the beam in the classical configuration. The gratings are located in a toroidal surface, formed by rotating the Rowland circle about an axis passing through the telescope focus and the first

order blaze focus (Den Herder et al., 2001).

The RGS instruments achieve high resolving power over a range from 5 to 35 Å[0.33 – 2.5 keV]. The effective area peaks around 15 Å[0.83keV] at about 150 cm^2 for the two spectrometers. Schematic layout of RGS is in Figure 1.12. (Note that XMM-OM data are not used in this thesis.)

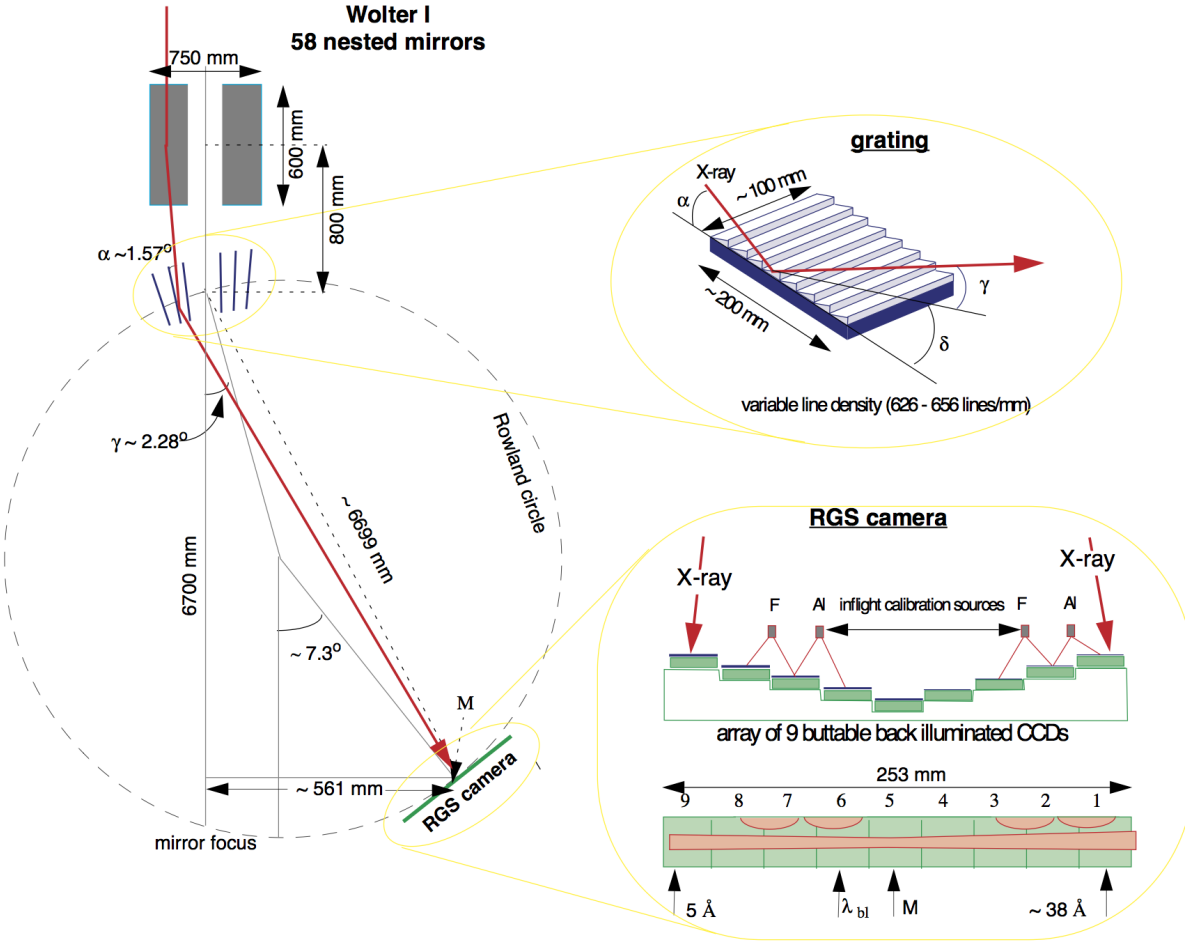

Figure 1.12: Figure taken from Brinkmam, Aarts and Den Boggende, 1998: Schematic layout of RGS.

1.6.2 Science data files and data flow

The XMM-Newton science data necessary to perform analysis is bundled into a data set known as Observation Data File (ODFs). The XMM Science Archive (XSA) contains all public XMM data including ODFs and preliminary processed EPIC images and RGS spectrum.

In order to process the ODFs, the data are correctly calibrated for further scientific analysis, this is done though the Current Calibration File (CCF) which is provided by XMM-Newton. The software used to perform interactive analysis of the data is also provided by the Survey Science Centre (SSC) and the Survey Operation Centre (SOC), the software known as the Science Analysis Sub-System (SAS, Section 2.3.1).

In Figure 1.13 (taken from Jansen et al., 2001) is the summary of the data flow in the XMM-Newton ground segment.

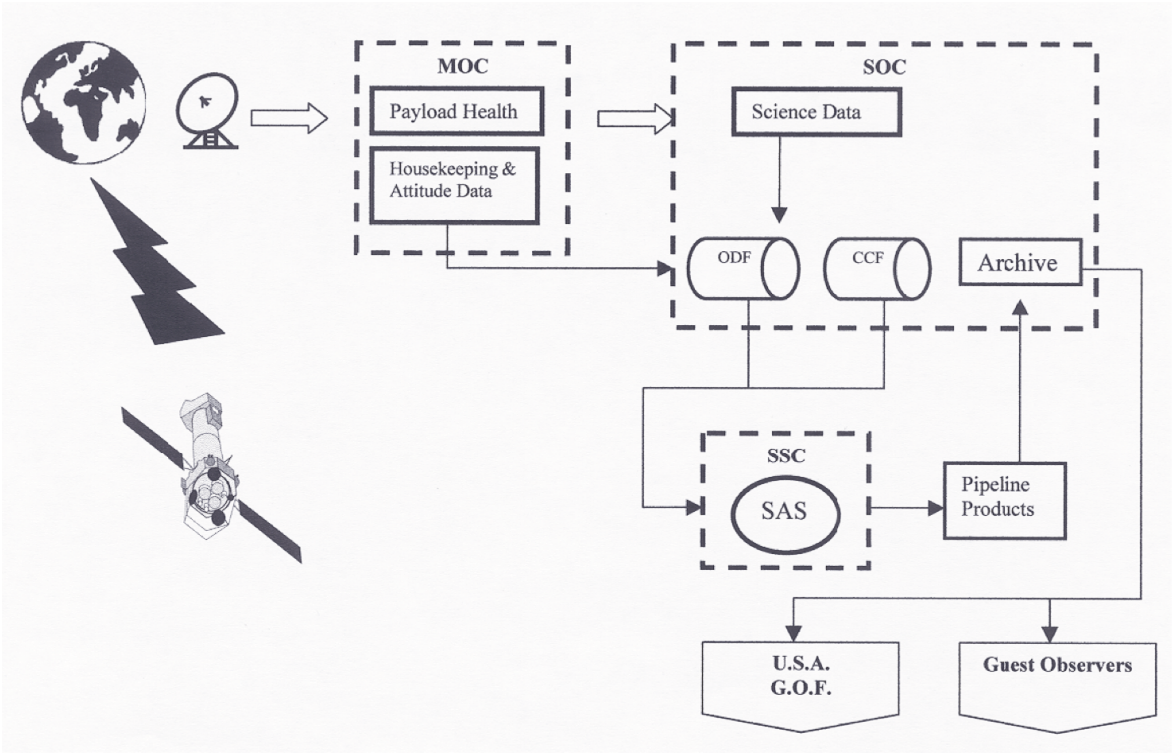

Figure 1.13: Figure and caption taken from Jansen et al., 2001: Summary of the data flow in the XMM-Newton ground segment.

1.7 Sloan Digital Sky Survey

We describe briefly the Sloan Digital Sky Survey (SDSS) (York et al., 2000). In this thesis we use the redMaPPer (SDSS DR8) catalog (Rykoff et al., 2013) to find clusters inside

the XMM observations and nearby XCS clusters (see Chapter 2 for a detail description).

Figure 1.14: Figure taken from Gunn et al., 2006: The SDSS 2.5m telescope, the mirror is enclosed in its rectangular wind baffle.

The SDSS survey uses a dedicated 2.5m telescope equipped with large-format mosaic CCD camera to image the sky in five optical bands, and two digital spectrographs to obtain the spectra of about 1 million galaxies and 100 000 quasars (York et al., 2000). The SDSS telescope is a $f/5$ Ritchey-Chretien wide-field altitude-azimuth telescope located at the Apache Point Observatory, Sunspot, New Mexico. The telescope achieves a very wide (3°) distortion-free field by the use of a large secondary mirror and two corrector lenses (Gunn et al., 2006). The SDSS imaging camera contains two sets of CCD arrays: The imaging array consists of 30 2048 × 2048 Tektronix CCDs, placed in an array of six columns and five rows, each row observes the sky through a different filter Figure 1.15 taken from Gunn et al., 1998 shows the camera array.

The redMaPPer algorithm was applied on SDSS eighth data release (DR8). DR8 (Aihara et al., 2011) is cumulative and includes all data from previous releases, it covers a total of $14,555$ deg^2 (~ 2500 deg^2 more than in DR7), Figure 1.17 shows the sky coverage of SDSS DR8. The sky-subtraction algorithm used by DR7 underestimated the brightness of large galaxies, DR8 reduces this problem by using an improved algorithm but it does not solve the problem completely. Also, the sky-subtraction algorithm used by DR7 has a problem with faint galaxies around bright galaxies suppressing the number density and distorting the shapes of those faint sources, DR8 has an improved sky subtraction (compared with DR7) reducing the number of faint galaxies assumed previously as background.

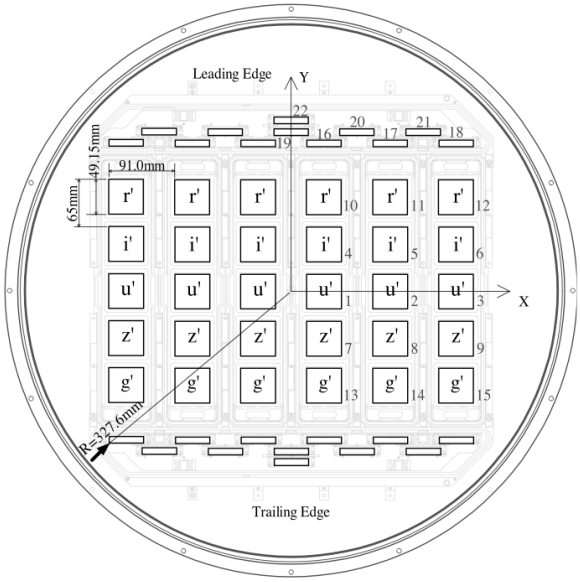

Figure 1.15: Figure and caption taken from Gunn et al., 1998: Optical layout of the focal plane of the SDSS camera. Field 22 are focus CCDs: fields $16-21$ are astrometric chips, and $1-15$ are the photometric array.

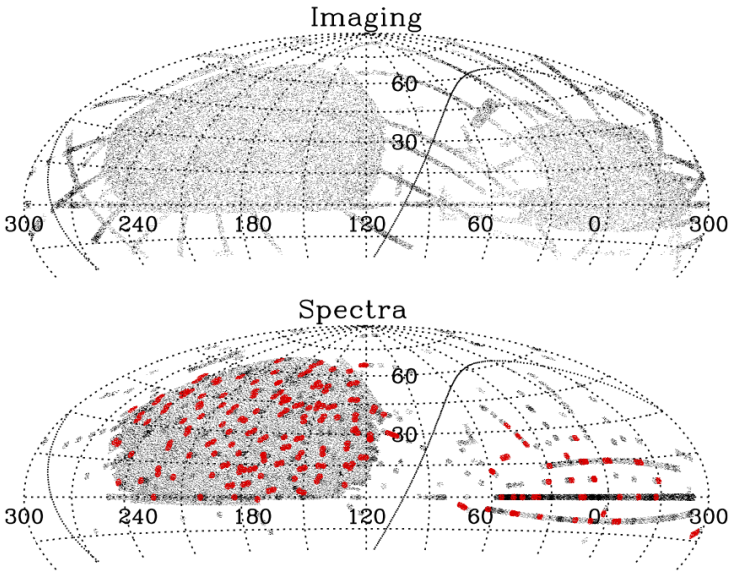

Figure 1.16: Figure and caption taken from Aihara et al., 2011: Sky coverage of DR8 in J2000 Equatorial coordinates, in imaging (upper) and spectroscopy (lower). Right ascension $\alpha = 120°$ is at the center of these plots.

Figure 1.17: Example of a galaxy (M51) observed with SDSS, image obtained with the SDSS sky server http://skyserver.sdss.org.

1.8 The Dark Energy Survey

The Dark Energy Survey (DES) (The Dark Energy Survey Collaboration, 2005) is an imaging survey of 5000 deg^2 of the southern sky, using a 570 megapixel camera on the Cerro Tololo Inter-American Observatory 4 m Blanco Telescope in Chile. The Dark Energy Camera (DECam) has a focal ratio at prime focus of $f/2.7$. The pixel scale was designed to be well matched with the image quality, 2 pixels correspond to 0.52 arcsec FWHM[2] DECam is optimized for the wavelength range $400-1000$ nm with four filters with nominal wavelength ranges: g band $(400-550$ nm). r band $(560-710$ nm), i band $(700-850$ nm), and z band $(830-1000$ nm), the DES images used during this thesis are made with the gri bands. Figure 1.18 show an example of the cluster XMMXCS J 224844.9-443141.7 observed by DES.

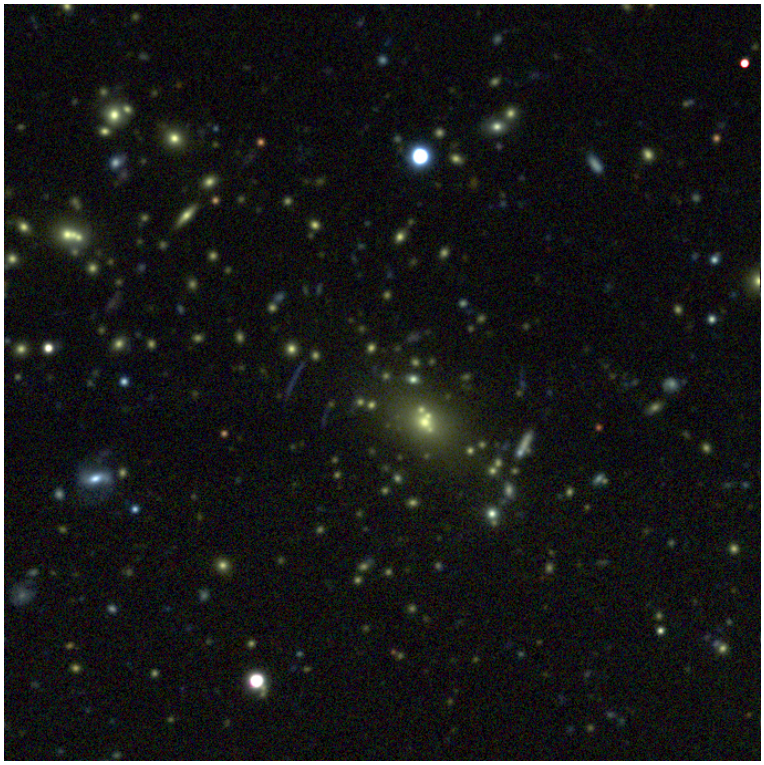

Figure 1.18: Example of DES observation (gri bands) of the cluster XMMXCS J 224844.9-443141.7, taken from the DESY1 data archive.

DECam has an array of 62 2048×4096 CCDs and 12 2048×2048 CCDs on its focal plane (see Figure 1.19), these 250 micron thick devices have high sensitivity and are designed to eliminate fringing. They achieve a quantum efficiency of $> 65\%$ in the z band, a factor ~ 10 higher than traditional astronomical devices (Flaugher et al., 2015).

[2]The technical term Full-Width Half-Maximum, or FWHM, is used to describe a measurement of the width of an object in an image.

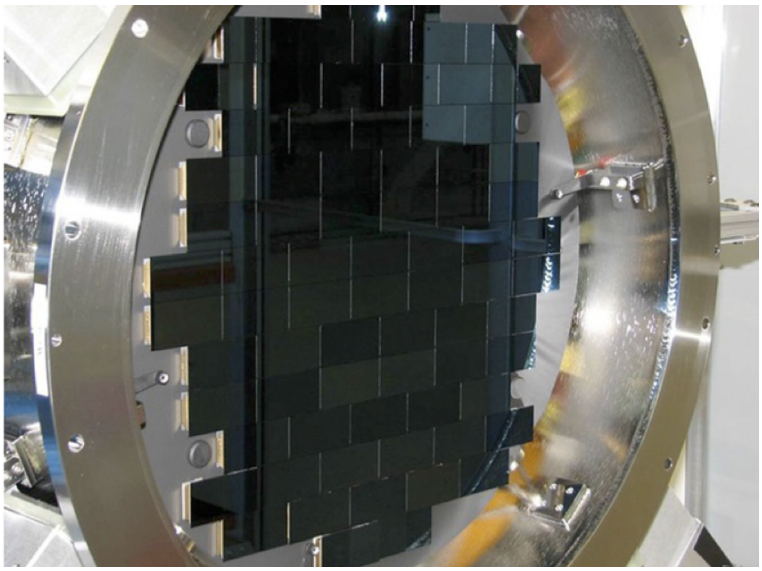

Figure 1.19: Figure taken from Flaugher et al., 2015: DECam focal plane showing the 62 2048×4096 CCDs and 12 2048×2048 CCDs.

1.8.1 The DES footprint

The DES footprint is shown in Figure 1.20. By design it overlaps with the SPT survey (Bleem et al., 2015), and the SDSS Stripe-82 survey (Jiang et al., 2014). Before the start of the main survey operations, there was a period of Science Verification (or SV). The SV region covers $\sim$ 250 deg^2 and has yielded dozens of science papers in its own right (e.g.Abbott et al., 2016a; Saro et al., 2017; Rykoff et al., 2016). At the time of writing, four of the five planned years of survey observations are complete.The sky coverage from years 1 and 2 (Y1 and Y2 hereafter) are shown in Figure 1.20. Already galaxy catalogues from SV+Y1+Y2+Y3, covering $\sim$ 5000 deg^2, are available to DES members. The depth and quality of those catalogues improves with every year of processed observations (the processing lags the observations by roughly 12 months due to its complexity). DES will yield 500M galaxies, all with associated photo-z and weak lensing shear estimates. Figure 1.20 also includes the 10 supernovae fields ($\sim$ 27 deg^2).

Science goals

The main goal of DES is to determine the dark energy equation of state w and other cosmological parameters to high precision (Abbott et al., 2016b). DES uses four complementary techniques to achieve its goals:

- Galaxy Clusters: The evolution of the galaxy cluster mass function and cluster spatial correlations provide a sensitive probe of the dark energy. DES provides

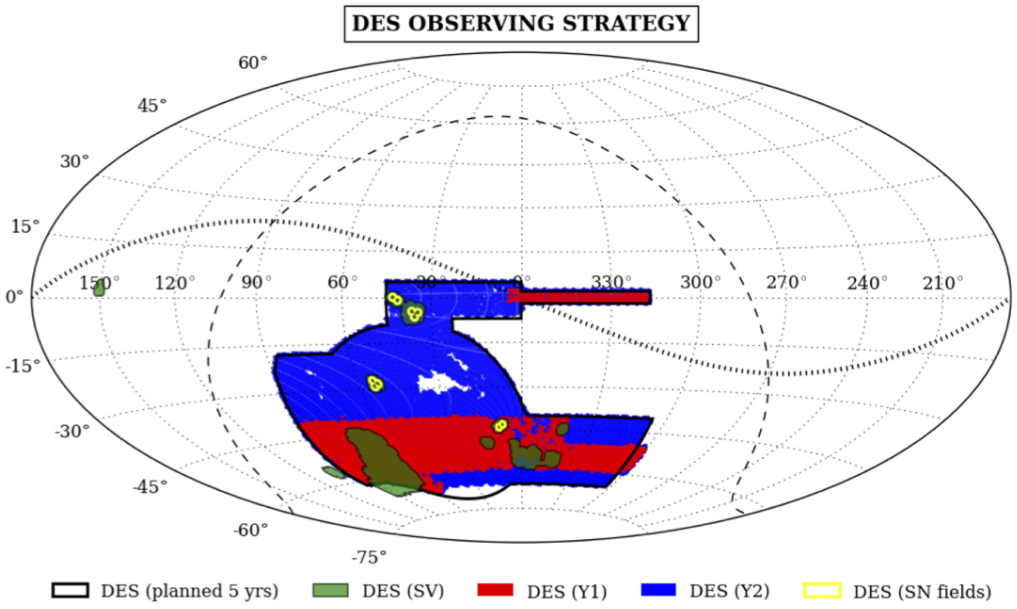

Figure 1.20: Figure and caption taken from Abbott et al., 2016b: Hammer projection in equatorial coordinates, with the dashed and dotted lines indicating the Galactic plane and the ecliptic plane, respectively. DES survey footprint for the SV, Y1, Y2 and the final 5 year survey.

detailed optical measurements of galaxy clusters including photometric redshifts.

- Weak Lensing: DES measure the weak lensing (WL) shear of galaxies as a function of photometric redshift. The evolution of the statistical pattern of WL distortions and the cross-correlation between foreground galaxies and background galaxy shear, are sensitive to the cosmic expansion history. DES measure shapes and photometric redshifts for ~ 300 million galaxies, enabling accurate measurement of lensing.

- Galaxy Angular Clustering: The galaxy power spectra has a broad peak as well as baryon wiggles arising from the baryon acoustic oscillations, these features serve as standard rules for distance measurements, providing a geodesic test for cosmological parameters. DES measure the angular clustering of galaxies in photometric redshift shells out to $z \sim 1.1$.

- Supernova Luminosity Distance: Type Ia supernovae provide distance estimates to constrain the properties of the dark energy. DES measure riz light curves for thousands (1 000 as of December 2015) type Ia supernovae in the redshift range $0.3 < z < 0.75$ though repeat imaging of 27deg^2 over 10 fields.

1.9 Thesis Overview

This thesis is organized as follows. In Chapter 2 we introduce the XMM Cluster Survey (XCS) and redMaPPer (RM) cluster catalogs from which X-ray and optical information is obtained. A description of the cluster finding methodology is also presented. In Chapter 3, we present a sample of RM clusters that have XCS counterpart within $1.5h^{-1}$Mpc and/or $3'$, the matching algorithm is described in detail. In Chapter 4 we present the third generation of the XCS Post Processing Pipeline (XCS3P-v3), this algorithm allows the calculation of spectroscopic X-ray temperature and bolometric luminosity, that are the observables to be scaled with optical richness. Differences with previous generations of XCS3P-v3 are described, this algorithm is validated by comparing the $L_{\rm X} - T_{\rm X}$ scaling relation with the results from previus generations. In Chapter 5 the XCS-RM (SDSS), XCS-RM (DES Y1) and XCS-RM (SDSS+DES Y1) are characterized, these samples remove previus multiple matches and all the clusters have passed an eye-ball examination in both X-ray and optical observations. Then, scaling relations are obtained between $T_{\rm X}$ and optical richness (λ), and $L_{\rm X} - \lambda$ for each of the three cluster samples mentioned above. Finally in Chapter 6 we validate the methodology described in Chapter 4, optical to X-ray scaling relations are obtained for two non-redMaPPer cluster catalogs, also microwave to X-ray scaling relations are also obtained for two SZ cluster catalogs (see Section 1.1.1).

Chapter 2

Data and Software Description

This thesis relies heavily on the outputs from two science collaborations: The XMM Cluster Survey and the RedMaPPer team. These projects are described below, together with details about the data inputs used in the thesis. We also describe below the software packages that have been essential to this thesis.

2.1 The XMM Cluster Survey

The XMM Cluster Survey (XCS) (Romer et al., 1999) collaboration is a multi-national team that aims to catalogue all clusters of galaxies that have been observed by the XMM-Newton satellite. This includes both serendipitous and targeted observations. The primary science goal of XCS is to constrain cosmological parameters using the evolution of abundance of clusters. Other goals include the determination of scaling relations, understanding the astrophysical processes and studies of galaxy evolution.

An initial data release (XCS-DR1) was made in 2012 (Mehrtens et al., 2012). XCS-DR1 covers a unique (non-overlapping) area of 276deg^2 (Lloyd-Davies et al., 2011) and included 3 675 clusters (993 with measured $T_{\rm X}$ values). At the time of writing, the beta version of XCS-DR2 (XCS-DR2-β hereafter) covered an unique area of $1,050$deg^2, following the analysis of over $9,000$ XMM observations (Rooney, 2015). An overview of the methodology underlying XCS-DR1 and XCS-DR2-β is provided in Sections 2.1.1 to 2.1.4 below (for a more in depth discussion, see Lloyd-Davies et al., 2011 and Rooney, 2015).

2.1.1 XCS Data reduction

XCS uses XMM data in the form of XMM observation data files (ODFs), there is an ODF file per observation, these data files are downloaded automatically into the Apollo super

computer for further reduction and processing. ODFs contain uncalibrated science files, which cannot be directly used for scientific analysis.

The tasks of acquiring and reducing XMM data, and of creating images, is done in XCS with an IDL[1] based pipeline known as: The XCS Event List Cleaning and Image Making Pipeline (or XIP).

The XIP pipeline creates calibration files for each observation using the command (Section 2.3.1) `cifbuild`. The next step is to extract information from the calibration database and incorporate this information into what is referred as the ODF summary file, this is done with the command `odfingest`. Event lists are created with `epchain` and `emchain` (for EPIC PN and EPIC MOS respectively). Event lists record the characteristics of incoming photons, i.e. information as to where, when, and with what energy, a photon hit occurred on an XMM detector.

Before the creation of any image using information from the event lists, it is necessary to account for background contamination. Some segments of an observation can be contaminated, these need to be removed before any further analysis takes place (i.e. image creation, source detection). XIP generates light curves in 50 seconds time bins in both the hard $(12-15$ keV) and soft $(0.1-1$ keV) bands. An example of the soft band light curve extraction for a PN event list is:

```
evselect 'raw_events_pn.fits' expression="#XMMEA_EP && (PATTERN <= 4) &&
(FLAG .eq. 0) && (PI in [100:1000])" rateset='raw_events_pn_lc.fits'
timebinsize=5- maketimecolumn=true
```

The soft band light curves account for instrumental noise, solar wind charge exchange, and high energy particles interacting with the structure in and around the detectors. the hard band line curves account for the quiescent particle background. An iterative three sigma clipping is then carried out on the light curves. The 50 seconds time bins that pass the clipping are saved as good time intervals.

2.1.2 XCS Image Production

Once the data has been reduced and cleaned, XIP generates single camera images by extracting data from the cleaned event lists in the $0.5-2.0$ keV and $2.0-10.0$ keV energy bands, making a two dimensional image using the `evselect` command, e.g.

```
evselect table=eventslist.fits withimageset=yes imageset=image.fits xcolumn=X
```

[1] http://www.harrisgeospatial.com/ProductsandSolutions/GeospatialProducts/IDL.aspx

```
ycolumn=Y imagebinning=binSize ximagebinsize=50 yimagebinsize=50 expression=
"#XMMEA EM && PI in [500:2000]" writedss=yes squarepixels=yes ximagesize=512
yimagesize=512 ximagemin=3649 ximagemax=48106 withxranges=yes yimagemin=3649
yimagemax=48106 withyranges=yes imagedatatype=Real64 ,
```

here `#XMMEA_EM` selects the events flagged as *good* (only events likely to be caused by an astronomical source have this classification). `PI in [500:2000]` specify the energy range ($0.5 - 2.0$ keV for this example), `ximagesize=512 yimagesize=512` produces an image of 512 sq pixels (with pixel size 4.35×4.35 arcsec^2).
Exposure maps are generated with the `eexmap` command, e.g.

```
eexpmap imageset=image.fits attitudeset=ATTHK.fits eventset=eventslist.fits
expimageset=expmap.fits pimin=500 pimax=2000
```

Exposure maps give an effective exposure time for each pixel in the image. The whole EPIC field of view is exposed for the same time, but these exposure maps consider instrumental effects such as chip gaps and vignetting. Examples of single camera images and their exposure maps are shown in Figure 2.1, 2.2 and 2.3.
XIP can produce images that merge all the available images and maps from each camera. MOS images and exposure maps must be scaled to replicate the sensitivity of the PN detector. The scaling requires the energy conversion factors (ECFs) that map camera count rate with energy flux. Energy fluxes are calculated with XSPEC by considering an absorbed power-law model (typical for AGN which are the predominant type of extragalactic X-ray source in the universe), and neutral hydrogen column that depends on the pointing position of the observation.
Not all the ObsIDs have information of the three cameras, in that case only the available observation are merged. Figure 2.4 shows an example of merged image and exposure map made from MOS1, MOS2 and the PN.

2.1.3 XCS Source Detection

XCS detect sources on XMM observations with the XCS Automated Pipeline Algorithm (XAPA), this software is based on WAVDETECT (Freeman et al., 2002). Using merged XMM images (produced by XIP), XAPA performs a wavelet analysis at nine different scales ($\sqrt{2}, 2, 2\sqrt{2}, 4, 4\sqrt{2}, 8, 8\sqrt{2}, 16, 32$ pixels). The analysis is done in two stages (run 1 and 2), first bright compact sources are located at scale 1 and 2. Then, sources found on

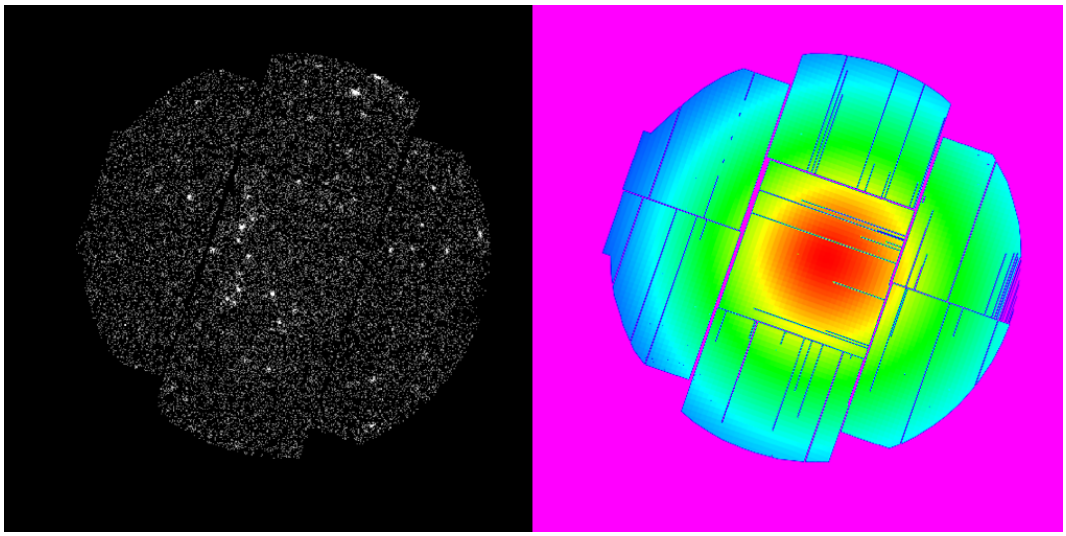

Figure 2.1: Example of a XIP image of the ObsID=0094310201, on the left is the image in the $(0.5 - 2.0$ keV) band. On the right is the exposure map, effective exposure is highest in the centre and then drops off due vignetting. Dark lines represent chip gaps and bad columns.

run 1 are masked out before a run 2 on scales 3 to 9, this measure is taken because bright sources can pollute the wavelet signal on large scales making false extended regions.

A source list is generated for each image, this sources are made by collecting significant pixels together into source cells. Multiple objects detected at multiple scales are filtered using a *vision model*. This model is able to recognize when a point source is embedded in an extended source by comparing maximum pixel values of each sources at each wavelet scale, we refer the reader to LD11 for more detail on this process.

During the run 1, some genuine extended sources can be excluded, to reduce this possibility, a cuspiness test is performed. A grid Q of 5×5 pixels is centred on each source detected during run 1, cuspiness is defined as

$$C = \frac{Q_{max} - Q_{min}}{Q_{max}}. \tag{2.1}$$

Real point sources have $C \geq 0.85$, if after run 1 a source have $C < 0.85$, then the source is removed from the list defined on run 1 so it is included for further analysis at run 2. The effect of the cuspiness test is exemplified on Figure 2.5 taken from LD11.

2.1.4 XCS Source Classification

Once the XAPA source finding subroutines have been run, it proceeds to classify the resulting sources. The background counts within each source is calculated, then the significance

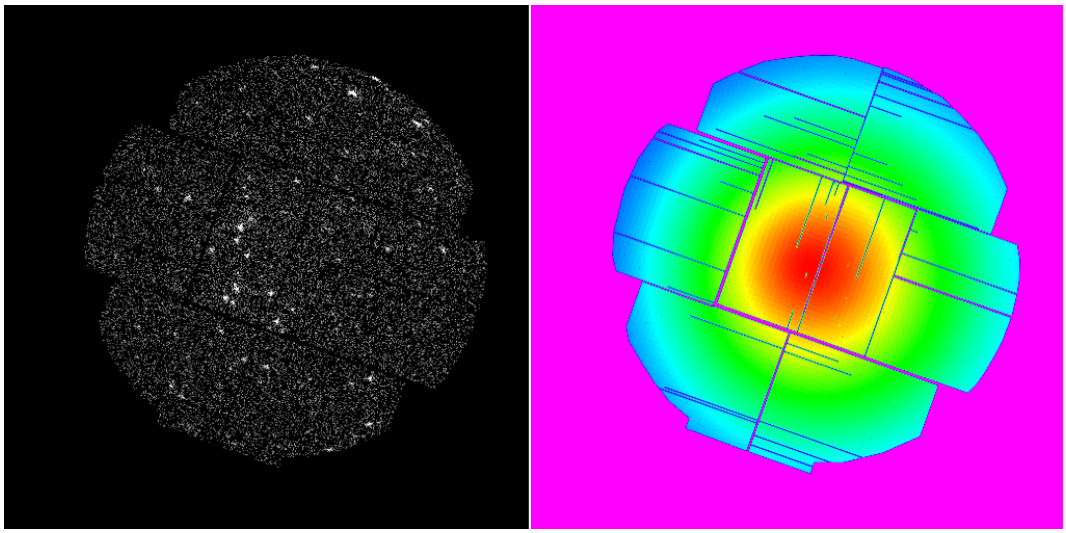

Figure 2.2: Similar to Figure 2.1, but for the MOS2 image of ObsID=0094310201.

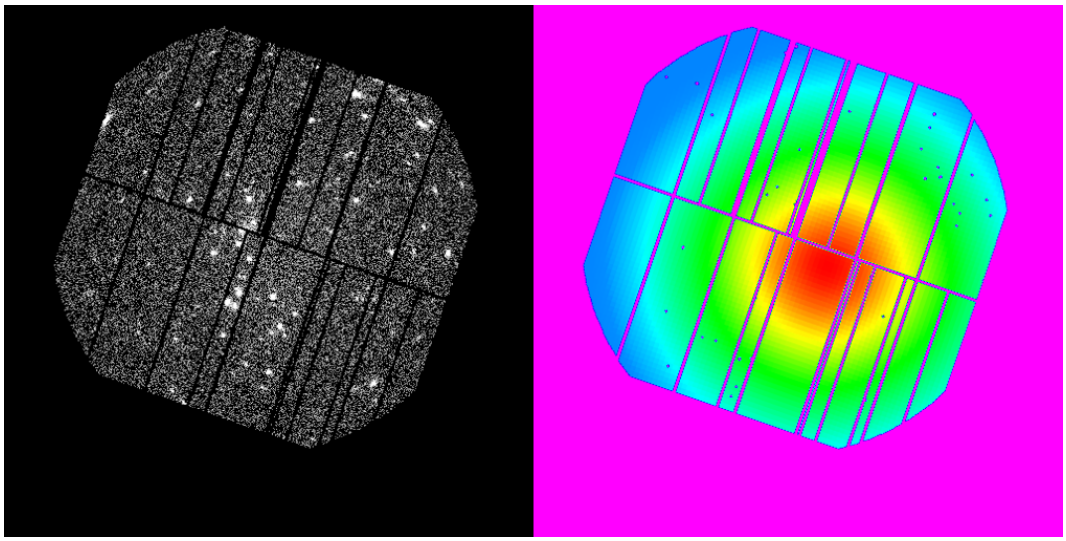

Figure 2.3: Similar to Figure 2.1, but for the PN image of ObsID=0094310201.

of the detected source is calculated by computing the probability that the background could produce the detected number of counts in the source aperture, this is done assuming a Poisson distribution for the background counts. Sources with a probability higher than 0.000 032 are removed from the source list, sources comprised of only a pixel are also removed as they are likely hot pixels or sources that are too faint to be accurately parametrized.

Finally, XAPA subroutine `find_srcprop` is run on the remaining sources in order to classify them as point-like or extended.

The XMM Point Spread Function (PSF) is not simple to characterize. In can be modeled at low energies and in the centre of the FOV as circular with an FWHM of 4.5 arcsec.

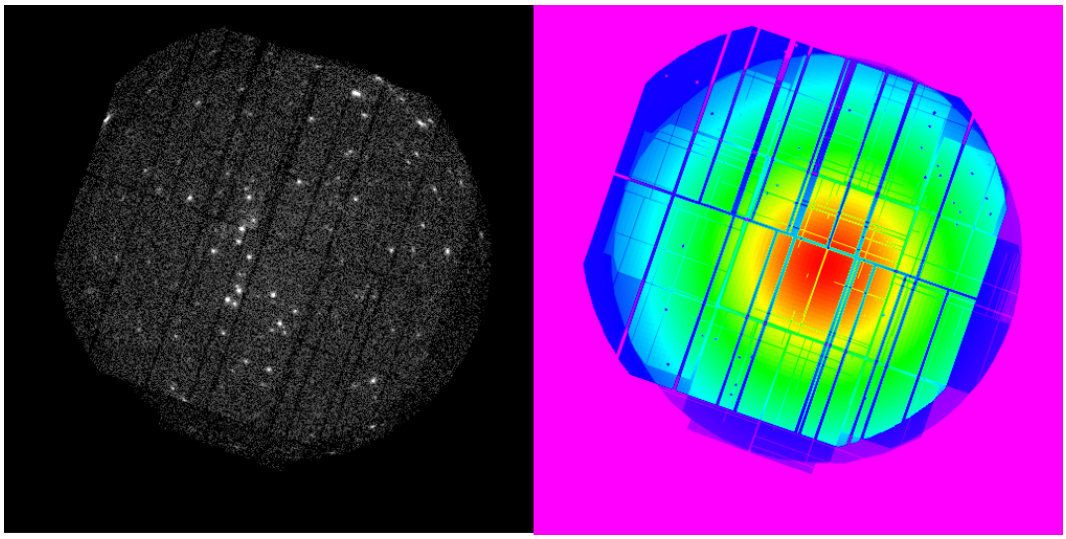

Figure 2.4: Example of a XIP merged (PN+MOS1+MOS2) image and exposure map of ObsID=0094310201. This image is generated by scaling the MOS1 and MOS2 images and exposure maps to the higher sensitivity of the PN camera.

Approaching the edge of the FOV the FWHM is progressively larger and the shape tends to form an ellipse.

To classify sources as extended or pointed it is necessary to compare the sources with the XMM PSF. A Kalmogorov-Smirnov test is used to find if the measured enclosed energy fraction within a XAPA source is consistent with the enclosed energy fraction of the PSF at the source location. The enclosed energy fraction records the fraction of the total energy of a source as a function of increasing aperture size. For this test XCS adopted the XMM Extended Accuracy PSF model at the respective off-axis angle, XAPA tests 200 realizations of the PSF. The source is classified as extended if the probability of it being a point source that has been misclassified as extended is 0.005 or less. Extended sources are flagged as PSF-sized if the sources are slightly larger than the PSF, these sources are considered extended and are cluster candidates, experience has shown that most of them are misclassified point sources, although real clusters also have been found under this classification. Figure 2.6 shows an example of the XAPA classifications.

After source classification, XAPA records for each source, information including the centroid position, the ellipse parameters (minor axis, major axis, rotation angle), the background subtracted count rate , the flux and the extent classification.

Finally, XAPA creates a Master Source List with the information of all the detections. To remove duplicates, by cross matching source detections in different observations. The program matches point sources within 5 arcsec and extended sources within 30 arcsec, if

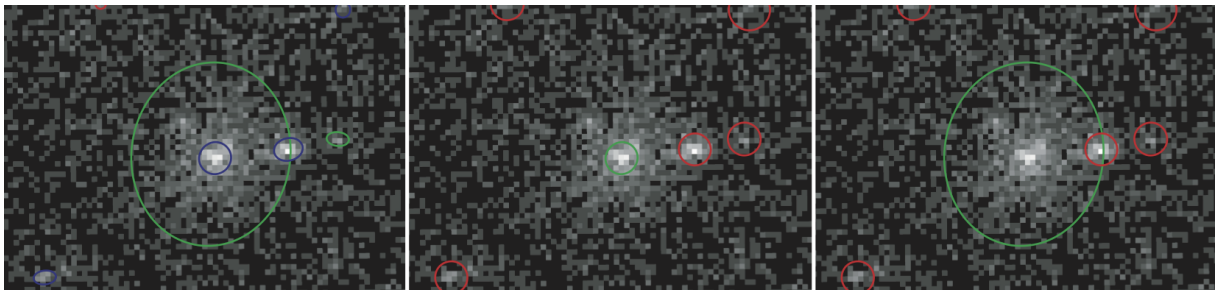

Figure 2.5: Figure and caption taken from reference LD11: Illustration of the effect of extended source cuspiness. Left: the original XAPA Run 1 (blue) and Run 2 (green) detections. Middle: the final source list if the cuspiness is not performed. Right: the final source list (after cuspiness test was introduced). Extended and point sources have green and red outlines, respectively.

there are duplicates within this radius, the code keeps only the source with most counts.

Galaxy clusters dominate the extended extragalactic source population in X-rays, for this reason the XCS extended sources are the cluster candidates to be analyzed in this thesis.

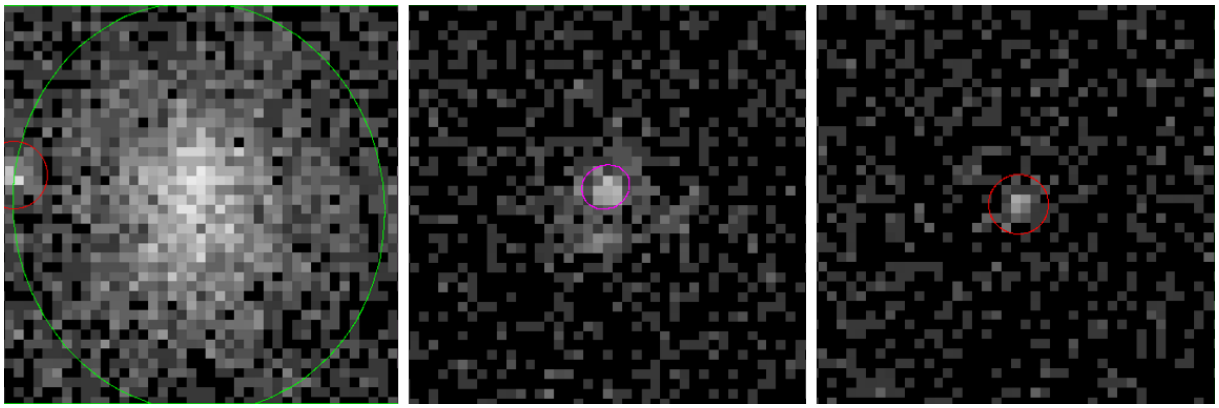

Figure 2.6: XAPA source classification of extended (left), PSF-size (middle) and point (right) sources. Each source is enclosed on a 3×3 arcmin box.

Further efforts have been done by the XCS team to make cleaner and better images combining the available observations from MOS 1, MOS 2 and PN. Phil Rooney made several images of XCS sources where the exposure map is considered as well as a normalization of the background, to produce clean images. Figure 2.7 shows a comparison between the common and the corrected images, notice how the corrected image (b) has a significantly lower background noise compared with its common version. In this work we used the common images instead of the corrected as the code needed is still not yet completely reliable as it fails to produce an output for some particular observations.

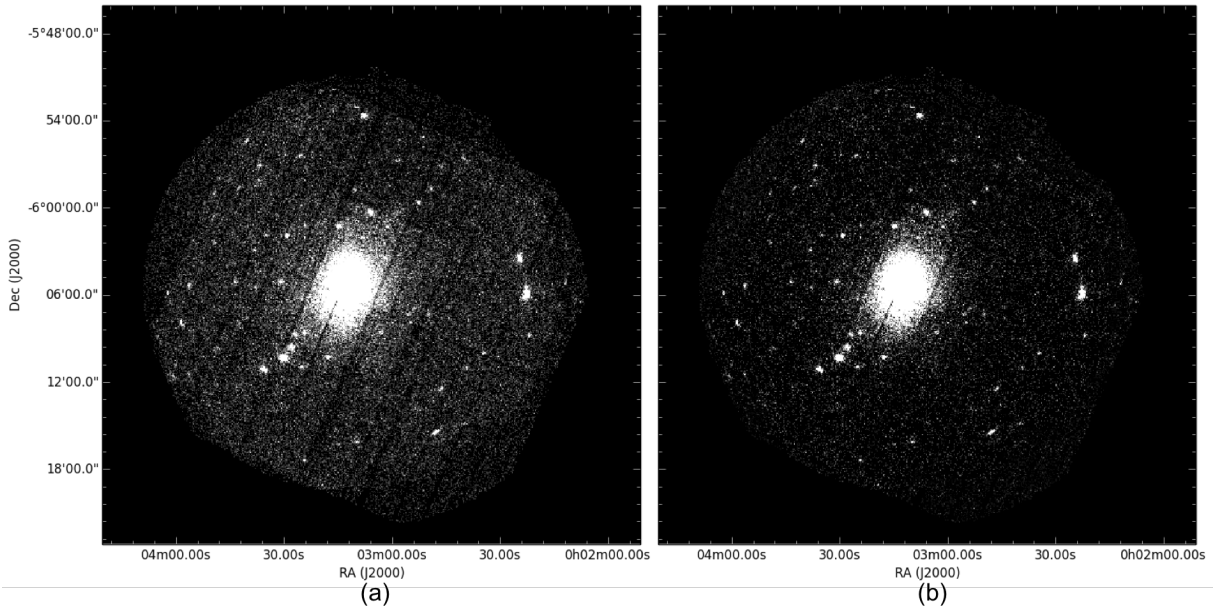

Figure 2.7: Comparison of the regular (a) and background corrected (b) merged images from an XMM observation (OBSID=0652010401). A pointed cluster can be seen in the middle of the observation, pointed and extended sources can be seen clearly on (b) without the backgrpund noice.

2.1.5 XCS Catalog Characterization

The sample of X-ray cluster candidates used in this work is a result of the updated XCS-DR2 methodology, this sample now contains a total of $32,276$ cluster candidates, both serendipitous and targeted. However, from the total, $24,700$ have more than 50 photon counts in the X-ray soft band. Only clusters above this limit are considered as a reliable sample.

In figure 2.8 is shown the position of the XCS extended sources used in this thesis. The size of the dots does not represent any physical property. This figure has made using an Aitoff projection.

2.2 The redMaPPer cluster finding algorithm

The red-sequence Matched-filter Probabilistic Percolation (or redMaPPer) cluster finding algorithm (Rykoff et al., 2013, Rykoff and Rozo, 2014, Rozo et al., 2014, Rozo et al., 2015) has been designed to find clusters from photometric galaxy catalogues. The redMaPPer (RM hereafter) algorithm iteratively self-trains the red sequence model (Section 1.1.1) using any available spectroscopic redshifts. RM estimates cluster richness as the sum of probabilities of cluster members. Cluster centering is given as a probability as well as the

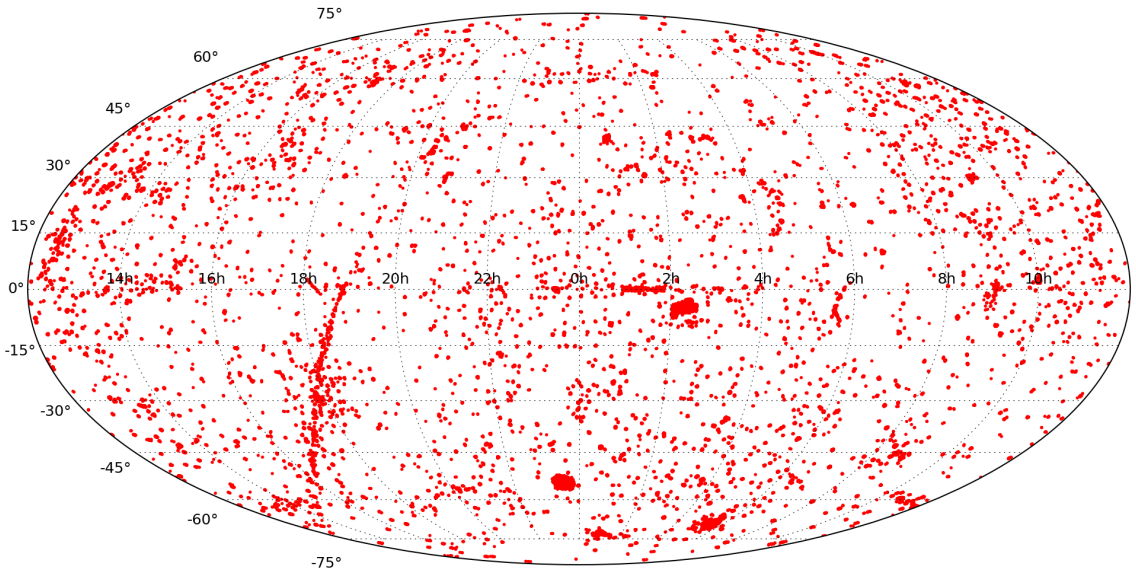

Figure 2.8: XCS extended sources from XCS-DR2-β with more than 50 photon counts on the X-ray soft band. There are 32,276 points in this plot. Figure made using an Aitoff projection.

redshift distribution. RM also calculates iteratively trained photometric redshift for each cluster. RM was designed to analyse any arbitrary photometric galaxy catalogue, with an arbitrary number of bands ≥ 3.

2.2.1 RM Richness Estimator

RM defined the richness, or λ, of a cluster to be the sum of membership probabilities over all the galaxies within a scale radius R_λ(Rykoff et al., 2016).

$$\lambda = \sum_{R<R_\lambda} p_{\rm mem}\theta_L\theta_R, \tag{2.2}$$

where θ_L and θ_R are the luminosity and radius-dependant weights, R_λ is a cutoff radius:

$$R_\lambda = R_0(\lambda/100.0)^\beta, \tag{2.3}$$

where $R_0 = 1.0h^{-1}$Mpc and $\beta = 0.2$. Previous work Rykoff et al., 2012 found that R_0 and β minimize the scatter in the richness mass relation. The sum on Equation 2.2 is restricted to galaxies brighter than $0.2L_*$.

The presence of galaxies near limits of the richness calculation ($L > 0.2L_*$ and $R < R_\lambda$) can result in macroscopic changes to the richness (Rozo et al., 2014). To solve this problem, the RM team introduced top-hat functions θ_L and θ_R:

$$\theta_L = \frac{1}{2}\left[1 + \mathrm{erf}\left(\frac{m_{\rm max} - m_i}{\sigma_i}\right)\right], \tag{2.4}$$

$$\theta_R = \frac{1}{2}\left[1 + \mathrm{erf}\left(\frac{R(\lambda) - R}{\sigma_R}\right)\right], \tag{2.5}$$

where $m_{\max}$ is the magnitude corresponding to $0.2L_*$, σ_i is the photometric error for the galaxy i, and $\sigma_R = 0.05h^{-1}\mathrm{Mpc}$.

2.2.2 RM Photometric Redshifts

The RM team developed a cluster photometric estimator z_{red}, specifically designed to work on red sequence galaxies. This z_{red} value is the starting point of an iterative process. First, it calculates the richness and the set of membership probabilities for each redshift. Then, it selects high membership probabilities galaxies to estimate a new redshift. This process will continue until the absolute difference between two consecutive redshifts is less than 0.0002. The resulting redshift is called z_λ.

In Figure 2.9 we see the performance of z_λ compared with spectroscopic redshifts on the SDSS sample. Notice the presence of few outliers (red points that constitute 1.1% of the total sample). Rykoff et al., 2016 conclude that the redshift information provided by RM is reliable.

2.2.3 RM Cluster Centering

Galaxy cluster centering is very important as a bad estimation could lead to significant errors in weak-lensing mass estimates (Melchior et al., 2016), velocity dispersions and most important for RM: richness calculation. The RM algorithm assumes that every cluster has a bright red centre galaxy, which is the case in most of the massive clusters. However, there are exceptions such as strong cool-core clusters, which tend to have centrals with a high star formation rate (Rykoff et al., 2013). This leads to miscentering which is a well known problem with the RM algorithm.

Under the consideration that central galaxies are red-sequence, the centering success rate reported by RM is $\approx 85\%$ (Rykoff and Rozo, 2014).

2.2.4 The RM SDSS-DR8 catalogue

The redMaPPer algorithm was run on SDSS DR8 data(Aihara et al., 2011), covering a total area of $\approx 10,000\mathrm{deg}^2$. Richness estimates are corrected for masked areas due to survey edges, bright stars and bad fields. Spectroscopic redshifts are derived from a compilation of SDSS data, they are used to train photometric redshifts as explain in Subsection 2.2.1. The RM SDSS-DR8 catalog contains a total of **396,047** clusters, of which **66,028** have richness $\lambda > 20$ (the reliability limit recommended by the RM team).

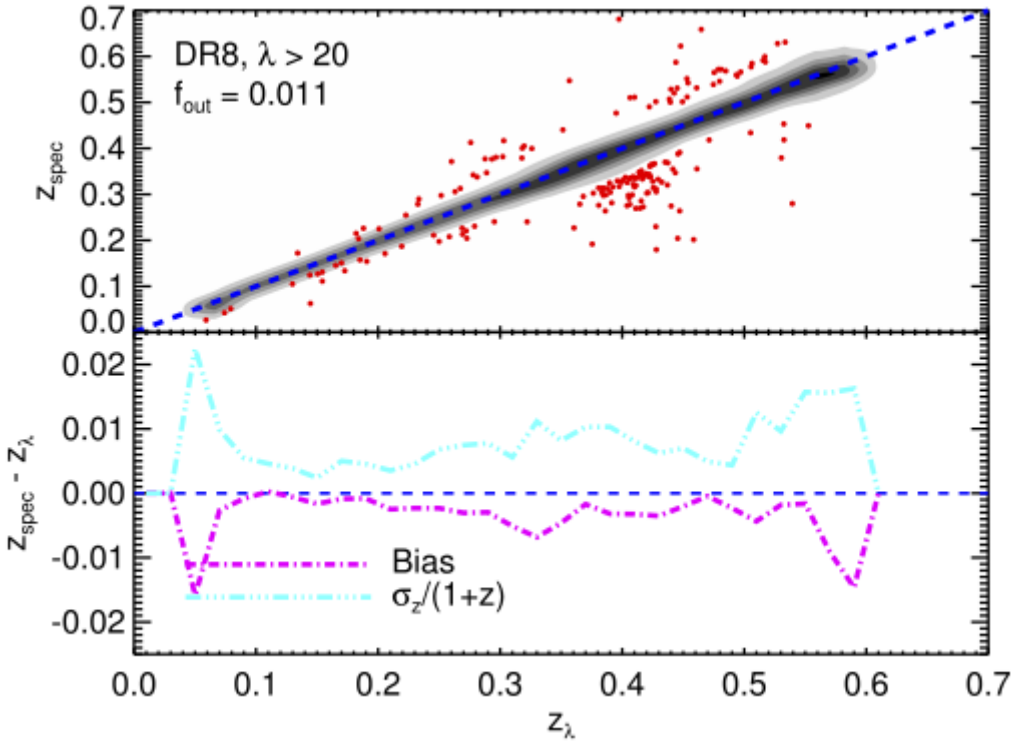

Figure 2.9: Spectroscopic redshift z_{spec} vs cluster photometric redshift Z_λ from SDSS clusters with $\lambda > 20$. Gray regions show 1σ, 2σ and 3σ density contour. The red points constitute 1.1% of the total sample. Notice that at $z = 0.4$ there is a clump, the RM team shows that for these particular clusters, the central galaxy was not a cluster member. Figure taken from Rykoff et al., 2016.

Figure 2.10 taken from Rykoff et al., 2013, shows the footprint of RM clusters from SDSS DR8, clusters with $\lambda > 5$ and $z \in [0.1 - 0.3]$ are plotted to illustrate the large-scale structure on the catalog.

2.2.5 The RM DES-SV catalogue

The RM algorithm has been applied to the DES Science Verification Data (Section 1.8) producing reliable cluster characterization (such as richness, photometric redshift, centering probability), this set of results was then with X-ray and millimetre observables using data from XMM, Chandra and SPT (Rykoff et al., 2016).

2.2.6 The RM DES-Y1 catalogue

The RM algorithm has been applied on DES Y1 data (Section 1.8). It has been made available to us ahead of publication by the RM team. In this thesis we use version `6.4.11` which contains **129 243** clusters, of which **23 795** have richness $\lambda > 20$. The RM team

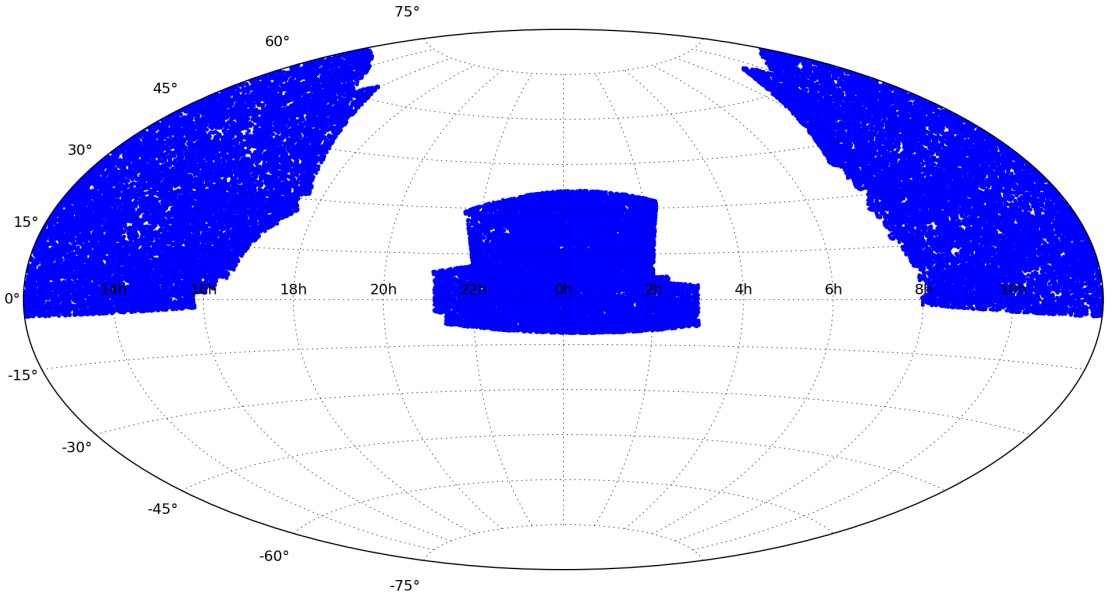

Figure 2.10: Footprint of redMaPPer SDSS DR8 clusters, clusters with $\lambda > 20$ and $z > 0.08$ are plotted.

claim the reliable redshift range for this catalog is $z_\lambda \in [0.2 - 0.8]$. Figure 2.11 shows the DES Y1 footprint of RM clusters.

2.3 Software description

Several software packages written by third parties (individuals and teams) are integral to the work described in this thesis, as described below. Almost all of the analysis presented herein was carried out on the Sussex Apollo supercomputer.

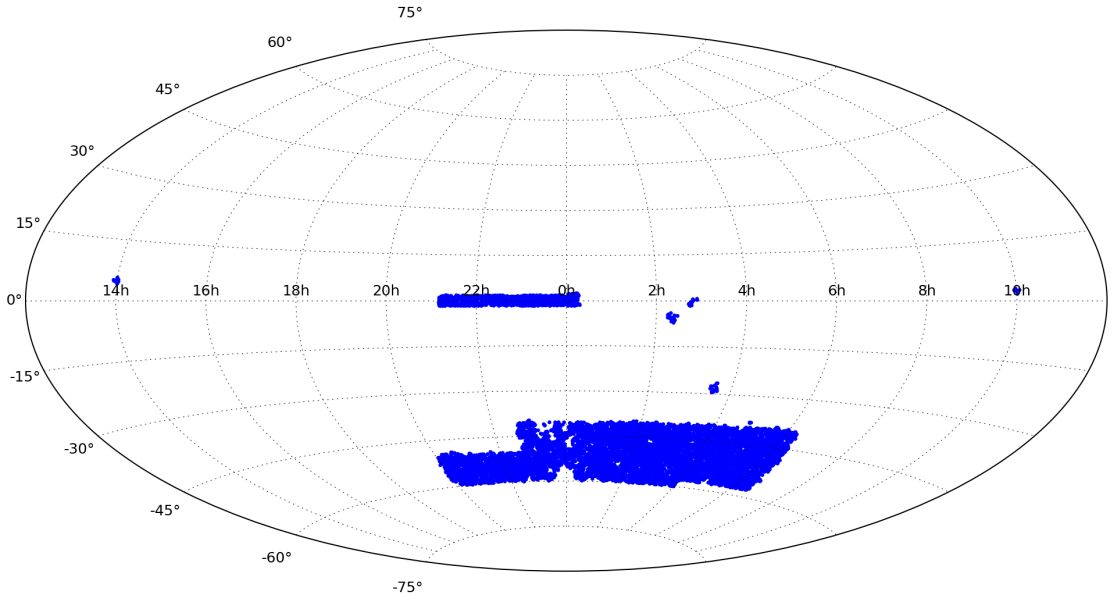

Figure 2.11: Footprint of redMaPPer DES Y1 clusters, clusters with $\lambda > 20$ and $z \in [0.2 - 0.8]$ are plotted.

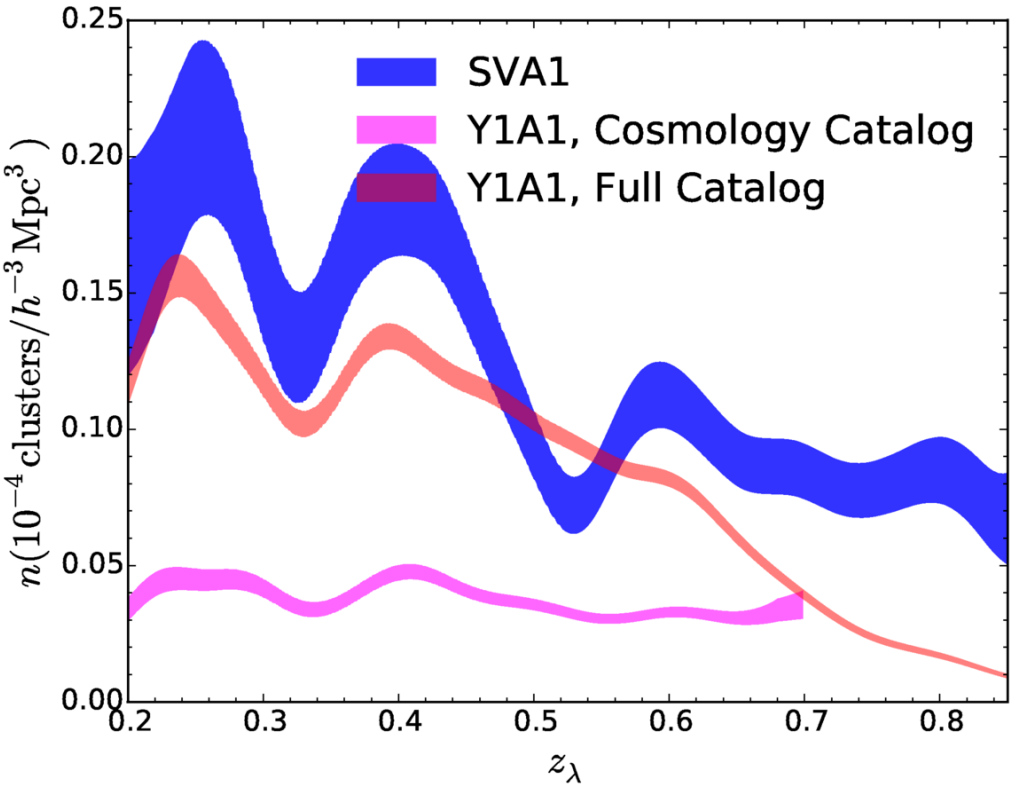

Figure 2.12: Figure courtesy of Eli Rykoff: Cluster density ($n(z)$) for the SVA1 catalog (blue), Y1A1 Cosmology catalog (magenta), and Y1A1 Full Catalog (reddish). The cosmology catalog is much lower density because $\lambda > 20$ with a $0.4L*$ cut is equivalent to a $\lambda >\sim 30$ cluster with the fiducial 0.2L* cut.

2.3.1 XMM-Newton SAS

The XMM Science Analysis Sub-System (SAS)[2] (Jansen et al., 2001) is an extensive suit of software tasks developed to reduce and analyze data from the XMM-Newton observatory. SAS includes calibration data or build a Calibration Index File (CIF). It allows the user to create scientific products such as spectra, images, light curves, filtered event lists, and response matrices. the The XCS team uses SAS to reduce XMM observations from Observation Data Files (ODFs). Note that tasks of data downloads and SAS processing are preliminary performed by XCS member Dr Philip Rooney (only a small number of OBSids have been processed by myself). Data products generated using SAS are a vital input to this thesis, for example to the post processing ($T_{\rm X}$ and $L_{\rm X}$) pipeline described in Chapter 4). Throughout this thesis we use SAS version 14.0.0.

2.3.2 HEAsoft

HEAsoft[3] is a range of packages that enable the manipulation of X-ray data (Drake, 2004). HEAsoft includes the Xanadu package which allows X-ray spectral, timing, and imaging data analysis. Ftools is also part of HEAsoft, this module includes mission-specific tools to manipulate FITS files. The version used in this thesis is 6.17.

2.3.3 XSPEC

The X-ray Spectral Fitting Package (Xspec)[4] is included in HEAsoft, it is a command-driven, interactive, X-ray spectral fitting program (Arnaud, 1996).
An important feature of Xspec is the wide range of theoretical models available, there are more than 50 build-in theoretical models, ranging from simple models like power-laws to complex models like thermal plasmas or comptonized emission. In this thesis, the model `Mekal×Wabs` is used, see Section 4.2.1.

2.3.4 TOPCAT

Topcat[5] is a user-friendly graphical program for viewing, analysis and editing tables. It has facilities for plotting, cross matching, row selection, sorting and manipulating data and metadata (Taylor, 2005).

[2] https://www.cosmos.esa.int/web/xmm-newton/sas
[3] https://heasarc.gsfc.nasa.gov/lheasoft/
[4] https://heasarc.gsfc.nasa.gov/xanadu/xspec/
[5] http://www.star.bris.ac.uk/7Embt/topcat/

TOPCAT was widely used in this thesis to manipulate data tables. For example data from several catalogues (e.g. the XMM-Newton public observations catalogue and the SDSS-DR8 RM catalogue) can be loaded into, and compared, using TOPCAT. The data can be loaded from locally stored catalogues or from online databases (e.g. the XMM-Newton Science Archive[6]). Results from the application of TOPCAT can be found in Section 3.3. The version used in this thesis is TOPCAT 4.3.

2.3.5 SAOImage DS9

SAOImage DS9[7] is an astronomical imaging and data visualization application (Joye et al., 2003). It supports FITS images and binary tables, multiple frame buffers, region manipulation, and many scale algorithms and colour maps. DS9 also supports advanced features such as multiple frame buffers, mosaic images, geometric region markers, colour map manipulation, scaling, and a vaiety of coordinate systems. DS9 was used in this thesis to visualize X-ray and optical observations, manipulate region files and to inspect XMM FITS file. The DS9 version used in this thesis is 7.3.2. See Figures 2.1, 2.4.

2.3.6 Python

Python[8] is a object-oriented, interpreted, and interactive programming language. It has modules, classes, exceptions, very high level dynamic data types, and dynamic typing. Most of the algorithms (e.g cross match, image creation, relation fitting) employed in this thesis are written in this programing language, using Python version 2.7.

Python modules used extensively in this thesis include:

Astropy

The `astropy` package (Robitaille et al., 2013) contains various classes, utilities, and a packing framework intended to provide commonly-used astronomy tools.

In this thesis `astropy` has been used to calculate cosmological quantities (e.g. Hubble parameter for ΛCDM cosmology, diameter angular distance (d_A), comoving distance) that are needed in the cross match 1 (CM1) procedure (see Section 3.3).

[6] http://nxsa.esac.esa.int

[7] http://ds9.si.edu/site/Home.html

[8] https://www.python.org

APLpy

The Astronomical Plotting Library in Python (`APLpy`) is a Python module aimed at producing publication-quality plots of astronomical imaging data in FITS format. It is capable of creating output files in several graphic formats (Robitaille and Bressert, 2012).
In this thesis `APLpy` has been used to create images of XMM-Newton observations where information about source regions and/or surface brightness contours need to be overlaid, e.g. Figures 4.2.a, 4.7, 5.5.

Matplotlib

`Matplotlib` is a Python plotting library which produces publication quality figures in a variety of hardcopy and interactive environments across platforms. `Matplotlib` was used in this thesis to produce the majority of the figures in this thesis, e.g. Figures 4.8, 5.9, 6.5.

Chapter 3

A new sample of RM clusters with XMM counterparts

3.1 Overview

Motivation To date, published results on the X-ray properties of redMaPPer (RM) selected optical clusters have been based on small samples (Rykoff and Rozo, 2014, Rykoff et al., 2016). In order to increase the size of the X-ray RM samples it is necessary to explore X-ray archives for observations of RM cluster locations (either deliberately, i.e. targeted, or by accident, i.e. serendipitously). In this chapter we describe how we have identified a large number of candidate X-ray RM clusters based on the XCS analysis of the XMM public archive. (Our collaborators at UCSC, Tesla Jeltema et al., have performed a parallel study using Chandra public archive.)

Governing Assumptions

1. If a RM cluster is located in an XMM observation of sufficient depth, then the XCS Xapa source detection software will have located it and categorized it as being extended.

2. The XCS Xapa defined centroid is a better, than RM, measure of the centre of mass of a given cluster.

3. The RM determined photometric redshift of a given cluster is correct to within a small margin of error.

4. There are no true matches between XCS extended sources and RM clusters beyond a projected radius of $1.5h^{-1}$Mpc.

5. Most XCS sources defined as being extended trace the X-ray emission from a cluster.

6. It is not worth using XCS sources detected with less than 200 background corrected soft XMM counts in our scaling relation study (because derived properties, such as X-ray temperature, will carry large errors).

Methodology New automated techniques have been designed to interrogate the XMM observation log and the XCS master source list. It was also necessary to carry out an eye-ball check (using a `PHP` interface) of the respective XMM postage stamp images, to filter out obvious contamination.

Results A comparison with the XMM public archive demonstrated that 5 143 SDSS-RM and 2 052 DESY1-RM clusters fall in the field of view of XMM observations. Of these, 3 090 SDSS-RM and 938 DESY1-RM clusters fall within $1.5h^{-1}$Mpc and/or $3'$ of an extended source in the latest version of the XCS Master Source List. These numbers dropped further after an eye-ball check of the respective XMM data (to 1 314 SDSS-RM and 293 DESY1-RM clusters). These two final samples (Table 3.2) are used in subsequent chapters in the thesis.

An analysis of the 330 $\lambda < 20$ clusters that fall in the XMM footprint, but were not matched to XCS extended sources has revealed that in most cases low exposure times and/or location on the edge of the XMM FOV is to blame. That said, there are a small number of cases where XAPA has failed, either to detect an obvious (by eye) extended source at all, or where it has categorized it as being point-like.

Conclusions and Future work A total of 1 607 RM clusters have been associated with XCS extended X-ray sources. This is a significant increase compared to previous work, e.g. Rykoff and Rozo, 2014. We have shown that (projected) source crowding in the RM catalogue often results in multiple matches to a given XCS source, and that it is not correct to assume that the closest projected match is the best one.

Future work planned by the XCS team includes: the extension of this analysis to a recent update of the XCS database (it was expanded in size by $\simeq 5\%$ in April 2017), and a more detailed investigation into the reasons why some RM clusters were not detected by XCS despite falling in XMM images. An aspiration would be to refresh the parts of the XCS pipelines that are generating the erroneous sources that led to some of type of "bad matches" due to saturation issues.

3.2 Redmapper clusters in the XMM-Newton footprint

In order to find which Redmapper (RM) clusters lie within the field of view of one or more XMM-Newton observations (ObsIDs), a procedure know as SF1 (source finding 1) was developed. A new procedure was necessary because the on-line search[1] provided by the XMM Science Centre has three issues: (i) it is not optimised to handle the tens of thousands of centroid matches we require for this project, (ii) there are several incidences of inaccurate ObsID centroids in the XMM database (e.g. where a negative declination is recorded as positive), and, (iii) for mosaic sequences (Section 1.6), only the centroid of the first observation in the sequence is recorded.

Therefore, the SF1 procedure uses the coordinate information recorded in the `.fits` headers of all XCS images (Section 2.1.1) stored on the University of Sussex Apollo supercomputer. The XCS centroid information is accurate and available for every processed ObsID (including those generated during a mosaic sequence). For this thesis, all observations available in the XMM public archive in June 2016 were included.

SF1 projects the pixel coordinates of each corner of an XMM ObsID into world coordinates using the WCS conversion factor saved in the header, see code snippet below. SF1 is shown complete on Appendix A.

```
header = hdulist_XMM[0].header
proj = wcs.Projection(header)
world_edge = proj.toworld(corner_coordinate)
world_origin = proj.toworld(origin_coordinate)
ra_i = world_edge[0]
dec_i = world_edge[1]
ra_f = world_origin[0]
dec_f = world_origin[1]
```

The code checks every RM cluster against every ObsID to see which are covered by the XMM archive footprint. To ensure completeness, the match radius is set to being just larger than the radius of the XMM-Newton FOV. When a match is found, SF1 appends the respective Xapa region file (Section 2.1.3) for that ObsID with information about the RM cluster(s) therein. This in turn allows us to generate images of the ObsID with both XCS source regions and RM cluster radii (R_Λ, Section 2.2.1) projected over the top of the XMM data, for example see Figure 3.1. We note that the R_Λ values are stored in the RM

[1] http://nxsa.esac.esa.int/nxsa-web/#search

database in units of h^{-1}Mpc. Therefore SF1 makes a conversion into units of XCS image pixels using the angular diameter distance (Equation 1.15). The SF1 code closely follows the method of Wright, 2006 to convert between metric and angular distance, under the assumption of a flat ΛCDM cosmology (Section 1.2).

In total, 5 143 (1 002 with $\lambda > 20$) RM-SDSS clusters fall inside the active Field of View of one or more XMM ObsIDs. The equivalent number for RM-DESY1 is 2 052 (378 with $\lambda > 20$). See Table 3.1.

Catalog	RM clusters	RM [$\lambda > 20$]	$\langle z \rangle$	XMM ObsIDs
RM (SDSS-DR8)	5 143	1 002	0.38	1 808
RM (DES Y1)	2 052	378	0.58	535

Table 3.1: Characterization of RM clusters inside the XMM footprint.

3.3 Matching Redmapper clusters to XCS cluster candidates

The work presented in this thesis focuses on those RM clusters that have XCS cluster candidate counterparts. Not all of the 5 143 (2 052) RM-SDSS (RM-DESY1) clusters in the XMM footprint will have such counterparts because: (i) the respective XMM observation has a low exposure time and/or high background, or (ii) the RM cluster falls on the edge of the field of view and/or in an EPIC chip gap, or (iii) the RM cluster is not a physical system.

The CM1 procedure (for cross match 1) was developed to make initial matches between RM clusters and XCS cluster candidates. CM1 makes the following assumptions: (i) all physical matches will occur within 1.5 Mpc of the RM centre (assuming the X-ray source to be at the RM redshift), (ii) all physical matches will occur within a projected separation of $3'$, and (iii) all physical matches will be contained within the sub-set of XCS sources that are defined as being extended (including those flagged as being `PSF-like`, Section 2.1.4) and that were detected with at least 200 background subtracted matches.

In total 5 143 (2 052) RM-SDSS (RM-DESY1) clusters in the XMM footprint were matched to one or more XCS extended source using CM1. We note that not all XCS extended sources (> 50 counts) were matched to RM clusters, and that some were matched to multiple RM clusters. Not all of these matches are reliable (even in the one-to-one match cases). Additional filtering was, therefore, necessary. See Sections 5.2.1 and 5.2.2.

3.3.1 Filtering out obvious "bad matches"

All RM clusters flagged by the CM1 procedure were checked by eye to remove obvious "bad matches". For this, XMM images in the soft band $(0.5 - 2.00)$ keV were generated with both the XAPA and RM regions overlaid (Figure 3.1). Examples of the types of "bad matches" identified are given below.

An interactive PHP webpage[2] was made to perform the eyeballing, figure 3.2 shows an example. Two PHP flags were included, "flag 1" indicates an obviously "good" match, whereas "flag 2" indicates a possible match. Obviously "bad" matches are not flagged, but by are rejected from the sample by default. If a given RM cluster is matched to more than one XCS extended source, all those sources are shown in subsequent webpage rows. At the end of the "X-ray eyeball" process, 1 314 (293) RM-SDSS (RM-DESY1) clusters remained (i.e. had been flagged as "good" or "likely"). Of these, 95 (4) RM-SDSS (RM-DESY1) were still associated with two or more XCS cluster candidates, see Table 3.2. In Section 5.2, we explain how the sample was further refined to ensure reliable, one-to-one, matches.

Catalog	XCS-RM Matches	$z \in [0.08, 0.3]$	$z \in [0.3, 0.7]$	$z \in [0.7, 1.2]$
SDSS DR8	1319	458	861	0
DES Y1A1	293	43	199	51

Table 3.2: Table showing the samples after the eyeball process (Section 3.3.1), indicating the total number of RM clusters in XMM and the characterization of the matches between XCS and RM.

Good Match Type 1: RM cluster matched to an XMM target source

In Figure 3.3, the XMM target is Abell cluster 1576 (Abell, Corwin, Harold G. and Olowin, 1989). In this case, the size and shape of the RM cluster (cyan circle, radius= R_λ) is almost the same as that of the XAPA defined extended source (green ellipse), but this similarity is not a requirement for a match to be considered "good".

Good Match Type 2: RM cluster matched to an XMM serendipitous source

In Figure 3.4 we show an example of an RM cluster (4616) with a good match to an XCS extended source (2695) of a cluster detected serendipitously by XMM. This cluster is

[2] (https://astronomy.sussex.ac.uk/~ab615/al.php)

close the edge of the observation, but there is very little offset between the RM and XCS centroid. The sizes of the RM cluster (cyan) and XCS source (green) are quite different, but this is still a "good" match by our definition.

Likely Match

From Figure 3.1 we observe that the XCS cluster (id = 922) is associated with two RM clusters (id= 106 and id=499) both RM radii overlap the extended source, since RM id=499 centre is at the edge of the XCS region, then the RM-XCS match: $499 - 922$ is flagged as "likely". Objects under this flag are kept for further X-ray analysis.

Bad Match Type 1: multiple RM clusters matched to a single XCS extended source

In Figure 3.5 it can been seen that several RM cluster regions (red and cyan circles) intersect with the XCS source ellipse (green cricle). There are no less than five RM clusters within a projected radius of 1.5Mpc from XCS source 559. Three of these have richness $\lambda < 20$ (red circles) and two $\lambda > 20$ (cyan circles). By eye it is possible to judge that RM cluster (55) includes the complete extended region within its R_λ aperture. It also has the smallest projected separation. Thus, the match XCS-RM $(559 - 55)$ is flagged as "good", and the rest as "bad".

Bad Match Type 2: multiple XCS sources matched to a single RM cluster

In Figure 3.6) it can be seen that the RM cluster (5) has four associated XCS extended sources $(847, 1887, 24526, 26638)$. By looking at the centroid offsets, it is clear that there is "good" match with XCS source 847. However, there is also a "likely" match to XCS source 1887 because it lies inside the R_λ region on RM cluster 5. Allowing the possibility for a duplicate match between RM and XCS is useful because at this stage we do not know if XCS source 1887 is a sub-component of XCS source 847.

Bad Match Type 3: Xapa failures

There are several cases where the X-ray observation has on its FOV a bright source (star, galaxy or even galaxy cluster) that saturates the observation. Sometimes the XCS cluster finding algorithm (Xapa) classify these saturation as extended sources. This is still a problem to be solved by XCS, but fortunately the probability to find such objects on a set of observations is low.

In Figure 3.7, it can been seen that XAPA has mistakenly broken up a single bright source (blazer Mkn 501) into multiple XCS "sources". Very bright sources illuminate the spoke pattern on the XMM window. These spokes mislead detection algorithms into "thinking" there are multiple sources. In this particular case, none of the three potential RM-XCS matches are flagged as "good" or "likely" because none of those XCS "sources" are real.

Bad Match Type 4: obvious projection issues

The most common reason for defining an RM to XCS match as "bad" is when the respective regions do not overlap, i.e. even though the centroids may be less than 1.5Mpc apart, the association is due to projection, rather than physical. For example, in Figure 3.8, the scaled R_λ and the XCS regions do not intersect. The reason this rejection mode was not automated is illustrated in Figure 3.9. Here the size of the bright extended source (number 3900) has been significantly underestimated by XAPA (magenta ellipse). In this case, the RM cluster in question (number 111821) is still a "bad" match. We note that the red hashing across the RM cluster indicates that it's redshift is lower than the limit defined by the RM team (for SDSS is $z = 0.08$, while for DES is $z = 0.2$).

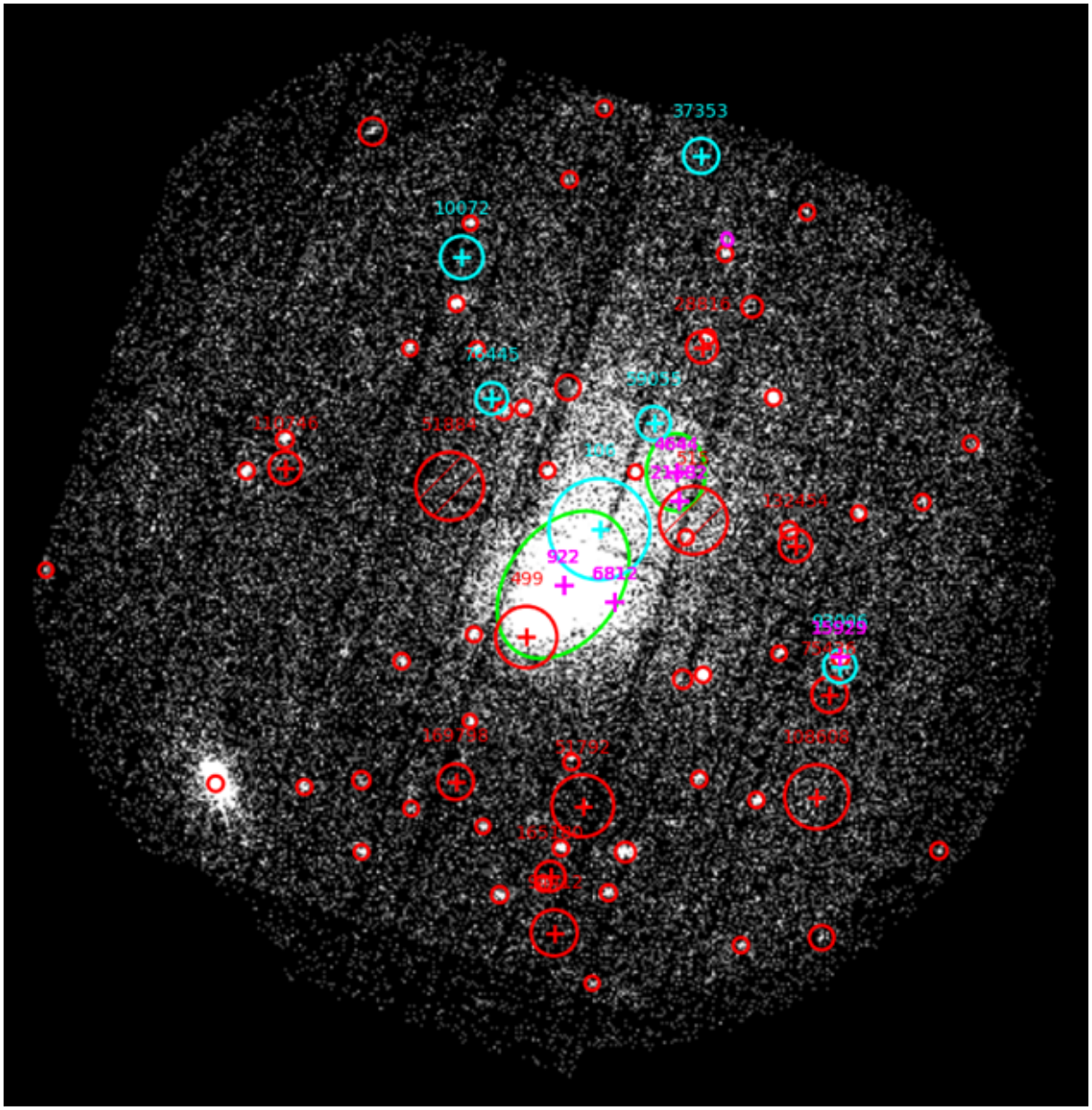

Figure 3.1: An example of an XCS processed XMM observations with RedMapper (RM) cluster outlines, radii (R_λ), superimposed. RM clusters with richness more (less) than $\lambda = 20$ have cyan (red) outlines. Note that XCS point sources also have red outlines, but these all have radii less than R_λ. The observation also include identification numbers for each cluster to facilitate the eyeballing.

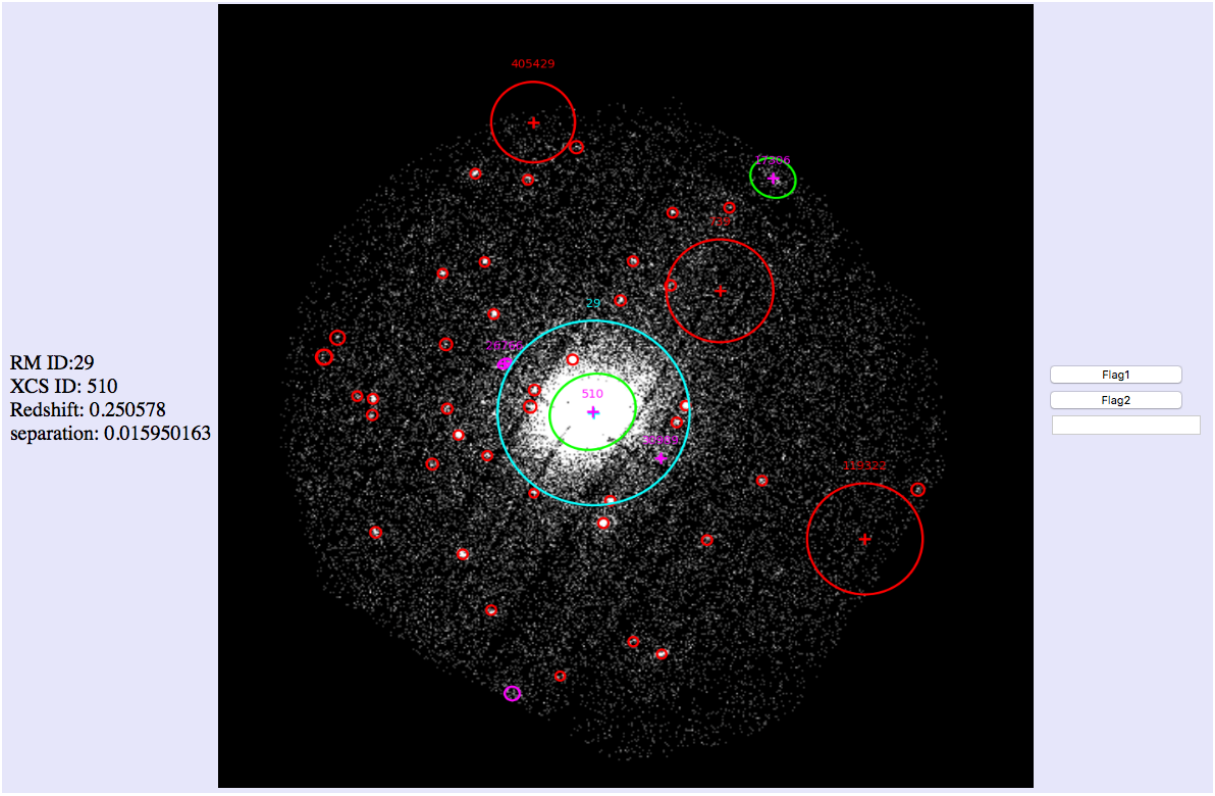

Figure 3.2: Example of a PHP webpage used to eyeballing the sample. For each RM cluster, the associated XCS source image(s) is (are) show. The selection were made using the buttons on the right, "flag 1" indicates good matches (in this example, RM cluster 29 is a good match to XCS extended source 510), and "flag2" for likely matches. If a match is not good, then no button is pressed.

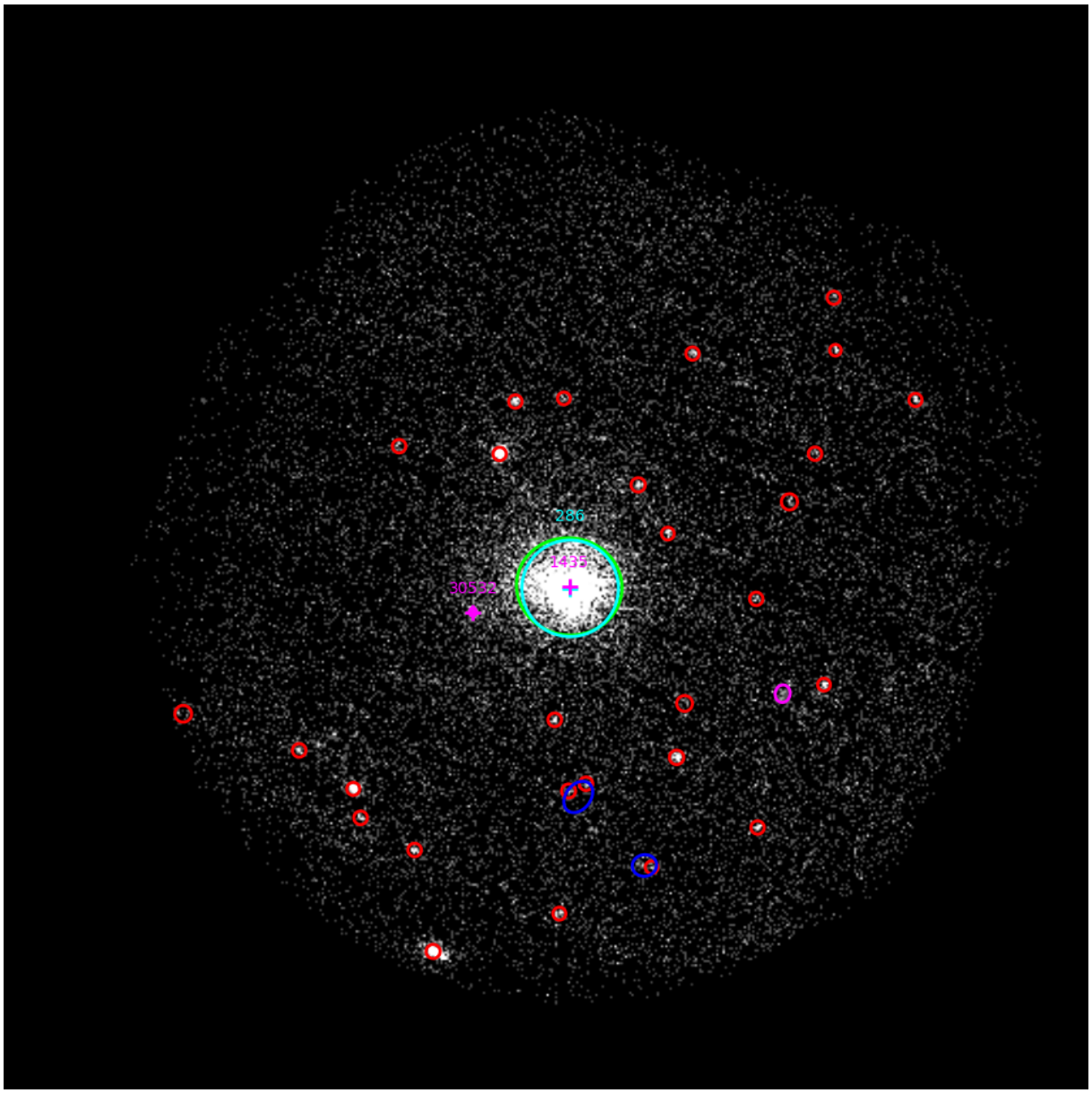

Figure 3.3: XMM observation 0402250101 with a cluster target (Abell cluster 1576). This is an example of a "good" match between XCS and RM. In this particular case, R_λ (cyan circle) has a similar size as the XAPA aperture (green elipse), but this is not a requirement for all "good" matches.

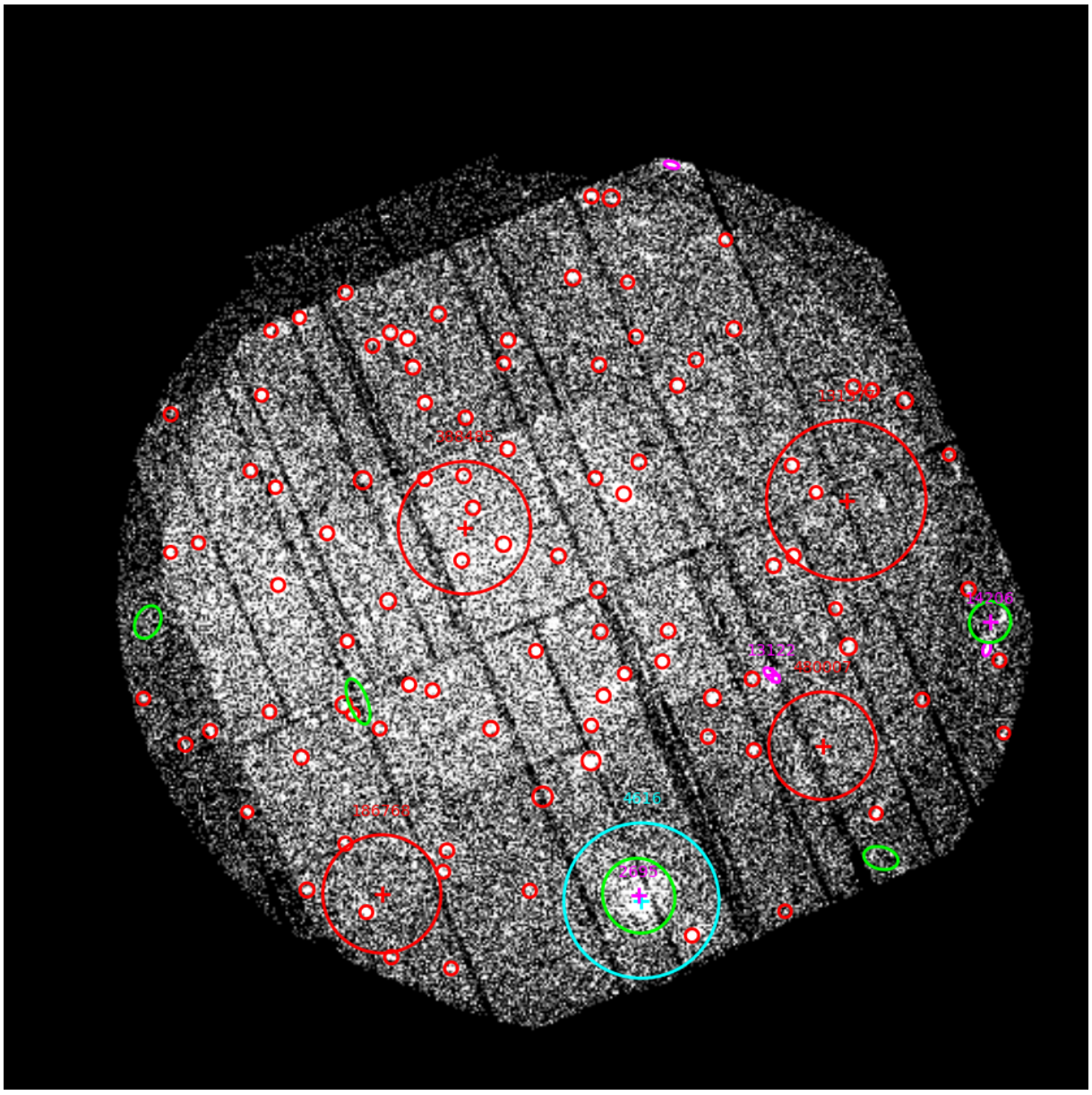

Figure 3.4: XMM observation 0722670101, this is an example of a good match between XCS and RM, the X-ray detection is serendipitous. It shows that good matches are not restricted to pointed observations.

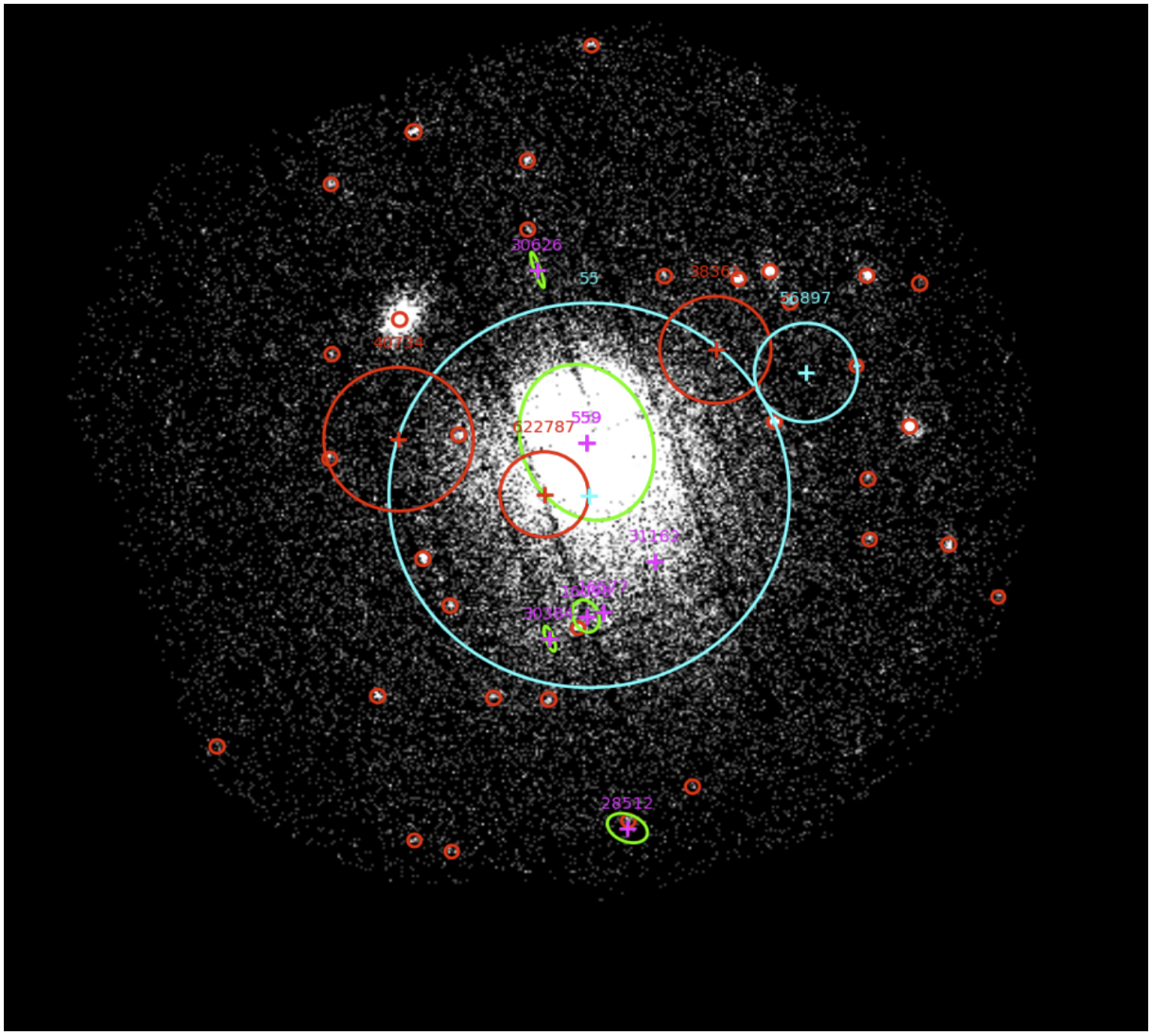

Figure 3.5: Example when several RM clusters are associated to a single XCS.

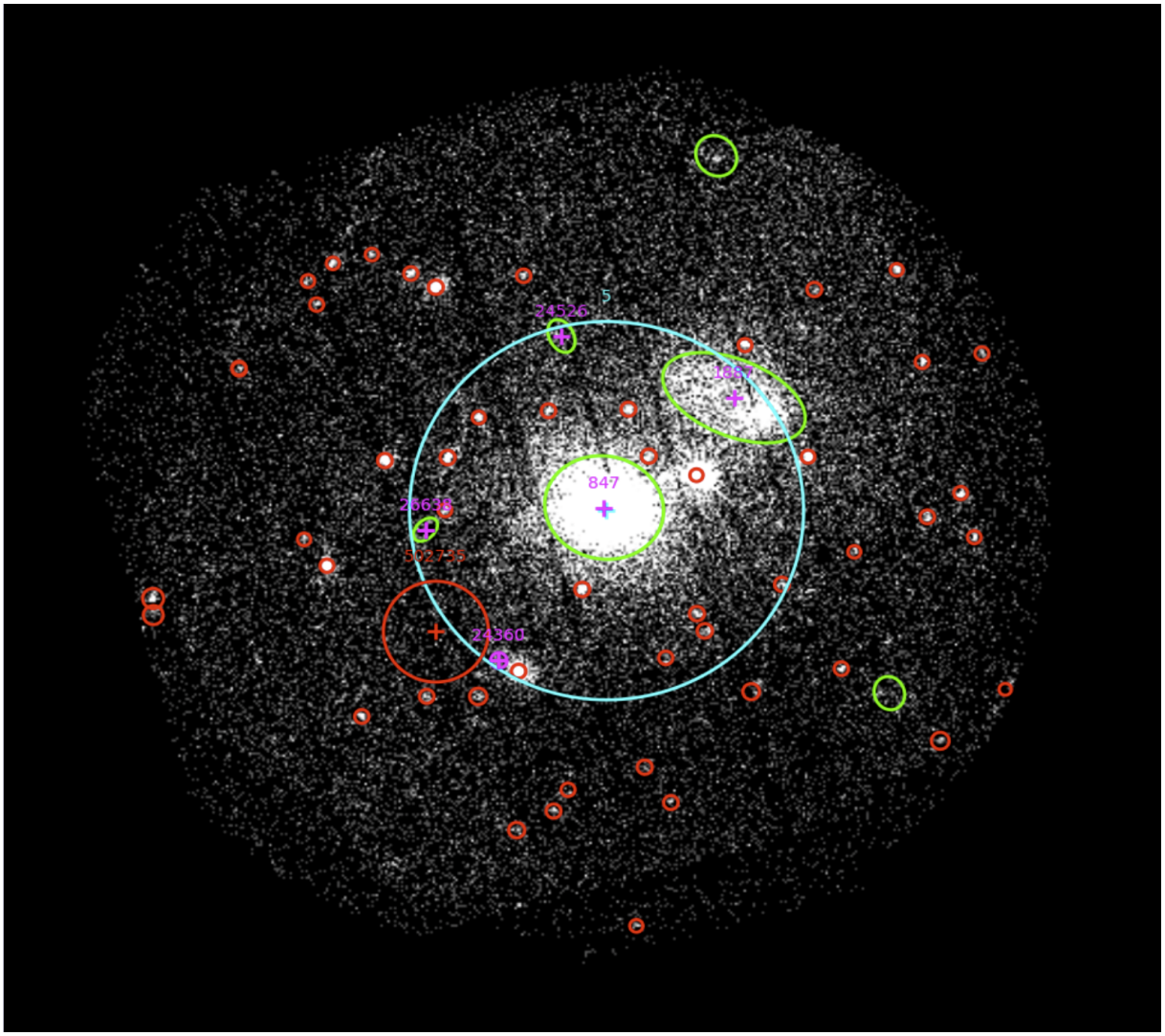

Figure 3.6: Example when several XCS clusters are associated to a single RM.

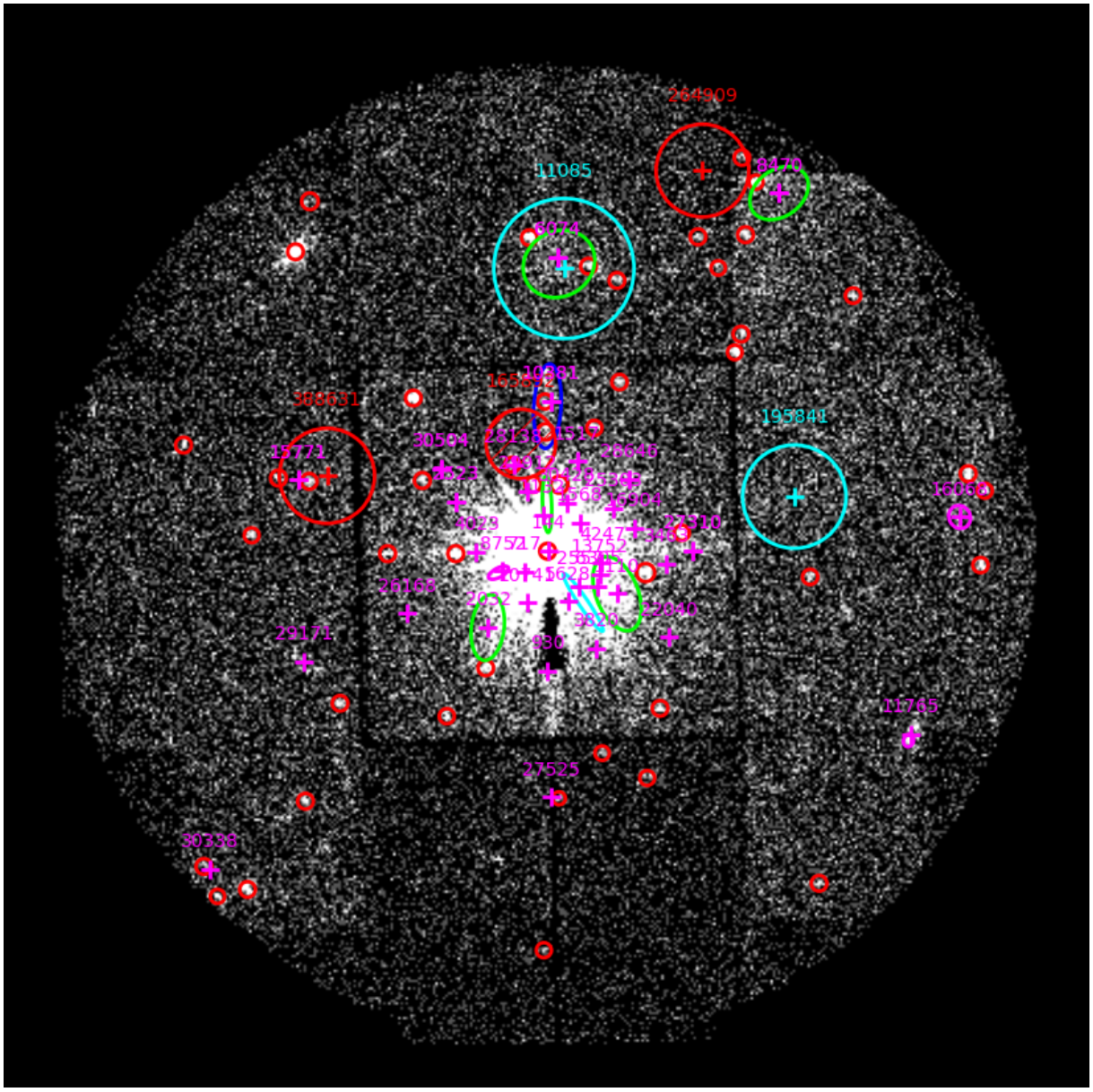

Figure 3.7: XMM observation 0652570101 pointed to the blazar Mkn 501, this object is classified by XAPA as a point source, its brightness creates saturation that is detected by XAPA as extended sources.

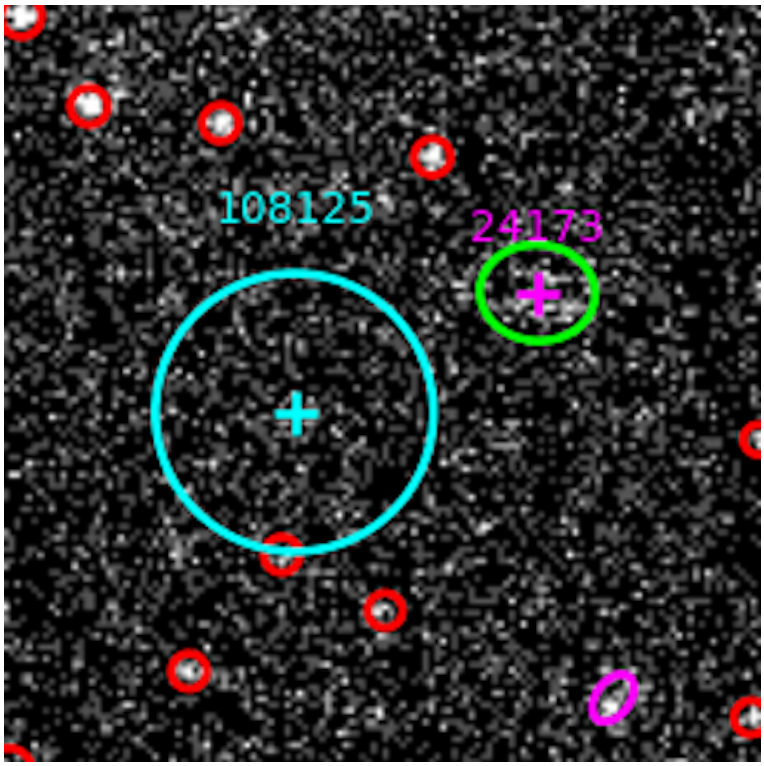

Figure 3.8: Example of a bad match between RM(108125) and XCS(24173), both sources are within 1.5Mpc however, the R_λ and XCS regions do not overlap.

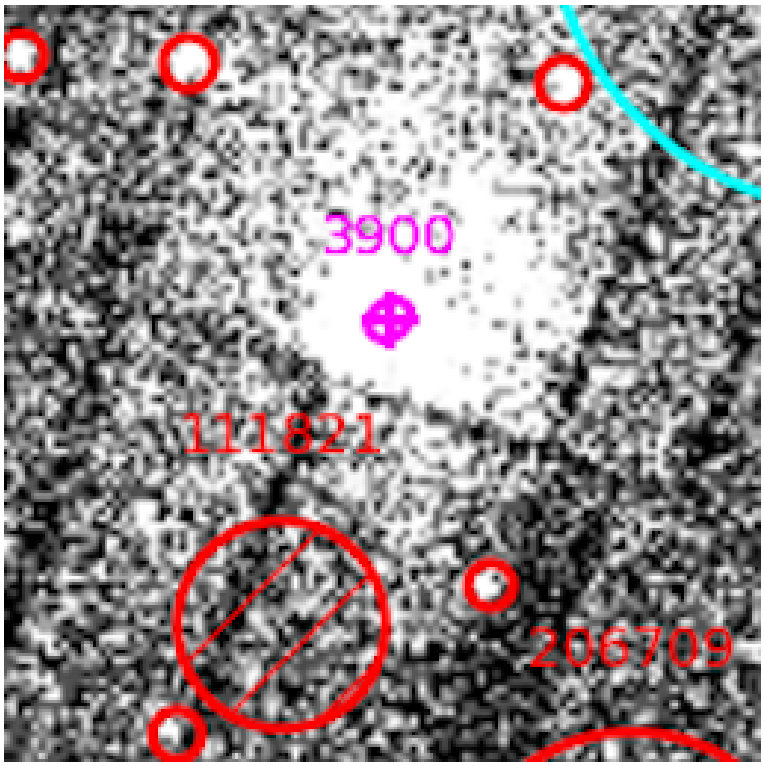

Figure 3.9: Example of a bad match between RM(111821) and XCS(3900), both sources are within 1.5Mpc but R_λ does not overlap with the XCS source. Notice that the RM source is red ($\lambda < 20$) and has diagonals bars indicating that it is a low redshift cluster that according to RM is not a reliable candidate.

3.4 Characterization of redMaPPer Clusters not detected by XCS

It is important to characterize the RM clusters that fall in the XMM footprint but were not matched to an XCS extended source by the $CM1$ algorithm. For this we have considered the RM SDSS catalog, for which there are in total of 2 765 clusters in the XMM footprint and without a match. This is too large a number to analysis in full, so we have only considered those in the ranges that the RM team define as relaible, i.e. $\lambda > 20$ and $z_\lambda > 0.08$. There are only **330** of these. The XMM postage stamps for all of them have been examined by eye and they have been found to fall into 5 broad categories:

1. **Low signal-to-noise ratio**: **40.6**% [**134**] have low signal-to-noise ratio ($SNR \sim 30$). This is lower than the ratio of the cluster with the lowest count rate in the final sample used to test X-ray to optical scaling relations ($SNR \sim 47$), e.g. Figure 3.10.a.

2. **High off-axis angle**: **46.36**% [**153**] are located near the edge of the observation. At this position the vignetted exposure map has its lowest values and the XMM PSF is poorly understood, e.g. Figure 3.10.b.

3. **Problematic XMM observation**: **4.8**% [**16**] clusters fall in "problematic" XMM observations, i.e. observations where: the background level is considerably high; there is a very bright source affecting the entire FOV (Xapa is unable to properly process such observations); there is a bright sources near to the RM position which effecting the local background, e.g. Figure 3.10.c.

4. **Xapa failures**: **1.51**% [**5**] cases reflect incidences where there is an X-ray source visible to the eye, but Xapa has failed to detect it. The example shown in Figure 3.10.d. is of a rich ($\lambda = 84.62$) cluster that was the intended target of the XMM observation. This example demonstrates that Xapa does not always work. However, after running Xapa a second time on the observation, the software did pick up the souce, and correctly identified it as extended.

5. **Point source classifications**: **6.66**% [**22**] of the RM clusters were classified by Xapa as point sources. As point sources are not considered by the CM1 algorithm, these clusters were excluded from further analysis, e.g. Figure 3.10.e.

Figure 3.10 illustrate each of these categories. It is important to mention that these common aspects are a result of the X-ray side alone, we need to analyze the optical

characteristics of these clusters as future work. From the complete sample, only five clusters are XAPA failures, this fact gives support to our ability to find clusters under the present methodology.

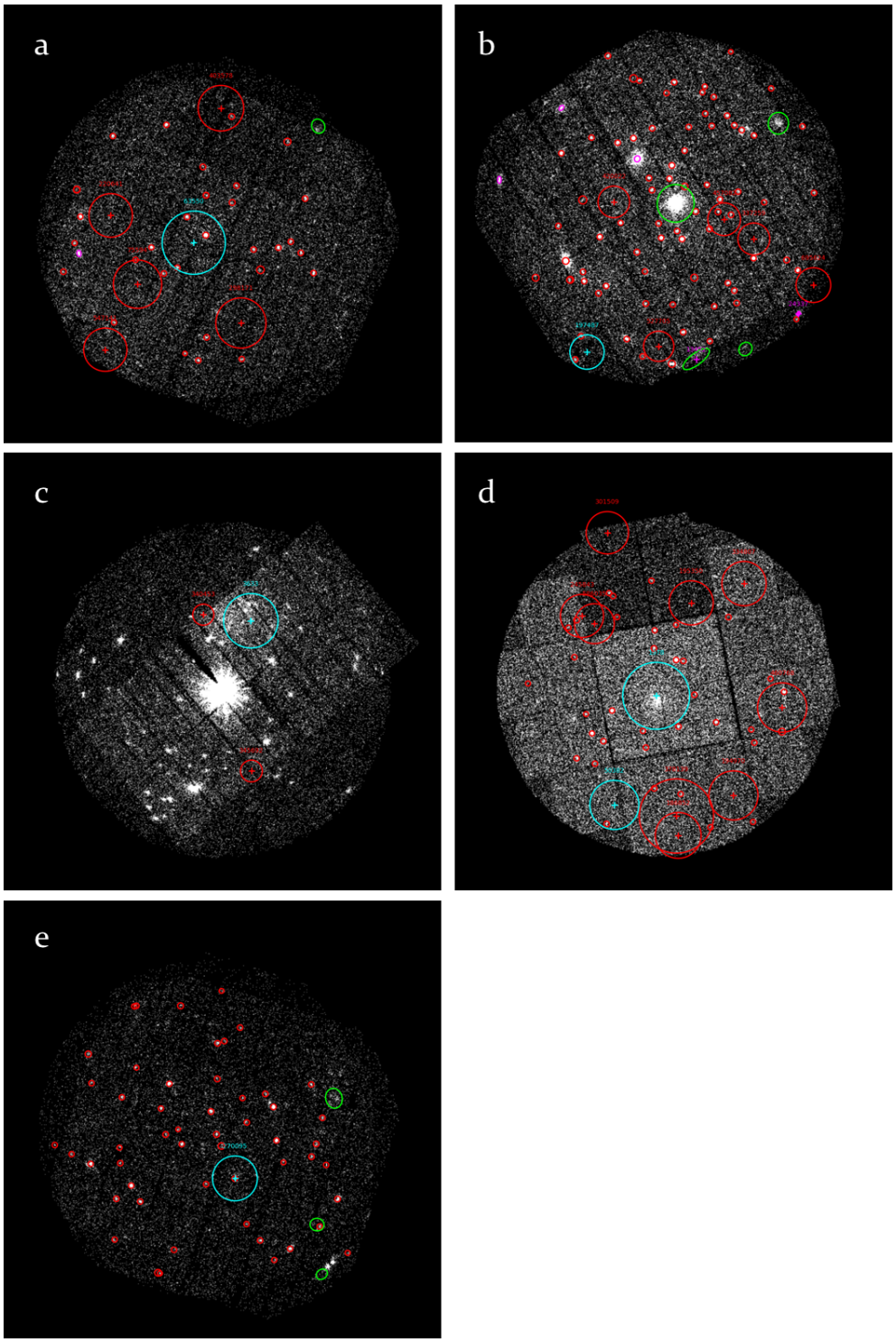

Figure 3.10: Several cases of RM clusters without XCS counterpart. Cyan circles are RM clusters with $\lambda > 20$, red circles are point sources, green and purple are XCS extended sources.

3.5 Conclusions and Future Work

3.5.1 Conclusions

1. The algorithm $SF1$ has been used to identify RM clusters that lie in the XMM footprint.

2. The algorithm $CM1$ has been used to match RM clusters to extended XCS sources within (projected) $1.5h^{-1}$Mpc and/or $3'$.

3. A new code to generate XCS postage stamps with overlaid RM information has been produced (circles of radius R_λ are shown in cyan if > 20, or red otherwise). This has significantly enhanced the ability to find the right match when there are several possibilities.

4. All the matched RM clusters were checked by eye using a PHP enabled webpage to weed out obvious failures and to assign a quality to the match (of "good" or "likely").

5. Two new samples of X-ray RM clusters have been defined from the RM-SDSS and RM-DESY1 catalogues (TableA3.2). It is important to mention that these samples are not yet "science ready". Additional filters need to applied first (see Section 5.2).

6. The procedures used in this Chapter are summarised in Figure 3.11.

7. We have investigated reasons why some RM clusters in the XMM footprint were not matched to XCS extended sources. In most cases this is due to the poor quality of the respective XMM observation.

3.5.2 Future Work

1. The extension of the analysis in this chapter to a recent update of the XCS database (it was expanded in size by $\simeq 5\%$ in April 2017).

2. A more detailed investigation into the reasons why some RM clusters were not detected by XCS despite falling in XMM images.

3. An aspirational goal would be to refresh the parts of the XCS pipelines that are generating the erroneous sources that led to some of type of "bad matches" due to saturation issues.

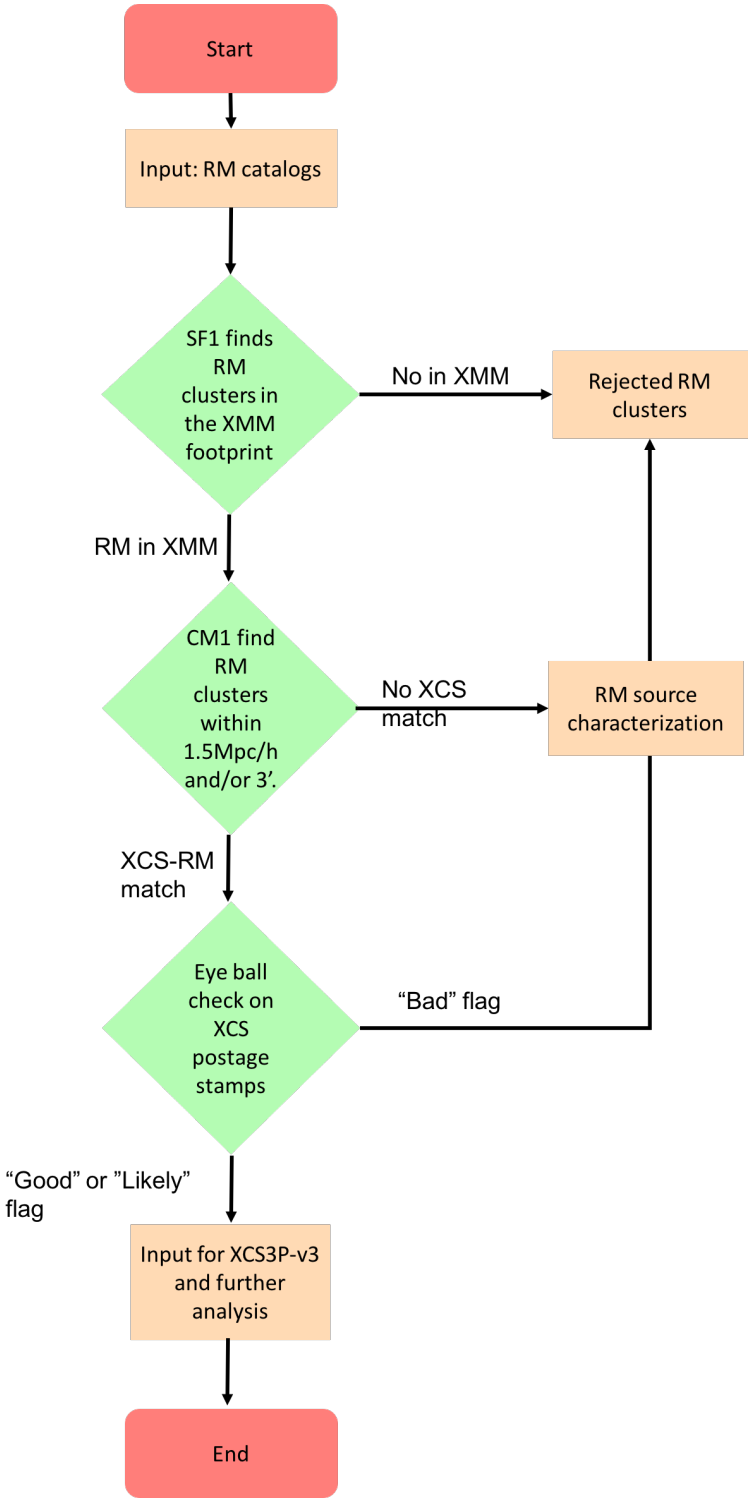

Figure 3.11: Flowchart of the main processes described in Chapter 3.

Chapter 4

XCS3P-v3: The third generation of the XCS Post Processing Pipeline

4.1 Overview

Motivation

Fundamental to our science goal (of measuring the slope, normalization, and scatter in the scaling relation between RM richness and XMM determined X-ray temperatures and luminosities, see above) is the measurement of $T_{\rm X}$ and $L_{\rm X}$ values for as many XCS-RM clusters as possible. The samples described in Chapter 3 are too large to make it practical to adopt the traditional "by hand" methods to derive these quantities from X-ray observations. Therefore, we need to ensure that they can be derived reliably using a pipeline approach.

Governing Assumptions

1. It is possible to derive X-ray parameters for clusters using a pipeline approach.
2. The XCS defined XAPA regions are sufficient to remove line of sight contamination from the cluster and background spectral apertures.
3. The post-processing pipelines previously developed by XCS are generally fit for purpose, but there is still room for improvement.
4. The XCS defined XAPA regions for extended sources are a better description of the underlying source shape than a circle.

5. X-ray parameters measured directly inside R_{500} are preferable to those interpolated to R_{500}.

Methodology

The approach taken was to make small adaptations to the version of the post processing pipeline (XCS3P-v2) developed during the thesis work of Philip Rooney (Rooney, 2015). A particular feature of the work herein is the detailed examination of individual clusters to diagnose subtle problems with XCS3P-v2. Corrections to these problems have required: new (less conservative) approaches to the exclusion of line of sight contamination; an additional (more conservative) quality filter related to an iterated extraction radius; and a correction to a previously flawed error estimation technique.

Results

The adaptations to XCS3P have resulted in: a) more clusters running successfully through the pipeline. This was primarily due to the application of the coefficient of variation filter; b) a reduction in the number of "successfull" runs that produced erroneous results. This was primarily due to the improvement in the sizing of the line of sight contamination exclusion regions; c) a solution to a years old "mystery" in XCS as to why some 1 upper limits to the $L_{\rm X}$ values were lower than the best fit value. This was due to a reworking of the TCL scripts used to drive XSPEC. A like-for-like comparison with the $L_{\rm X}$ - $T_{\rm X}$ scaling relation work in H12 and Rooney, 2015 demonstrated that the changes were only significant for a fraction of the clusters, i.e. as an ensemble the behaviour is unchanged compared to XCS3P-v2.

Conclusions and Future work

The new version of the post processing pipeline (XCS3P-v3) has been run, so far, on $\simeq$ 1 600 clusters. The new pipeline has been shown to be superior to the previous versions. The $L_{\rm X}$ and $T_{\rm X}$ parameters so derived have then been used in Chapter 5 to determine optical to X-ray scaling relations.

Future work planned by the XCS team includes a more in depth analysis of the $L_{\rm X}$ errors. The new approach is now mathematically correct, but there remains a concern that the XSPEC derived values do not properly propagate the uncertainty in the $T_{\rm X}$. Collaborators in Porto (Viana et al.) are already writing up the XCS3P-v3 $L_{\rm X}$ - $T_{\rm X}$ scaling relation work into a formal journal article. An aspiration of the XCS team is to switch to the `cflux` methodology in XCS3Pv4.

4.2 Introduction to XCS3P

The XCS team has developed a pipeline approach to perform quantitative analyses of the XMM data from which cluster candidates are identified using the XAPA software package. This pipeline is known as the XCS post processing pipeline, or XCS3P. The methodology underlying XCS3P is described below.

4.2.1 XSPEC model fits

As is typical in X-ray astronomy, the XCS team uses the NASA XSPEC package to carry out spectral analysis of XMM data. Both plasma temperatures ($T_{\rm X}$) and bolometric luminosities ($L_{\rm X}$) are determined by fitting a model spectrum to XMM data. The model used by XCS is `wabs x mekal`. This combination is commonly used in X-ray cluster astronomy, e.g. Borgani et al., 2004 and Mantz, Allen and Rapetti, 2010.

The `wabs` component accounts for photoelectric absorption by neutral hydrogen along the line of sight to the cluster. It uses the so-called "Wisconsin"(Morrison and McCammon, 1983) cross-sections:

$$M(E) = \exp\left[-n_H \sigma(E)\right], \tag{4.1}$$

where $\sigma(E)$ is the photoelectric cross-section and n_H is the hydrogen column given in units of 10^{22} atoms per cm^2. The n_H value in `wabs` can be left as a free-parameter, but during XCS fits, it is fixed at the value given in Dickey and Lockman, 1990.

The `mekal` component models the emission spectrum from hot diffuse gas based on (Mewe, Lemen and Oord, 1986), this model considers line emissions from several elements (C, N, O, Ne, Na, Mg, Al, Si, S, Ar, Ca, Fe, Ni). Relative abundances of these elements are defined their ratios to Solar abundances (Z). The Z value in `mekal` can be left as a free-parameter, but during the XCS fits used in this thesis, it is fixed at 0.3×Solar, i.e. the typical for X-ray clusters Kravtsov and Borgani, 2012. The redshift value is also fixed during the fits. The only parameters left "free" are the normalisation of the model and the plasma temperature. The normalisation is defined as

$$\frac{10^{-14}}{4\pi[D_A(1+z)]^2}\int n_e n_H dV, \tag{4.2}$$

where D_A is the angular diameter distance to the cluster, n_e and n_H are the electron and hydrogen densities, respectively, inside the cluster. After the best fit spectrum has been determined, one can extract a luminosity for the respective cluster using the `lumin` command.

Figure 4.1 is taken from Lloyd-Davies et al., 2011 (LD11, hereafter) and shows how the errors on fitted-T_X values vary with the number of detected counts and true-T_X of a cluster (fewer counts and higher temperatures lead to lower precision). When T_X or L_X relative errors are quoted by XCS (and in this thesis), the following convention is used:

$$\delta T_X = \frac{\Delta T_X}{T_X}, \ \delta L_X = \frac{\Delta L_X}{L_X}, \tag{4.3}$$

where ΔT_X (ΔL_X) is the difference between the upper and lower one sigma errors bounds on the T_X (L_X) fit.

Figure 4.2 (a) shows a high signal to noise XMM image of the extended XCS source XMMXCS J024803.3-033143.4, which is also a RM-SDSS cluster. The outline of the RM cluster is shown with the cyan circle, and of the XCS source with a green ellipse. This observation yielded the three camera spectra (data points) shown in Figure 4.2 (b). The XSPEC fit to these spectra (solid lines) constrained the plasma temperature to within 0.5%, i.e. $\delta T_X < 0.01$.

4.2.2 Overview of XCS3P

The XSPEC model fitting approach described above has been adapted by the XCS team to run in a pipeline fashion on multiple (up to 1000's) of clusters at a time. This innovative approach has allowed XCS to generate the largest catalogue of homogeneously analysed T_X values to date. The first generation of the XCS post processing pipeline (or XCS3P-v1) was used as part of the first XCS data release (XCS-DR1 Mehrtens et al., 2012), and is described in detail in LD11. Since XCS-DR1 there have been two significant upgrades, one presented in Rooney, 2015 (XCS3P-v2), and the one presented herein (XCS3P-v3, Section 4.3). The second generation pipeline has not been published, so we include some salient details (through comparison to XCS3P-v1) below (Section 4.2.3).

Aspects of XCS3P-v1 that have not been changed include the following:

1. Spectra are generated in the $0.3 - 7.9$keV band.
2. The model fitting is done using Cash (Cash, 1974) statistics.
3. The model used is `wabs x mekal` (Section 4.2.1).
4. Photons from other (to the cluster under test) sources were excluded from the source and background apertures using the XAPA defined region files.

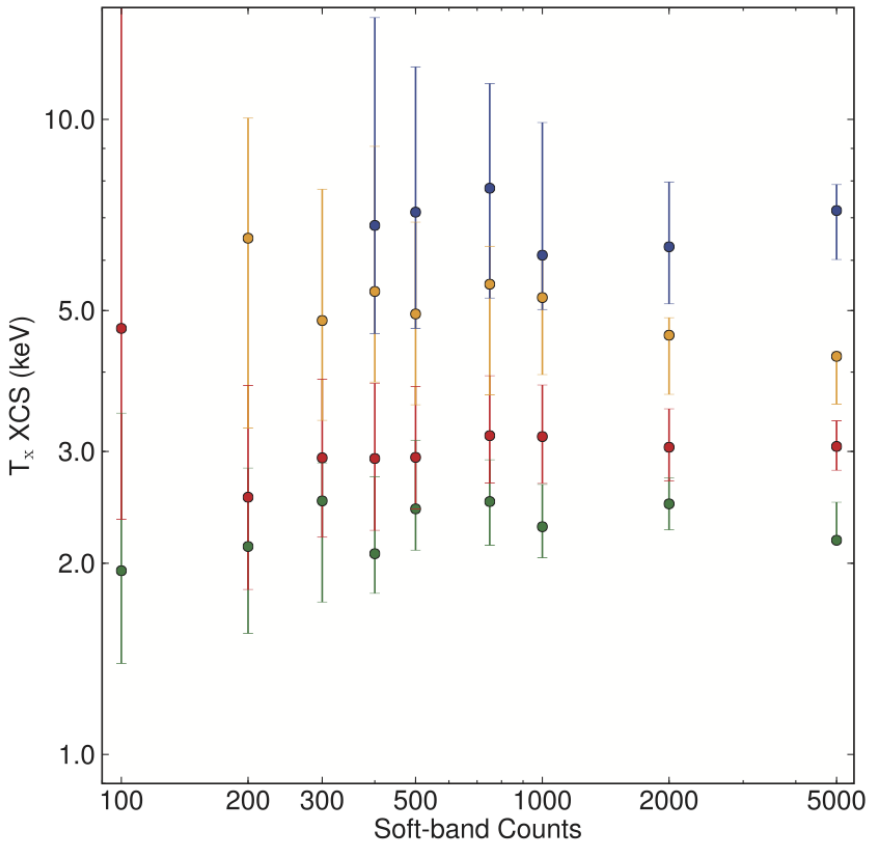

Figure 4.1: Figure taken from LD11: Demonstration of the impact of the number of background subtracted counts on the precious of extracted $T_{\rm X}$ values. The colours represent four different clusters that were detected with at least 5000 counts. Their respective exposures were then artificially reduced to generate lower signal to noise spectra. The best fit values, and the one-sigma upper and lower error bounds, were derived using XSPEC.

4.2.3 Changes implemented in XCS3P-v2

These aspects of XCS3P-v1 were changed in XCS3P-v2:

Aperture used to define $T_{\rm X}$

In v1, the $T_{\rm X}$ estimates were derived from the photons detected inside a circular region with a radius set by the major axes of the XAPA defined source aperture.
In v2, the $T_{\rm X}$ estimates were derived from the photons detected inside an elliptical aperture that retains the shape of the original XAPA region, but where the major axis has been scaled to an approximation of R_{500}. The R_{500} was estimated using the relation given in Arnaud, Pointecouteau and Pratt, 2005:

$$E(z)R_{500} = 1.104\,((T_X/5.0))^{0.57}\,, \tag{4.4}$$

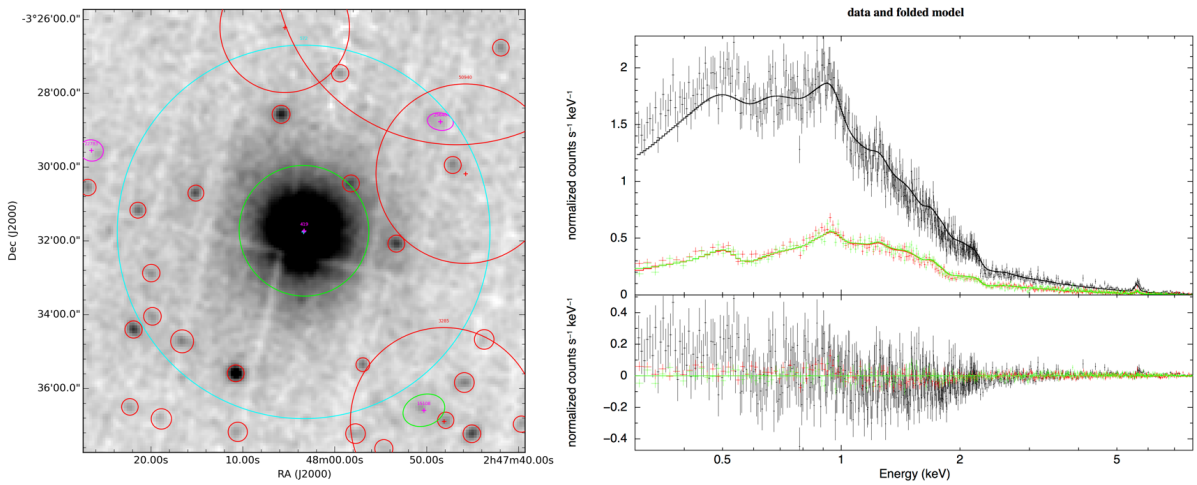

(a) (b)

Figure 4.2: XMMXCS J024803.3-033143.4, (a) A 6′ by 6′ region of an XMM observation. The region is centred on the centroid of an extended XCS source. The cyan circle indicates a $\lambda > 20$ RM cluster associated with that source. Small red small circles indicate XCS point sources. The other red circles indicate the locations of other low-richness RM clusters. (b) Energy spectra from three EPIC cameras are shown, EPIC-PN (black), EPIC-MOS1 (red), EPIC-MOS2 (green). Continuous lines indicate the best fit model (residuals in the lower panel).

where R_{500} has h^{-1} Mpc units and where $E(z) = \sqrt{0.27(1+z)^3 + 0.73}$. Clearly, the $T_{\rm X}$ value needs to be known before R_{500} can be calculated, so an iterative process needed to be used: An intial $T_{\rm X}$ value is calculated using the XAPA aperture. Then a R_{500} estimate is made and $T_{\rm X}$ is recalculated. Then the process was repeated i times until the ratio of $R_{500,i-1}/R_{500,i}$ converged (defined to be > 0.9 and < 1.1). Typically, the R_{500} scaled apertures were larger than those of the initial XAPA region (Figures 4.3 and 4.4).

Spectra used to define $T_{\rm X}$

In v1, all available EPIC observations of a given cluster were used to constrain $T_{\rm X}$ in a simultaneous XSPEC fit. Usually this was just the three EPIC camera observations that comprise most[1] XMM observations. However, in some cases, there are multiple observations of the same part of the sky, and so there can be more than three spectra (and in some cases over 50) included in the $T_{\rm X}$ fit.

When v1 was developed, it was assumed that adding more spectra would always improve signal to noise. When v2 was being developed, this assumption was tested. It was shown in

[1] In a minority of XMM observations, data from one or more cameras is not recorded.

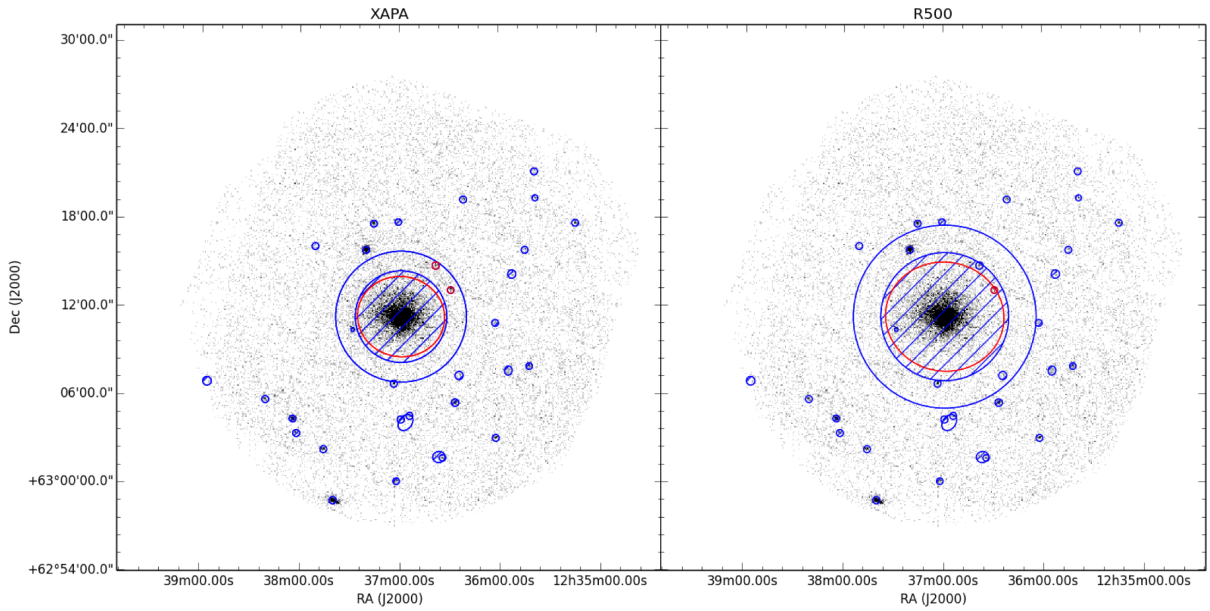

Figure 4.3: The XMM targeted observation of Abell cluster 1576 (XMMXCSJ 123658.8+631117.9). Right: the XAPA source region (red ellipse) used to derive the initial $T_{\rm X}$ value needed for XCS3P-v2. Left: the final XAPA source region (red ellipse) used to derive the final $T_{\rm X}$ value after an iteration that scales the major axis to R_{500}. The blue circles de-limit the background annulus. The small red circles enclose XAPA detected point sources - photons detected inside these circles are not included in the source and background spectra.

Rooney, 2015 that it is better to limit the number of spectra used to those that individually have sufficient signal to noise to permit a $T_{\rm X}$ fit. The $T_{\rm X}$ fit to an individual spectrum needs to be in the range $0.08 < T_{\rm X} < 30$ keV (no XCS clusters will be genuinely hotter than 30keV, and few will be colder than 0.08keV). Moreover, the fit must include both upper and lower 1σ errors. If either of those conditions are not met, then the respective spectrum is excluded from the simultaneous joint fit. As shown in Figure 4.5, these filters can lead to a dramatic reduction in the number of spectra used. However, the net result is an improvement on the $T_{\rm X}$ measurements, as shown in Figure 4.6.

Spectral models used to fit $T_{\rm X}$

In v1, four different spectral fits were performed:

1. n_H and Z frozen at measured (Dickey and Lockman, 1990) and $Z = 0.3{\rm M}_{\odot}$ respectively,

2. n_H and Z free,

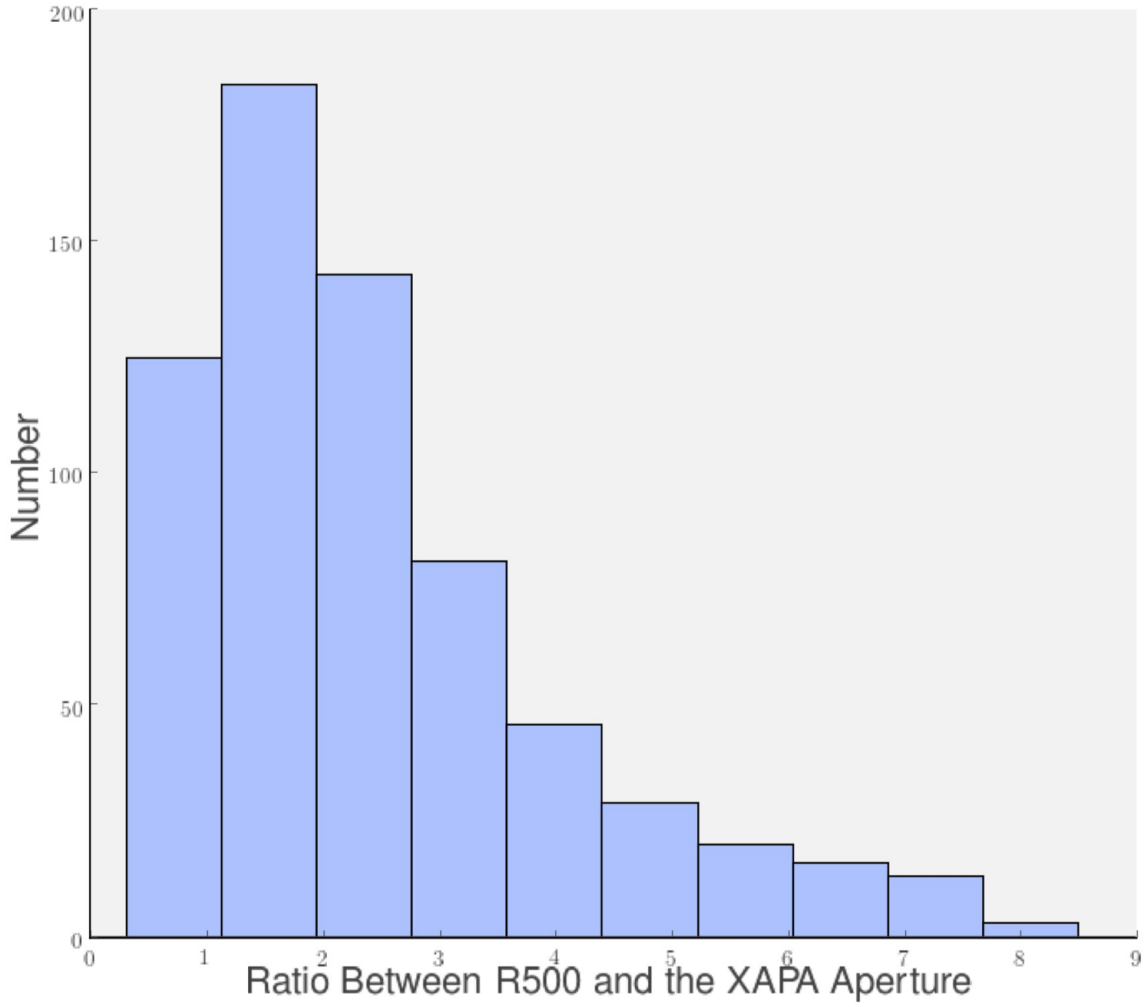

Figure 4.4: Figure from Rooney, 2015: The ratio of the R_{500} and XAPA apertures (based on 660 clusters)

3. n_H and Z free plus extra power law component (to account for possible AGN contamination),

4. n_H and Z free plus extra `mekal component (to account for a cool core).`

When more than one of the four model variations produced an acceptable fit (defined as $(0.3 < T_{\rm X} < 17.0\text{keV})$), the $T_{\rm X}$ value with the smallest relative error was adopted.
In v2, the code was simplified and only the first model was tested.

XSPEC interpolation method

In v1, the `switch` control parameter in the XSPEC `mekal` model was set to 1, i.e. the model was interpolated over a grid of temperatures with pre-calculated spectra. In v2, `switch` was set to 0 to increase the accuracy of the fits, i.e. XSPEC calculated the model

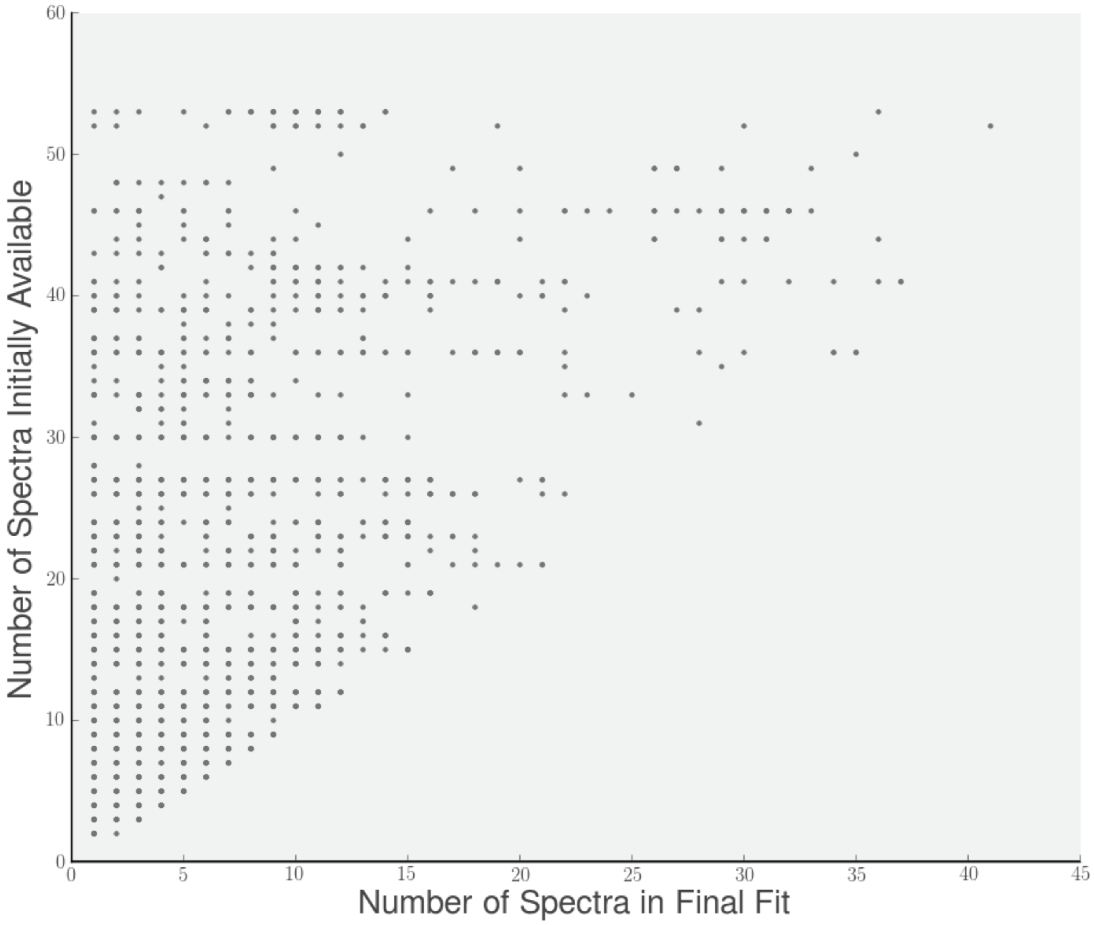

Figure 4.5: Figure from Rooney, 2015: Comparison between total available spectra and spectra used in the final XCS3P-v2 fit, each point represents a different cluster.

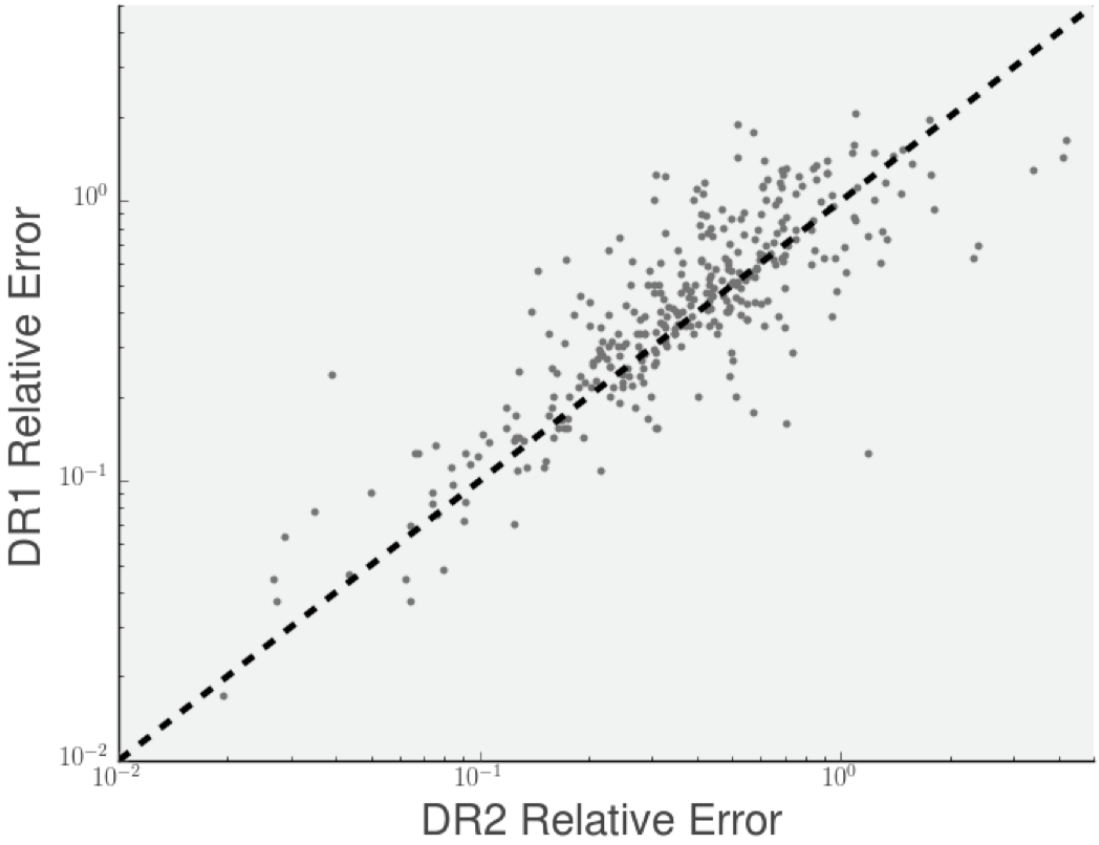

Figure 4.6: Figure from Rooney, 2015: Comparison of the relative error on $T_{\rm X}$ for clusters in common between XCS-DR1 (using XCS3O-v1) and XCS-DR2 (using XCS3O-v2).

spectrum for each temperature rather than using interpolation. The reduction in run speed was more than compensated by the use more nodes on the APOLLO supercomputer.

Aperture used to define $L_{\rm X}$

In v1, the bolometric luminosity calculation involved a spatial fit to the cluster surface brightness profile, assuming a circular β-profile:

$$S(r) = S(0)\left[1 + \left(\frac{r}{r_c}\right)^2\right]^{-3\beta+1/2}, \tag{4.5}$$

where r_c is the core radius and β is the density index parameter, and S is the surface brightness. Three different fits were performed:

1. centroid and normalisation were free to vary, but β was fixed to the canonical value of 2/3,
2. Similar to (1) but β is allowed to vary.
3. Similar to (2), but with an added central cusp (to account for a cool core) with two additional free parameters (cusp normalization and power law index).

The MINUT package (James and Roos, 1975) was used to find the best-fitting model from the three. Then this model was used to set an R_{500} radius (under the assumption of hydrostatic equilibrium). The ratio of the source count-rate inside this radius, to that inside the circularised XAPA radius used to fit $T_{\rm X}$, was calculated. The bolometric luminosity derived (using the XSPEC `lumin` command) from the best fit spectral model was then scaled by this ratio.
In v2, the code was simplified. Since the $T_{\rm X}$ value was now derived inside R_{500}, no spatial fitting was necessary to derive the bolometric $L_{\rm X}$ value inside R_{500}.

4.3 Changes implemented in XCS3P-v3

Section 4.2.3 gave a summary of the changes implemented in XCS3P-v2 by Rooney, 2015. In this Section I describe the changes made as part of the research presented in this thesis.

4.3.1 Exclusion of emission from nearby extended sources

When XCS3P-v3 was under development, it was noticed that some high signal to noise clusters were yielding poor quality $T_{\rm X}$ fits. Further investigation showed that this problem was confined to clusters with nearby (in projection) extended sources, but the underlying

reason was not immediately obvious. It was only after a procedure was written to generate figures that showed the regions used in the spectral fit (source, background, and excluded sources) that the problem was diagnosed.

In Figure 4.7, we show an XMM targeted observation of a cluster with a nearby extended source. On the left, we show the regions that are used by XCS3P-v2: the green ellipse defines the source region (scaled to R_{500}), and the blue circles outline the background region. The red hashed regions show places where photons are "drilled out" prior to spectral fitting because they have been deemed to be associated with another source. It is clear from the Figure that two much area has been drilled out around the nearby extended source. In this case only a small fraction of the intended source's flux has been drilled out, but in others we found that to be a significant problem. A detailed review of the XCS3P-v2 source code showed that nearby extended sources with more than 1000 source counts were expanded by a factor of 3 before the $T_{\rm X}$ fit took place:

```
if scts > 0.0:
        scale = math.pow(scts/1000.0,0.5)
        if scale > 1.0:
            if scale < 3.0:
                return scale*major, scale*minor
            else:
                return 3.0*major, 3.0*minor
        else:
            return major, minor
    else:
        return major, minor
```

In XCS3P-v3, we removed this scaling factor. On the right of Figure 4.7 we show how the "drilled out" regions are now defined. After applying this change, we were able to extract more $T_{\rm X}$ values than was possible with XCS3P-v2.

4.3.2 Improved method to iterate to R_{500}

In Section 4.2.3, we described how a method to iterate to an R_{500} was implemented in XCS3P-v2. The convergence criteria was simple, i.e. the ratio of the last radius to the second to last was within 10% of unity. After convergence, a final $T_{\rm X}$ fit is carried out, and following that, and $L_{\rm X}$ value is calculated.

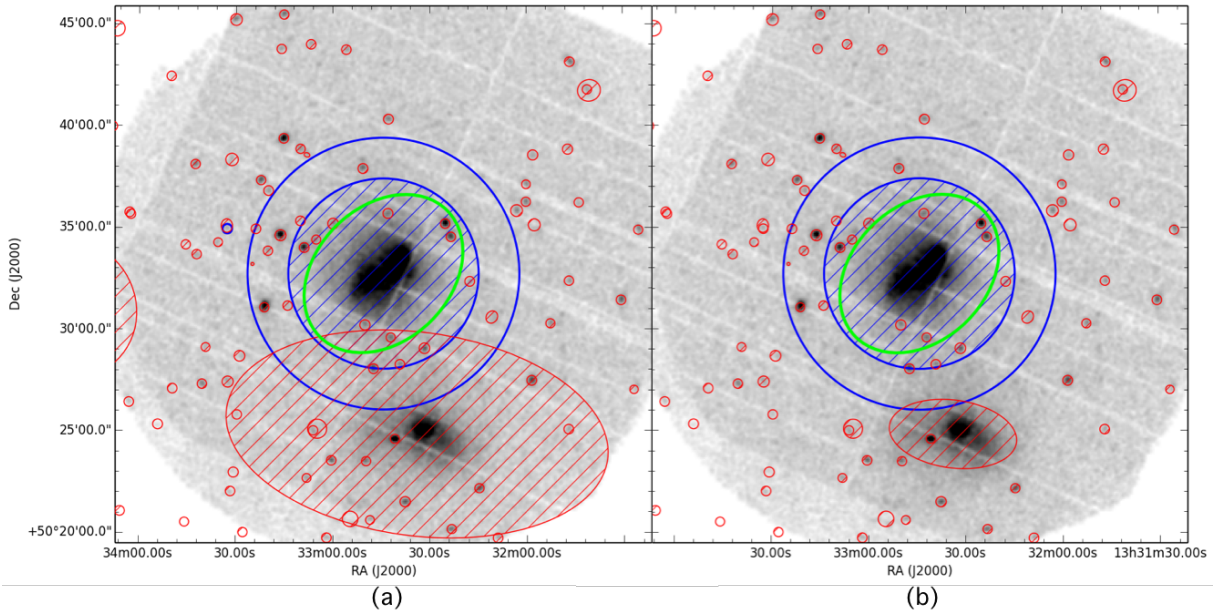

Figure 4.7: Left: background (region between outer and inner blue circles) and cluster (green) regions used on temperature-luminosity pipelines, red small circles are point sources. Notice how a nearby extended source (hash red ellipse) is taking part of the background and also the main source. On the right, nearby extended sources are re-sized by removing escalation with photon counts. Abell cluster 1758

When XCS3P-v3 was under development, it was noticed that some high signal to noise clusters were yielding $T_{\rm X}$ values that were offset from the expected $T_{\rm X} - \lambda$ scaling relation (e.g. from that presented in Rykoff and Rozo, 2014). An examination of the $T_{\rm X}$ values extracted after each iteration demonstrated that even if the R_{500} value is not changing much between steps, the $T_{\rm X}$ value can vary considerably (by more than 100% in some cases).

Therefore, we added to XCS3P a calculation of the coefficient of variation (Koopmans, Owen and Rosenblatt, 1964) of the $T_{\rm X}$ values at each R_{500} iteration step. This coefficient is defined as the ratio of the standard deviation (σ) to the mean(μ):

$$C_v = \frac{\sigma(T_{\rm X})}{\mu(T_{\rm X})}. \tag{4.6}$$

The coefficient is an standardized measure of dispersion of a frequency distribution. If $C_v < 1.0$ it is considered low-variance, in this work we adopted a range of $C_v \leq 0.25$ as an indicator of reliable measurement on the iterative R_{500} temperature.

Figure 4.8 shows the correlation between C_v and the relative temperature error (Equation 4.3) when XCS3P-v3 was applied to the 1 319 clusters in the SDSS-RM-XCS sample (row 1 of Table 3.2). Red (blue/green) points indicate clusters with relative errors $\delta T_{\rm X} \geq$

$(\leq)0.3$. The green points highlight cases where the errors on the temperature are acceptable ($\delta T_{\rm X} \leq 0.3$), but the coefficient of variation is not (i.e. $C_v > 0.25$). In total, 16% of the SDSS-RM-XCS sample were filtered out by this criterion.
In the following we show examples of clusters that passes and failed the coefficient of variation filter.

XMMXCS J104724.0

Figure 4.9 shows the XMM image of cluster XMMXCS J104724.0+151436.0 ($C_v = 0.001$, $\delta T_{\rm X} = 0.06$, $z = 0.208$) associated with a high richness ($\lambda = 127.65$) RM cluster. In this case, $T_{\rm X}$ has been measured to high precision and the coefficient of variation is very small.

XMMXCS J100117.6

Figure 4.10 shows the XMM image of cluster XMMXCS J100117.6+285109.2 ($C_v = 0.358$, $\delta T_{\rm X} = 0.17$, $z = 0.09$) associated with a low richness ($\lambda = 11.34$) RM cluster. In this case, $T_{\rm X}$ has been measured to acceptable precision, but the coefficient of variation is large.

XMMXCS J130534.5

Figure 4.11 shows the XMM image of cluster XMMXCS J130534.5+175656.3 ($C_v = 0.504$, $\delta T_{\rm X} = 0.98$, $z = 0.52$) associated with a high richness ($\lambda = 90.63$) RM cluster. In this case, $T_{\rm X}$ has been measured with an unacceptable precision, and the coefficient of variation is large. From the figure it is clear that a large fraction of the very bright source to the top right of the image was not enclosed by a XAPA aperture and therefore that those photons would be polluting the spectral fit.

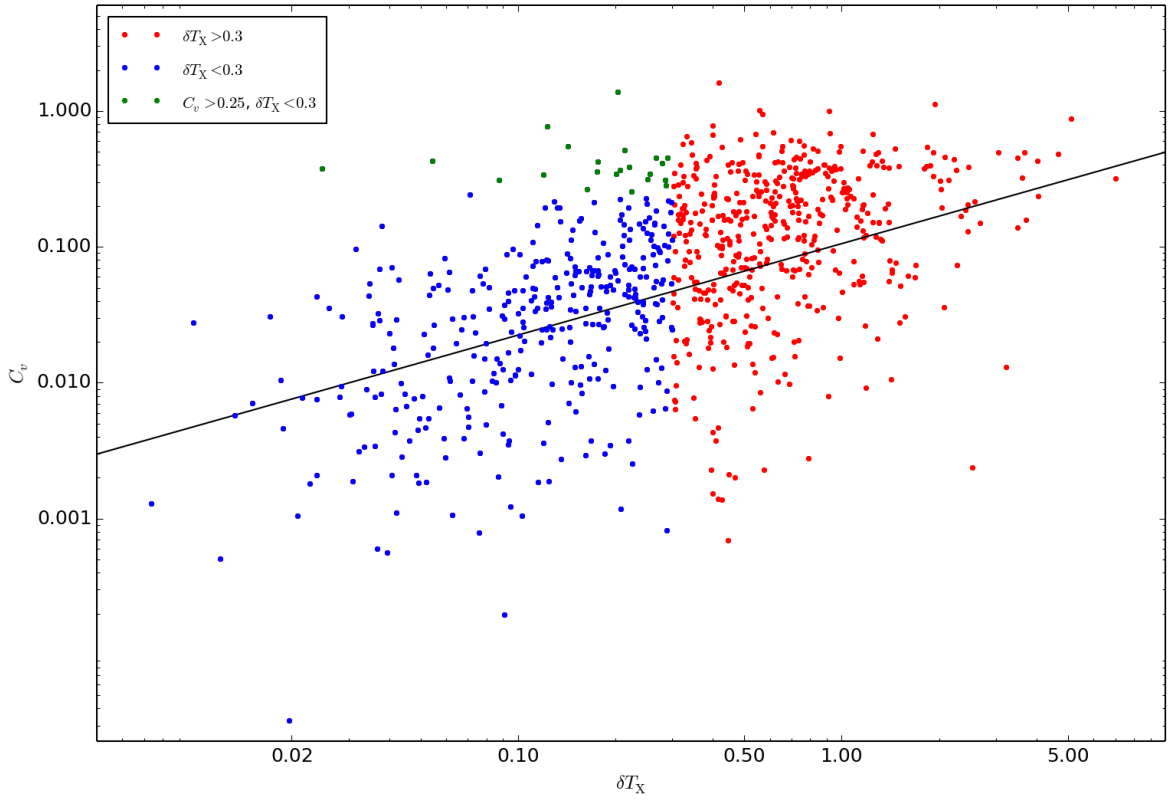

Figure 4.8: Coefficient of variation vs relative error in measured plasma temperature.

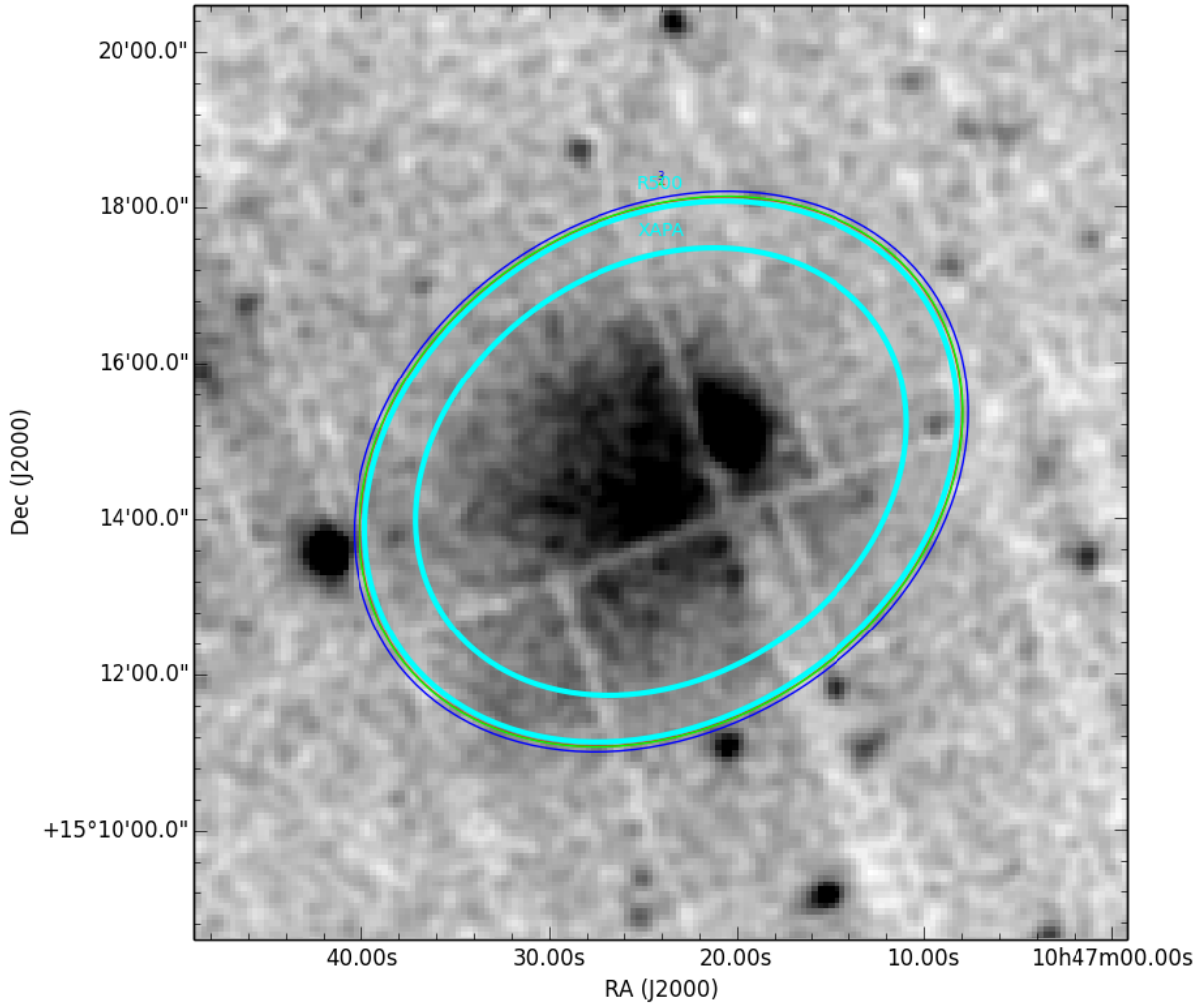

Figure 4.9: XMM observation of the cluster XMMXCS J104724.0+151436.0 and the source extraction regions for $T_{\rm X}$ calculation during the R_{500} iteration. The cyan ellipses indicate the initial (XAPA) and final (R_{500}) regions. The other coloured ellipses (which are very close together in this example) indicate the iterations until convergence was reached.

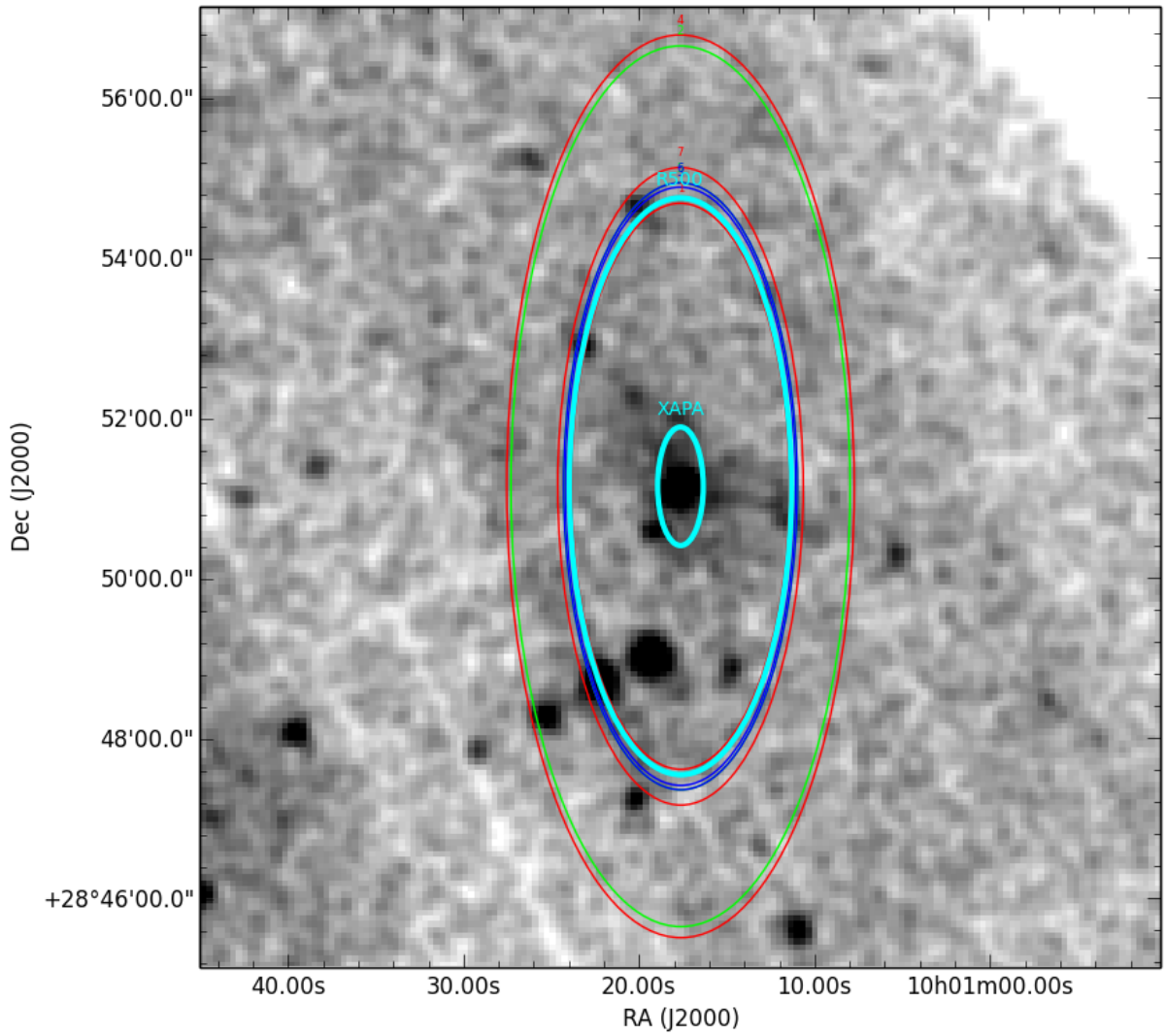

Figure 4.10: As Figure 4.9, but for cluster XMMXCS J100117.6+285109.2. Note that the region sizes change significantly between interations.

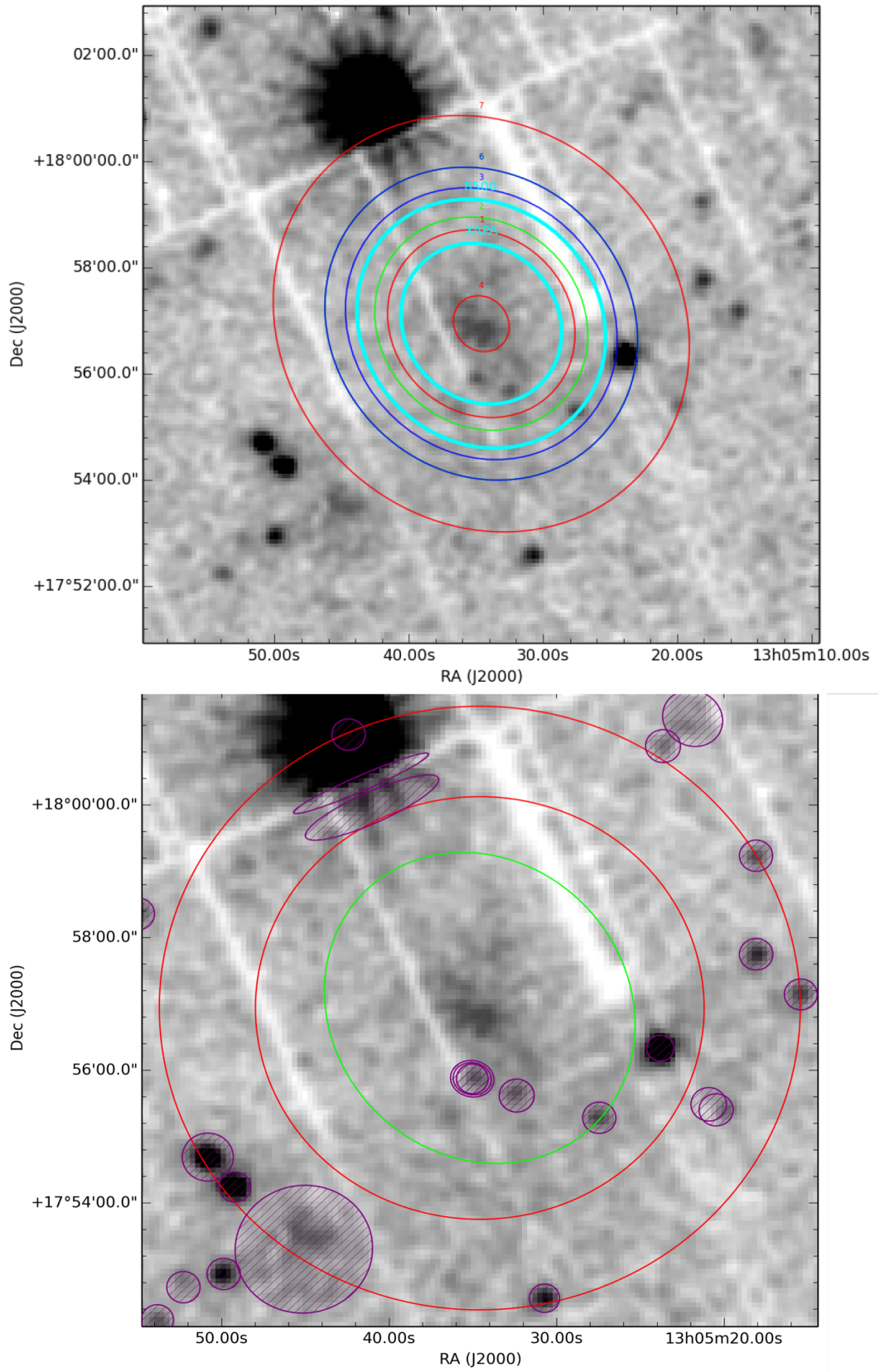

Figure 4.11: Top: Similar to Figure 4.9, but for cluster XMMXCS J130534.5+175656.3. Bottom: The source (green ellipse) and background (annulus between red circles) regions used during the final spectral fits. Hashed out red regions were "cheesed" out of the source or background spectra.

4.3.3 Improved method to measure luminosity errors

For several years, it had been noted by XCS team members that $L_{\rm X}$ errors were occasionally in error, in the sense that the one σ upper limit value could be lower than the best fit value. The reason for these only anomalies became clear after a careful inspection of the TCL (Section 2.3) script used by XCS3P-v1 (and again in XCS3P-v2) to determine $L_{\rm X}$ errors. The code snippet shown below was found to be at fault.

```
lumin 0.001 100.0 $z err 1000 68.3
scan [tcloutr lumin 1] "%f %f %f %f %f %f" lum llum ulum c d e
scan [tcloutr param 1] "%f" xnh
newpar 1 0.0 0.01 0.0 0.0 1000.0 1000.0
lumin 0.001 100.0 $z
scan [tcloutr lumin 1] "%f %f %f %f %f %f" lum0 a b c d e
newpar 1 $xnh 0.01 0.001 0.001 1000.0 1000.0
set scale [expr $lum0/$lum]
set lum $lum0
set llum [expr $llum*$scale]
set ulum [expr $ulum*$scale]
```

The issue lies in the fact that when the $T_{\rm X}$ fit takes place, the model under test includes absorption by neutral hydrogen along the line of sight to the cluster (most of which resides in our own Galaxy). However, the $L_{\rm X}$ needs to reflect the conditions at the cluster, and should reflect a model that includes no line of sight neutral hydrogen. This was the case in XCS3P-v1 (via the line `newpar 1 0.0 0.01 0.0 0.0 1000.0 1000.0`), so the *best fit* $L_{\rm X}$ values were correct (L_0). However, it is not possible to determine the *errors* when $n_{\rm H}$ has been set to zero, because the errors come from the spectral fit to the actual (absorbed) data. Therefore, the errors are determined using an initial luminosity ($L_{\rm ini}$) calculation before $n_{\rm H}$ has been set to zero (via the line `lumin 0.001 100.0 $z err 1000 68.3`). These errors are then scaled by the ratio of L_0 and $L_{\rm ini}$.

Here `scale`= $L_0/L_{\rm ini}$, the scaled errors are `llum`= $L_{{\rm x},l} * scale$ and `ulum`= $L_{{\rm x},u} * scale$. Also $L_{{\rm x},l} = L_{\rm X} - 1\sigma$ and $L_{{\rm X},u} = L_{\rm X} + 1\sigma$. Thus, scaling $L_{{\rm X},l}$ instead of the 1σ errors could lead to an underestimation of the associated luminosity errors.

As a proposed solution for XCS3P-v3, we modify the previous tcl script to:

```
lumin 0.001 100.0 $z err 1000 68.3
scan [tcloutr lumin 1] "%f %f %f %f %f %f" lum llum ulum c d e
```

```
scan [tcloutr param 1] "%f" xnh
newpar 1 0.0 0.01 0.0 0.0 1000.0 1000.0
lumin 0.001 100.0 $z

set lxl [expr $lum-$llum]
set lxu [expr $ulum-$lum]

scan [tcloutr lumin 1] "%f %f %f %f %f %f" lum0 a b c d e
newpar 1 $xnh 0.01 0.001 0.001 1000.0 1000.0
set scale [expr $lum0/$lum]
set lum $lum0

set sig_l [expr $lxl*$scale]
set sig_u [expr $lxu*$scale]

set llum [expr $lum-$sig_l]
set ulum [expr $lum+$sig_u]
```

Here first the upper and lower 1σ errors are found by `set lxl [expr $lum-$llum]` and `set lxu [expr $ulum-$lum]`, then these values are multiplied by the scale factor defining a new variable `sig_l`$= 1\sigma_l * scale$, `sig_u`$= 1\sigma_u * scale$. Finally we redefine the upper and lower luminosity values as $L_{\mathrm{X},l} = L_{\mathrm{ini}}-$`sig_l` and $L_{\mathrm{X},u} = L_{\mathrm{ini}}+$`sig_u`.

4.4 XCS3P-v3 validation

4.4.1 Comparison with the `cflux` technique

The technique described in Section 4.3.3 to estimate L_{X} errors, i.e. by setting the hydrogen column to zero and then re-scaling, is a "fudge". Subsequent discussions with collaborators in the Dark Energy Survey collaboration (Devon Hollowood and Tesla Jeltema, UCSC) alerted us to an XSPEC technique they have been using for their analysis of cluster data from the Chandra X-ray Telescope. The UCSC team calculate bolometric luminosity using the `wabs*cflux*mekal` model, not `wabs*mekal`. The use of `cflux` circumnavigates the need to set n_{H} to zero.

I have run fits on several clusters using both the XCS3P-v3 method and the `cflux` method

and have confirmed that both the best fit luminosity and the errors bounds are consistent between the two approaches.

4.4.2 Comparison with Hilton et al., 2012 and Rooney, 2015

We want to test the XCS3P-v3 methodology by comparing the $T_X - L_X$ scaling relation with the results obtained on XCS DR1 data by Hilton et al., 2012 (through XCS3P-v1) and Rooney, 2015 (through XCS3P-v2).

It is important to mention that the results from XCS3P-v1 and XCS3P-v2 are a review and no new material is presented in the subsections 4.4.2, 4.4.2.

L_X -T_X Fitting Method

The model used to fit the $T_X - L_X$ relation in H12, Rooney, 2015, and in this thesis, is as follows:

$$\log(E^{-1}(z)L_X) = A + B\log(T_X/5\text{ keV}) + C\log(1+z), \tag{4.7}$$

where L_X is the bolometric luminosity, T_X is the X-ray temperature in keV, A is the normalisation, B is the slope and $C\log(1+z)$ accounts for redshift evolution. Luminosities has been scaled by $E(z)^{-1}$ which is the evolution of the Hubble parameter, $E(z) = [\Omega_m(1+z)^3 + \Omega_\Lambda]^{1/2}$, which is the evolution expected in the self-similar model.

Parameters in this model are obtained using Markov Chain Monte Carlo (MCMC), implemented using the Metropolis et al., 1953 algorithm. Two different fitting methods were used which both take into account the intrinsic scatter and the measurement errors. H12 define an orthogonal and bisector regression methods. **Orthogonal Method** The orthogonal regression method defined in H12 considers the probability density for a given cluster as:

$$P_{\text{model}} = \frac{1}{\sqrt{2\pi(\Delta r^2 + S^2)}} \exp\left[-\frac{(r - r_{\text{model}})^2}{2(\Delta r^2 + S^2)}\right], \tag{4.8}$$

where $r - r_{\text{model}}$ is the orthogonal distance from the cluster to the model relation in the $\log L_X$-$\log T_X$ plane, Δr is the error on the orthogonal distance calculated from the errors in temperature and luminosity, and S is the orthogonal intrinsic scatter.

The likelihood $\mathcal{L}$ of a given model is the product of P_{model} for each cluster in the sample, for the orthogonal model:

$$\mathcal{L}(L_X, T_X|A, B, C, S) \propto P_{\text{prior}}(A, B, C, S)\prod_i P_{\text{model,i}}, \tag{4.9}$$

$P_{\text{prior}}(A, B, C, S)$ take specific range for each variable, Table 4.1 shows each variable range.

Parameter	Prior	Notes
A	$(41, 47)$	-
B	$(1, 5)$	-
C	$(-3, 3)$	-
S	$(0.01, 0.5)$	Orthogonal method only
$\sigma_{\log L_X}$	$(0.01, 0.5)$	Bisector method only
$\sigma_{\log T_X}$	$(0.01, 0.5)$	Bisector method only

Table 4.1: Table taken from Hilton et al., 2012. Priors on the L_X-T_X relation fit parameters.

Bisector Method In this method, scatter and measurement errors in each axis are treated independently. $P_{\rm model}$ is the product of the Gaussian probabilities of the residuals of L_X and T_X from the given bisector best-fitting line, instead of $r_{\rm model}$ they use:

$$y_{\rm model} = \log(E^{-1}(z)L_X - [A + B\log(T/5) + C\log(1+z)], \quad (4.10)$$

$$x_{\rm model} = \log(T/5) - [\log(E^{-1}(z)L_X) - A - C\log(1+z)]/B, \quad (4.11)$$

and replace r and Δr as appropriate on Equation 4.8). S is replaced by $\sigma_{\log L_X}$ and $\sigma_{\log T_X}$. In a similar way, the likelihood is given by

$$\mathcal{L}(L_X, T_X | A, B, C, \sigma_{\log L_X}, \sigma_{\log T_X}) \propto P_{\rm prior}(A, B, C, \sigma_{\log L_X}, \sigma_{\log T_X}) \prod_i P_{\rm model,i}, \quad (4.12)$$

L_X -T_X Scaling Relations derived using XCS3P-v1 and XCS3P-v2

The H12 analysis was based on the 221 XCS-DR1 (**2012**) clusters with spectroscopic redshifts and version 1 of XCS3P. These clusters cover a redshift range of $0.06 \leq z \leq 1.46$ (with median redshift, $z = 0.28$) and temperature range of $0.6 \leq T_X \leq 9.8$ keV (median $T_X = 2.9$ keV). Figures 4.12 and 4.13 and Table 4.2 show the results of applying the method described in Section 4.4.2 to these 221 XCS-DR1 clusters.

Redshift range	N	A	B	$\sigma_{\log L_X}$
$0.0 - 0.25$	96	44.63 ± 0.10	3.18 ± 0.22	0.33 ± 0.04
$0.25 - 0.5$	77	44.47 ± 0.07	2.82 ± 0.25	0.23 ± 0.04
$0.5 - 1.5$	38	44.28 ± 0.07	2.89 ± 0.45	0.24 ± 0.05

Table 4.2: Table taken from Hilton et al., 2012: L_X-T_X relation fit parameters derived from the orthogonal method, for XCS-DR1 subsamples in redshift bins.

H12 slope and intrinsic scatter At low redshift ($z < 0.25$), Hilton et al., 2012 measured similar slope to the value obtained by REXCESS (Pratt et al., 2009). Lower normalization was measured for XCS-DR1 data in comparison with clusters in the REXCESS sample. This discrepancy could be due differences in the spectral fitting methods (XCS used Cash statistics while REXCESS used Chi Squared), another explanation is the detection of a higher proportion of cool core clusters. The bisector fit slope shows the expected signature of Malmquist bias, whereas the orthogonal fit shows no evolution. The intrinsic scatter appears to decrease with redshift, this suggests there might be a decreasing fraction of cool core clusters at high redshift.

H12 normalisation The evolution parameter C on Equation 4.7) was fit to the four parameter model described in sub-section(4.4.2). The normalization parameter A is consistent with that found by Pratt et al., 2009 within less than 2σ. Using the orthogonal method, the evolution of the normalisation is negative ($C = -1.5 \pm 0.5$), this indicates that the evolution in luminosity at fixed temperature is significantly less than the self-similar prediction ($C = 0$). Considering the bisector method, the evolution parameter is found to be closer to self-similar prediction ($C = -0.05 \pm 0.3$), this could be explained by the much lower $z = 0$ normalisation found using the bisector method. Thus, regardless of the fitting method, XCS-DR1 data are consistent with negative evolution of the normalisation of the $L_{\rm X}$-$T_{\rm X}$ relation with respect to the self-similar prediction.

XCS3P-v2 results The Rooney, 2015 analysis was based on the same sample of clusters as H12. Figure 4.14 and Table 4.3 show the results of applying the method described in Section 4.4.2 to these 221 XCS-DR1 clusters. The normalisation is found to be considerably higher than H12 for clusters with redshift $z < 0.5$, but comparable at $z > 0.5$. The slope of the scaling relation evolves with redshift, in accordance to the Malmquist bias (Salpeter, 1955). The evolution of the normalisation is consistent with self-similarity ($C = 0.2 \pm 0.5$), i.e. in conflict with the findings of H12. Considering only clusters with $z < 0.5$ the evolution parameter changes ($C = 0.43 \pm 0.91$) and has a higher uncertainty. The work in Rooney, 2015 showed that the H12 results were not robust the a change in the XCS post processing pipeline.

The XCS3P-v3 $L_{\rm X} - T_{\rm X}$ Scaling Relation

XCS3P-v3 was applied to almost the same cluster sample as H12 and Rooney, 2015. It was not possible to use exactly the same sample because 30 of the XCS-DR1 clusters

Redshift range	N	A	B	$\sigma_{\log L_X}$
$0.0 - 0.25$	96	44.97 ± 0.01	3.25 ± 0.22	0.34 ± 0.04
$0.25 - 0.5$	77	44.82 ± 0.08	3.05 ± 0.29	0.35 ± 0.05
$0.5 - 1.5$	38	44.20 ± 0.05	2.41 ± 0.32	0.22 ± 0.04

Table 4.3: Table taken from Rooney, 2015: L_X-T_X relation fit parameters derived from the orthogonal method, for XCS-DR2-β subsamples in redshift bins.

are not included in the XCS Master Source List available at the time of writing (the reasons for their omission are still under investigation by other members of the XCS team). Figures 4.15 and 4.16 and Table 4.4 show the results of applying the method described in Section 4.4.2 to these 221 XCS-DR1 clusters. The slope found by XCS3P-v3 is within 1σ of the results from XCS3P-v1 and XCS3P-v2 for any redshift bin.
We note that a subset of 28 of these clusters failed the coefficient of variation test (i.e. $C_v \leq 0.25$). When these were excluded from the best fit expression changed from

$$E^{-1}(z)L_X = 10^{44.42\pm0.09}(T_X/5)^{3.17\pm0.18}(1+z)^{0.43\pm0.48}, \tag{4.13}$$

to

$$E^{-1}(z)L_X = 10^{44.62\pm0.10}(T_X/5)^{3.48\pm0.19}(1+z)^{-0.36\pm0.48}. \tag{4.14}$$

Using XCS3P-v3 we find evidence for mild positive evolution ($C = 0.43 \pm 0.48$), although, like the mild negative evolution found using XCS3P-v2, it is within 1σ of the self similar predictions. In conclusion, XCS3P-v3 has produced similar results with regard to the L_X -T_X relation to XCS3P-v2.

Redshift range	N	A	B	$\sigma_{\log L_X}$
$0.0 - 0.25$	81	44.53 ± 0.01	3.51 ± 0.29	0.41 ± 0.04
$0.25 - 0.5$	66	44.51 ± 0.08	3.02 ± 0.26	0.30 ± 0.04
$0.5 - 1.5$	37	44.39 ± 0.06	2.25 ± 0.38	0.22 ± 0.04

Table 4.4: The L_X-T_X obtained with XCS3P-v3 using the orthogonal fitting method defined in Hilton et al., 2012, for each redshift range.

.

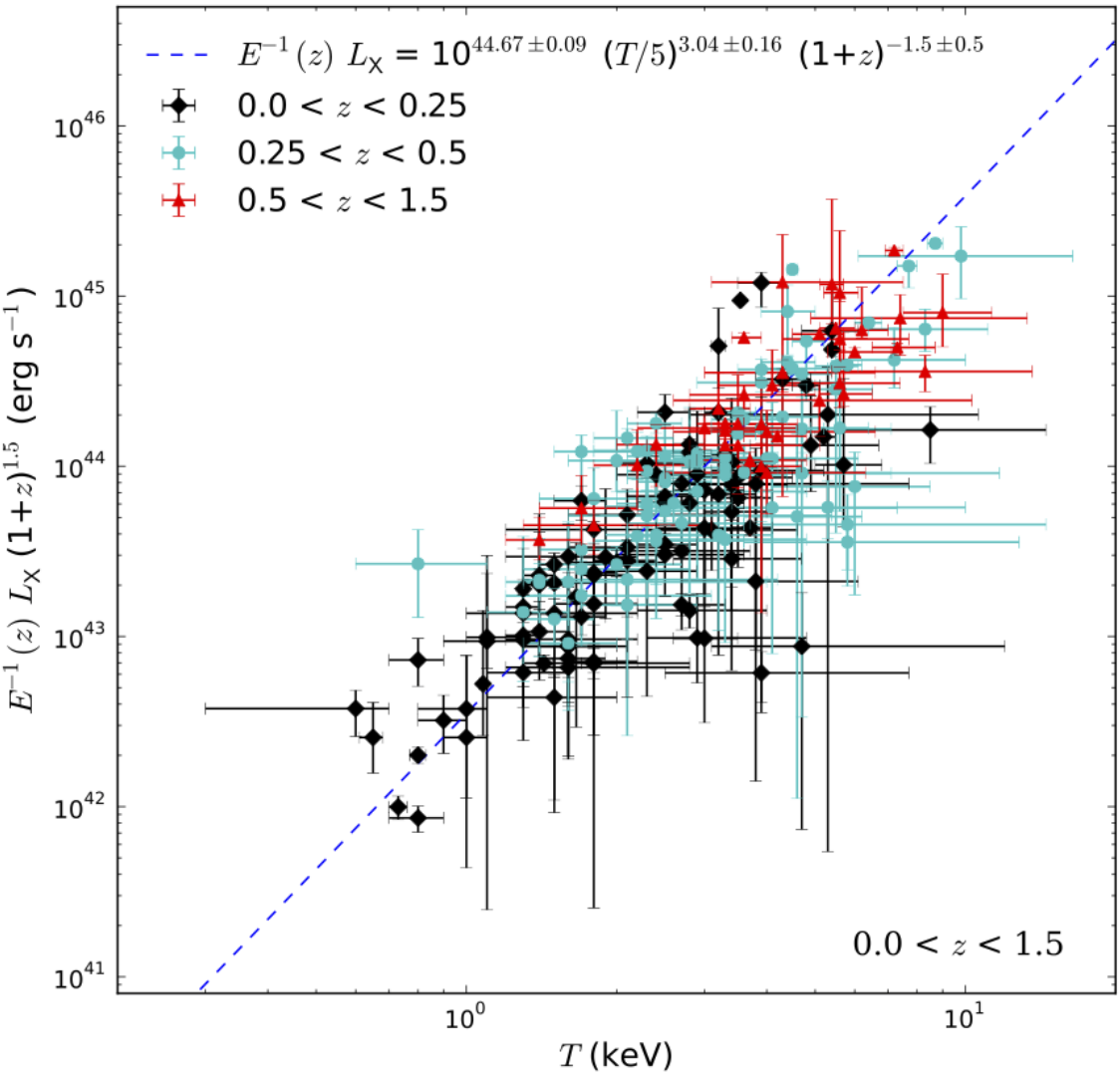

Figure 4.12: Figure and caption taken from Hilton et al., 2012: The L_X-T_X relation for the 211 XCS-DR1 clusters with spectroscopic redshifts. The dashed line is the best-fitting four parameter model (Equation 4.7), determined using the orthogonal fitting method. The luminosities have been scaled to take into account the evolution in the normalisation as a function of redshift inferred from the best-fitting model parameters, as well as the $E^{-1}(z)$ evolution expected in the self-similar case.

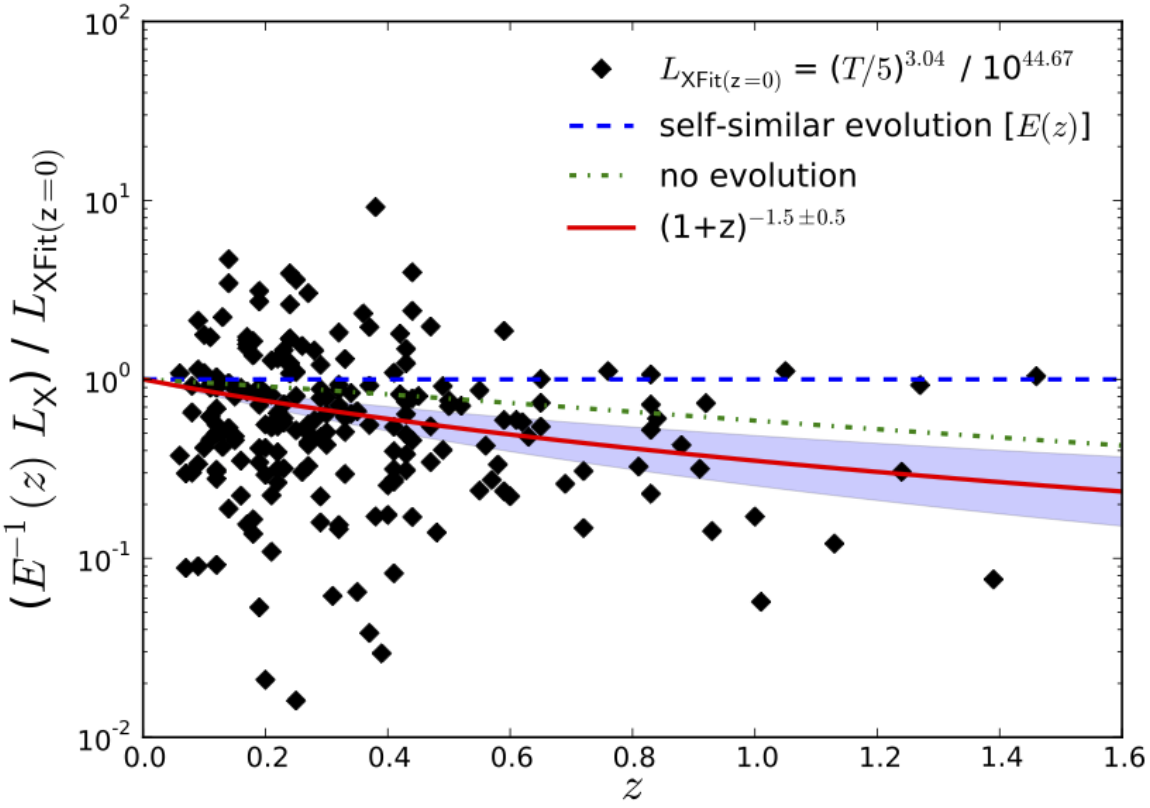

Figure 4.13: Figure and caption taken from Hilton et al., 2012: Evolution of the normalisation of the L_{X}-T_{X} relation relative to the self-similar case [$E(z)$], as inferred from the best-fitting four parameter model (Equation 4.7), using the orthogonal fitting method. The shaded area shows the marginalised 68 per cent confidence region on the evolution derived using MCMC. The dot-dashed line shows the track for no redshift evolution in the normalisation of the relation. The black diamonds show individual XCS clusters, errors not shown to avoid cluttering the plot.

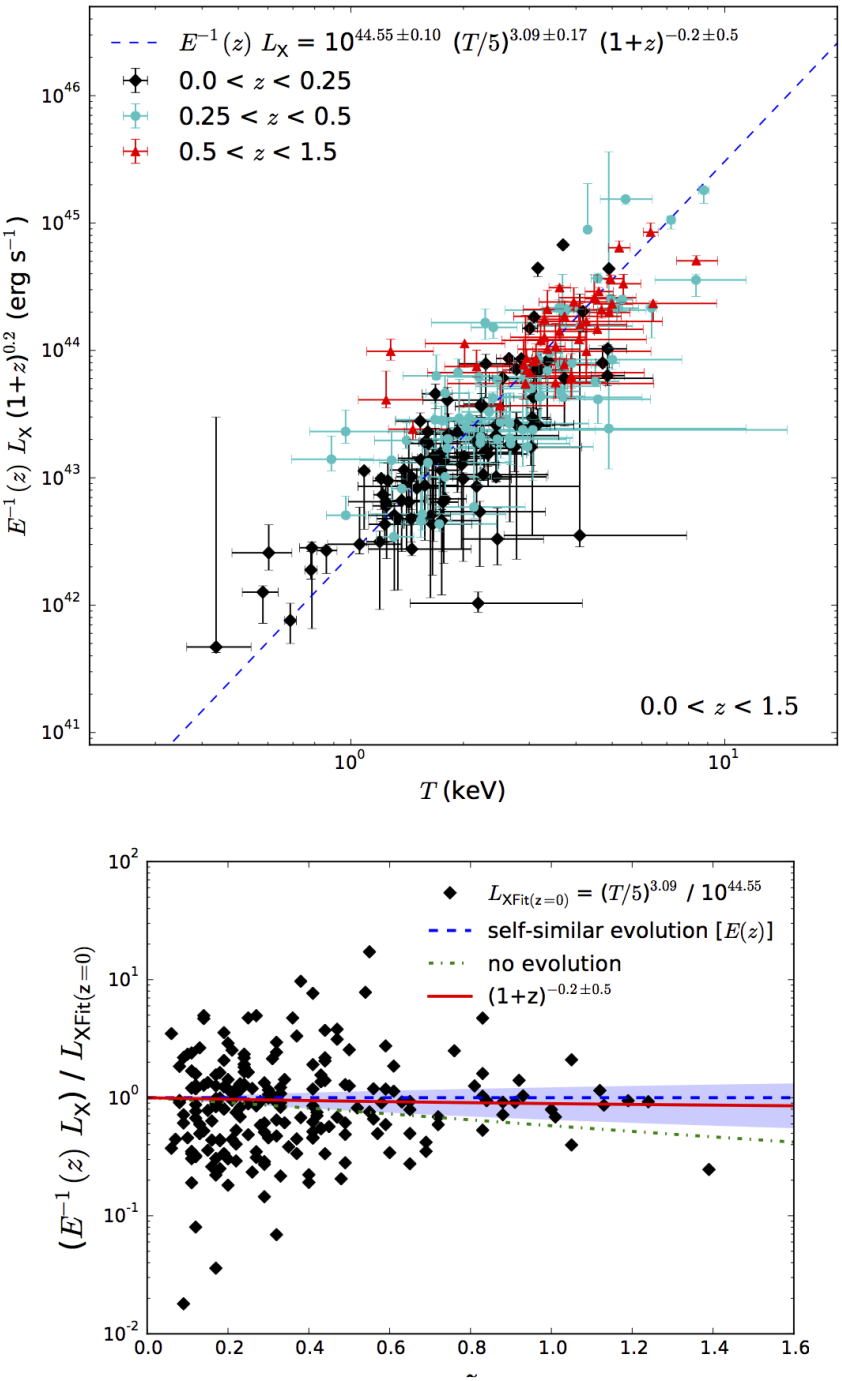

Figure 4.14: Figure taken from Rooney, 2015 Upper:The L_X-T_X relation obtained through XCS3P-v2. The dashed line is the best-fitting four parameter model (Equation 4.7). Lower:Evolution of the normalisation of the L_X-T_X relation relative to the self-similar case [$E(z)$]. The shaded area shows the marginalised 68 per cent confidence region on the evolution derived using MCMC. The dot-dashed line shows the track for no redshift evolution in the normalisation of the relation.

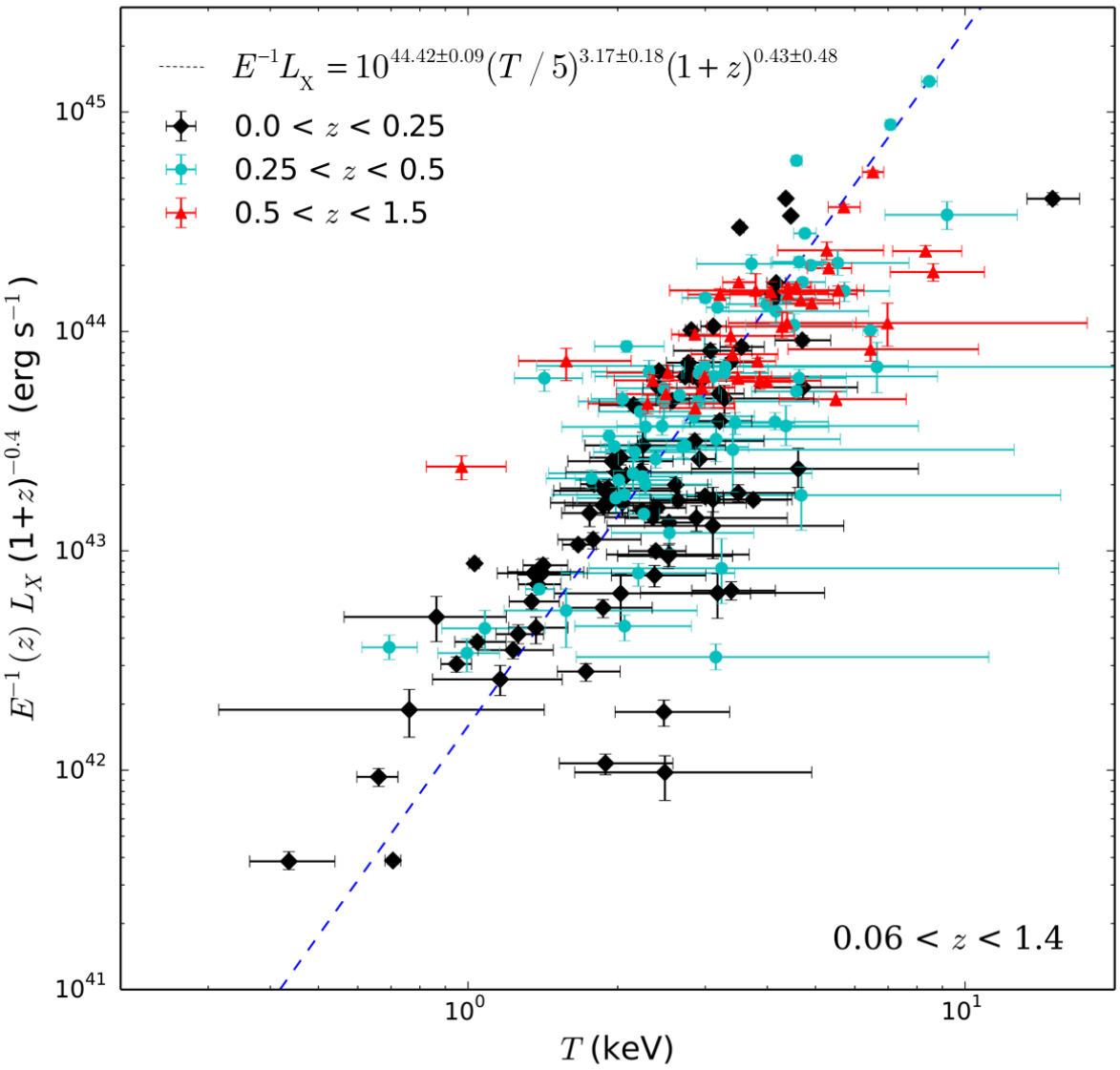

Figure 4.15: Similar to Figure 4.12: The $L_{\rm X}$-$T_{\rm X}$ relation obtained through the XCS3P-v3 methodology. The dashed line is the best-fitting four parameter model (Equation 4.7). Clusters in black are within $z \in [0.0 - 0.25]$, cyan $z \in [0.25 - 0.5]$ and red $z \in [0.5 - 1.5]$.

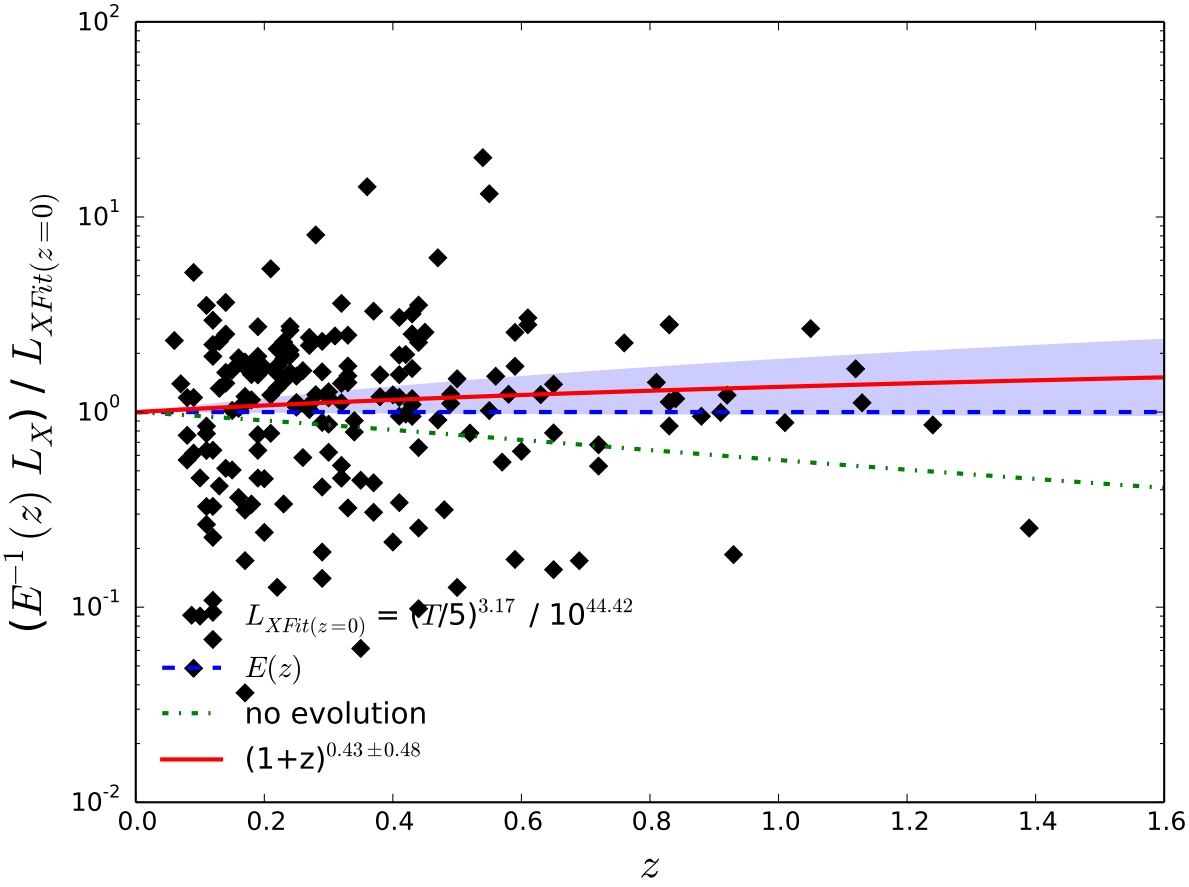

Figure 4.16: Similar to Figure 4.13: Evolution of the normalisation of the $L_{\rm X}$-$T_{\rm X}$ relation relative to the self-similar case [$E(z)$], as inferred from the best-fitting four parameter model (Equation 4.7), using the orthogonal fitting method. The shaded area shows the marginalised 68 per cent confidence region on the evolution derived using MCMC. The dot-dashed line shows the track for no redshift evolution in the normalisation of the relation. The black diamonds show individual XCS clusters (error bars are omitted for clarity).

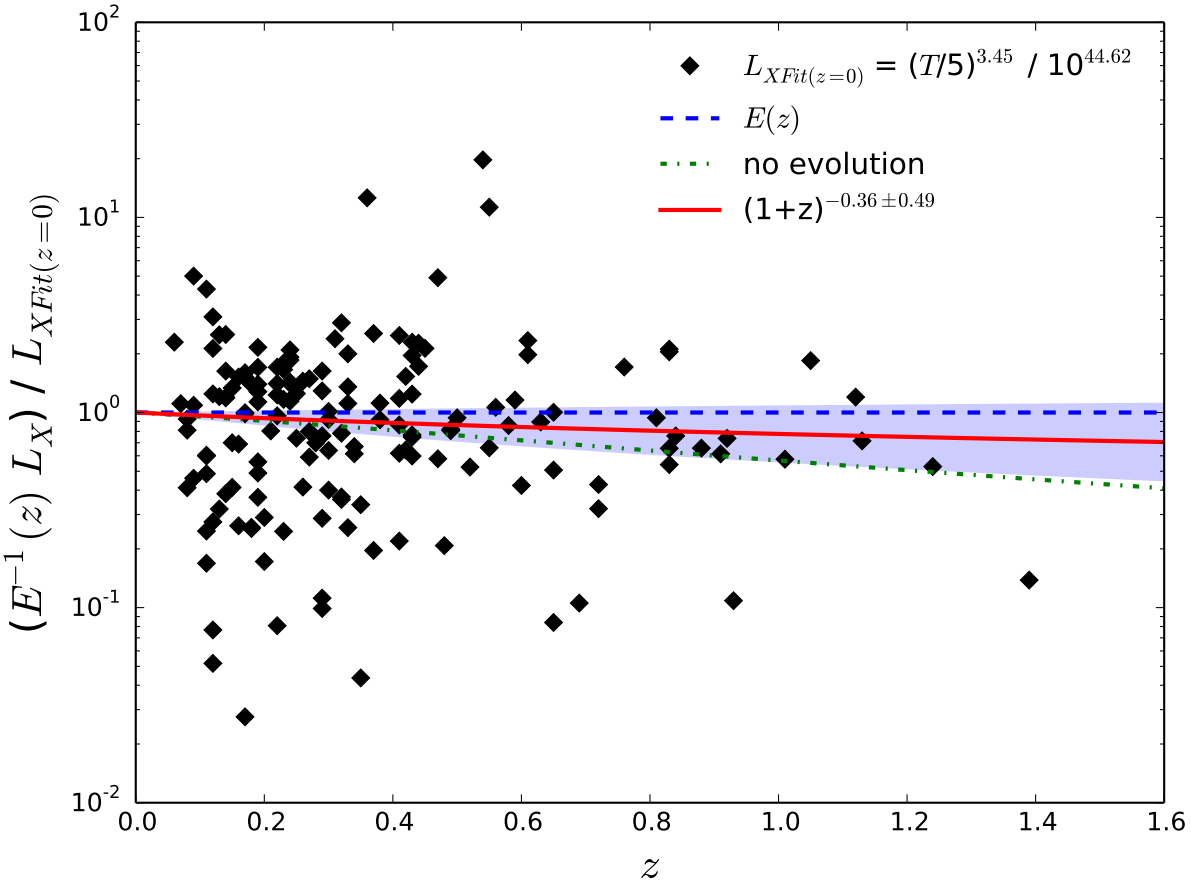

Figure 4.17: Similar to Figure 4.16, C_v criteria was used to make a sub-sample of XCS DR1 clusters with spectroscopic redshifts.

4.5 Methodology results comparison between XCS3P-v3, XCS3P-v2 and XCS3P-v1

It is not possible to compare directly the results from each methodology as XCS3P-v1 (followed by LD11 for XCS DR1) finds only serendipitous clusters, while XCS3P-v2 and XCS3P-v3 find clusters in all the XMM FOV. In order to make a fair comparison, I obtained the clusters from XCS DR1 with a counter part in the RM-SDSS catalogue, the redshift information is congruent between both catalogs, then it was not necessary to calculate temperature and luminosity. However, L_X and T_X were calculated for that particular sample (XCS DR1 in RM-SDSS) following the XCS3P-v2 and XCS3P-v3 methodologies. In total, the sample has 200 objects for which there is information from each methodology. The redshift range of this sample is $z = [0.05 - 0.6]$.

We compared the results by calculating the relative error of temperature and luminosity (defined in Equation 4.3). Next table shows the results.

	XCS3P-v1	**XCS3P-v2**	**XCS3P-v3**
No T_X/L_X	22	0	0
$\delta T_X \leq 15\%$	58	62	61
$\delta T_X \leq 20\%$	89	62	61
$\delta T_X \leq 30\%$	123	91	90
$\delta T_X \leq 50\%$	160	169	169
$\delta L_X \leq 15\%$	27	143	138
$\delta L_X \leq 20\%$	35	165	152
$\delta L_X \leq 30\%$	64	186	184
$\delta L_X \leq 50\%$	103	199	184

Table 4.5: Relative error comparison between the results obtained through XCS3P-v1, XCS3P-v2 and XCS3P-v3

.

From Table 4.5 it is possible to see that XCS3P-v1 did not converge for 22 clusters while the other two methodologies obtained results. In terms of the precision of the measurement, which is given by the relative error, we see that the numbers for δT_X are similar between versions (see Figure 4.19). The big difference is on the luminosity, where XCS3P-v1 has lower quality than the other versions (five times lower) this can be explained by the fact that version 2 and 3 do a simultaneous fit of the available spectra to obtain the luminosity.

XCS3P-v2 had a mistake on the error calculation, this led to an underestimation of the associated errors, this fact can be seen on the results as the relative error associated to the luminosity is smaller for XCS3P-v2 than XCS3P-v3, see Figure 4.20.

There are interesting cases where the temperature measured by XCS3P-v2 differs from the value obtained by XCS3P-v3. One of them is the cluster XMMXCS J015315.1+010214.9, where the difference in temperature is 3.54 keV. The relative errors associated to the temperature are considerably low on both methodologies, let us remember that this parameter indicates the precision of the measurement. The image of this cluster is shown in Figure 4.18, on the left (a) the cluster source regions and background using the XCS3P-v2 methodology, on the right (b) source regions and background for the XCS3P-v3 methodology. In both cases, the green and purple regions represent the source for the first and last iteration accordingly. Red regions are the background for the last iteration. We can see on (a) that the cluster region on the final iteration is almost as large as the XMM field of view and its background is even larger, on top of that, the extended region of the pointed cluster has been scaled and takes out a significant part of the source. The reported temperature for this cluster using XCS3P-v2 is 4.47 keV. In the other hand, (b) shows a source for the final iteration as expected for a low redshift cluster like this ($z = 0.06$), its background is removing the nearby extended region accordingly (see Section 4.3.1 for more details about the background corrections), the temperature reported using XCS3P-v3 is 0.93 keV. This value is close to the one reported in XCS-DR1 (1.08 keV) for the same cluster. In conclusion, the temperatures obtained by XCS3P-v2 and XCS3P-v3 are in general really close in terms of precision and value; nonetheless, there are particular cases where XCS3P-v3 have shown more realistic results than its previous version.

4.6 Conclusion and Future Work

4.6.1 Conclusions

The new version of the post processing pipeline (XCS3P-v3) has been run, so far, on $\simeq$ 1 600 clusters. The changes implemented in this version are: an improved method to mask the emission from extended X-ray sources near to the source of interest; the introduction of a convergence criteria to filter out clusters for which the iteration to R_{500} is unstable; and the correction of an error in the calculation of $L_{\rm X}$ error bounds. Tests were carried out to ensure that the underlying $L_{\rm X}$ error bound technique (designed by Ed Lloyd-Davies for XCS3P-v1) was rigorous - through a comparison with the more conventional

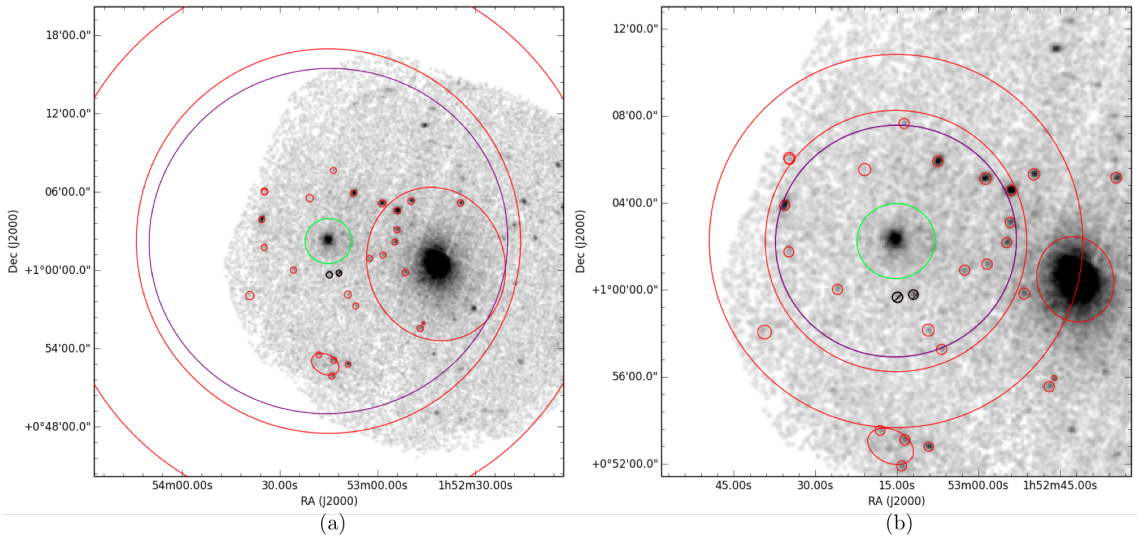

Figure 4.18: Cluster XMMXCS J015315.1+010214.9: (a) The calculation done using XCS3P-v2, (b) spectral analysis using XCS3P-v3. Green ellipse represents the source region during the first iteration, while the purple region represents the source during the last iteration. Red regions are the background during the last iteration. The difference in temperature measured using XCS3P-v2 and XCS3P-v3 is 3.54 keV.

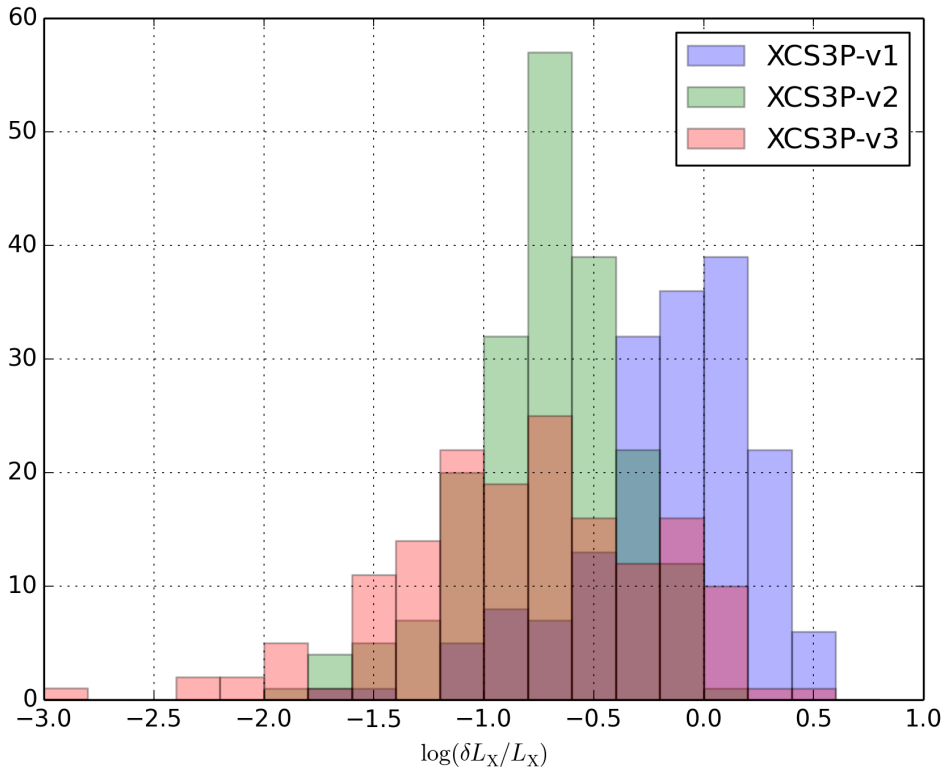

Figure 4.19: Comparison of the precision in X-ray temperature, obtained from each XCS3P methodology.

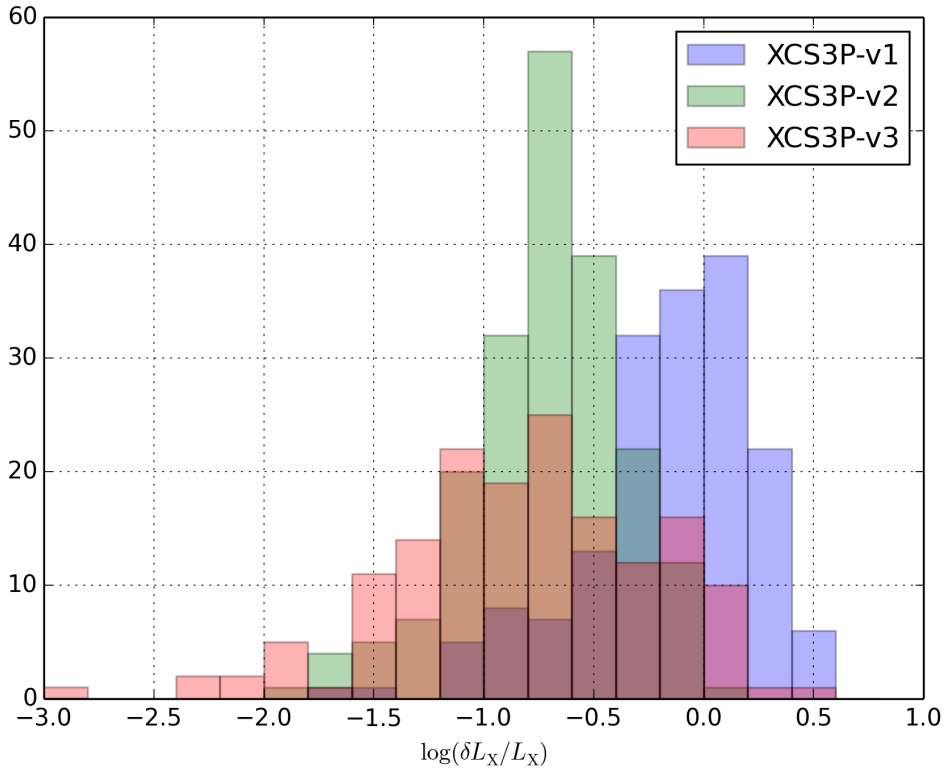

Figure 4.20: Comparison of the precision in bolometric luminosity, obtained from each XCS3P methodology.

`cflux` approach.

The XCS3P-v3 has been compared to XCS3P-v1 and XCS3P-v2 via an application to the cluster sample used in Hilton et al., 2012, specifically to an examination of the L_X - T_X scaling relation. Similar to the results in Rooney, 2015 for XCS3P-v2, it was shown that the outputs from XCS3P-v3 produce significantly different L_X -T_X evolution results to XCS3P-v1. The differences between XCS3P-v2 and XCS3P-v3 were found to be insignificant, except for a small number of specific clusters for which XCS3P-v3 performs better (e.g. when there is a nearby extended source).

The L_X and T_X parameters derived using XCS3P-v3 form the basis of the optical to X-ray scaling relations presented in Chapter 5.

4.6.2 Future work

Future work planned by the XCS team includes a more in depth analysis of the L_X errors. The new approach is now mathematically correct, but there remains a concern that the XSPEC derived values do not properly propagate the uncertainty in the T_X . Another investigation that is needed is to determine why some high signal to noise clusters are failing to produce a T_X value. In some cases this is because the iteration to R_{500} does not converge. In others, XSPEC is not able to deliver a fit to the required mode. Examples of each failure mode need to be examined in detail. It is possible that XAPA failures are to blame (see example in Figure 5.25). A further aspiration of the XCS team is to switch to the `cflux` methodology in XCS3P-v4.

The L_X - T_X scaling relation work presented in this chapter has demonstrated the need for a follow-up paper to H12, to address the erroneous measurement of negative evolution therein. The work presented here uses an input sample constrained in size to that used by Hilton et al., 2012 (H12). I am working with XCS collaborators in Porto (Viana et al.) who are writing up a new XCS3P-v3 based L_X - T_X scaling relation paper that uses a larger cluster sample compared to H12.

Chapter 5

Optical to X-ray Scaling Relations

5.1 Overview

Motivation In this chapter we present the key results from the thesis, i.e. the slope, normalization, and scatter in the scaling relation between RM richness and XMM determined X-ray temperatures and luminosities; the evolution of those quantities; and the distribution of RM centroid offsets.

Governing Assumptions

1. There are underlying power law scaling relations between the X-ray and optical properties of clusters of galaxies.

2. There is intrinsic scatter in those relations which reflects the diversity of environments and evolution history of clusters (even those at the same redshift and with the same dark matter halo mass).

3. That it is important to remove any sources of systematic bias in the samples under test, as these bias's could mask the underlying scaling relations and artificially boost the measured scatter.

Methodology The samples of RM-XCS clusters that were generated as described in Chapter 3 and processed (to yield $T_{\rm X}$ and $L_{\rm X}$ values) as described in Chapter 4 need to be filtered to ensure only genuine one-to-one matches between RM and XCS are included in the scaling relation. The filtering involved setting limits to the allowed level of error on the λ and $T_{\rm X}$ parameters (these limits were defined using preliminary scaling relation tests). A second filter involved carrying out an eye-ball examination of the both the optical (SDSS or DES) and X-ray images each cluster. An investigation was made into the properties of

RM clusters that were common between SDSS and DES (regardless of whether they had an XCS counterpart). This showed that it was valid to combine the XCS-DESY1-RM and XCS-SDSS-RM samples when measuring scaling relations. An offset analysis of the final, joint, sample was then carried out.

Using an MCMC approach, scaling relations fits to the $T_{\rm X}$ -λ and $L_{\rm X}$ -λ relations were performed. Outliers were examined individually to understand if these reflected the underlying scatter or if they were caused by systematic effects. Comparisons of the scaling relation fits were made to previous measurements.

Results The work presented here represents the most comprehensive examination of the $T_{\rm X} - \lambda$ and $L_{\rm X} - \lambda$ relations for optical clusters to date. The analysis of the RM centroid offset distribution is also the best in the world to date. Additional results include the demonstration that a) it is possible to combine RM samples generated from different photometric datasets, b) the importance of richness error information when defining samples to test, c) the scatter in the measured scaling relations is due to the underlying astrophysics, rather than to issues with the data inputs.

Conclusions and Future work The work presented demonstrates that there is a strong correlation between the X-ray and optical properties of RM selected clusters. The X-ray properties can be traced to the underlying mass of the cluster using analytical and numerical methods. My work confirms that it is possible to connect the optical properties to the underlying mass. In turn this then supports the premise that catalogues of optically selected clusters to be used to measure cosmological parameters. As expected, there is more scatter in the $L_{\rm X}$ -λ relation.

In future, the XCS team plan to add more RM clusters to the $L_{\rm X}$ -λ analysis, by included those that have significant XAPA detections, but not sufficient counts for a $T_{\rm X}$ measurement. This extension will double the number of clusters in the test, and compensate somewhat for the intrinsic scatter. It will also demonstrate the value (or otherwise) of adding e-ROSITA[1] data to the DES-cluster cosmology analysis. The "$L_{\rm X}$ -only" clusters will also be used to improve understanding in the RM centroid offset distribution (as it is not necessary to have a $T_{\rm X}$ value to measure a centroid offset). Other planned work includes a synthesis of the XCS-RM work with the Chandra-RM work being carried out at UCSC.

[1] e-ROSITA is an X-ray survey telescope due for launch in 2018. It will generate tens of thousands of cluster detections (and hence $L_{\rm X}$ values), but comparitively (to XCS) few $T_{\rm X}$ measurements.

5.2 Refining sample for the scaling relations analysis

In Table 3.2 we defined two samples of RM clusters that were associated with XCS extended sources: 1319 from SDSS-RM and 293 from DES-Y1. We do not use all of these systems in the scaling relations analysis. Additional filters are applied first. These include the coefficient of variability filter described in Section 4.3.2. The other filters are described below: cuts made on $T_{\rm X}$ and λ accuracy (Section 5.2.1), and cuts made after an eye-ball inspection of the clusters (Section 5.2.2). After applying these filters, all RM clusters in the sample have a single (unique) match to an XCS extended source.

5.2.1 Filtering on relative error

In this thesis we aim to measure the intrinsic scatter in the optical to X-ray scaling relations. To this end, we have chosen to exclude clusters from the analysis if they had large relative errors in λ or in the X-ray parameters ($T_{\rm X}$ and $L_{\rm X}$). Relative error on a given parameter x is defined as

$$\delta x = \frac{\Delta x}{x}, \tag{5.1}$$

where $\Delta x = x_u - x_l$ are the upper and lower errors of the variable x, e.g. a relative error of $\delta x = 0.3$ indicates associated 1σ errors of $\pm 15\%$ on average.

The acceptable limits on the relative errors were determined by carrying out a preliminary $T_{\rm X} - \lambda$ BCES (Akritas and Bershady, 1996) scaling relation fit using subsets of the XCS-RM clusters that passed the coefficient of variability test. Following the prediction from self-similarity (see Section 1.3) we fit with BCES a power-low relation in the form:

$$\log T_{\rm x} = A \log\left(\frac{\lambda}{\lambda_0}\right) + B, \tag{5.2}$$

where A and B are the free parameters of the model, λ_0 is a pivot value usually taken as the median value of the richness. It also follows the orthogonal method described in Section 4.4.2.

This test was done under the assumption that significant sample-dependent variation in the fitting would indicate an underlying problem in the X-ray or optical analysis. The subsets were defined by the $T_{\rm X}$ and λ relative errors: $30\%, 25\%, 20\%, 15\%$. In each case, the other parameter was not constrained, e.g. for clusters with λ relative errors of $< 15\%$, no cut was made on the $T_{\rm X}$ relative error.

Figure 5.1 shows the $T_{\rm X} - \lambda$ scaling relation for each of the eight sub-samples, each black dot represents an individual cluster. The top figure shows how the BCES fit changes with $\delta T_{\rm X}$. The bottom figure shows how the fit changes with $\delta\ \lambda$. It is clear that while there

is no need to restrict the error on T_X , there is a need to restrict the error on λ : the best fit slope steepens with decreasing $\delta\ \lambda$. This suggests that there are systematic errors in the RM catalogue that are not accounted for in their error budget.

Our collaborators on the RM team reviewed Figure 5.1 and suggested that we make the following cuts: $z \in [0.1 - 0.3]$, $\lambda > 20$. They also pointed out that in Rykoff and Rozo, 2014, they had set a limit on $\delta\lambda$ of $< 15\%$. The result of making their suggested cuts is shown in Figure 5.2. The slope of the fits is now indistinguishable between $\delta\lambda < 15\%$ and $< 20\%$. A similar analysis was performed across a wider redshift range $z \in [0.08 - 0.56]$, again restricted to $\lambda > 20$. No discernible change in slope with either $\delta\ T_X$ or $\delta\lambda$ was measured in this wider redshift sample. As a result of these investigations, we applied different filters according to redshift range and value, see Table 5.1.

We note that, despite the suggestion from our RM collaborators, some $\lambda < 20$ clusters were included in our analysis of optical to X-ray scaling relations. But in this case only those in the optimal redshift range $z \in [0.1 - 0.3]$ and with associated errors $< 15\%$ in both T_X and λ were considered. An example of one of these low richness X-ray clusters is shown in Figure 5.3.

A similar analysis was made on the 293 clusters in RM-DESY1 sample, see Figure 5.4. Unlike with the RM-SDSS, the slope does not change with the limit set on $\delta\ \lambda$, this is valid only for clusters in the RM-DESY1 optimal redshift range $z \in [0.2 - 0.8]$ and for clusters with $\lambda > 20$. The filters used for the RM-DESY1 sample are listed in able 5.2.

Redshift range	Associated error range λ	Associated error range T_X
$z \in [0.08 - 0.1]$	$\lambda_{\rm err} \leq 15\%$	$T_{X,\rm err} < 30\%$
$z \in [0.1 - 0.3]$	$\lambda_{\rm err} \leq 20\%$	$T_{X,\rm err} < 30\%$
$z \in [0.3 - 0.4]$	$\lambda_{\rm err} \leq 20\%$	$T_{X,\rm err} < 30\%$
$z \in [0.4 - 0.5]$	$\lambda_{\rm err} \leq 15\%$	$T_{X,\rm err} < 30\%$
$z \in [0.5 - 0.56]$	$\lambda_{\rm err} \leq 20\%$	$T_{X,\rm err} < 30\%$
$z \in [0.1 - 0.3] \cap \lambda < 20$	$\lambda_{\rm err} \leq 15\%$	$T_{X,\rm err} < 15\%$

Table 5.1: Selection criteria for the XCS-RM SDSS sample, based on redshift range and associated errors in λ and T_X.

Redshift range	Associated error range λ	Associated error range T_X
$z \in [0.2 - 0.4]$	$\lambda_{\rm err} \leq 30\%$	$T_{X,\rm err} < 30\%$
$z \in [0.4 - 0.6]$	$\lambda_{\rm err} \leq 30\%$	$T_{X,\rm err} < 30\%$
$z \in [0.6 - 0.8]$	$\lambda_{\rm err} \leq 30\%$	$T_{X,\rm err} < 30\%$
$z \in [0.2 - 0.8] \cap \lambda < 20$	$\lambda_{\rm err} \leq 15\%$	$T_{X,\rm err} < 20\%$

Table 5.2: Selection criteria for scaling relation for the DES Y1 sample, based on redshift range and associated errors in richness and temperature.

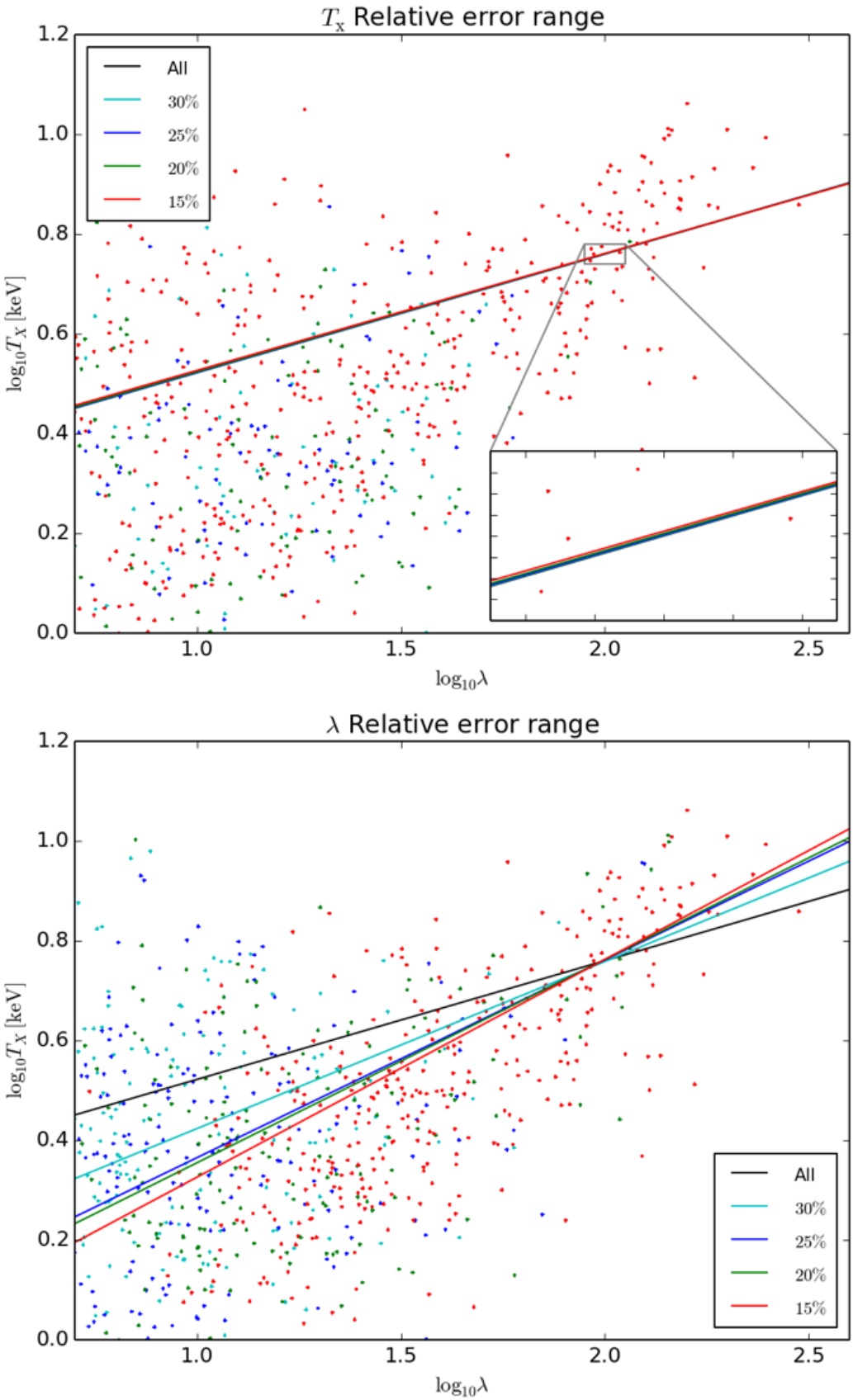

Figure 5.1: $T_X - \lambda$ scaling relation for several sub-samples of δT_X (top) and $\delta\lambda$ (bottom). Each point represent an individual cluster, errors are not plotted to avoid cluttering the plot.

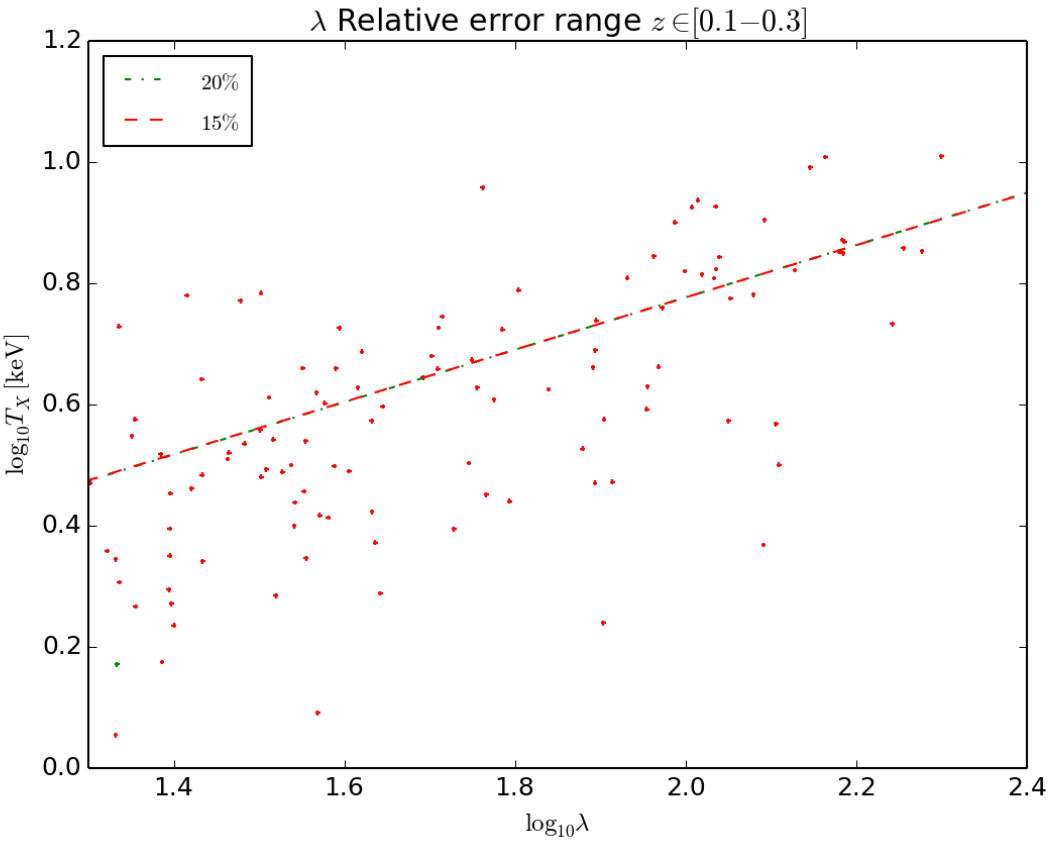

Figure 5.2: $T_{\rm X} - \lambda$ scaling relation for clusters within $z \in [0.1 - 0.3]$ and $\lambda > 20$ from the XCS-RM SDSS sample, the change in relative errors on optical richness do not have an effect on the fitting.

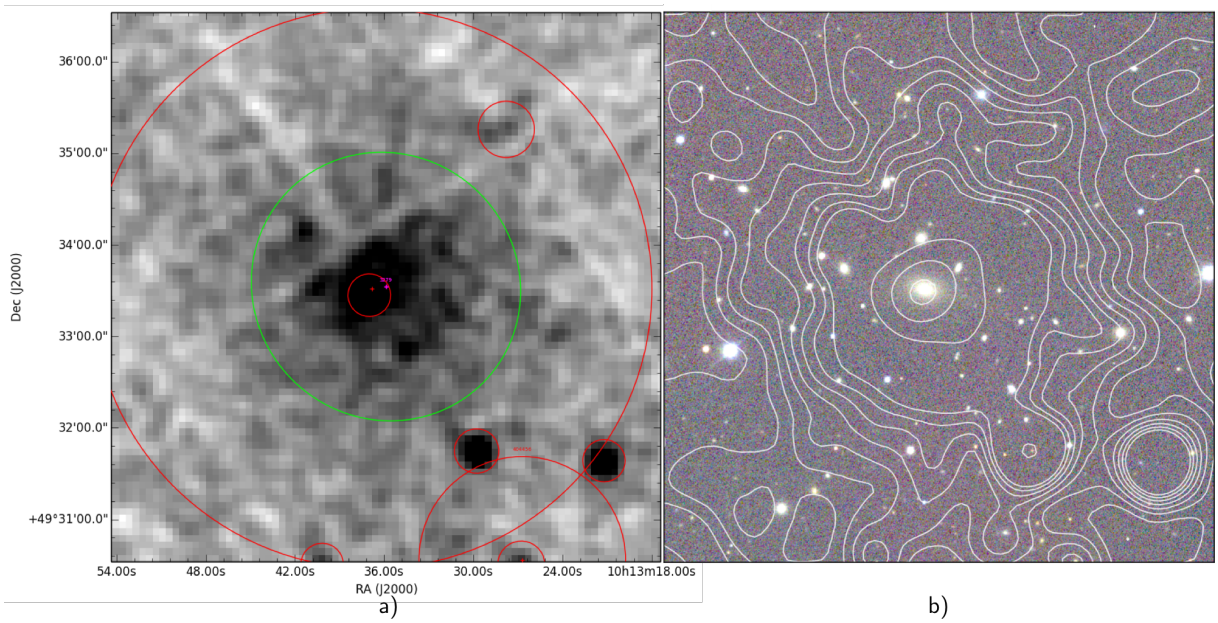

Figure 5.3: XMM (left) and SDSS (right) observation of the cluster XMMXCS J101335.8+493332.7 associated to a redMaPPer cluster with low richness ($\lambda = 17.64$). This is an example of a nice cluster below the $\lambda = 20$ limit. Green circle indicates the XCS source, big red circles are low richness RM clusters and small red circles are point sources. The SDSS image has X-ray contours information from XMM.

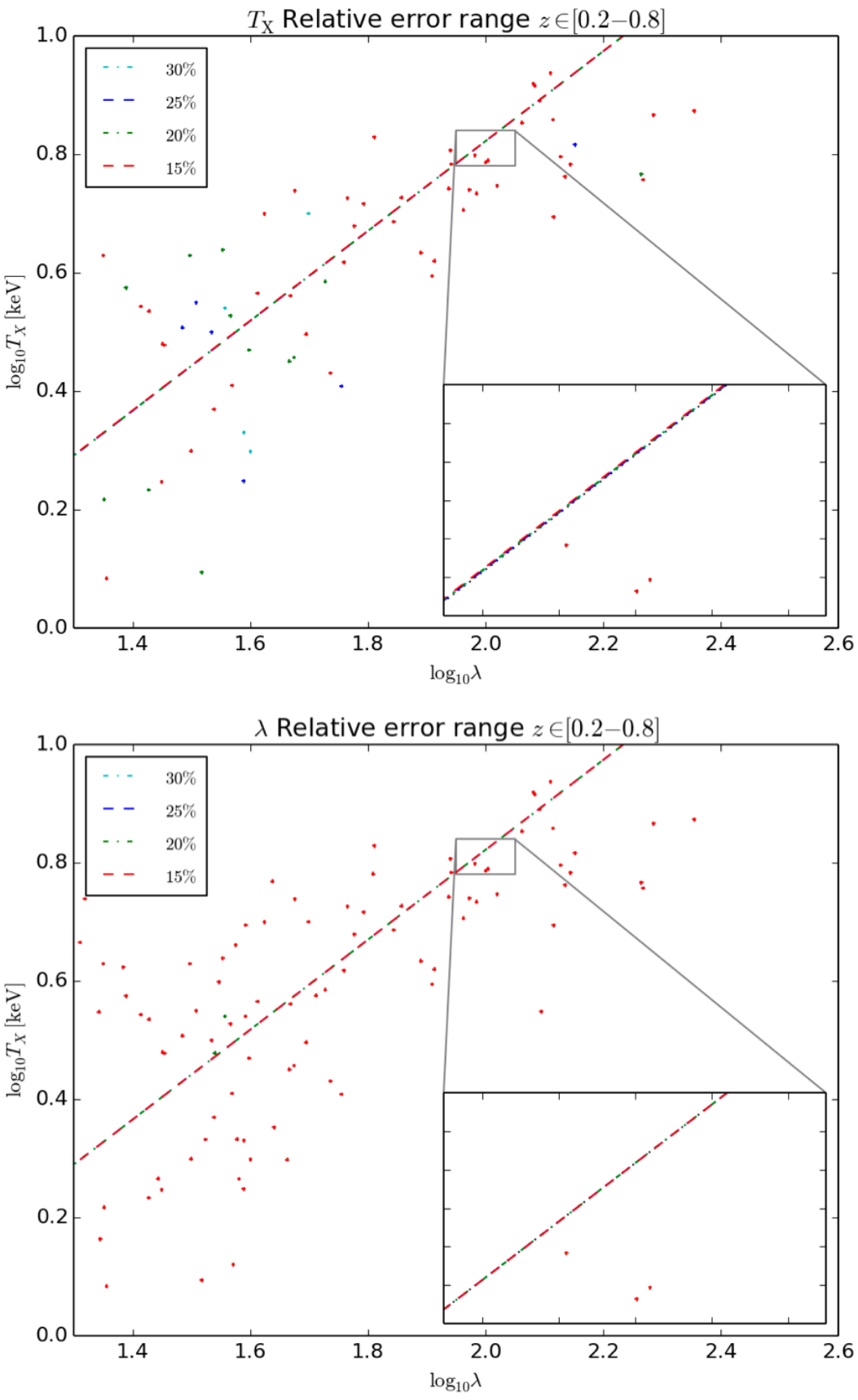

Figure 5.4: $T_X - \lambda$ scaling relation, considering clusters with $z \in [0.2 - 0.8]$ and $\lambda > 20$ from the XCS-RM DES Y1 sample, sub-samples are defined by changing δT_X (top) and $\delta\lambda$ (bottom). Varying relative errors in both observables do not have an effect on the fitting.

5.2.2 Filtering using optical images

Even after filtering on δT_X and $\delta\lambda$, it is still possible for a given RM cluster to be associated to several XCS extended sources and vice versa. Therefore, before performing the optical to X-ray scaling relation analysis, it was important to determine the best one-to-one match between RM and XCS objects. For this, I carried out an eyeball inspection of the optical images of the clusters. The SDSS images (with XMM contours overlaid) were generated by a collaborator in Edinburgh, Maria Manolopoulou. The DESY1 images (with XMM contours overlaid) were generated by a collaborator in Sussex, Carlos Vergara.

The eyeballing was carried out using a webpage that shows for each RM to XCS association: the XCS image (a $6' \times 6'$ postage stamp centred on the XAPA position); the corresponding optical (SDSS or DES) postage stamp; two classification options. The options indicated either a reliable match or an erroneous association. An example of a reliable match, i.e. where the X-ray contours define the boundary of an obvious galaxy over density, is shown in Figure 5.5. There were 261 and 77 such cases in total in the XCS-RM (SDSS) and XCS-RM (DES Y1) samples respectively. The remaining 10 (SDSS) and 4 (DESY1) cases were deemed to be erroneous associations. It is important to remove such cases before carrying out X-ray to optical comparisons: they will lead to non-physical scatter in the scaling relations and misleading inputs to the centroid offset analysis (Section 5.3.2). Two examples are shown in Figures 5.6 and 5.7, see below. For completeness, all 14 erroneous associations are presented in Appendix C.

In the first example (Figures 5.6), it is clear that the X-ray source originates from nearby stars, not from an intracluster medium. The RM cluster has a low richness = 17.06, the association was flagged only as a *likely* (flag= 2) match during the first eyeball check (Section 3.3.1), and the XAPA source was detected both with relatively few counts (softCts = 137) and with only a marginal extent probability (it was flagged as "PSF sized", see Section 2.1.4). Finally, the separation between the respective centroids was quite large (0.40 h^{-1}Mpc). Therefore, it is not a surprise that this association was erroneous.
In contrast, the second example (Figures 5.7) was flagged as a *likely* (flag= 1) match during the first eyeball check, the RM cluster has an acceptable richness (= 24), and the XAPA source was detected with unusually high counts (softCts = 11,822) and with a significant extent probability. Therefore, it might be a surprise that this association was erroneous. However, the SDSS image demonstrates that the X-ray source is associated with a nearby galaxy ($z = 0.02$ Bai et al., 2015) and not with an intracluster medium originating from

the RM cluster. It is possible that the RM cluster has an associated extended X-ray source, but we cannot detect it with XMM because of the projected proximity of the galaxy.

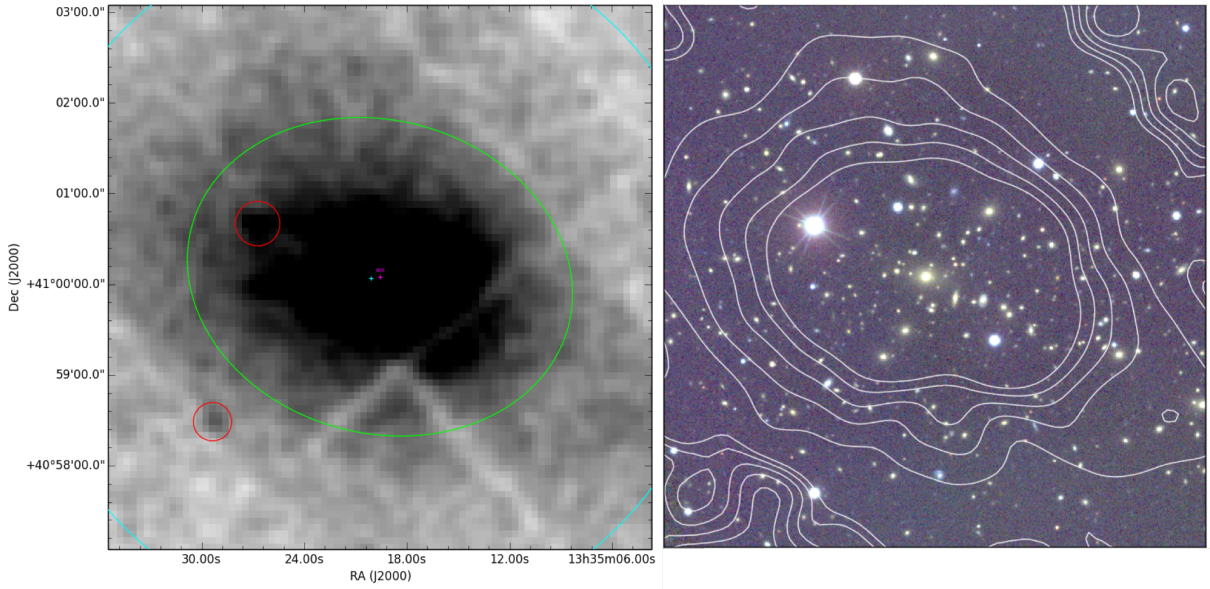

Figure 5.5: Cluster XMMXCS J133519.5+410004.9 ($z = 0.23$), on the left XMM-Newton observation, green ellipses are XCS extended sources, cyan circle represent the RM cluster, red circles are point sources defined by XAPA. On the right, optical image from SDSS with added X-ray contours from XMM-Newton (separation between the two centroids is 0.02 h^{-1}Mpc).

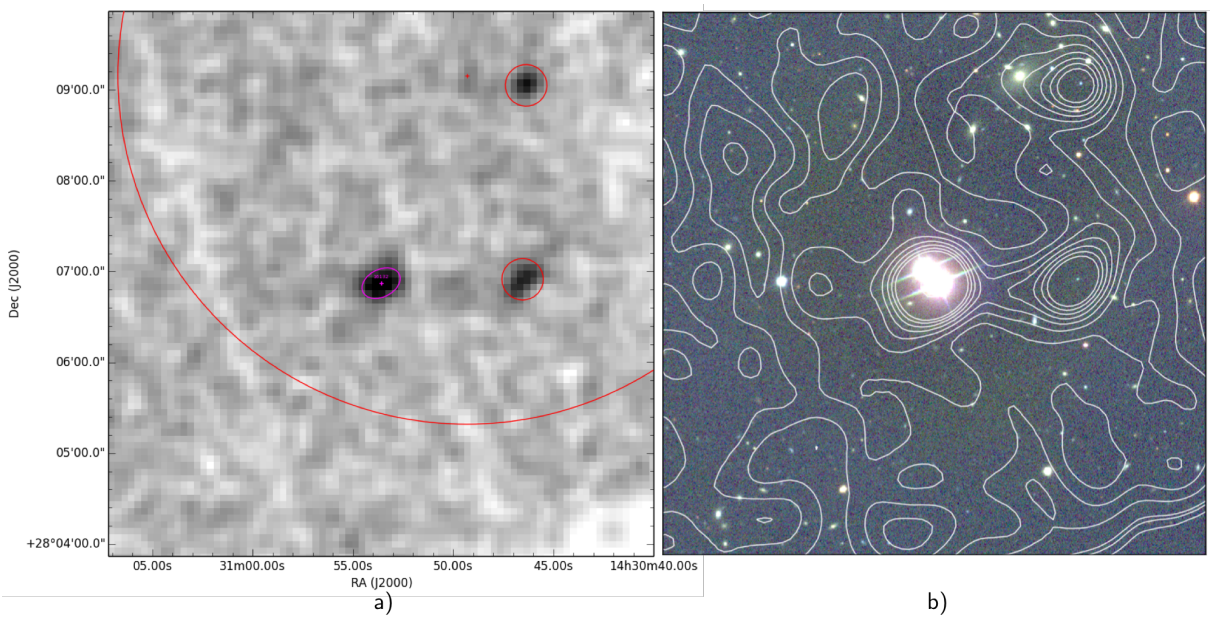

Figure 5.6: Cluster candidate XMMXCS J143053.5+280652.2, on the left XMM-Newton observation, purple ellipse is the PSF XCS source, large red circle represent the low richness RM cluster ($\lambda < 20$), red circles are point sources defined by XAPA. On the right, optical image from SDSS with added X-ray contours from XMM-Newton centred on the XCS position.

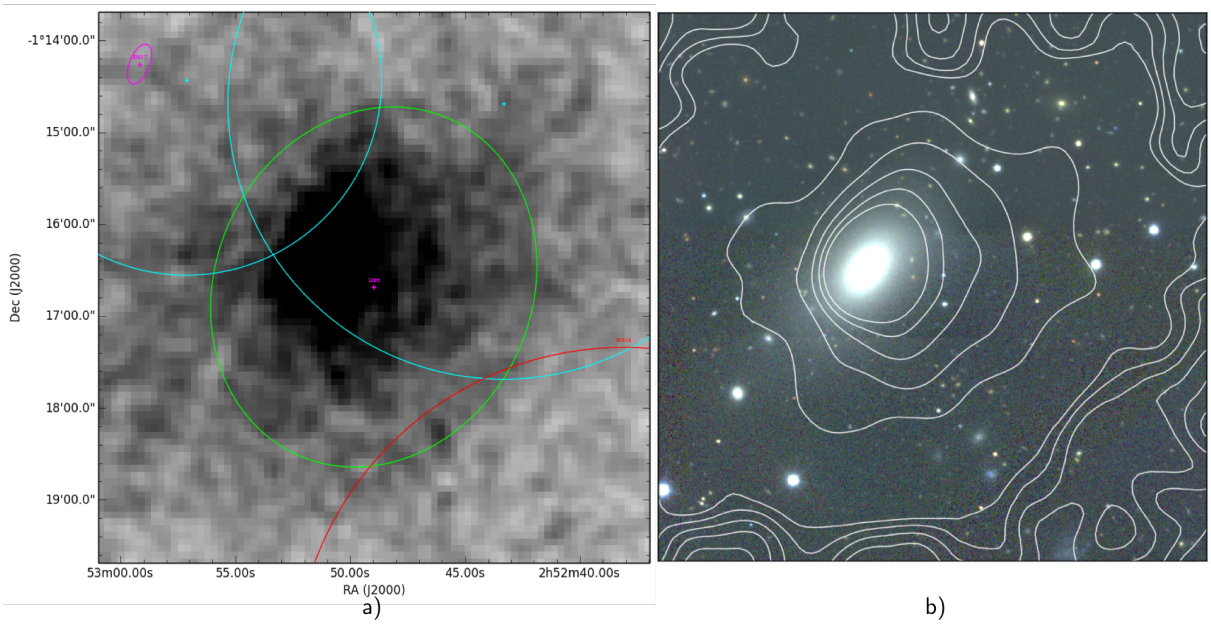

Figure 5.7: Cluster candidate XMMXCS J025248.9-011640.9, on the left XMM-Newton observation, green ellipses are XCS extended sources, cyan circle represent ($\lambda > 20$) RM clusters, large red circle is a nearby low richness ($\lambda < 20$) RM cluster, red circles are point sources defined by XAPA. On the right, optical image from SDSS with added X-ray contours from XMM-Newton.

5.3 Sample Characterization

After application of the filters described above (Section 5.2), we are left with two samples of RM clusters with unique matches to XCS extended sources (likewise, each XCS source is only matched to a single RM cluster): 261 from SDSS-RM and 77 from DES-Y1 (with 11 in common). It is these two samples that are used as inputs to the cluster scaling relations analysis presented in Section 5.4.

Table 5.3 shows the characteristics of the **261** clusters selected from the SDSS-DR8 catalog. It spans a redshift range of $0.08 \leq z \leq 0.58$ and a temperature range of $0.65 \leq T_X \leq 11.52$ keV.

Redshift range	N	$\langle z \rangle$	$\langle T_{\rm X} \rangle$ [keV]	$\langle L_{\rm X} \rangle [10^{44}$ ergs/s]	$\langle \lambda \rangle$
$[0.08 - 0.1]$	20	0.09	3.56	1.96	44.90
$[0.1 - 0.3]$	134	0.19	3.81	5.74	54.78
$[0.3 - 0.5]$	94	0.37	4.26	7.21	69.78
$[0.5 - 0.58]$	13	0.54	6.81	19.35	117.53

Table 5.3: Characterization of XCS-RM (SDSS-DR8) sample: Average redshift, average temperature and average richness are given for each redshift bin. The sample has a total of 261 clusters.

Table 5.4 shows the characteristics of the **77** clusters selected from the DES-Y1 catalog. It spans a redshift range of $0.2 \leq z \leq 0.74$ and a temperature range of $1.24 \leq T_X \leq 11.51$ keV.

Redshift range	N	$\langle z \rangle$	$\langle T_{\rm X} \rangle$ [keV]	$\langle L_{\rm X} \rangle [10^{44}$ ergs/s]	$\langle \lambda \rangle$
$[0.2 - 0.3]$	18	0.24	4.84	9.62	74.94
$[0.3 - 0.4]$	17	0.34	4.18	8.56	63.42
$[0.4 - 0.5]$	23	0.43	4.20	6.36	68.34
$[0.5 - 0.6]$	6	0.57	5.42	37.22	76.79
$[0.6 - 0.74]$	13	0.67	4.75	6.42	77.97

Table 5.4: Characterization of XCS-RM (DES-Y1) sample: Average redshift, average temperature and average richness are given for each redshift bin. The sample has a total of 77 clusters.

Between XCS-RM (SDSS-DR8) and XCS-RM (DES-Y1) there are 11 common clusters (i.e. where the RM defined centroids are within 1.0 arcsec). To form a joint sample, I

considered each of the 11 pairs of clusters and selected the one the smaller $\delta T_{\rm X}$ and $\delta\lambda$ values for the joint sample. In all cases, the RM defined redshifts of the clusters in the pair were consistent within 1 σ. (The validity of using a joint sample has been explored in Section 5.3.1). Table 5.5) shows the characterization of the XCS-RM (SDSS+DES-Y1) joint sample. It spans a redshift range of $0.08 \leq z \leq 0.74$ and a temperature range of $0.65 \leq T_X \leq 11.52$ keV. This sample has **327** clusters.

Redshift range	N	$\langle z \rangle$	$\langle T_{\rm X} \rangle$ [keV]	$\langle L_{\rm X} \rangle [10^{44}$ ergs/s]	$\langle \lambda \rangle$
$[0.08 - 0.2]$	89	0.13	3.33	2.86	43.28
$[0.2 - 0.3]$	78	0.24	4.44	8.71	68.74
$[0.3 - 0.4]$	77	0.34	4.36	7.41	67.06
$[0.4 - 0.5]$	51	0.43	4.01	7.06	71.45
$[0.5 - 0.6]$	19	0.55	6.37	24.99	104.66
$[0.6 - 0.74]$	13	0.67	4.75	6.42	77.97

Table 5.5: Characterization of joint sample XCS-RM (SDSS+DES-Y1): Average redshift, average temperature and average richness are given for each redshift bin. The sample has a total of 327 clusters.

The redshift, temperature and luminosity distributions for the two separate samples and the joint sample are shown in Figures 5.8, 5.9, 5.10 respectively.

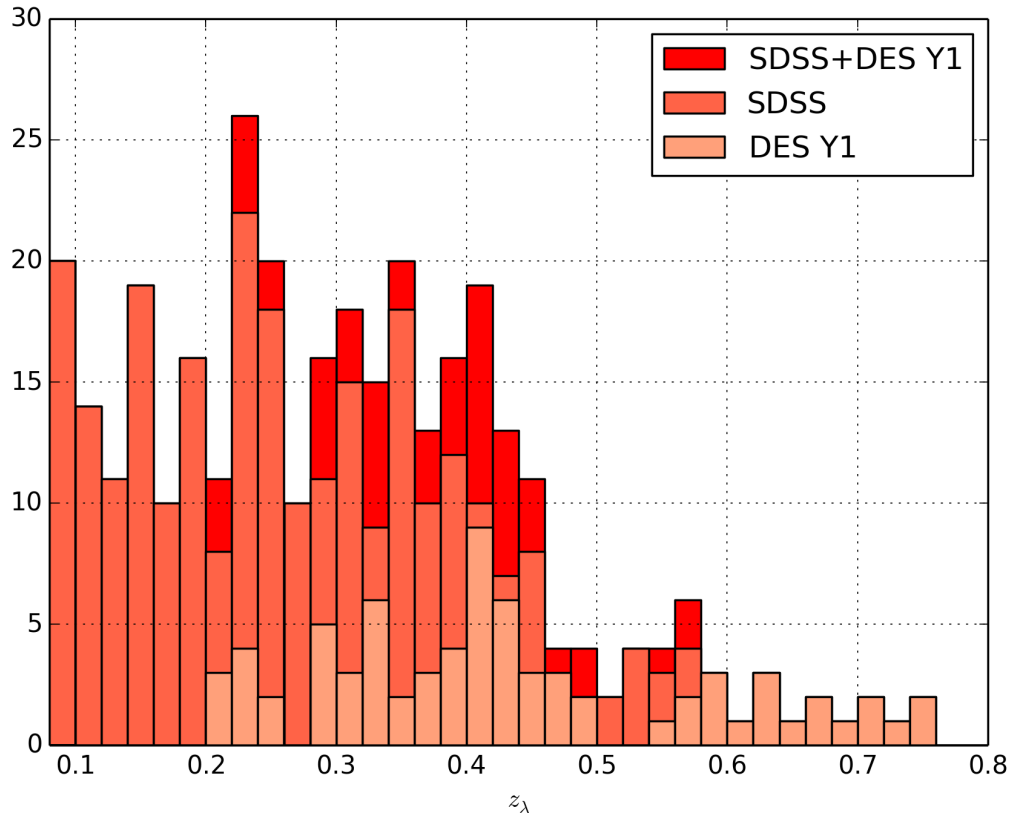

Figure 5.8: Redshift distribution of joined sample XCS-RM (SDSS+DES-Y1).

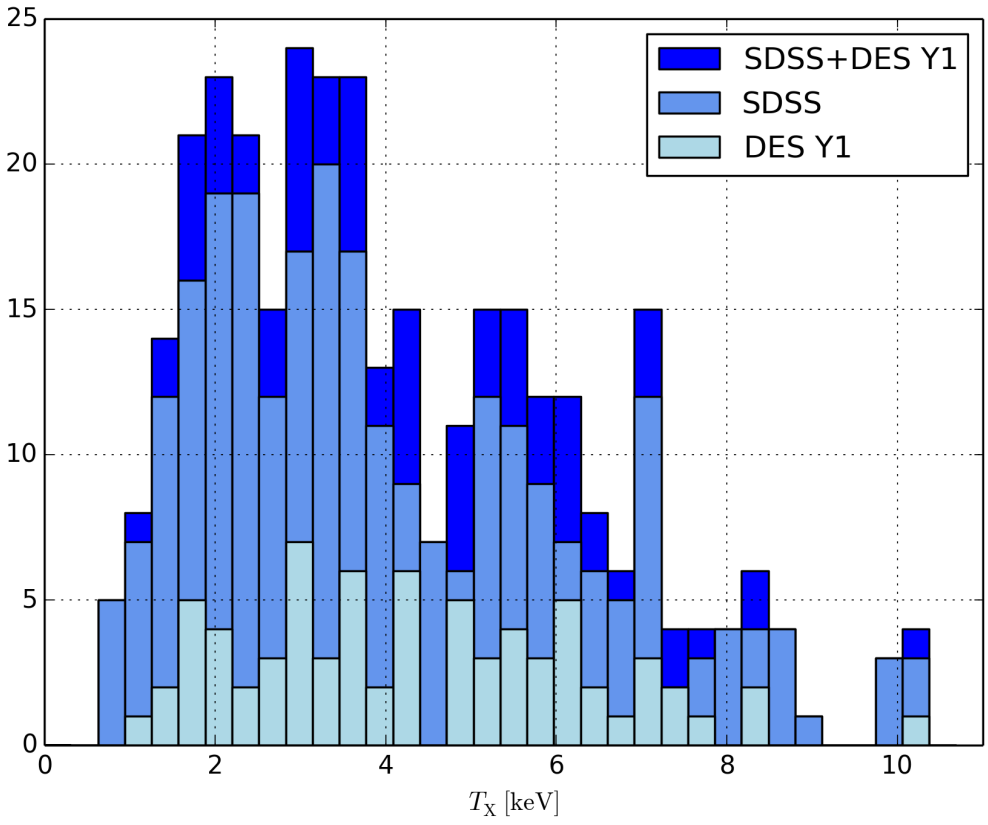

Figure 5.9: $T_{\rm X}$ distribution of joined sample XCS-RM (SDSS+DES-Y1).

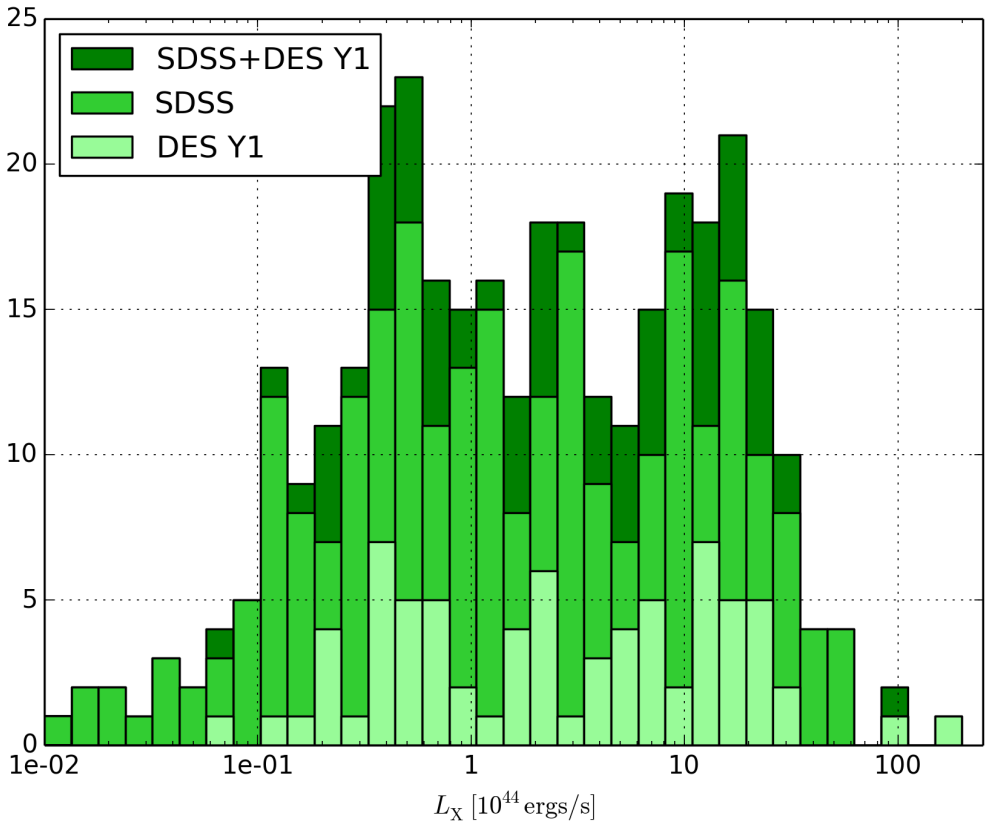

Figure 5.10: $L_{\rm X}$ distribution of joined sample XCS-RM (SDSS+DES-Y1).

5.3.1 Comparison of the RM-SDSS and RM-DESY1 samples

As mentioned above, I have used a joint sample of RM-SDSS and RM-DESY1 clusters in the scaling relations analysis. To verify that this approach is valid, it was important to confirm that the richness and redshift estimations are consistent between the two RM catalogues. Taking the full, i.e. ignoring overlap with the XMM archive, redMaPPer catalogs (SDSS and DES Y1) as a starting point, I found 2695 clusters in common, assuming a 1.0 arcsec matching radius. Of these, 398 have relative errors in λ of 15% or less ($\delta\lambda \leq 0.3$) in both richness calculations.

Figures 5.11 and 5.12 show the comparison of the λ and redshift values for the clusters in each of the 398 pairs. By eye it is clear that there is good consistency between the catalogues, despite them being based on photometry from two different telescopes. A MCMC analysis (From Hilton et al., 2012, see Section 4.4.2) demonstrated that the scatter in $\Delta$was $\sigma_\lambda = 0.066$ and $\sigma_z = 0.015$ in Δz. There are no outliers in the distributions. We conclude that it is possible to merge both catalogs without adding significant scatter to the optical to X-ray scaling relations, as long as $\delta\lambda < 0.3$.

5.3.2 Centroid Offset Analysis

Following the analysis done by Rykoff et al., 2016 (ER16), from the XCS-RM (SDSS+DES Y1) sample we characterize the offset distribution by defining a variable x as:

$$x = \frac{R}{R_\lambda}, \tag{5.3}$$

where R is the separation given in units of $[h^{-1}\text{Mpc}]$ and R_λ is the radius defined by RM given in the same units as R. Figure 5.13 contains the histogram of the offset distribution. It is similar to the results obtained from the redMaPPer DES SV catalog on ER16 (Figure 5.14).

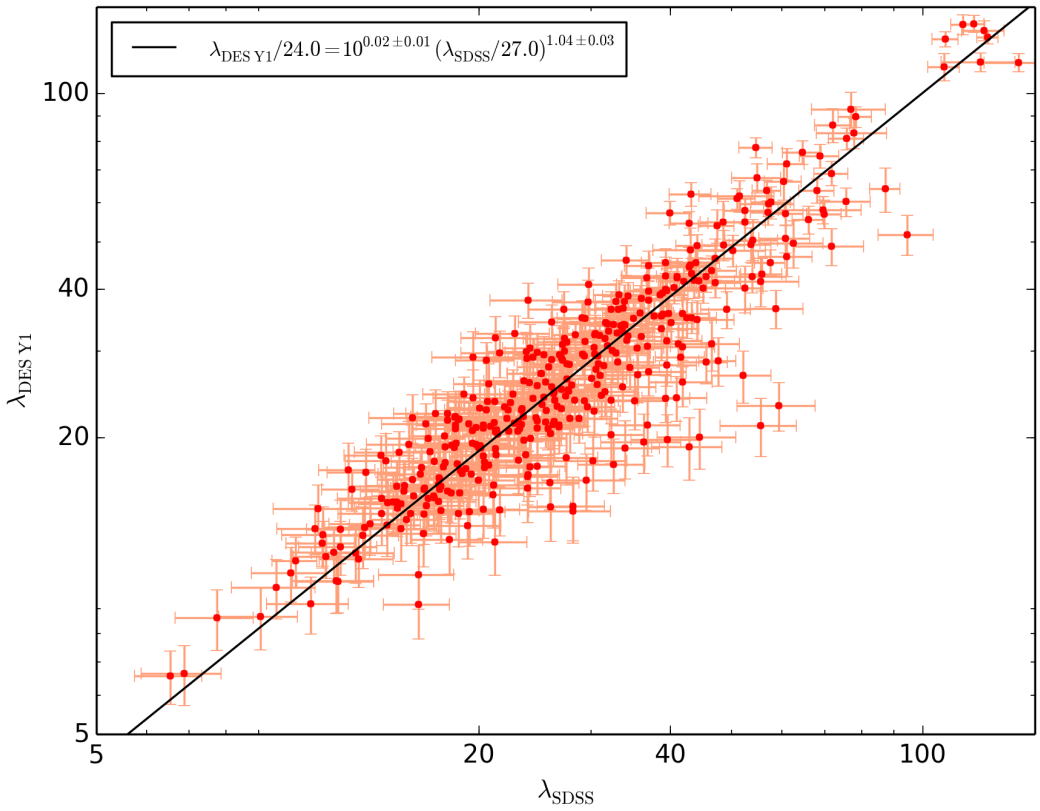

Figure 5.11: Comparison of richness (λ) calculation of common clusters between the redMaPPer SDSS DR8 and redMaPPer DES Y1 catalogs. These clusters are within 1arcsec and have $\delta\lambda \leq 0.3$.

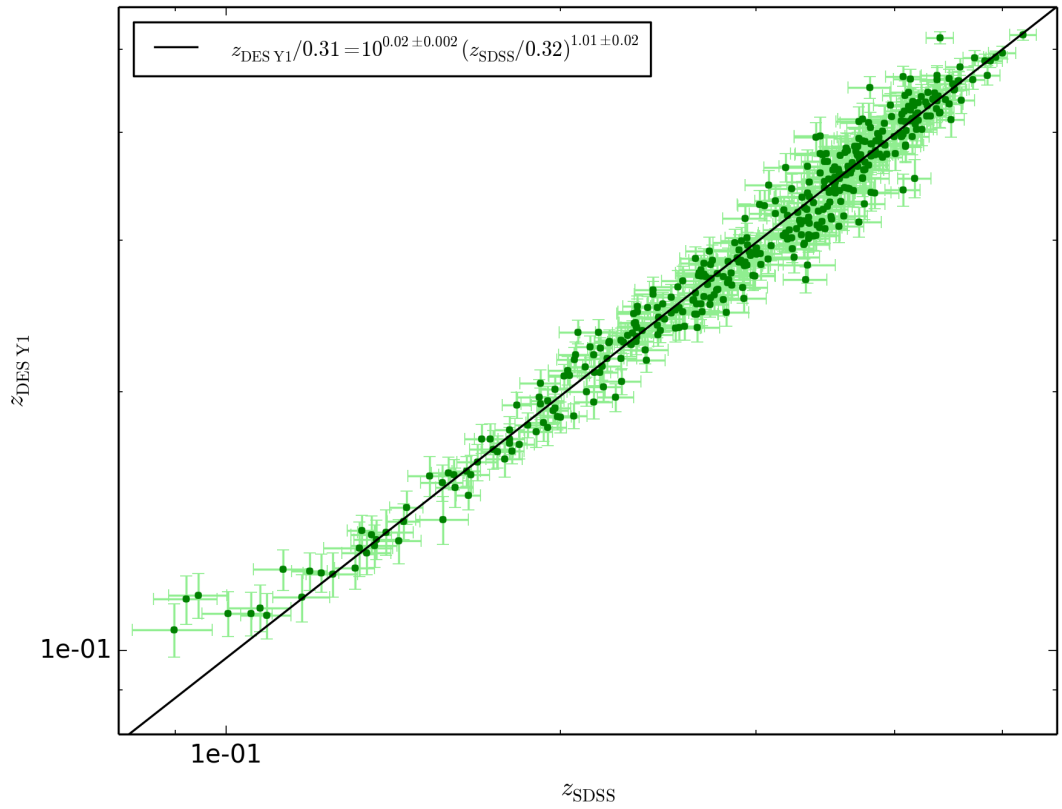

Figure 5.12: Comparison of redshift (z) calculation of common clusters between the redMaPPer SDSS DR8 and redMaPPer DES Y1 catalogs. These clusters are within 1arcsec and have $\delta\lambda \leq 0.3$.

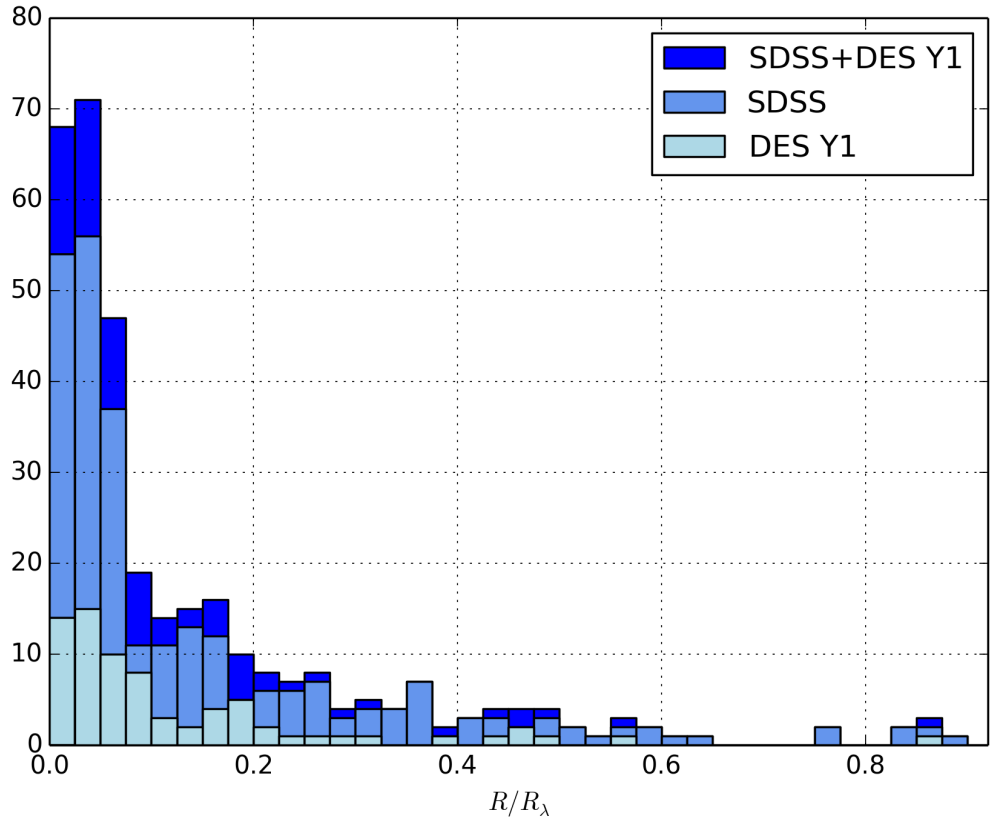

Figure 5.13: Separation distribution R/R_λ where R is the separation in units of h^{-1}Mpc and R_λ is the RM radius defined for each cluster with similar units as R. All the samples are plotted XCS-RM SDSS, XCS-RM DES Y1 and XCS-RM SDSS+DES Y1

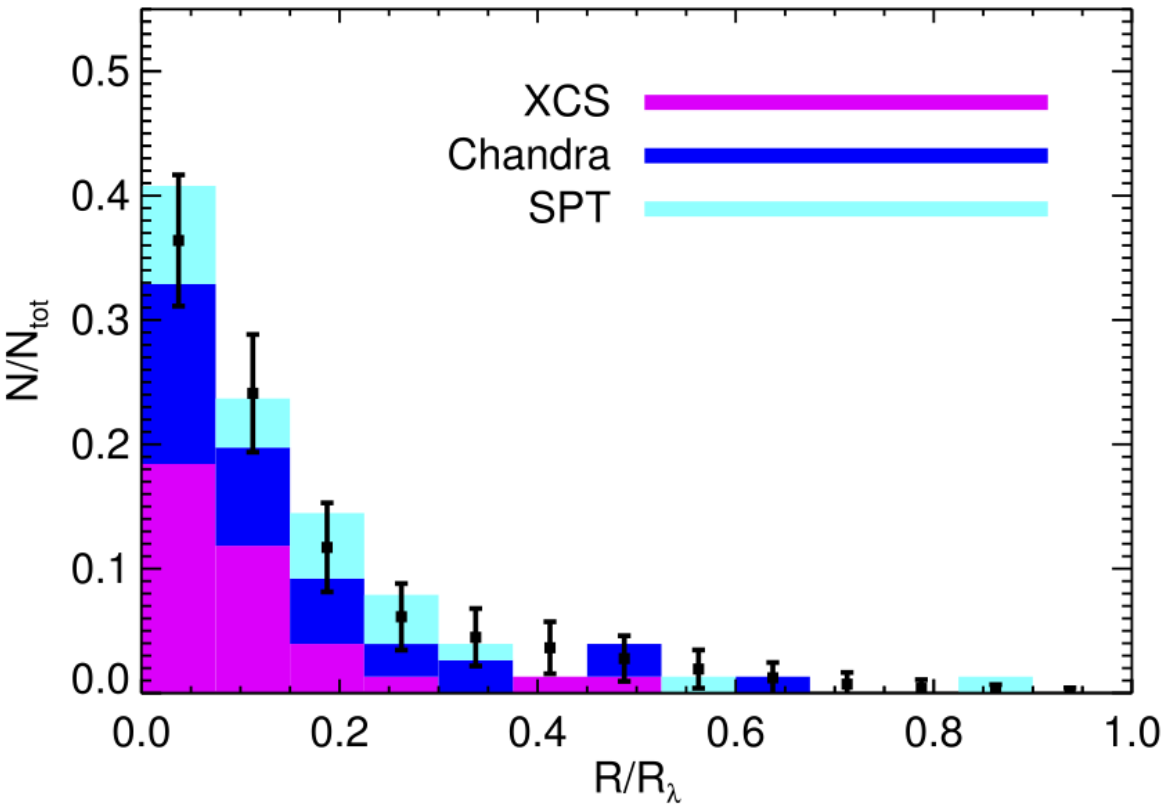

Figure 5.14: Figure and caption taken from Rykoff et al., 2016:Histogram of positional offsets for the combined cluster sample as a function of R/R_λ . XCS clusters are shown in magenta, Chandra clusters in blue, and SPT clusters in cyan. The best-fit offset model, binned according to the data, is shown with black points. For reference, the average value of $\langle R \rangle = 0.85\ h^{-1}$ Mpc, and the largest cluster offset is $0.75\ h^{-1}$ Mpc.

5.4 The XCS-RM $T_{\rm X}-\lambda$ Scaling Relation

5.4.1 Input Data

The data used to obtain the XCS-RM $T_{\rm X}-\lambda$ scaling relation is as described in Section 5.3. It consists of XCS clusters from the SDSS-RM sample (261 clusters), the RM-DESY1 sample (77 clusters) and the joint SDSS+DESY1-RM sample (327 clusters).

5.4.2 Fitting Method

The model used in this thesis to fit the $T_{\rm X}$-λ scaling relation is based on the model described by Rozo, Vikhlinin and More, 2012 and Rozo et al., 2012. Given two arbitrary cluster observables ψ and χ, it is assumed that the probability distribution $P(\psi|\chi)$ is a log-normal distribution. The mean of the log-normal distribution is modeled as a linear relation in log scale:

$$\langle \ln \psi|\chi\rangle = a_{\psi|\chi} + \alpha_{\psi|\chi} \ln(\chi/\chi_0), \tag{5.4}$$

where $a_{\psi|\chi}$ is the amplitude parameter and $\alpha_{\psi|\chi}$ is the slope. The parameter χ_0 is the pivot point of the correlation, it is selected to decorrelate the amplitude and slope parameters. The scatter in $\ln\psi$ at fixed χ is assumed to be constant, it is given by:

$$\mathrm{Var}(\ln\psi|\chi) \equiv \sigma^2_{\psi|\chi} \tag{5.5}$$

Adapted to the data in this thesis, the model for the $T_{\rm X}$-λ scaling relation is:

$$\ln T_{\rm X} = \beta + \alpha \ln\left(\frac{\lambda}{\lambda_0}\right). \tag{5.6}$$

Amplitude (α) and slope (β) are the free parameters of the model. These are constrained using Markov Chain Monte Carlo (MCMC) techniques.

5.4.3 Results

The $T_X - \lambda$ scaling relation for the XCS-RM (SDSS DR8) sample is given by the equation:

$$\ln T_{\rm X} = 1.17^{+0.02}_{-0.02} + 0.59^{+0.03}_{-0.03} \ln\left(\frac{\lambda}{\lambda_0}\right), \tag{5.7}$$

which can be rewritten as

$$T_{\rm X} = (3.23 \pm 0.07)(\lambda/\lambda_0)^{0.59\pm0.03}, \tag{5.8}$$

where $\lambda_0 = 40$ and it is the pivot value mentioned in Section 5.4.2. The scatter associated to the data is fit during MCMC, for the XCS-RM (SDSS DR8) sample is $\sigma = 0.33^{+0.02}_{-0.02}$.

The plot of $T_X - \lambda$ is in Figure 5.15, the blue line represents the fitting described by Equation 5.8), grey and light gray represent the 1σ and 2σ scatter respectively.

For the DES-Y1 RM sample, the $T_X - \lambda$ scaling relation is given by the equation:

$$\ln T_{\rm X} = 1.22^{+0.03}_{-0.03} + 0.58^{+0.04}_{-0.04} \ln\left(\frac{\lambda}{\lambda_0}\right), \tag{5.9}$$

which can be rewritten as

$$T_{\rm X} = (3.37 \pm 0.12)(\lambda/\lambda_0)^{0.58\pm0.04}, \tag{5.10}$$

similar to the SDSS fitting $\lambda_0 = 40$.

Similar to Figure 5.15, Figure 5.17 shows the XCS-RM (SDSS+DES-Y1) sample with the $T_X - \lambda$ scaling relation

$$\ln T_{\rm X} = 1.18^{+0.02}_{-0.02} + 0.59^{+0.02}_{-0.02} \ln\left(\frac{\lambda}{\lambda_0}\right), \tag{5.11}$$

also written as:

$$T_{\rm X} = (3.25 \pm 0.06)(\lambda/\lambda_0)^{0.59\pm0.02}. \tag{5.12}$$

The pivot value $\lambda_0 = 40$ as for the SDSS and DES Y1 samples. The intrinsic scatter is $\sigma = 0.32 \pm 0.01$.

Similar to Figure 5.15, Figure 5.19 shows the XCS-RM (SDSS+DES-Y1) sample with the $T_X - \lambda$ scaling relation. Gray regions represent the 1σ, 2σ and 3σ.

Table 5.6 shows the fitting results for each sample.

Sample	α	β	σ
SDSS Dr8	0.59 ± 0.03	1.17 ± 0.02	$0.33^{+0.02}_{-0.02}$
DES Y1	0.58 ± 0.04	1.22 ± 0.03	$0.24^{+0.03}_{-0.02}$
SDSS+DES Y1	0.59 ± 0.02	1.18 ± 0.02	$0.31^{+0.01}_{-0.01}$

Table 5.6: Fitting results of the $T_{\rm x} - \lambda$ scaling relation. The model assumed has the form $\ln T_{\rm x} = \beta + \alpha \ln(\lambda/\lambda_0)$ where $\lambda_0 = 40$ for all the samples.

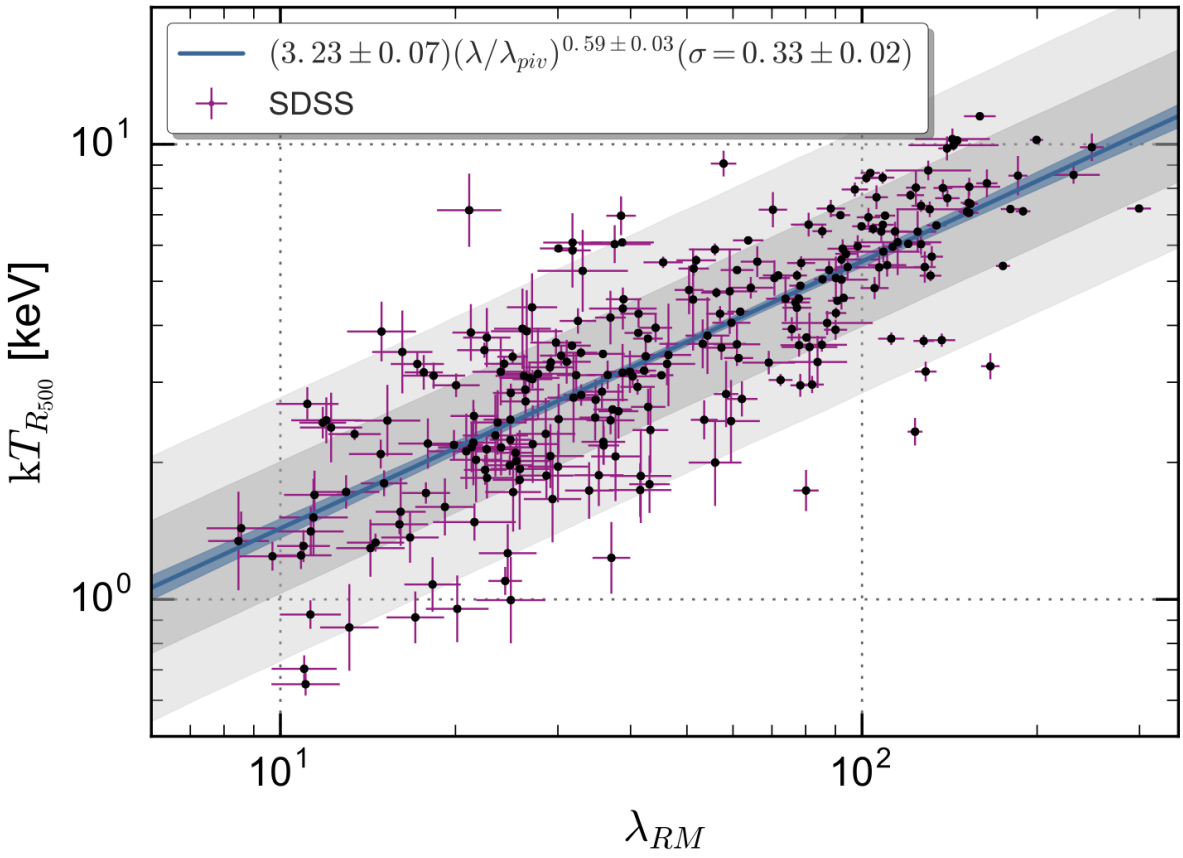

Figure 5.15: Optical to X-ray scaling relation between optical richness (λ) and X-ray temperature ($T_{\rm X}$) for the XCS-RM (SDSS-DR8) sample.

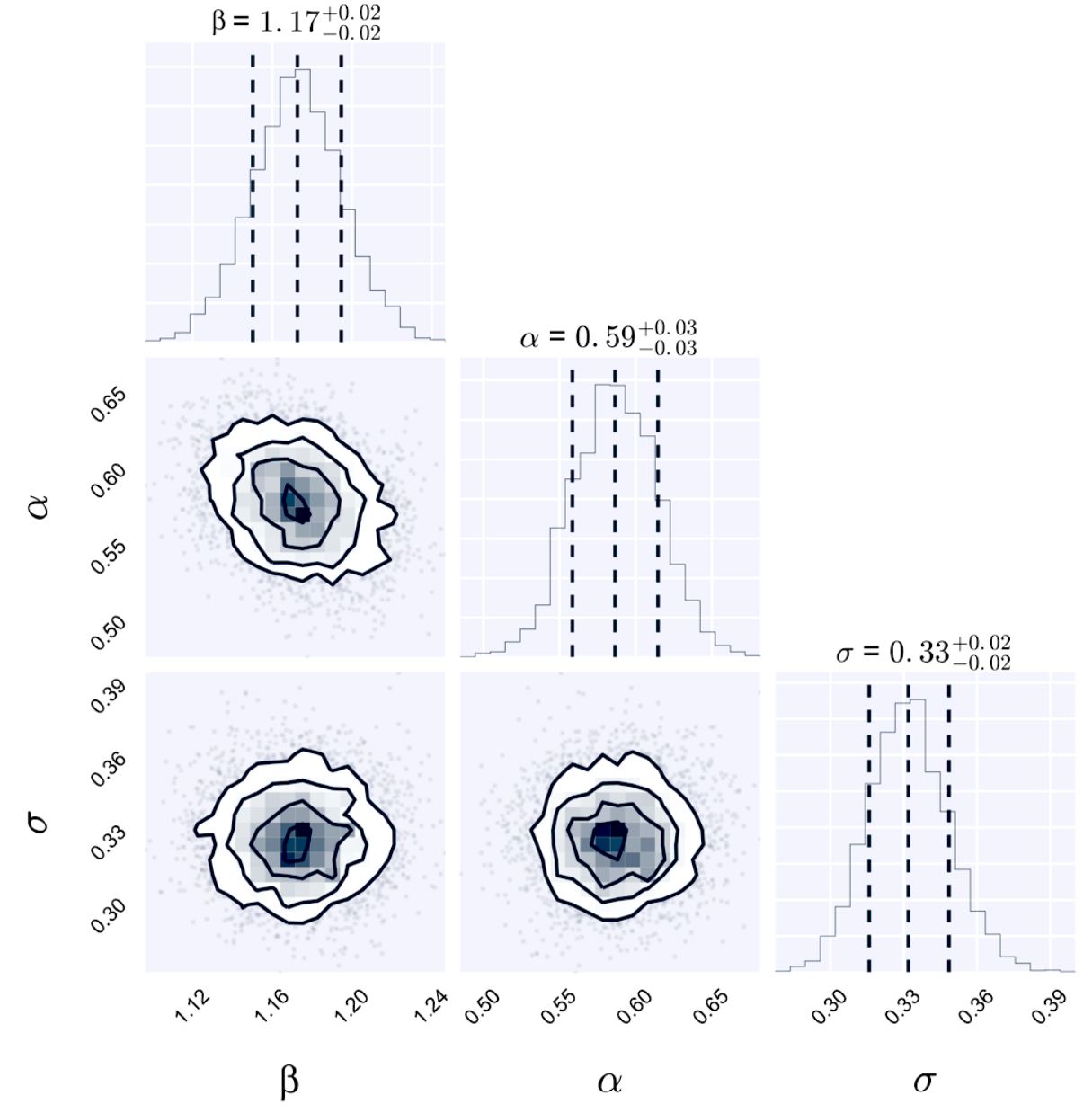

Figure 5.16: Triangle plot of the free parameters of Equation 5.6) for $T_{\rm X} - \lambda$ scaling relation, using data from the XCS-RM (SDSS DR8) sample.

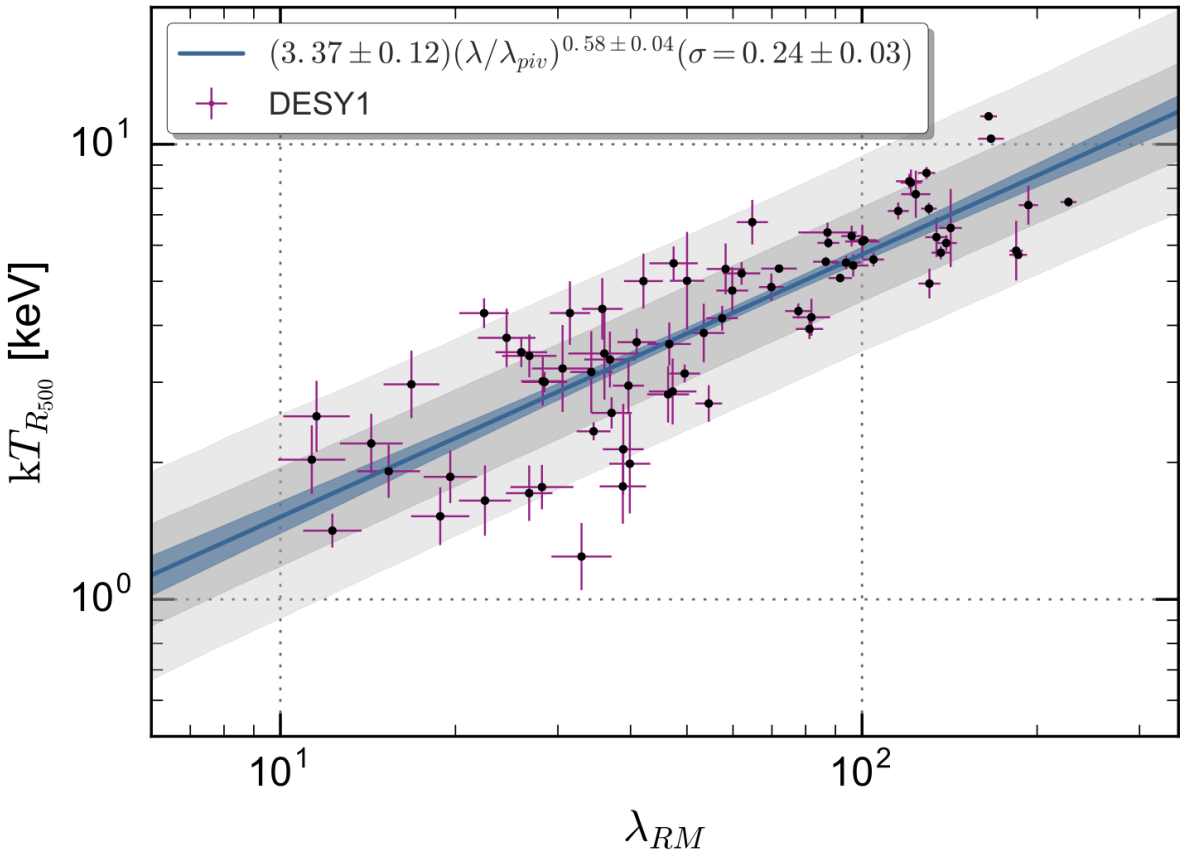

Figure 5.17: Optical to X-ray scaling relation between optical richness (λ) and X-ray temperature ($T_{\rm X}$) for the XCS-RM (DES Y1) sample. The gray shading represents the 1σ (dark) and 2σ (light) confidence regions.

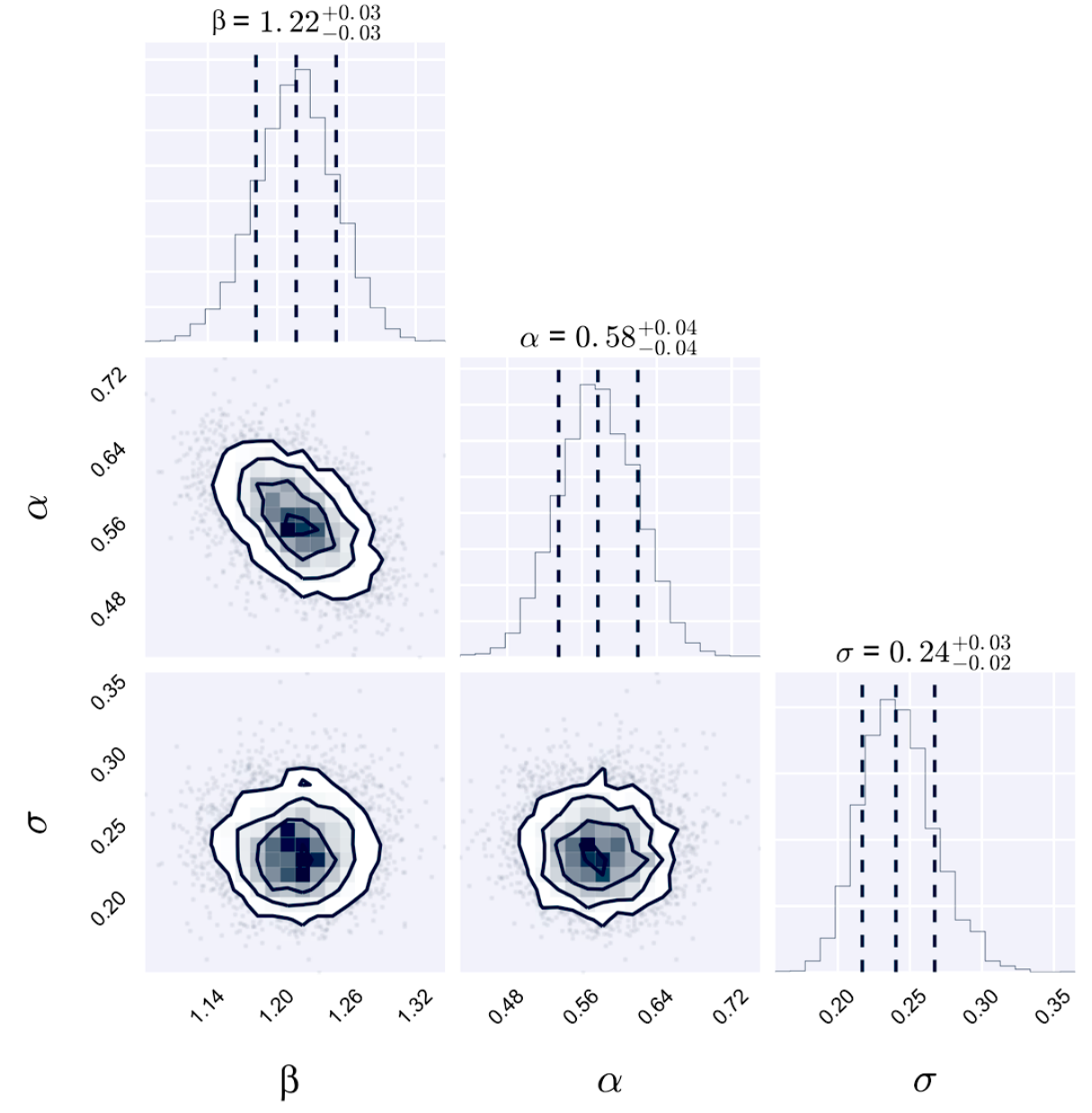

Figure 5.18: Triangle plot of the free parameters of Equation 5.6 for $T_{\rm X} - \lambda$ scaling relation, using data from the XCS-RM (DES Y1) sample.

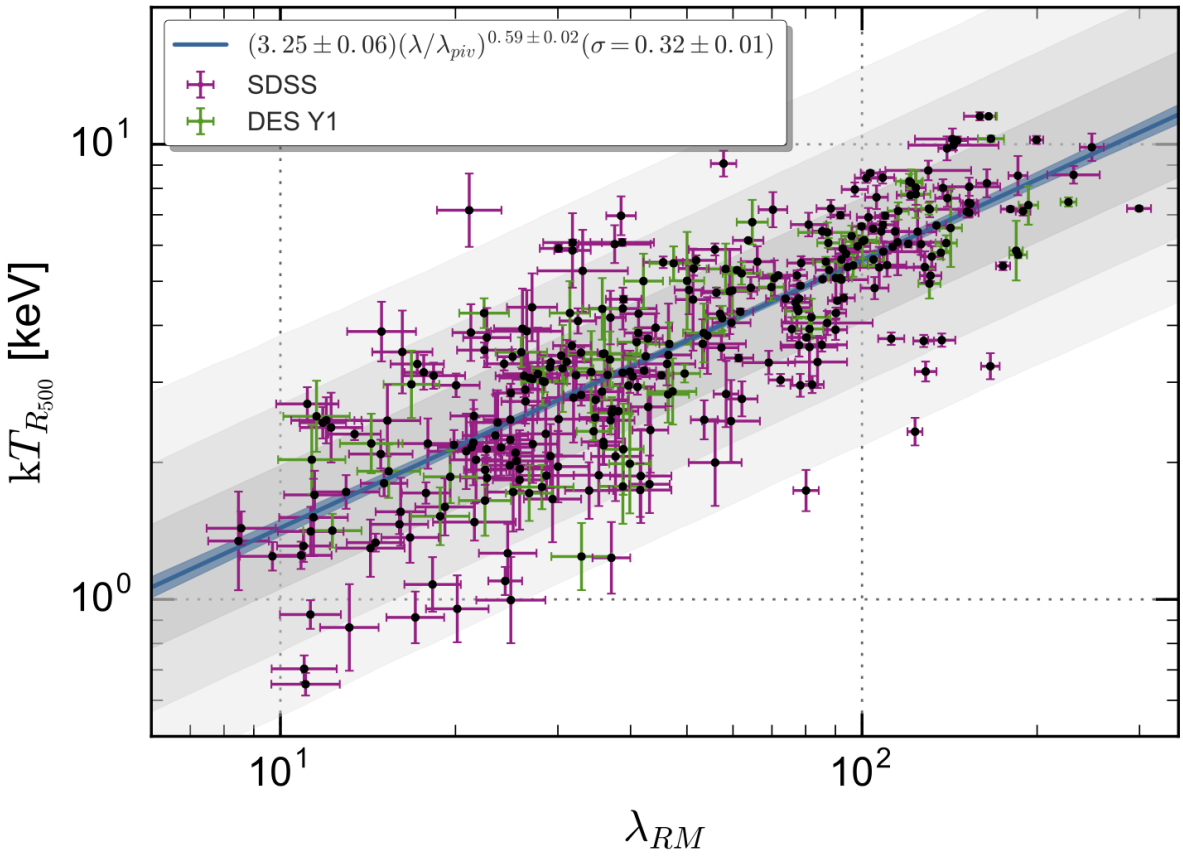

Figure 5.19: Optical to X-ray scaling relation between optical richness (λ) and X-ray temperature ($T_{\rm X}$) for the XCS-RM (SDSS+DES Y1) sample. The gray shading represents the 1σ (dark) and 2σ (light) confidence regions.

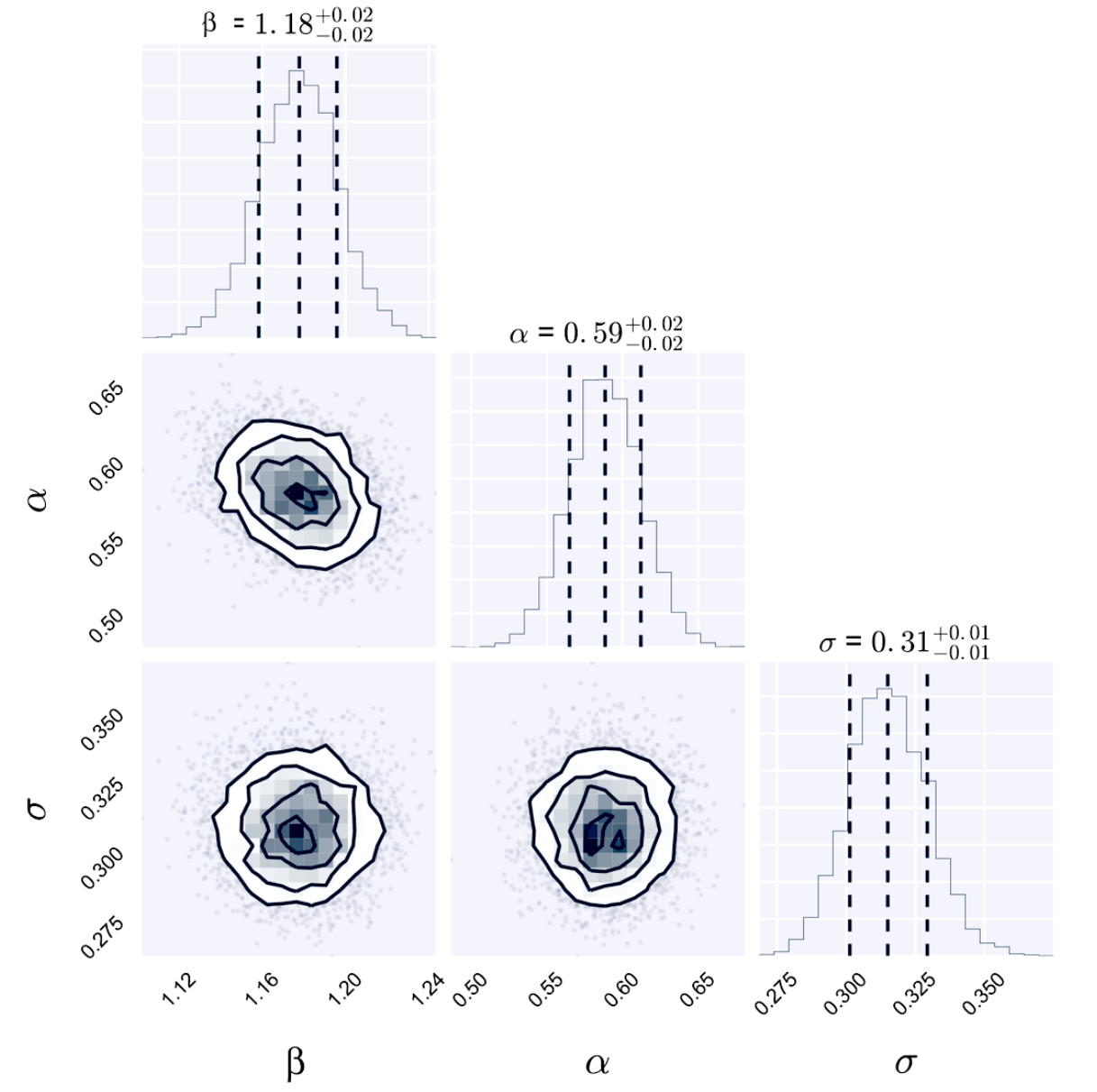

Figure 5.20: Triangle plot of the free parameters of Equation 5.6) for $T_{\rm X}-\lambda$ scaling relation, using data from the XCS-RM (SDSS+DES Y1) sample. The gray shading represents the 1σ (dark), 2σ (lighter), and 3σ (lightest) confidence regions.

5.4.4 Outlier Analysis

In Figure 5.21 four clusters have been highlighted. These four lie more than 2σ from the best fit $T_X - \lambda$ scaling relation to the joint (SDSS+DES-Y1) XCS-RM sample. It is important to investigate these outliers to determine if they represent the underlying scatter in the scaling relation, or if they are due to issues with the XMM data/analysis, the optical data/analysis, or with the XCS to RM matching process.

XMMXCS J004630.7+202803.6

This cluster has a measured X-ray temperature of 2.32 keV, an optical richness of $\lambda = 123.35$, and a RM determined photometric redshift of $z_\lambda = 0.104$. For that richness, the best fit scaling relation (Equation 5.8) would predict $T_{\rm X} \simeq 6.27$ keV. Figure 5.22 shows the optical and X-ray observations of this cluster, the SDSS observation is overlaid with the XMM X-ray contours. Both observations are centred on the XCS position. The XCS source and the RM cluster are separated by $R/R_\lambda = 0.037$, and the relative error on $T_{\rm X}$ and are both "acceptable" (Section 5.2): $\delta T_{\rm X} = 0.14$ and $\delta\lambda = 0.06$.

There are no obvious problems with either the X-ray or optical data and I conclude that this is a genuine physical system, with associated galaxies and intracluster medium. This system reflects the underlying scatter in the scaling relation: it is unusually cool for the corresponding richness, or unusually rich for the corresponding temperature. The latter scenario is more likely: the RM radius is much larger than the X-ray source (it is not even visible in 5.22.a). I note that the lower richness cluster ($\lambda = 14.81$) that is visible in 5.22.a is in the background of the X-ray cluster (it has a redshift of $z_\lambda = 0.36$).

XMMXCS J231148.8+034046.7

This cluster has a measured X-ray temperature of 3.48 keV, an optical richness of $\lambda = 166.20$, and a RM determined photometric redshift of $z_\lambda = 0.30$. For that richness, the best fit scaling relation (Equation 5.8) would predict $T_{\rm X} \simeq 7.48$ keV. Figure 5.23 shows the optical and X-ray observations of this cluster, the SDSS observation is overlaid with the XMM X-ray contours. Both observations are centred on the XCS position. The XCS source and the RM cluster are separated by $R/R_\lambda = 0.11$, and the relative error on $T_{\rm X}$ and are both "acceptable" (Section 5.2): $\delta T_{\rm X} = 0.13$ and $\delta\lambda = 0.07$.

There are no obvious problems with either the X-ray or optical data and I conclude that this is a genuine physical system, with associated galaxies and intracluster medium. This system reflects the underlying scatter in the scaling relation: it is unusually cool for the

corresponding richness, or unusually rich for the corresponding temperature. In this case, I cannot predict which scenario is more likely. I note that the bright nearby (in projection) extended source (low-right corner) is also an X-ray cluster. I have checked the source and background regions for XMMXCS J231148.8 at each iteration (Section 4.3.2) and have confirmed that photons from this brighter source do not pollute the spectral aperture. (In earlier versions of XCS3P that would have been the case, see Section 4.3.1.)

XMMXCS J120352.5+014730.0

This cluster has a measured X-ray temperature of 1.95 keV, an optical richness of $\lambda = 80.12$, and a RM determined photometric redshift of $z_\lambda = 0.24$. For that richness, the best fit scaling relation (Equation 5.8) would predict $T_X \simeq 4.86$ keV. Figure 5.24 shows the optical and X-ray observations of this cluster, the SDSS observation is overlaid with the XMM X-ray contours. Both observations are centred on the XCS position. The XCS source and the RM cluster are separated by $R/R_\lambda = 0.13$, and the relative error on T_X and are both "acceptable" (Section 5.2): $\delta T_X = 0.13$ and $\delta\lambda = 0.07$.

In Figure 5.24.b it is possible to see a galaxy overdensity (albeit without an obvious central concentration) within the region defined by the RM radius (cyan circle). However, in Figure 5.24.a it is not possible to see a similar overdensity in X-ray surface brightness, despite the fact that XAPA has found an extended source (green ellipse). In this case there are two different XMM observations of this location (ObsID=0723800601 and ObsID=0723800701). Figure 5.24.a shows the image from the former. In the latter, the XAPA source at that location is recorded to have a negative number of background subtracted counts. These "inverse" sources are rare in the XCS master source list, and indicate incidences of sources detected in regions of unusually high background. The target of both ObsIDs is a bright extended source (the edge of which is visible in the top left corner of Figure 5.24.a). In this case, I conclude that pollution by the background has influenced the measured T_X value, and that this system does not reflect the underlying scatter in the scaling relation.

XMMXCS J222824.6-051941.9

This cluster has a measured X-ray temperature of 7.16 keV, and optical richness of $\lambda = 21.11$, and a RM determined photometric redshift of $z_\lambda = 0.36$. For that richness, the best fit scaling relation Equation 5.8) would predict $T_X = 2.21$ keV: this is the only example of the four outliers of a cluster that is *hotter* than predicted. Figure 5.25 shows the optical

and X-ray observations of this cluster, the SDSS observation is overlaid with the XMM X-ray contours. Both observations are centred on the XCS position. The XCS source and them RM cluster are separated by 0.28 h^{-1}Mpc, and the relative error on T_X and richness are both "acceptable".

In Figure 5.25.b it is possible to see a galaxy overdensity with a central concentration within the region defined by the RM radius (cyan circle). In Figure 5.24.a an associated enhancement in X-ray surface brightness is centred in the same location. However, it is clear that the XAPA region is enclosing a second, brighter, X-ray source to the upper left. The resulting aperture used for the spectral fitting will therefore be heavily polluted by the second source and the T_X fit will not reflect the properties of the intracluster medium. I have investigated the properties of the second source using the NASA/IPAC Extragalactic Database (NED)[2] and determined that it is an X-ray quasar (PHL 5200, Brinkmann, Ferrero and Gliozzi, 2002). Figure 5.26 shows the position of the quasar and the 1465 MHz VLA radio contours. Quasars are known to have harder spectra than clusters, so it is not surprising that the T_X of the cluster was over estimated. I conclude that this system does not reflect the underlying scatter in the scaling relation.

[2] https://ned.ipac.caltech.edu

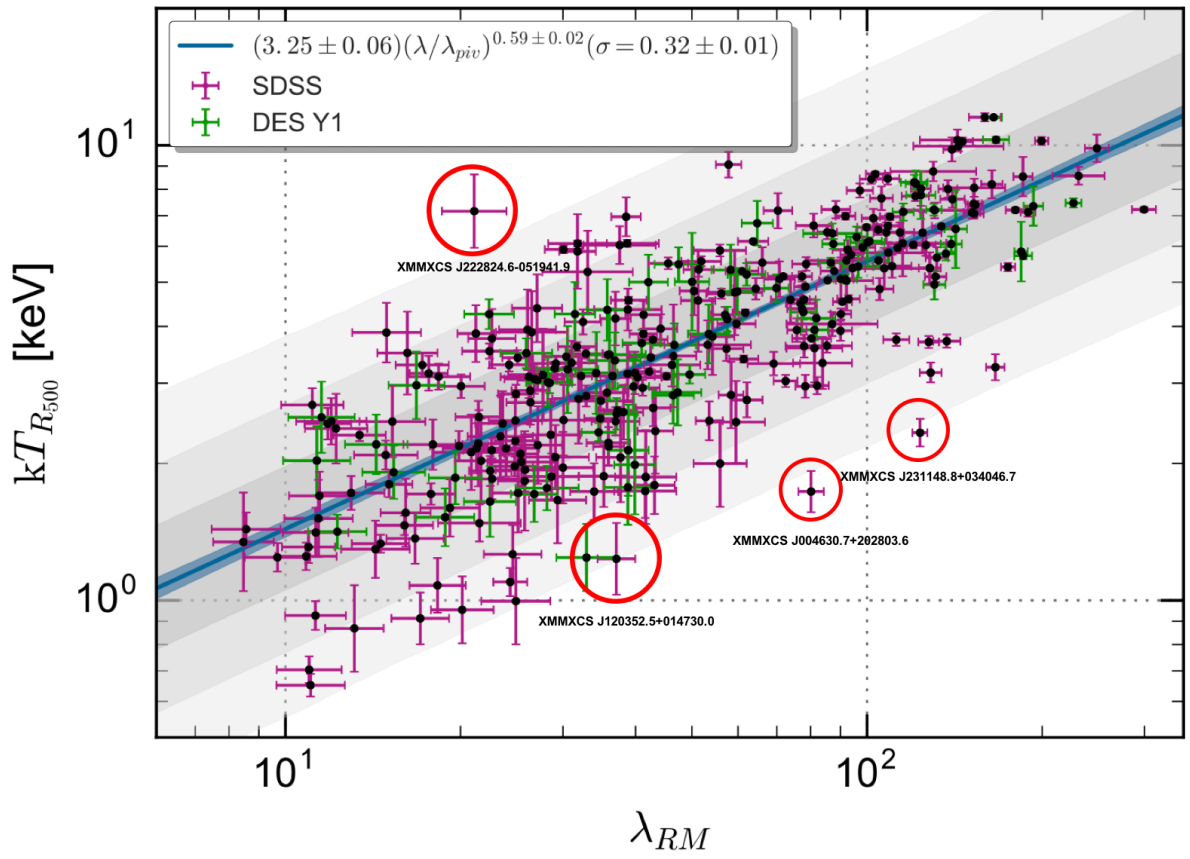

Figure 5.21: As Figure 5.19, but with $> 2\sigma$ outliers circled and annotated.

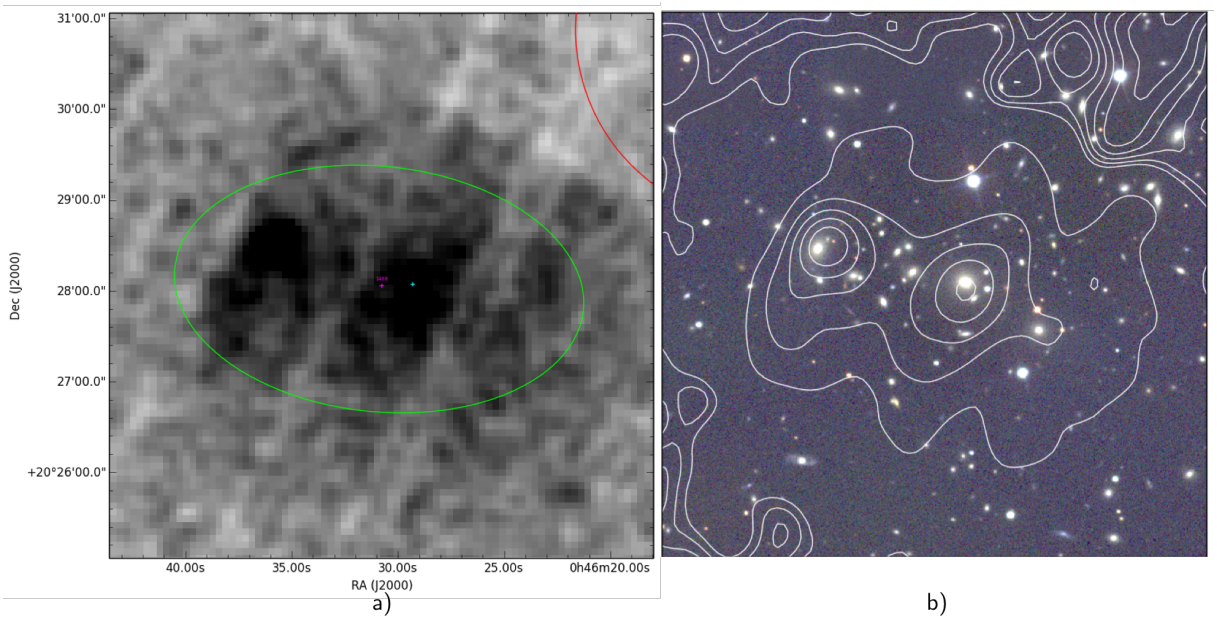

Figure 5.22: Cluster XMMXCS J004630.7+202803.6: (a) XMM-Newton observation centred on the XCS position, green ellipse represents the XCS cluster, cyan circle is RM cluster with $\lambda > 20$, big red circle is RM cluster with $\lambda < 20$, small red circles are point sources. (b) Optical observation from SDSS with X-ray contours information from XMM.

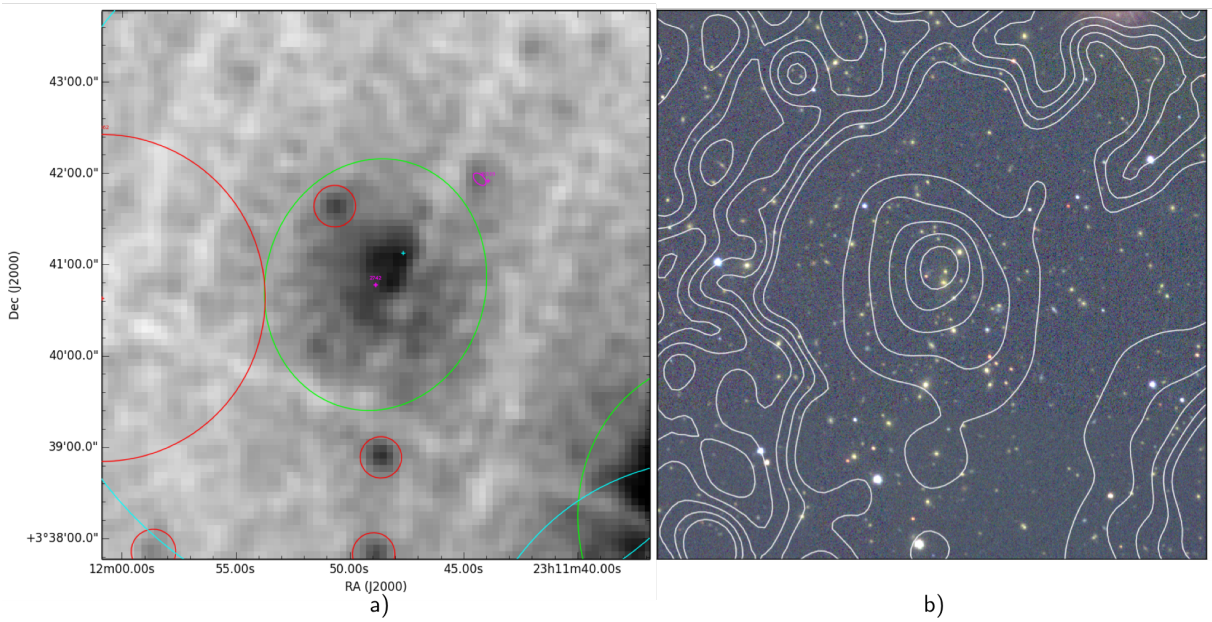

Figure 5.23: Cluster XMMXCS J231148.8+034046.7: (a) XMM-Newton observation centred on the XCS position, green ellipses represent XCS clusters, cyan circles are RM clusters with $\lambda > 20$, big red circle is RM cluster with $\lambda < 20$, small red circles are point sources. (b) Optical observation from SDSS with X-ray contours information from XMM.

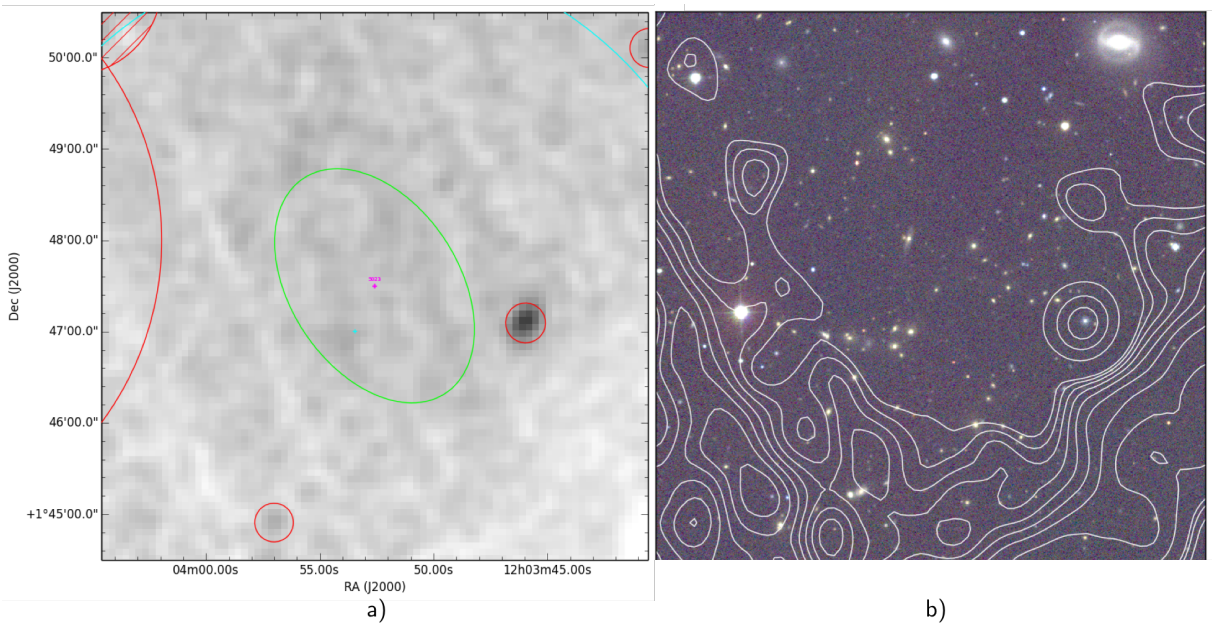

Figure 5.24: Cluster XMMXCS J120352.5+014730.0: (a) XMM-Newton observation centred on the XCS position, green ellipse represents the XCS cluster, cyan circle is RM cluster with $\lambda > 20$, big red circle is RM cluster with $\lambda < 20$, small red circles are point sources. Crossed circle represent a RM cluster with $z_\lambda < 0.08$. (b) Optical observation from SDSS with X-ray contours information from XMM.

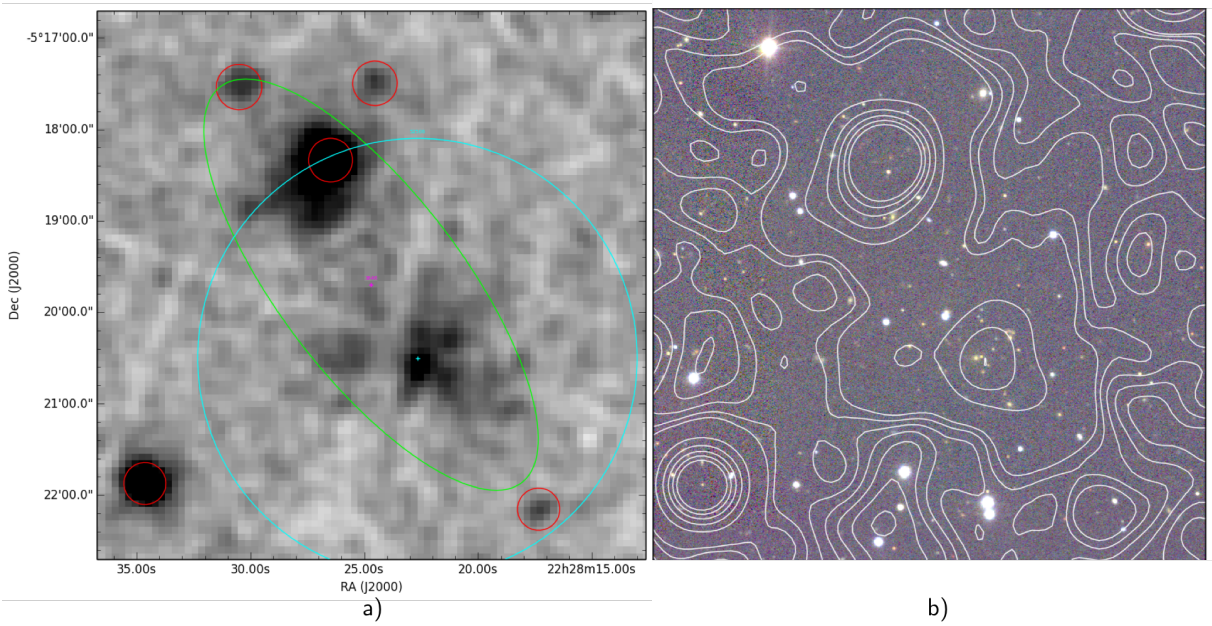

Figure 5.25: Cluster XMMXCS J222824.6+051941.9: (a) XMM-Newton observation centred on the XCS position, green ellipse represents the XCS cluster, cyan circle is RM cluster with $\lambda > 20$, big red circle is RM cluster with $\lambda < 20$, small red circles are point sources. Crossed circle represent a RM cluster with $z_\lambda < 0.08$. (b) Optical observation from SDSS with X-ray contours information from XMM.

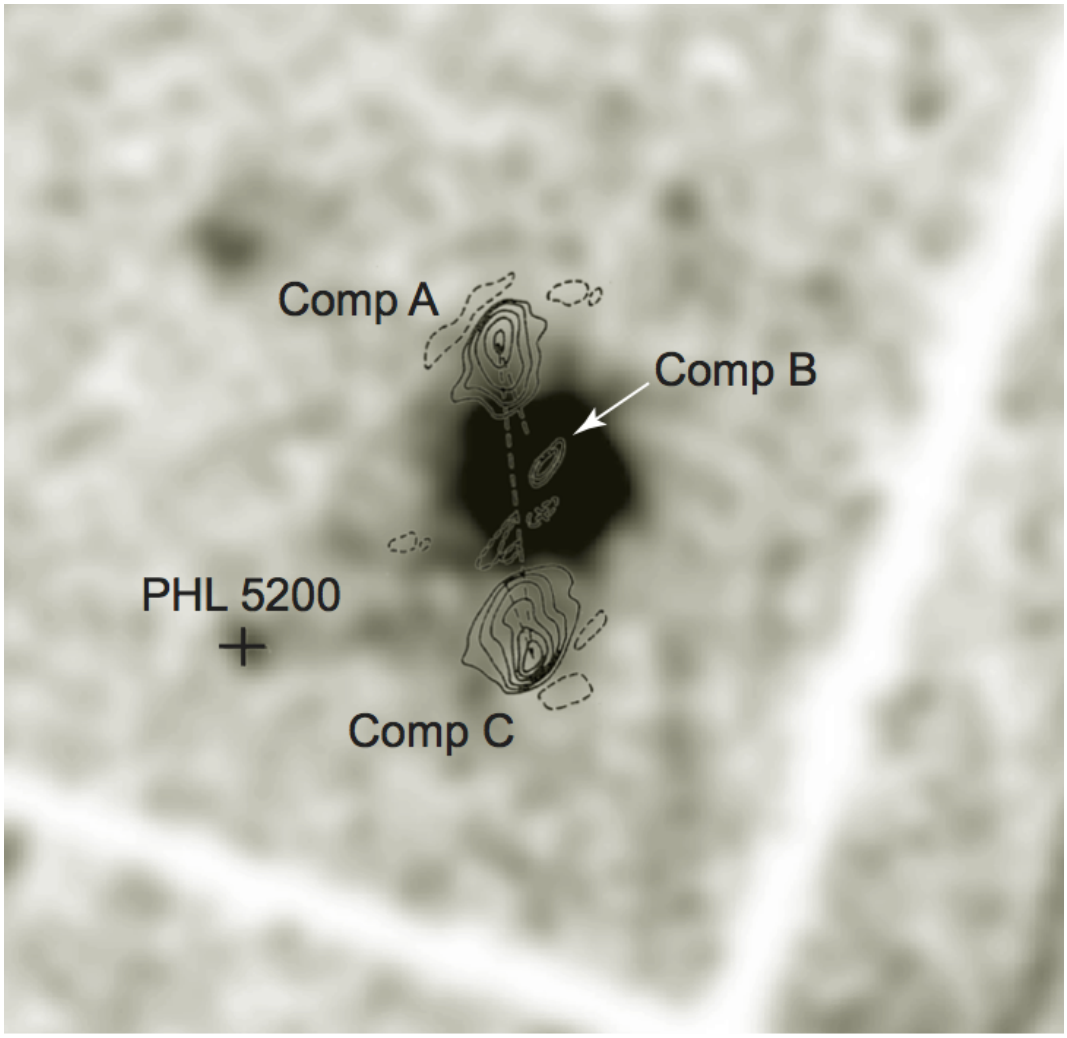

Figure 5.26: Figure and caption taken from Brinkmann, Ferrero and Gliozzi, 2002: Gaussian smoothed PN image of an $\sim 7.5 \times 7.5$ sky region around PHL 5200, overlaid with the 1465 MHz VLA radio contours. The position of the quasar is marked by a cross

5.4.5 Comparison to previous analyses

Rykoff and Rozo, 2014 (R14) evaluate the performance of the RM SDSS catalog by comparing its results with X-ray and Sunyaev-Zeldovich selected catalogs. They calculated the $T_X - \lambda$ scaling relation using data from the RM SDSS DR8 catalog (version of 2014) and the XCS DR1 catalog (Mehrtens et al., 2012). Considering a matching radius of 1.5 Mpc they obtained a total of 98 common clusters between RM and XCS, this sample was selected taking only clusters with associated errors of 15% or less in both T_X and λ. Their scaling relation is shown in Figure 5.28.

The offset between ACCEPT and XCS temperatures can be explained[3] by the fact that there is a known temperature offset between CHANDRA and XMM due to undiagnosed calibration issues (e.g. Schellenberger et al., 2015).

R14 used the following model to fit their scaling relation:

$$\ln T_X = A + \alpha \ln(\lambda/\lambda_{\rm pivot}), \tag{5.13}$$

where A is the amplitude and α is the slope. The fitting is done over three redshift bins ($z \in (0.1, 0.3), z \in (0.3, 0.5), z \in (0.1, 0.5)$) considering a Bayesian approach. The constrains of the free parameters of the model are given in Table 5.7.

R14 do not provide a list of the M12 XCS-DR1 clusters they used, but we have fitted their same relation, over the same redshift intervals, to the SDSS-RM sample defined in Section 5.3. For this we used the BCES technique (from Hilton et al., 2012), described in Section 4.4.2. In Table 5.7 we compare our best fit values to those in R14.

R14 do not report a table with clusters identifications and positions, thus, no direct comparison can be made with the data reported in this thesis. Figure 5.28 plot a comparison between the constrains obtained by R14 and this work for the wider redshift range $z \in [0.1, 0.5]$ with clusters in the XCS-RM (SDSS DR8) sample. There is good consistency in all redshift bins, despite the change from XCS3P-v1 to XCS3P-v3 (Section 4.2.3) and the difference in the sample selection.

A similar analysis was done in Rykoff et al., 2016 (ER16) to validate the redMaPPer DES SV catalog, I participated as coauthor in this paper doing the X-ray analysis of RM clusters.

X-ray clusters from Chandra and XMM, and SPT clusters were correlated with the RM clusters in the DES SV sample. The analysis of SPT and RM clusters in the DES SV

[3] Although the authors of R14 erroneously diagnosed it as being due to the exclusion of core emission by the ACCEPT team.

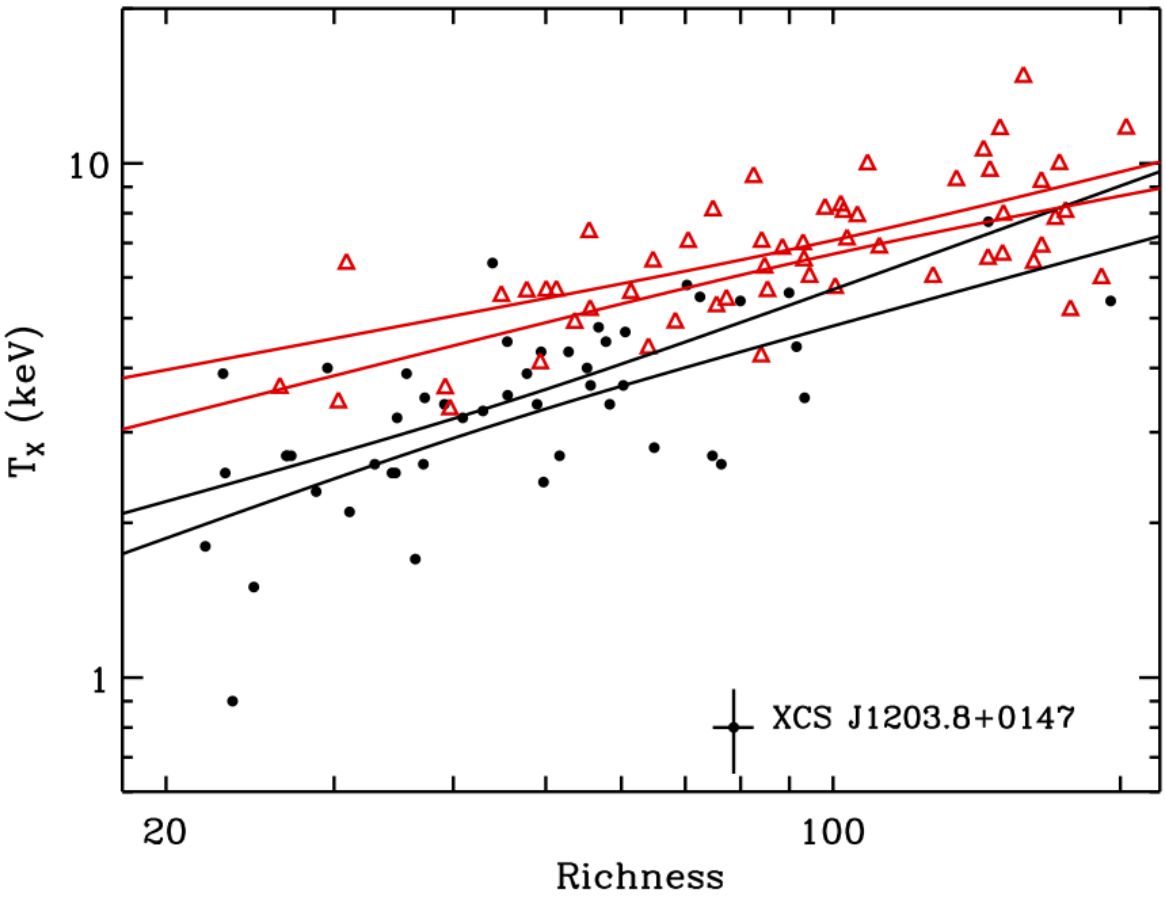

Figure 5.27: Figure and caption taken from reference Rykoff and Rozo, 2014, $T_{\rm X} - \lambda$ relation for XCS (black dots) and ACCEPT (red triangles) galaxy clusters. The bands show the uncertainty in the main relation.

footprint is already published in Saro et al., 2017.

The sample consists of 25 SPT clusters between $0.1 < z < 0.8$, 38 from Chandra (15 had sufficient statistics to fit a temperature). For XMM, I cross matched the RM DES SV catalog with the XCS DR2 positions using a radius of 1.5 h^{-1}Mpc, although I noticed that all of the verified matches were within 0.4 h^{-1}Mpc. I found 29 clusters and calculate $T_{\rm X}$ using the methodology described in Section 4.2, assuming redshift information from RM. 14 temperatures were obtained.

Before fitting the $T_{\rm X} - \lambda$ scaling relation, I made a correction between the Chandra and XMM temperatures. For this, I analyzed the Chadra and XCS clusters that have a correlation with RM in the SDSS sample. In total, there were 41 clusters in common between these samples, allowing to fit a correlation factor in the form:

$$\log_{10}\left(\frac{T_{\rm X}^{Chandra}}{1\ \rm keV}\right) = 1.0133\log_{10}\left(\frac{T_{\rm X}^{XMM}}{1\ \rm keV}\right) + 0.1008, \tag{5.14}$$

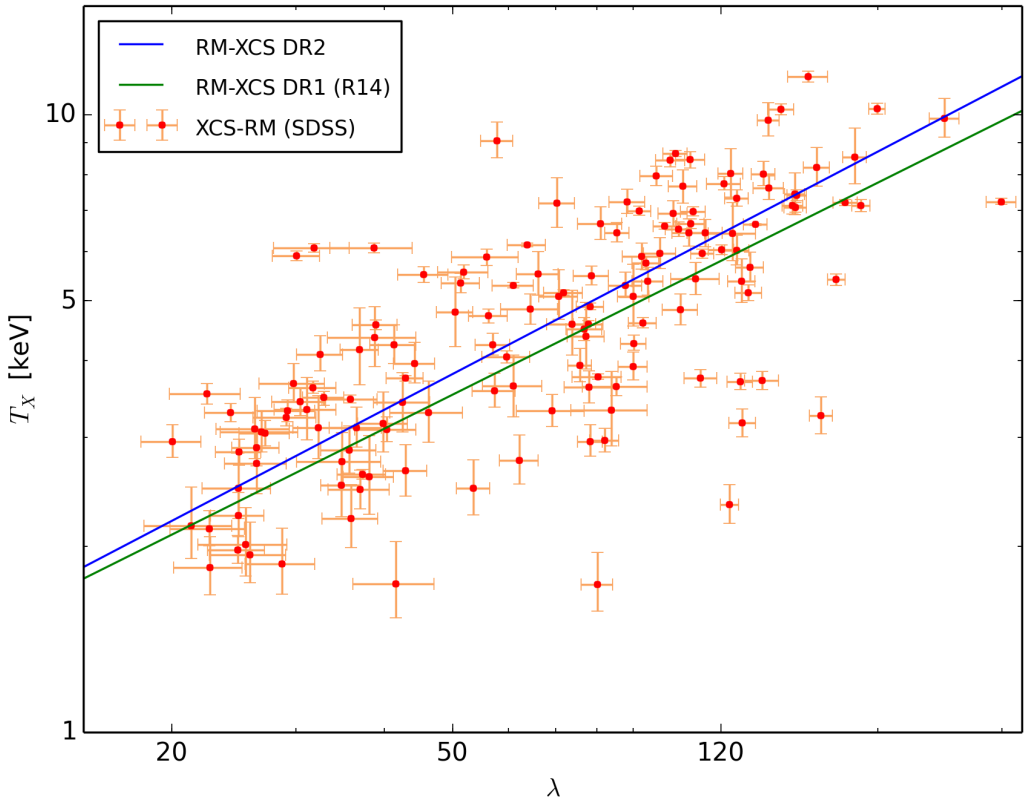

Figure 5.28: $T_{\rm X} - \lambda$ for XCS-RM (SDSS DR8) sample, only clusters with $\delta T_{\rm X} \leq 0.3$ and $\delta\lambda \leq 0.3$. Green line indicates the fitting obtained by R14 while the blue line fit the current data.

Once all the Chandra temperatures were corrected to the XMM values using equation 5.14, the $T_{\rm X} - \lambda$ scaling relation was fitted using a modified version of equation 5.13:

$$\ln T_{\rm X} = \alpha + \beta \ln(\lambda/50) + \gamma \ln[E(z)/E(0.4)], \tag{5.15}$$

where the redshift evolution parameter is fixed at $\gamma = -2/3$, assuming self-similar evolution. Through MCMC the free parameters were found for the combined sample (Chandra+XMM): $\alpha = 1.31 \pm 0.07$, $\beta = 0.60 \pm 0.09$, and $\sigma = 0.28^{+0.07}_{-0.05}$. Figure 5.29 show the $T_{\rm X} - \lambda$ scaling relation where Chandra and XCS clusters are plotted.

It is possible to compare this result with the $T_{\rm X} - \lambda$ scaling relation obtained from XCS DR2 and RM DES Y1 (see Section 5.4) where both use DES data. ER16 provides data tables with the information of Chandra and XMM clusters, thus a direct comparison can be made with the XCS-RM (DES Y1) sample, see Figure 5.30.

Similar to the SDSS comparison, there is good consistency for the DES samples (DES SV from ER16 and DES Y1 from this thesis), despite several modifications to the XCS3P-v3

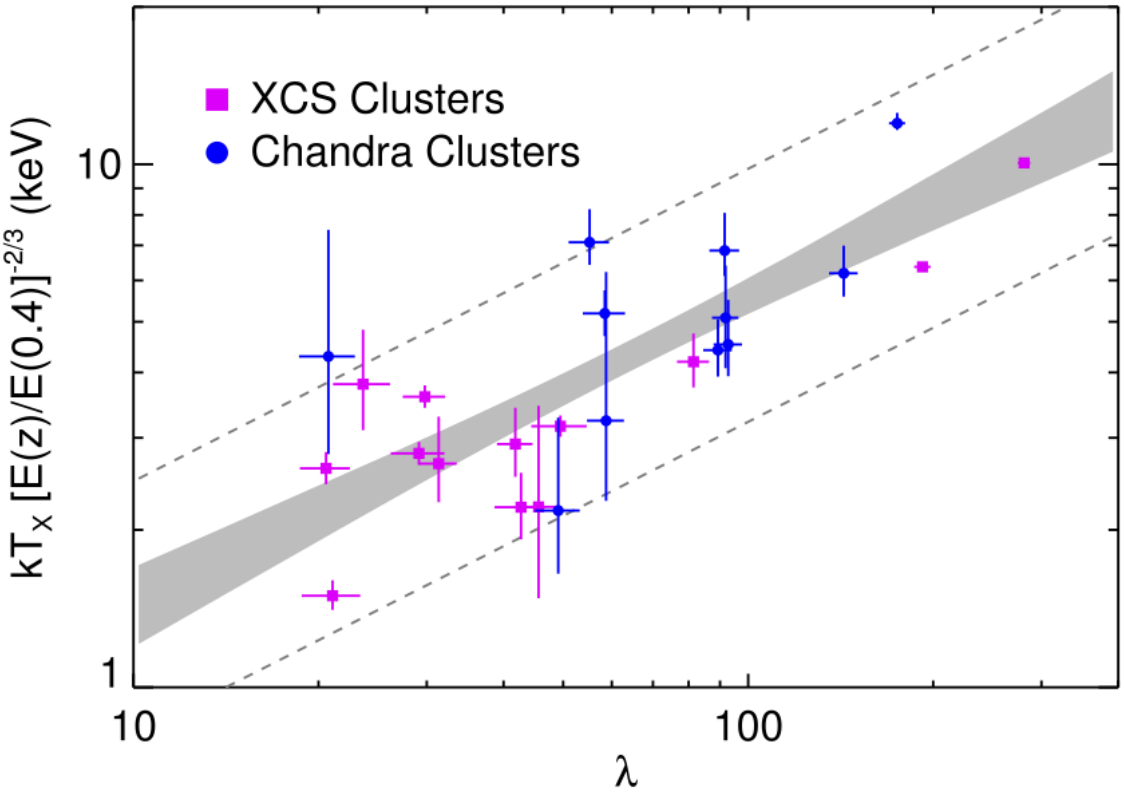

Figure 5.29: Figure and caption taken from Rykoff et al., 2016: $T_X - \lambda$ scaling relation derived from XCS (magenta squares) and Chandra (blue circles) clusters. All Chandra temperatures have been corrected according to equation 5.14. The grey band shows the best-fit ($\pm 1\sigma$) scaling relation, the dashed gray lines show 2σ intrinsic scatter constraints.

made after 2016.

Catalog	Redshift Bin	$\lambda_{\rm pivot}$	Amplitude	Slope	Scatter	N
XCS DR1	$[0.1, 0.3]$	40.9	1.129 ± 0.056	0.56 ± 0.14	0.194 ± 0.055	25
XCS DR1	$[0.3, 0.5]$	49.7	1.283 ± 0.071	0.57 ± 0.15	0.234 ± 0.062	24
XCS DR1	$[0.1, 0.5]$	45.6	1.206 ± 0.044	0.57 ± 0.10	0.225 ± 0.042	49
XCS-RM (DES Y1)	$[0.1, 0.3]$	40.9	1.234 ± 0.052	0.58 ± 0.07	0.145 ± 0.011	85
XCS-RM (DES Y1)	$[0.3, 0.5]$	49.7	1.296 ± 0.050	0.63 ± 0.06	0.120 ± 0.012	62
XCS-RM (DES Y1)	$[0.1, 0.5]$	45.6	1.280 ± 0.037	0.60 ± 0.04	0.133 ± 0.008	147

Table 5.7: Constrains of the $T_X - \lambda$ relation from Rykoff and Rozo, 2014 and XCS-RM (DES Y1). The model used is $\ln T_X = A + \alpha \ln(\lambda/\lambda_{\rm pivot})$, where A is the Amplitude, α is the slope and $\lambda_{\rm pivot}$ is taken to be the median cluster richness.

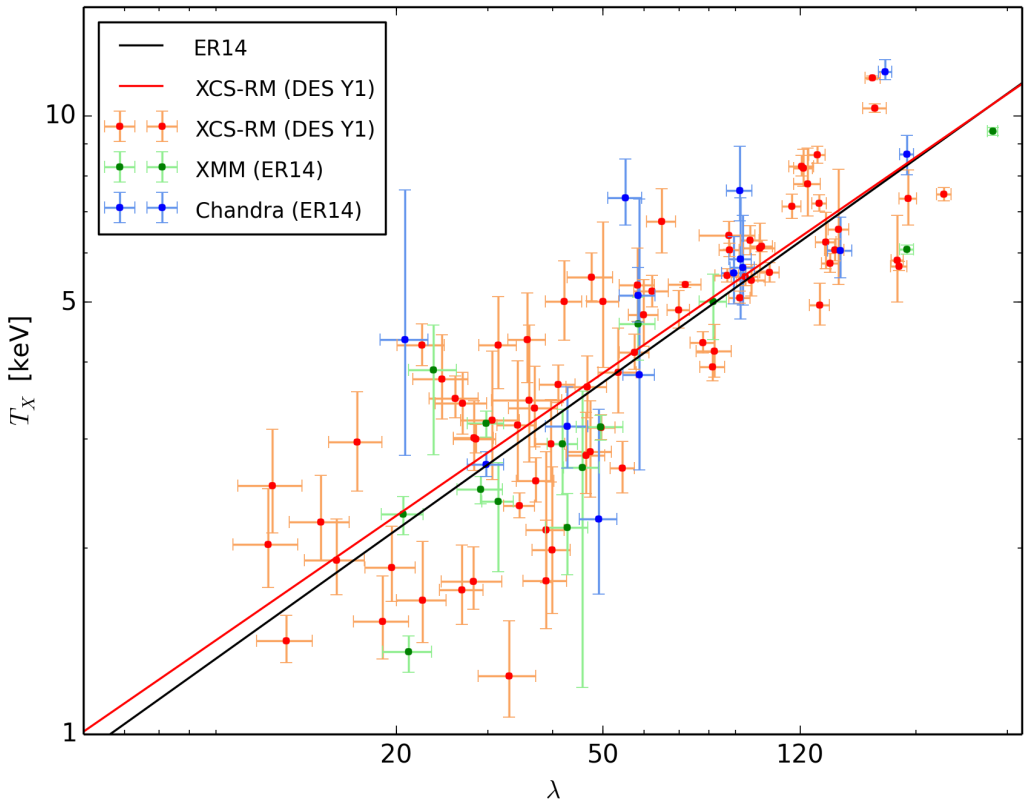

Figure 5.30: Figure and caption taken from Rykoff et al., 2016: Comparison of the $T_{\rm X} - \lambda$ scaling relation obtained by ER16 and the results of this thesis for the XCS-RM (DES Y1) sample. Black line shows the best-fit from ER16 for the combined (XMM and Chandra) data, the red lines shows the best fit (equation 5.10), green and blue circles are XMM and Chandra clusters respectively from ER16, red dots are XCS-RM (DES Y1) clusters.

5.5 The XCS-RM $L_{\rm X}-\lambda$ Scaling Relation

5.5.1 Input Data

The data used to obtain the $L_{\rm X}-\lambda$ scaling relation is as described in Section 5.3 (and used in Section 5.4). It consists of XCS clusters from the SDSS-RM sample (261 clusters), the RM-DESY1 sample (77 clusters) and the joint SDSS+DESY1-RM sample (327 clusters).

5.5.2 Fitting Method

The fitting method is based on the Equation 5.16, where the two arbitrary observables are the bolometric luminosity ($L_{\rm X}$) and the optical richness (λ). Thus, the model is described by the equation:

$$\ln L_{\rm X} = \beta + \alpha \ln\left(\frac{\lambda}{\lambda_0}\right), \tag{5.16}$$

where λ_0 is the pivot equal to 40, similar to the value used to fit the $T_{\rm X} - \lambda$ relation.

5.5.3 Results

The MCMC process constrains the free parameters in Equation 5.16. For the XCS-RM (SDSS DR8) sample the $L_{\rm X} - \lambda$ scaling relation is given by:

$$\ln L_{\rm X} = 0.01^{+0.07}_{-0.07} + 2.00^{+0.09}_{-0.09} \ln\left(\frac{\lambda}{\lambda_0}\right), \tag{5.17}$$

which can be written as

$$L_{\rm X} = (1.01 \pm 0.07)\left(\frac{\lambda}{\lambda_0}\right)^{2.00\pm0.09}, \tag{5.18}$$

The data along with the $L_{\rm X} - \lambda$ relation is plotted in Figure 5.33. Similar to Figure 5.15, blue line represents the fitting described by Equation 5.18), grey and light gray represent the 1σ and 2σ scatter respectively.

For the XCS-RM (DES Y1) sample, the $L_{\rm X} - \lambda$ scaling relation is given by:

$$\ln L_{\rm X} = 0.16^{+0.10}_{-0.10} + 2.05^{+0.12}_{-0.12} \ln\left(\frac{\lambda}{\lambda_0}\right), \tag{5.19}$$

written also as

$$L_{\rm X} = (1.18 \pm 0.12)\left(\frac{\lambda}{\lambda_0}\right)^{2.05\pm0.12}. \tag{5.20}$$

Considering the joined sample XCS-RM (SDSS+DES Y1), the $L_{\rm X} - \lambda$ scaling relation is:

$$\ln L_{\rm X} = 0.04^{+0.06}_{-0.06} + 2.02^{+0.07}_{-0.07} \ln\left(\frac{\lambda}{\lambda_0}\right), \tag{5.21}$$

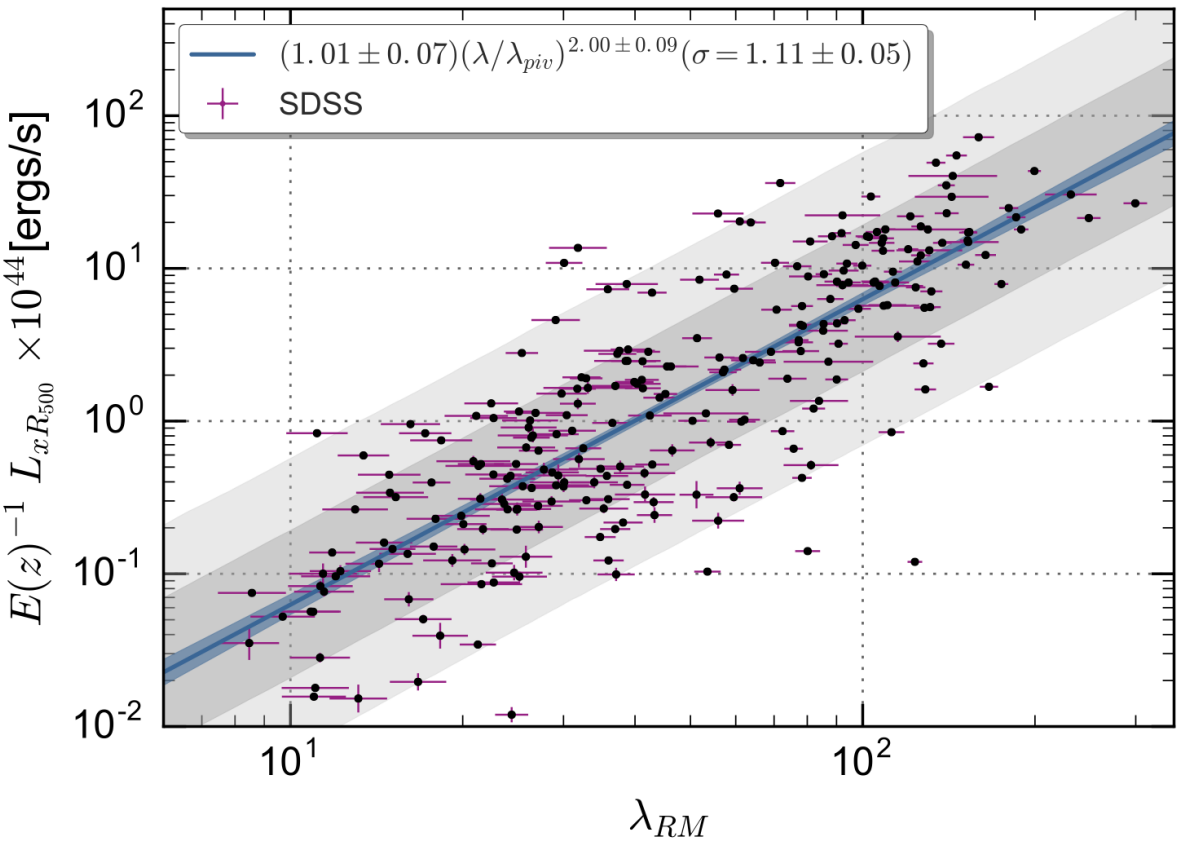

Figure 5.31: Optical to X-ray scaling relation between optical richness (λ) and Bolometric luminosity ($L_{\rm X}$) for the XCS-RM (SDSS-DR8) sample.

also written as:

$$L_{\rm X} = (1.04 \pm 0.06)\left(\frac{\lambda}{\lambda_0}\right)^{2.02 \pm 0.07} \tag{5.22}$$

Figure 5.35 shows the XCS-RM (SDSS+DES Y1) data with the $L_{\rm X} - \lambda$ scaling relation, grey regions represent 1σ, 2σ and 3σ. Table 5.8 shows the MCMC fitting results for sample.

Sample	α	β	σ
SDSS Dr8	2.00 ± 0.09	0.01 ± 0.07	$1.11^{+0.05}_{-0.05}$
DES Y1	2.05 ± 0.12	0.16 ± 0.10	$0.78^{+0.07}_{-0.06}$
SDSS+DES Y1	2.02 ± 0.07	0.04 ± 0.06	$1.04^{+0.04}_{-0.04}$

Table 5.8: Fitting results of the $L_{\rm x} - \lambda$ scaling relation. The model assumed has the form $\ln L_{\rm x} = \beta + \alpha \ln(\lambda/\lambda_0)$ where $\lambda_0 = 40$ for all the samples.

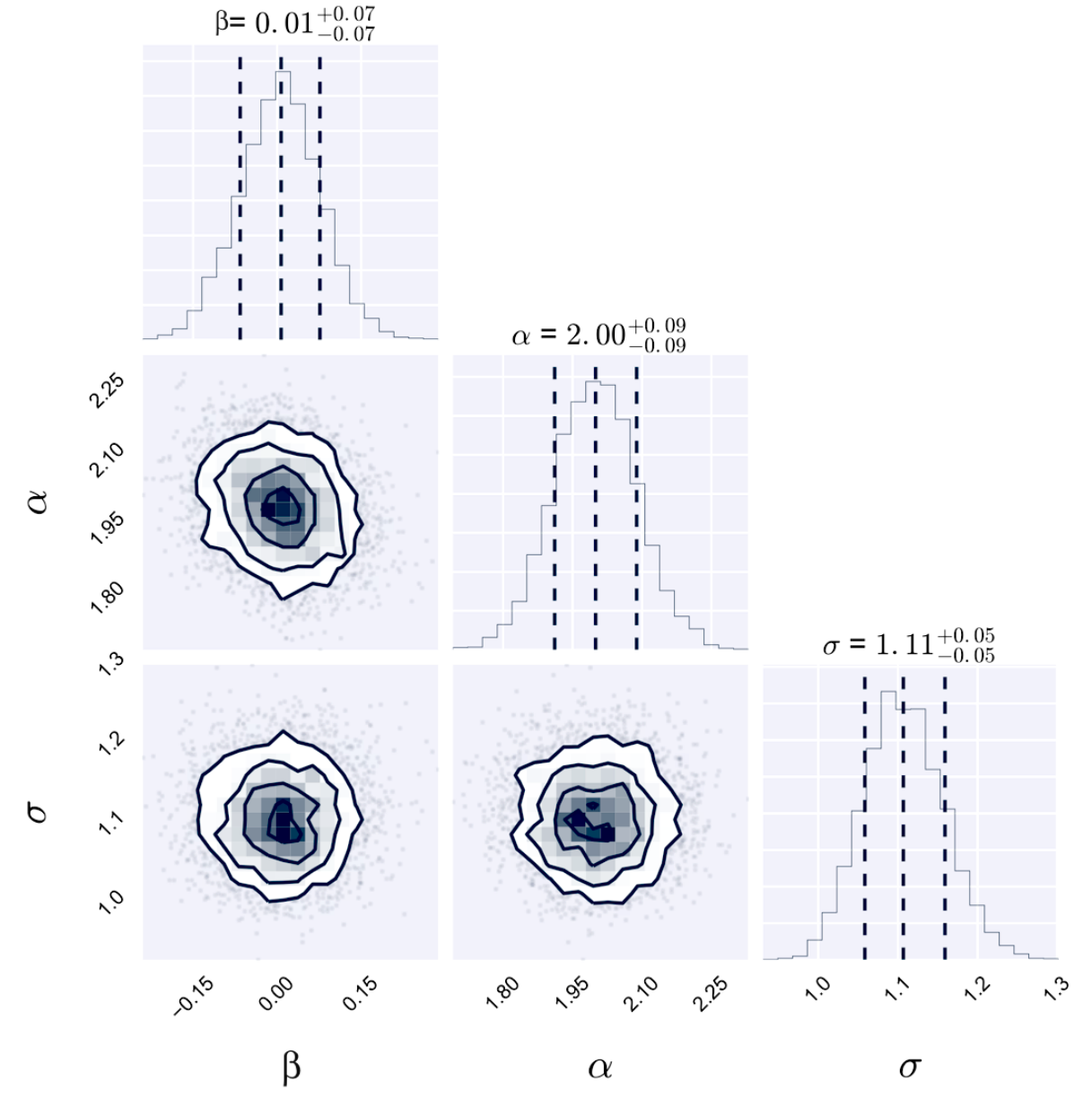

Figure 5.32: Triangle plot of the free parameters of Equation 5.16) for $L_{\rm X} - \lambda$ scaling relation, using data from the XCS-RM (SDSS DR8) sample.

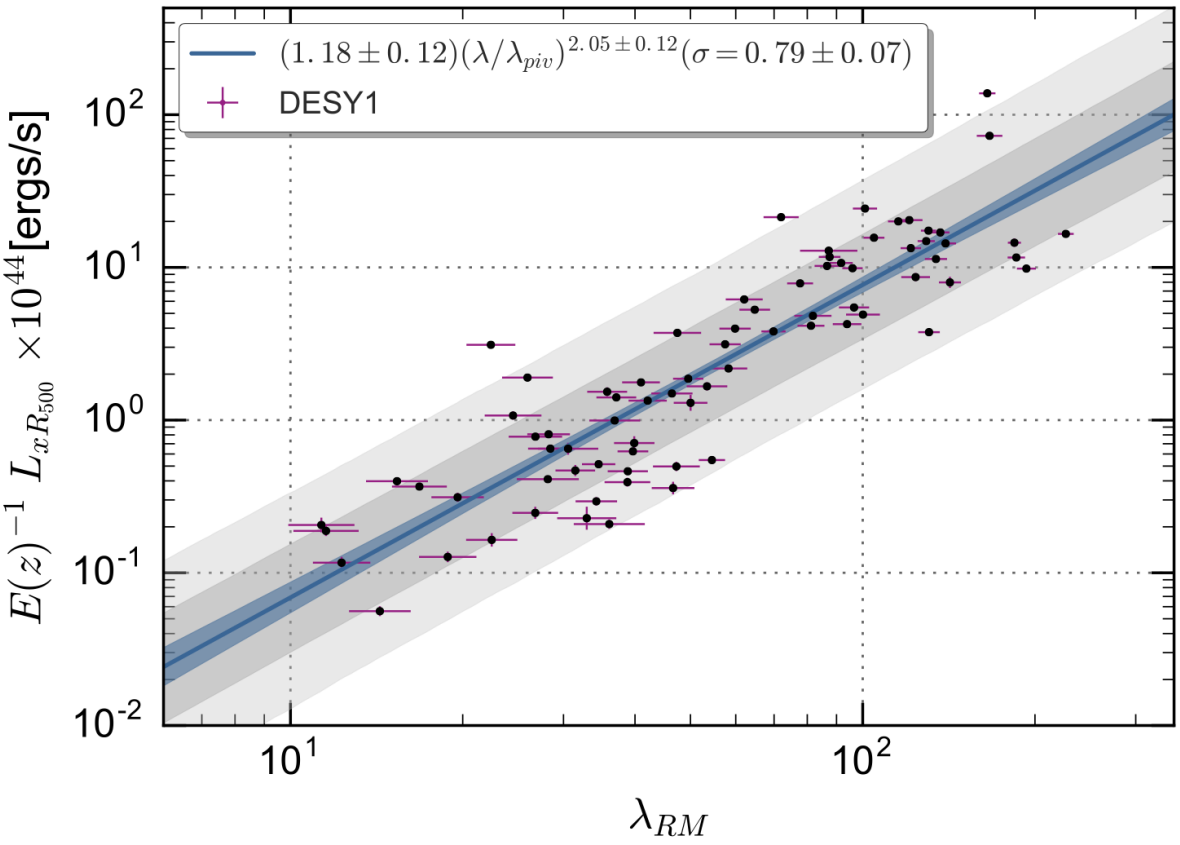

Figure 5.33: Optical to X-ray scaling relation between optical richness (λ) and Bolometric luminosity ($L_{\rm X}$) for the XCS-RM (DES Y1) sample.

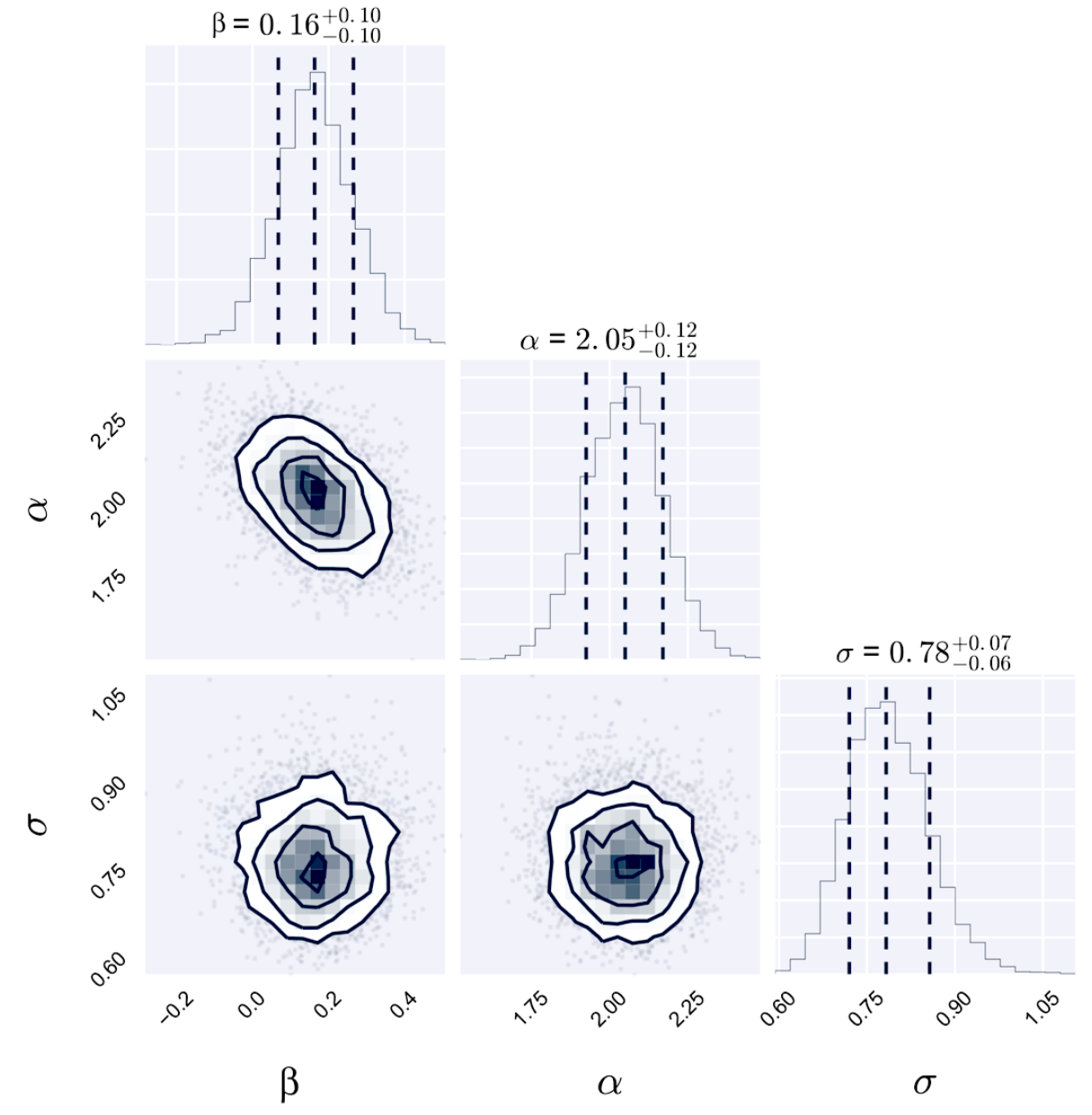

Figure 5.34: Triangle plot of the free parameters of Equation 5.16) for $L_X - \lambda$ scaling relation, using data from the XCS-RM (DES Y1) sample.

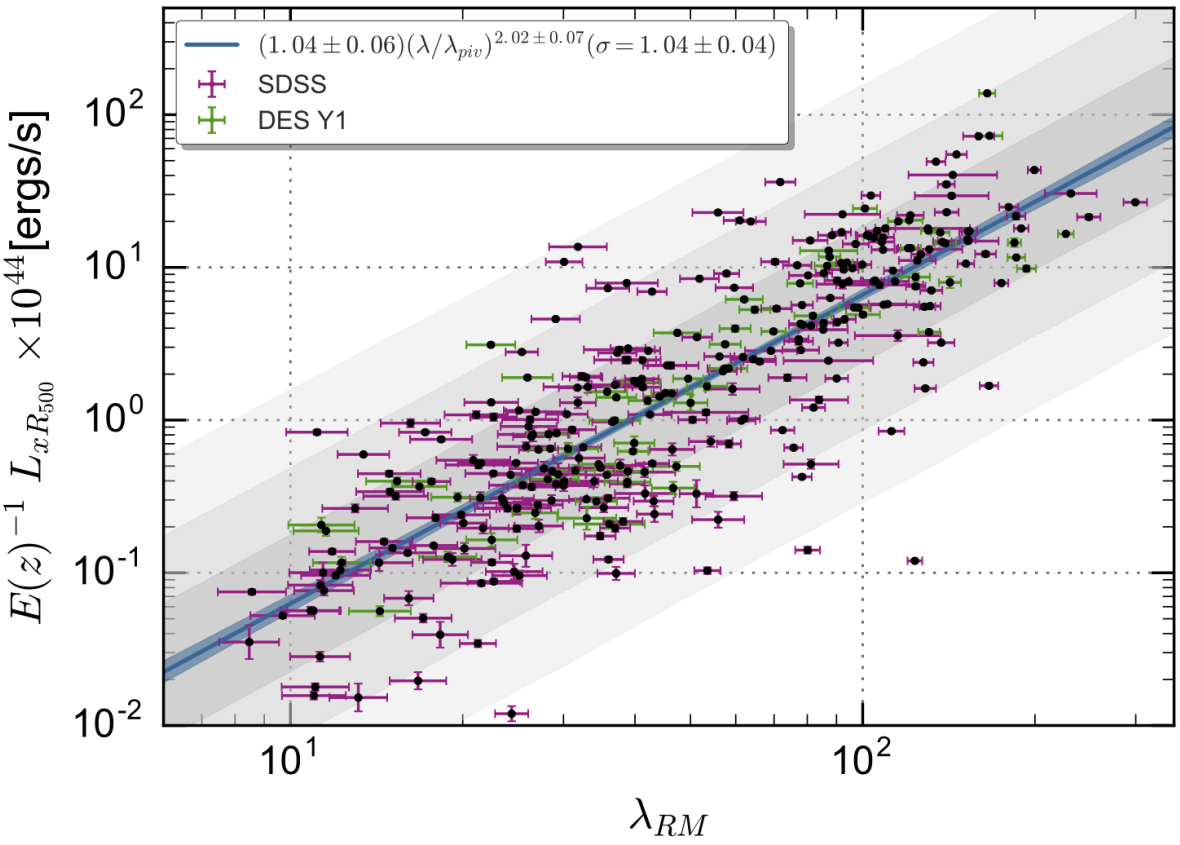

Figure 5.35: Optical to X-ray scaling relation between optical richness (λ) and Bolometric luminosity ($L_{\rm X}$) for the XCS-RM (SDSS+DES Y1) sample.

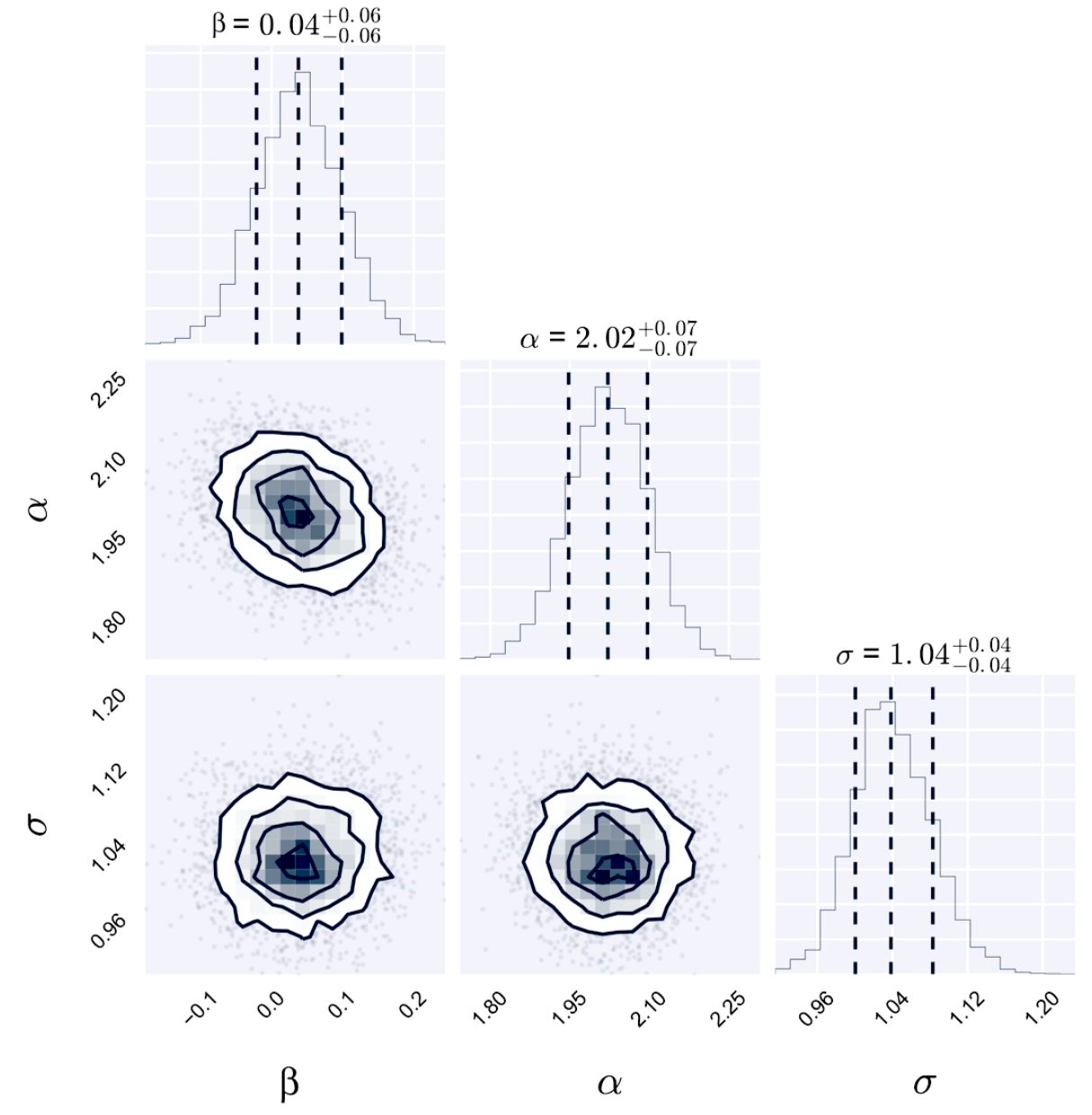

Figure 5.36: Triangle plot of the free parameters of Equation 5.16) for $L_X - \lambda$ scaling relation, using data from the XCS-RM (SDSS+DES Y1) sample.

5.5.4 Outlier Analysis

In Figure 5.37 three clusters have been highlighted. These three lie more than 2σ from the best fit $L_X - \lambda$ scaling relation to the joint (SDSS+DES-Y1) XCS-RM sample. Two of these clusters are also outliers from the $T_X - \lambda$ scaling relation and already discussed in Section 5.4.4: XMMXCS J004630.7+202803.6 (Section 5.4.4), which has a measured $L_X = 0.12 \times 10^{44}$ [ergs/s], which is much smaller than the predicted value of $L_X \simeq 11.48 \times 10^{44}$; XMMXCS J120352.5+014730.0 has a measured $L_X = 0.15 \times 10^{44}$ [ergs/s], which is much smaller than the predicted value of $L_X \simeq 4.23 \times 10^{44}$ [ergs/s]. The third L_X outlier is described below.

XMMXCS J080712.4+152658.7

This ($z = 0.09$) cluster has a measured bolometric luminosity of $L_X = 0.01 \times 10^{44}$ ergs/s, and a richness of $\lambda = 24.35$. From Equation 5.22, the predicted luminosity is $L_X = 1.54 \times 10^{44}$ ergs/s. Figure 5.38 shows the optical and X-ray observations of this cluster, the SDSS observation is overlaid with the XMM X-ray contours. Both observations are centred on the XCS position.

Figure 5.38.a shows that the XCS cluster is close to the edge of the XMM field of view, its centre is covered only by the EPIC-MOS1 and EPIC-MOS2. Even when combined MOS images are less sensitive than a single PN image (Section 1.6.1). Looking at the exposure maps for the MOS cameras, the effective exposure has it lowest at the edge of the observation. Figure 5.38.b illustrates several galaxies concentrated on the RM centre. I conclude that this is a genuine physical system, with associated galaxies and intracluster medium. Based on the existing XMM data, this system is under luminous for the corresponding richness. That said, it would be worth obtaining an on-axis re-observation to get a more precise estimate of the luminosity. It is also worth mentioning that this cluster is outside the range of redshift that the RM team claims is reliable for their SDSS clusters ($0.1 \leq z \leq 0.3$, see Section).

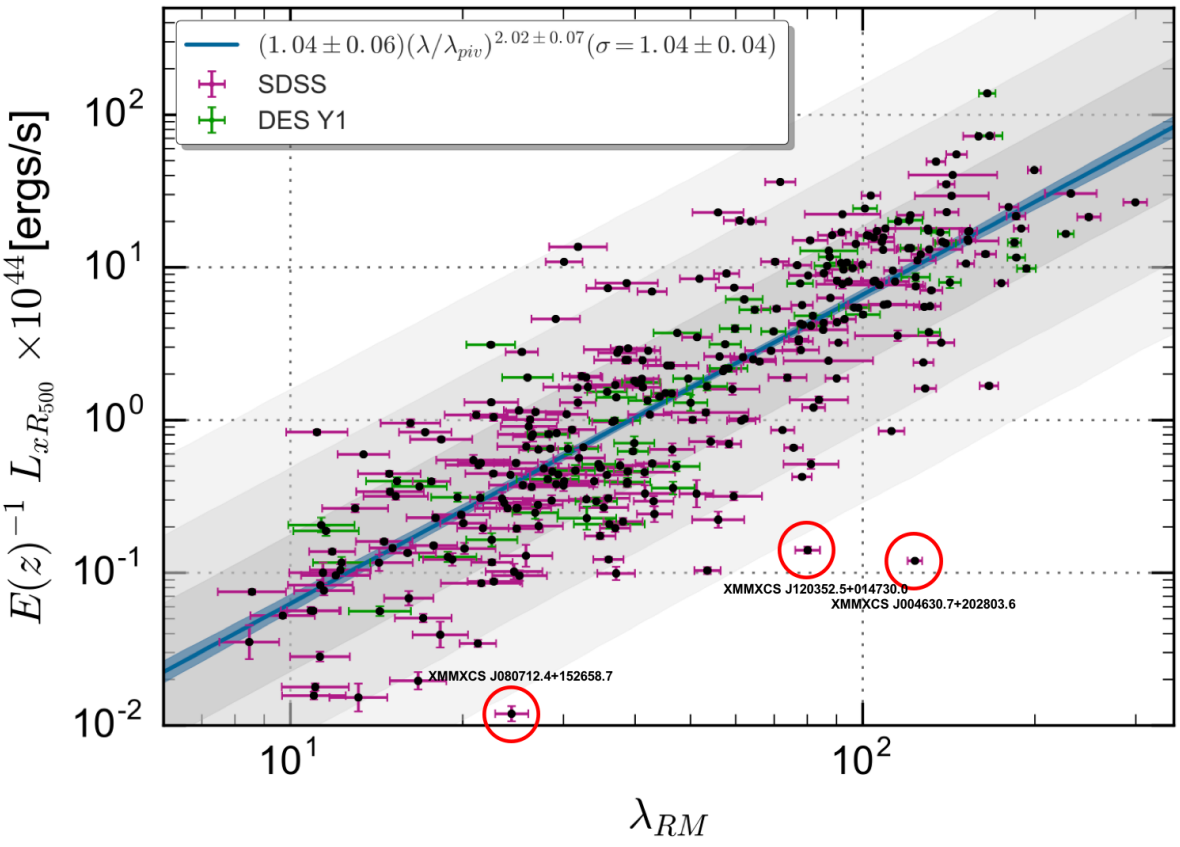

Figure 5.37: As Figure 5.35, but with $> 2\sigma$ outliers circled and annotated.

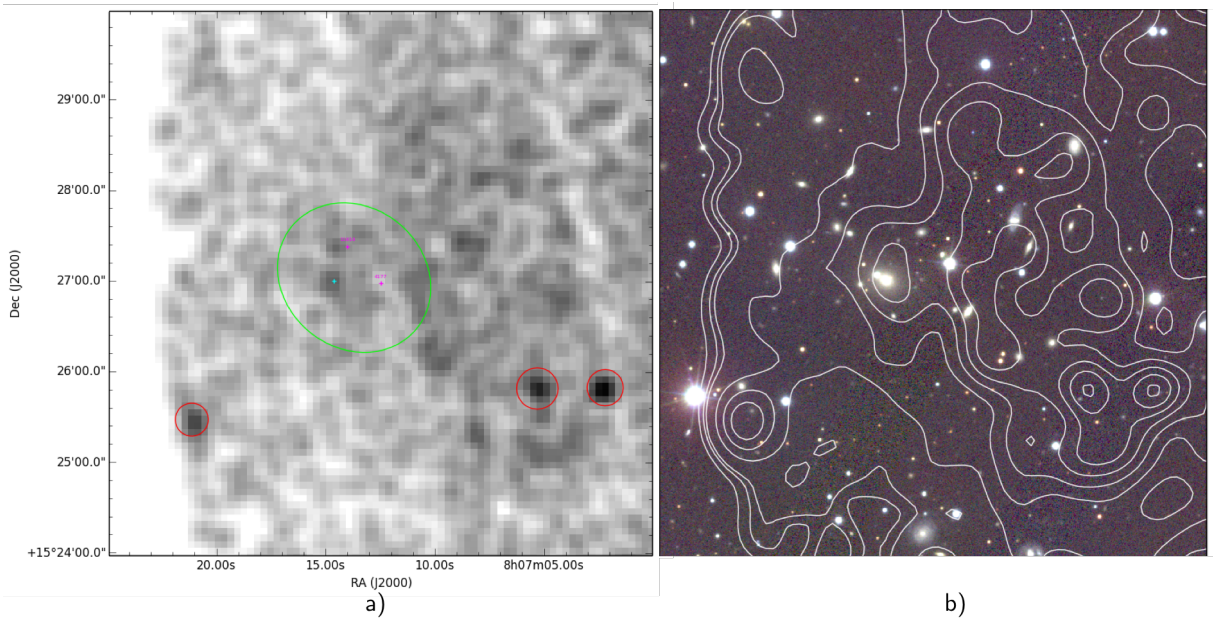

Figure 5.38: Cluster XMMXCS J080712.4+152658.7: (a) XMM-Newton observation centred on the XCS position, green ellipse represents the XCS cluster, cyan circle is RM cluster, small red circles are point sources. (b) Optical observation from SDSS with X-ray contours information from XMM.

5.5.5 Comparison to previous analyses

Rykoff et al., 2008 (ER08) studied the $L_X - N_{200}$ relation (N_{200} is the optical richness calculated over a radius of R_{200}). Using optical data from SDSS DR5, clusters are found using the maxBCG algorithm (Koester et al., 2007), similar to the redMaPPer algorithm, maxBCG finds clusters as red sequence overdensities. For each cluster the brightest cluster galaxy (BCG) is defined and a richness estimation is done over a radius of R_{200} to which the mass density is 200 times the critical density (ρ_c see Section 1.2), the centre for each cluster is defines as the location of the BCG. The public maxBCG catalog contains a total of 13 823 clusters from 7500 deg^2 covering a redshift range of $0.1 < z < 0.3$.

X-ray data consist of four sub catalogs made from the ROSAT All-Sky Survey (Voges et al., 1999): The ROSAT Bright Source Catalog (BSC) containing 18 811 sources with typical signal-to-noise ratio > 4, also the Faint Source Catalog (FSC) is considered, it contains 105 924 sources with typical signal-to-noise ratio > 2. The Northern ROSAT All-Sky galaxy cluster survey (Bohringer et al., 2000) is a catalog with 378 extended X-ray sources that have confirmed to be clusters via optical follow-up. Finally, the ROSAT-ESO Flux-Limited X-ray galaxy cluster survey (REFLEX, Böhringer, Schuecker and Guzzo, 2004) has 447 clusters, although only a small fraction ovelaps the max BGC survey area.

Optical and X-ray observables were obtained from a stacking clusters into nine richness (N_{200}) bins. ER08 calculate the $L_X - N_{200}$ from X-ray luminosity in the $0.1-2.4$ keV band and richness estimation over R_{200} and a fixed radius of 750 h^{-1}kpc both centred in the BGC position. Figure 5.39 (top) shows the mean $\bar{L}_X - \bar{N}_{200}$ relation for both apertures. The best-fit equation for the mean $\bar{L}_X - \bar{N}_{200}$ relation is

$$\bar{L}_X = e^{3.87\pm0.04}\left(\frac{\bar{N}_{200}}{40}\right)^{1.82\pm0.05} \times 10^{42} h^{-2} \text{ergs s}^{-1}, \tag{5.23}$$

To characterize the intrinsic scatter in the $L_X - N_{200}$ relation, ER08 found the relation using individual clusters, they considered a sample of the 955 richest clusters with $N_{200} \geq 30$. The best fit relation is:

$$L_X = e^{3.40\pm0.04}\left(\frac{N_{200}}{40}\right)^{1.61\pm0.13} \times 10^{42} h^{-2} \text{ergs s}^{-1}, \tag{5.24}$$

The resulting intrinsic scatter is $\sigma_{\ln L} = 0.86 \pm 0.03$.

No direct comparison can be made with the results from ER08 and the $L_X - \lambda$ relation obtained in this thesis due to the following reasons:

- ER08 reports X-ray luminosity on the $1.0-2.4$ keV while the XCS-RM (SDSS+DES Y1) considers bolometric luminosity.

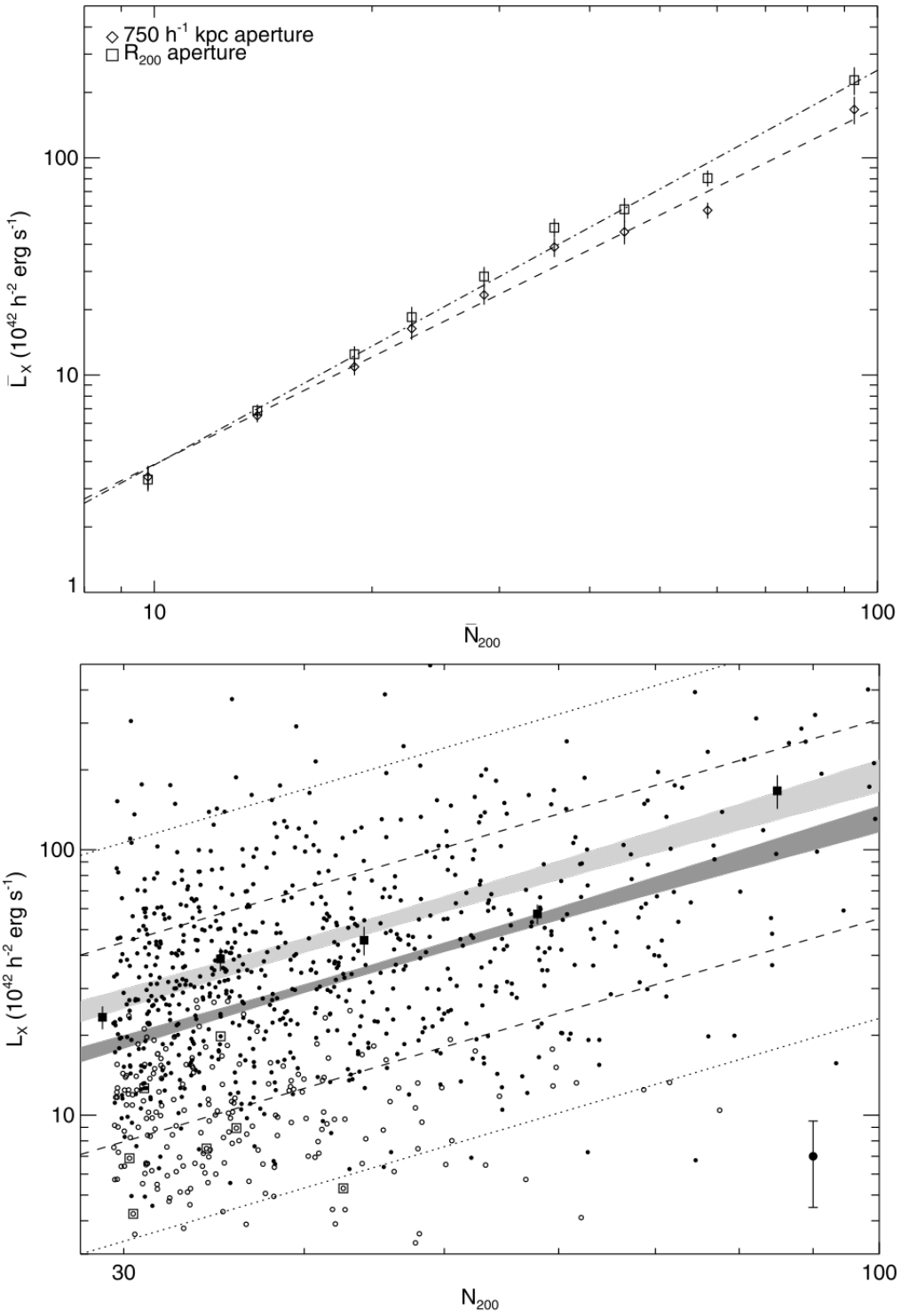

Figure 5.39: Figure taken from **2008** Top: mean $\bar{L}_{\rm X} - \bar{N}_{200}$ for the fixed 750 h^{-1}kpc apertures (diamonts) ans the scaled R_{200} apertures (squares). The best-fit scaling relation is plotted for each sample. Below: $L_{\rm X} - N_{200}$ for individual clusters with $N_{200} \geq 30$, the filled circles represent detections at the 1σ level, and open circles represent 1σ upper limits. Contours showing the $\pm 1\sigma$ on the best-fit median relation are shown in dark gray.

- ER08 uses the maxBGC algorithm to calculate richness inside a fixed radius (750 h^{-1}kpc) and within R_{200}. XCS-RM (SDSS+DES Y1) takes the richness estimation from redMaPPer which is estimated over R_λ (defined in equation 2.3, see Section 2.2.1) which is not necessarily equal to R_{200}.

- ER08 do not report the properties of the individual clusters.

However, it is possible to compare the intrinsic scatter from ER08 ($_{\ln L} = 0.86 \pm 0.03$) with the scatter from the $L_X - \lambda$ relation for the XCS-RM (SDSS+DES Y1) sample ($\sigma = 1.04 \pm 0.04$). Also, we noticed that the slope found in equation 5.22 is consistent with the ER08 results for the stacked analysis (equation 5.23).

5.6 The XCS-RM $T_X - L_X$ Scaling Relation

5.6.1 Input Data

The data used to obtain the $T_X - L_X$ scaling relation is as described in Section 5.3. It consists of XCS clusters in the RM-SDSS sample (261 clusters), the RM-DESY1 (77 clusters) and the joined sample SDSS+DES Y1 (327 clusters).

5.6.2 Fitting Method

The fitting model is similar to the one described in Equation 5.6, where the two variables are the X-ray temperature (T_X) and the bolometric luminosity (L_X). With these variables, the model has the form:

$$\ln L_X = \beta + \alpha \ln\left(\frac{T_X}{T_0}\right), \tag{5.25}$$

where $T_0 = 5$ keV is the pivot value of the temperature, α and β are the free parameters of the model.

5.6.3 Results

Using an MCMC orthogonal fitting (see Section 4.4.2) the free parameters are constrained. For the XCS-RM (SDSS) sample the $T_X - L_X$ relation is:

$$\ln\left(E(z)^{-1}L_X\right) = (0.697 \pm 0.03) + (3.58 \pm 0.1)\ln\left(\frac{T_X}{5\text{ keV}}\right). \tag{5.26}$$

From the XCS-RM (DES Y1) sample, the scaling relation has the form:

$$\ln\left(E(z)^{-1}L_X\right) = (0.723 \pm 0.04) + (3.69 \pm 0.2)\ln\left(\frac{T_X}{5\text{ keV}}\right). \tag{5.27}$$

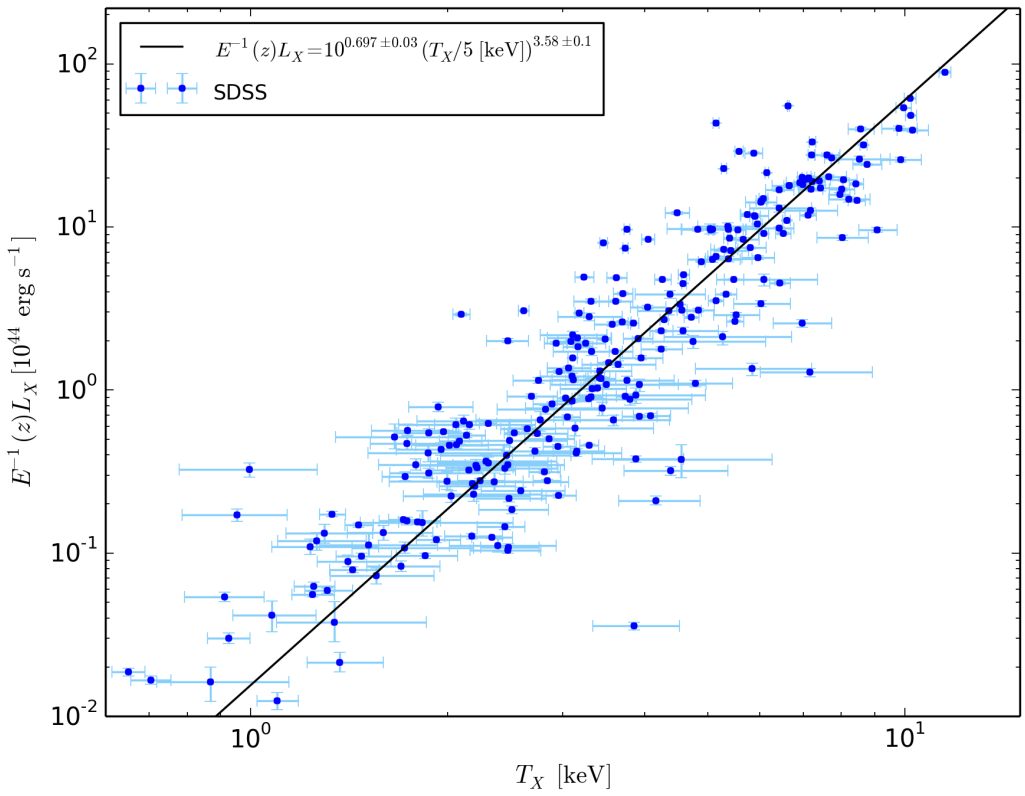

Figure 5.40: $T_{\rm X} - L_{\rm X}$ scaling relation for the XCS-RM (SDSS) sample.

Finally, from the XCS-RM (SDSS+DES Y1) joined sample, the resulting scaling relation is

$$\ln\left(E(z)^{-1}L_{\rm X}\right) = (0.702 \pm 0.02) + (3.59 \pm 0.1)\ln\left(\frac{T_{\rm X}}{5\ \mathrm{keV}}\right). \tag{5.28}$$

Figures 5.40, 5.41 and 5.42 show the data of the mentioned samples along with the scaling relation.

An overview of the results for this scaling relation is given in Table (5.9).

Sample	α	β	σ
SDSS Dr8	3.58 ± 0.1	0.697 ± 0.03	0.327 ± 0.01
DES Y1	3.69 ± 0.2	0.723 ± 0.04	0.252 ± 0.01
SDSS+DES Y1	3.59 ± 0.1	0.702 ± 0.02	0.314 ± 0.01

Table 5.9: Fitting results of the $T_{\rm X} - L_{\rm x}$ scaling relation. The model assumed has the form $\ln L_{\rm x} = \beta + \alpha \ln(T_{\rm X}/T_0)$ where $T_0 = 5$ keV for all the samples.

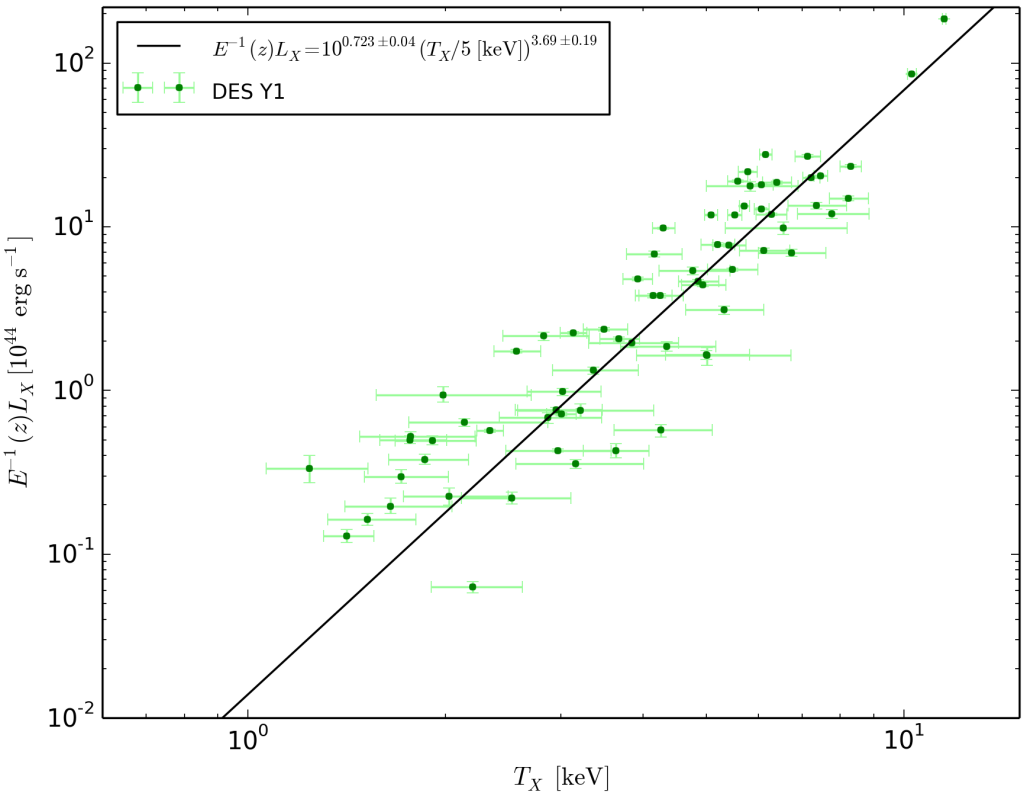

Figure 5.41: $T_{\rm X} - L_{\rm X}$ scaling relation for the XCS-RM (DES Y1) sample.

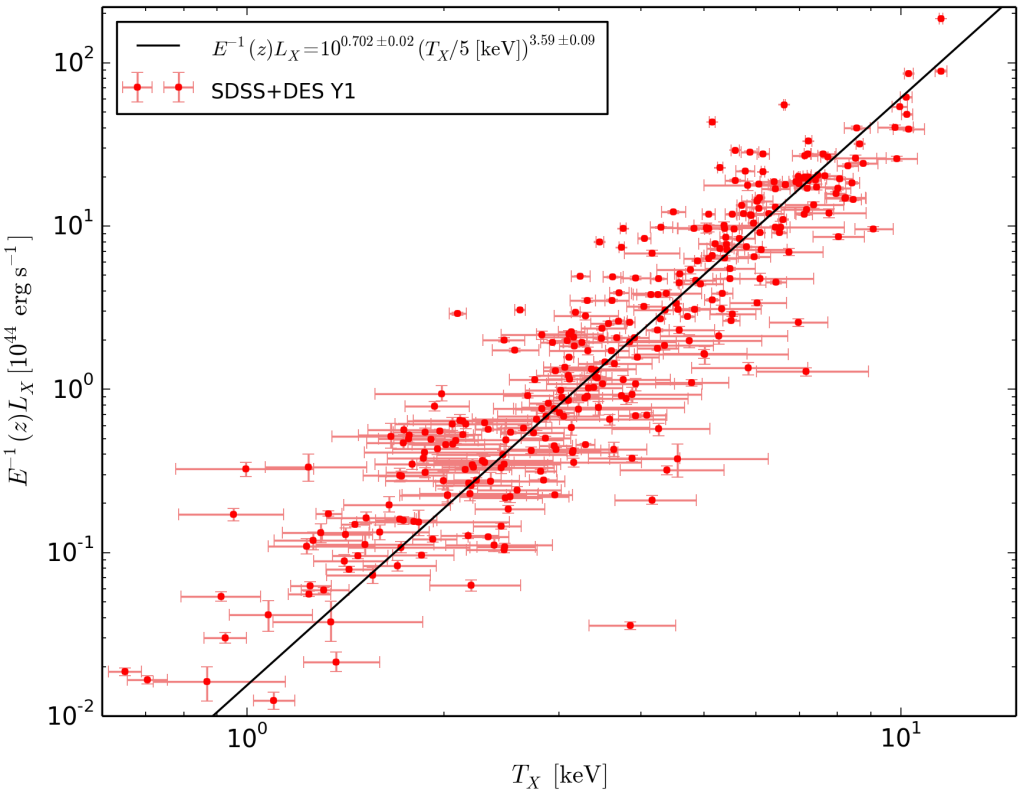

Figure 5.42: $T_{\rm X} - L_{\rm X}$ scaling relation for the XCS-RM (SDSS+DES Y1) sample.

5.7 Conclusions and Future Work

5.7.1 Conclusions

The work presented here represents the most comprehensive examination of the $T_X - \lambda$ and $L_X - \lambda$ relations for optical clusters to date. Three samples have been tested (SDSS, DES, and SDSS+DES) - a total of 327 unique clusters. The slopes and normalisations are consistent between the samples, with the most precise parameter fits coming from the largest sample. Compared to previously published work (Rykoff et al., 2016), the scatter on the relation is lower. This can be interpreted as being due to having access to larger samples of clusters and improved X-ray analysies (XCS3P-v3).

The work presented here demonstrates that there is a strong correlation between the X-ray and optical properties of RM selected clusters. The X-ray properties can be traced to the underlying mass of the cluster using analytical and numerical methods. My work confirms that it is possible to connect the optical properties to the underlying mass. In turn this then supports the premise that catalogues of optically selected clusters to be used to measure cosmological parameters. As expected, there is more scatter in the L_X -λ relation compared to T_X -λ .

Additional results in this chapter include the demonstration that it is possible to combine RM samples generated from different photometric datasets, although it is important to make cuts on richness error information when defining RM-XCS samples.

An investigation into clusters that lie more than 2σ from the best fit T_X and L_X to richness scaling relations has led to two conclusions: first that there are very few outliers (no more than expected from Gaussian statistics), and second that a majority (three of 5 checked) are due intrinsic scatter, rather than to issues with the data inputs.

5.7.2 Future Work

The XCS team plan to add more RM clusters to the L_X -λ analysis, by included those that have significant XAPA detections, but not sufficient counts for a T_X measurement. This extension will double the number of clusters in the test, and compensate somewhat for the intrinsic scatter. It will also demonstrate the value (or otherwise) of adding e-ROSITA[4] data to the DES-cluster cosmology analysis. The "L_X -only" clusters will also be used to improve understanding in the RM centroid offset distribution (as it is not necessary to

[4]e-ROSITA is an X-ray survey telescope due for launch in 2018. It will generate tens of thousands of cluster detections (and hence L_X values), but comparitively (to XCS) few T_X measurements.

have a $T_{\rm X}$ value to measure a centroid offset). Other planned work includes a synthesis of the XCS-RM work with the Chandra-RM work being carried out at UCSC.

Chapter 6

Additional Contributions

6.1 Overview

Motivation The overall motivation for the work presented in this chapter is to provide validation of the techniques used to derive the optical to X-ray scaling relations from the marriage of RM and XCS.

In order to validate the methodology used in Chapter 5, we have generated optical-to-X-ray scaling relations for two non-redMaPPer cluster catalogues. Both were derived from the SDSS photometric survey: CAMIRA (Oguri, 2014), and GMBCG (Hao et al., 2010). The methodology of the former catalogue will be applied to the HSC (Hyper Suprime Camera) Survey (Takada, 2010) and so, in future, will rival RM as a mechanism to derive cosmological parameters. The methodology of the latter catalogue was a precursor of RM, and the analysis presented here in allows us to make an objective analysis of the improvements (if any) in the change from GMBCG to RM.

In order to validate the methodology used in Chapter 4, we have generated microwave-to-X-ray scaling relations for two Sunyaev-Zeldovich (SZ) effect (Section 1.1.1) cluster catalogues. One was derived from ground based observations by the South Pole Telescope (SPT-SZ 2500d, Bleem et al., 2015) and one from space-based observations by the Planck satellite (Planck Collaboration et al., 2013). These two samples have the advantage over RM of being selected through a criterion (scattering of cosmic microwave background photons) that is more directly related to dark matter halo mass than galaxy richness. Moreover, all clusters in the SZ selected samples have been confirmed as being genuine physical systems (whereas some of the RM "clusters" will be due to projection effects). A strong, low scatter, correlation between XCS3P-v3 parameters and SZ signal will demonstrate that our post processing techniques are valid.

Governing Assumptions

1. The redshift estimates published in the four catalogues tested were correct.

2. The techniques developed earlier (and relevant governing assumptions) in this thesis for application to RM cluster samples are applicable to other optically selected cluster samples.

3. The quality of optically selected cluster samples varies, either because of the quality (and/or sensitivity) of the underlying photometry (and/or spectral training sets) or because of the selection technique.

4. Clusters in SZ selected catalogues are both genuine physical systems and not subject to the same centering issues as optically selected clusters.

5. It is possible to improve the precision of cosmological constraints derived from optical cluster samples by combining scaling relations derived from several observing techniques/wavebands.

Methodology

Matches between published cluster catalogues to XCS extended sources were carried out using the techniques described in Chapter 3. The $T_{\rm X}$ and $L_{\rm X}$ values were then calculated using XCS3P-v3 (Chapter 4). Automated filters were applied to clean the matched samples: the coefficient of variation filter described in Section 4.3.2, plus a filter on the relative $T_{\rm X}$ error of 15% (Section 5.2.1). Next, scaling relations were determined using the techniques described in Section 4.4.2.

Results From the optical catalogs (CAMIRA and GMBCG) the scaling relations $T_{\rm X}$ - λ and $L_{\rm X}$ -λ were obtained.

From the SZ catalogs (SPT and Planck) the scaling relation $T_{\rm X} - M_{SZ}$ and $L_{\rm X} - M_{SZ}$ were obtained.

Conclusions and Future Work

Future work will include a re-analysis of the scaling relations presented herein using the fitting approach used in Chapter 5, so that it will be possible to do a proper like for like comparison. The aim is to be able to quantify the quality of a given input catalogue without the requirement for painstaking eye-ball checks of the X-ray and/or optical images. Quantitative indicators of quality could include: centroid offset distribution; the number of outliers from the scaling relation; the robustness of fits to changing relative error filters; the number of X-ray under-luminous (and hence possible phantom projection effect) systems.

6.2 CAMIRA

6.2.1 CAMIRA: Catalog Description

CAMIRA is cluster catalog made by an algorithm based on stellar population synthesis models to predict colours of red sequence galaxies (Oguri, 2014). The algorithm was applied to 11960deg^2 of optical observations from the Sloan Digital Sky Survey (SDSS) Data Release 8. It has also been applied to early Hyper Supreme Camera (HSC) data (Takada, 2010), although the corresponding cluster catalogue had not been made public at the time of writing. CAMIRA spans a redshift range of $0.1 < z < 0.6$. The catalog has a total of 71 743 clusters.

There are 1 079 CAMIRA clusters overlapping with XMM-Newton observations. Of these, 526 are within 1.5 h^{-1} Mpc of an XCS extended source. These 526 matches were then passed to XCS3P-v3, so that $T_{\rm X}$ and $L_{\rm X}$ values could be obtained.

XCS3P-v3 converged for 463 of the 526 clusters, but only 306 of them had associated relative $T_{\rm X}$ errors of $< 30\%$. There are no errors reported on the CAMIRA richness, so it was not possible to apply an additional filter on richness error (as was done for RM clusters, Section 5.2.1.

6.2.2 CAMIRA: Optical to X-ray Scaling Relations

The model used to fit the $T_{\rm X}$-λ scaling relation is:

$$\log\left(\frac{T_{\rm X}}{T_0}\right) = A + B\log\left(\frac{\lambda}{\lambda_0}\right), \tag{6.1}$$

where T_0 and λ_0 are pivot values, λ is the richness defined by CAMIRA. This model is fit using MCMC techniques to find the free parameters A and B.

From the MCMC fit, the scaling relation is:

$$\log\left(\frac{T_{\rm X}}{T_0}\right) = (-0.06 \pm 0.01) + (1.20 \pm 0.04)\log\left(\frac{\lambda}{\lambda_0}\right), \tag{6.2}$$

where $T_0 = 3.5$ keV, $\lambda_0 = 37$. Figure 6.1 shows the data and the $T_{\rm X} - \lambda$ scaling relation.

Similar to Equation 6.1, the model used to fit the $L_{\rm X}$-λ scaling relation is:

$$\log\left(\frac{L_{\rm X}}{L_0}\right) = A + B\log\left(\frac{\lambda}{\lambda_0}\right), \tag{6.3}$$

L_0 and λ_0 are pivot values.

Figure 6.2 shows the data and the best fit scaling relation, which has the form:

$$\log\left(\frac{L_{\rm X}}{L_0}\right) = (-0.12 \pm 0.03) + (2.98 \pm 0.04)\log\left(\frac{\lambda}{\lambda_0}\right), \tag{6.4}$$

where $L_0 = 1.5 \times 10^{44}$ ergs/s and $\lambda_0 = 37$.

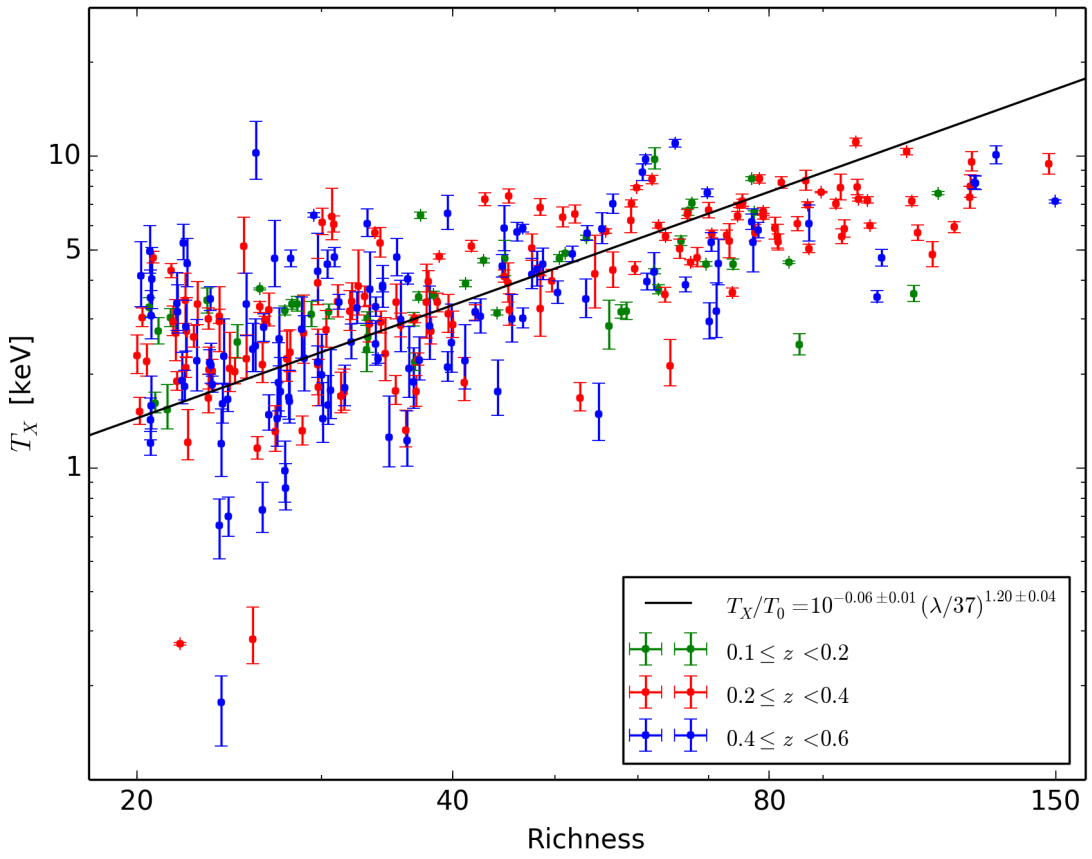

Figure 6.1: T_X-λ Scaling Relation from XCS and CAMIRA, straight line indicates the MCMC fit of equation 6.1.

6.3 GMBCG

6.3.1 GMBCG: Catalog Description

This catalog is produced applying the Gaussian Mixture Brightest Cluster Galaxy (GMBGC) algorithm to SDSS DR7 data (Hao et al., 2010). This algorithm finds galaxy clusters by identifying the red sequence and the Brightest Cluster Galaxy (BCG) which is only present on galaxy clusters. GMBGC was run on 8 240 deg^2 finding clusters over a redshift range of $0.1 < z < 0.55$. The catalog has a total of 55 424 clusters.

There are 1 108 GMBCG clusters overlapping with XMM-Newton observations. Of these, 350 are within 1.5 h^{-1}Mpc of an XCS extended source. These 350 matches were then passed to XCS3P-v3, so that T_X and L_X values could be obtained. XCS3P-v3 converged for 304 of the 350 clusters, but only 222 of them had associated T_X errors of $< 30\%$. Similarly to CAMIRA, no errors are reported on the richness, so the cross matched sample

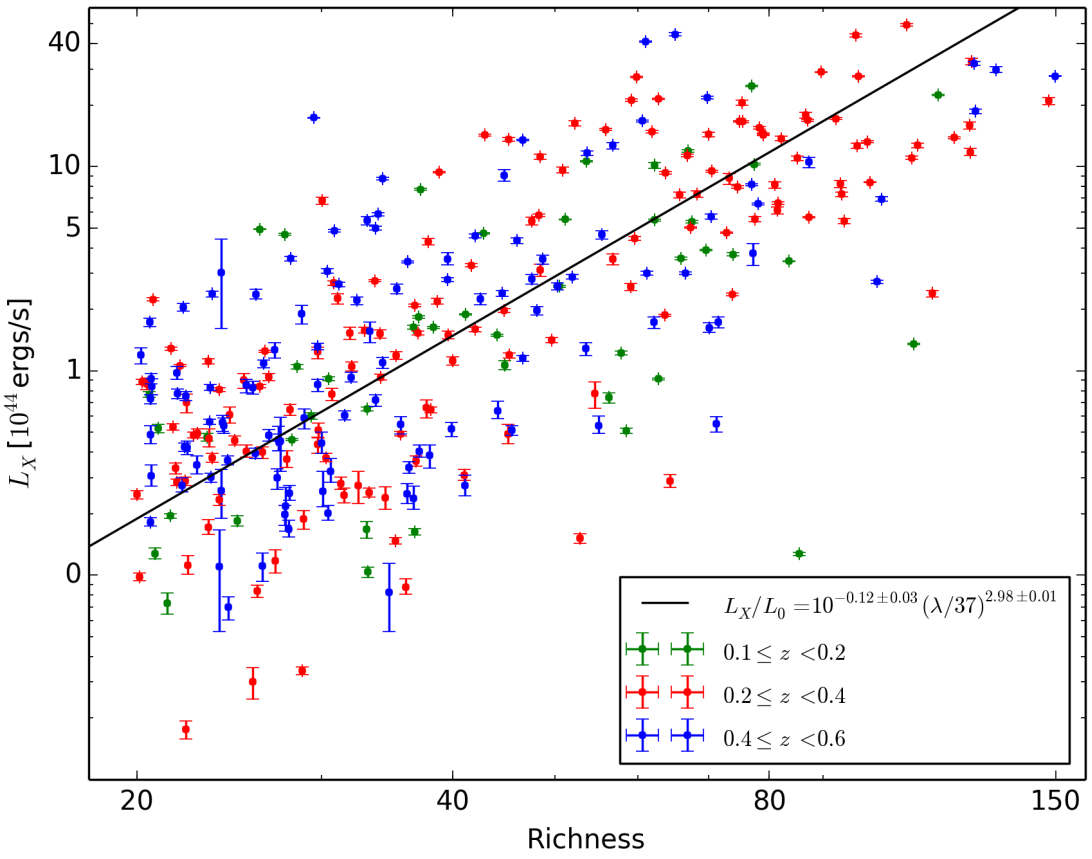

Figure 6.2: L_X-λ Scaling Relation from XCS and CAMIRA, straight line indicates the MCMC fit of equation 6.3.

could not be filtered on richness error.

6.3.2 GMBCG: Optical to X-ray Scaling Relations

The model used to fit the T_X-λ scaling relation is given in Equation 6.1. From the MCMC fit, the scaling relation is:

$$\log\left(\frac{T_X}{T_0}\right) = (-0.56 \pm 0.02) + (0.79 \pm 0.06)\log\left(\frac{\lambda}{\lambda_0}\right), \tag{6.5}$$

where $T_0 = 1$ keV and $\lambda_0 = 30$.

Figure 6.3 shows the data and the T_X -λ scaling relation.

The model used to fit the L_X-λ is given by Equation 5.16. Figure 6.4 shows the data and the best fit scaling, which has the form:

$$\log\left(\frac{L_X}{L_0}\right) = (0.28 \pm 0.03) + (2.53 \pm 0.09)\log\left(\frac{\lambda}{\lambda_0}\right), \tag{6.6}$$

where $L_0 = 1 \times 10^{44}$ergs/s and $\lambda_0 = 30$.

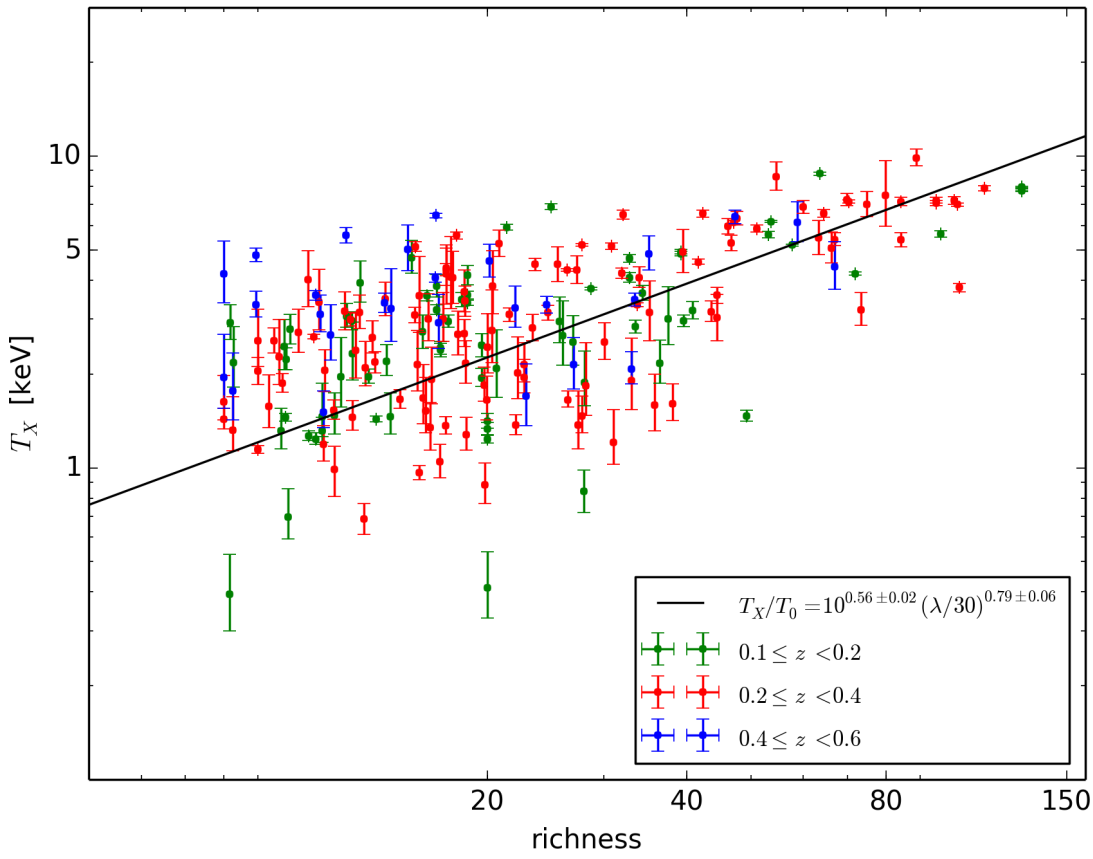

Figure 6.3: T_X-λ Scaling Relation from XCS and GMBCG, straight line indicates the MCMC fit of equation 6.1.

6.4 South Pole Telescope

6.4.1 SPT: Catalog Description

The 2500 deg^2 South Pole Telescope (SPT)-SZ survey (Bleem et al., 2015) contains 677 clusters spanning a redshift range of $0.05 < z < 1.7$. Of these, 73 clusters overlap with XMM-Newton observations, all of which lie within 1.5 h^{-1}Mpc of an XCS extended source. XCS3P-v3 yielded T_X values with relative errors of less than $< 30\%$ for all 73.

6.4.2 SPT: SZ to X-ray Scaling Relations

SPT provides a mass estimation M_{500} obtained from the SZ signal, in a R_{500} aperture. We use this quantity when fitting to the model:

$$\log\left(\frac{T_X}{T_0}\right) = A + B\log\left(\frac{M_{500}}{M_0}\right), \tag{6.7}$$

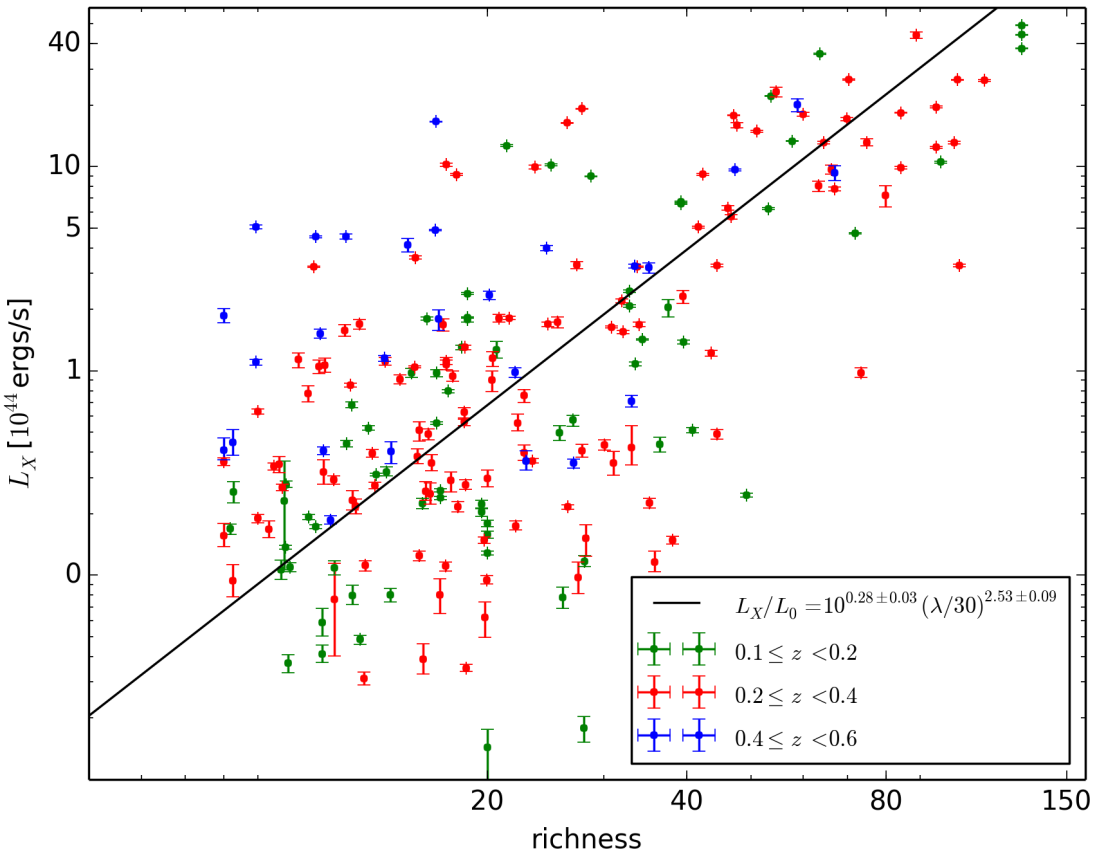

Figure 6.4: $L_{\rm X}$-λ Scaling Relation from XCS and GMBCG, straight line indicates the MCMC fit of equation 6.3.

where A and B are free parameters. From the MCMC fit, the scaling relation is:

$$\log\left(\frac{T_{\rm X}}{T_0}\right) = (0.72 \pm 0.01) + (0.53 \pm 0.05)\log\left(\frac{M_{500}}{M_0}\right), \tag{6.8}$$

where $T_0 = 1$keV and $M_0 = 5 \times 10^{14} M_\odot$ (Figure 6.5).

The model used to fit the $L_{\rm X} - M_{500}$ relation is:

$$\log\left(\frac{L_{\rm X}}{L_0}\right) = A + B\log\left(\frac{M_{500}}{M_0}\right). \tag{6.9}$$

Figure 6.6 shows the data and the best fit relation, which has the form:

$$\log\left(\frac{L_{\rm X}}{L_0}\right) = (0.76 \pm 0.04) + (2.49 \pm 0.22)\log\left(\frac{M_{500}}{M_0}\right), \tag{6.10}$$

where $L_0 = 1 \times 10^{44}$ergs/s and $M_0 = 5 \times 10^{14} M_\odot$.

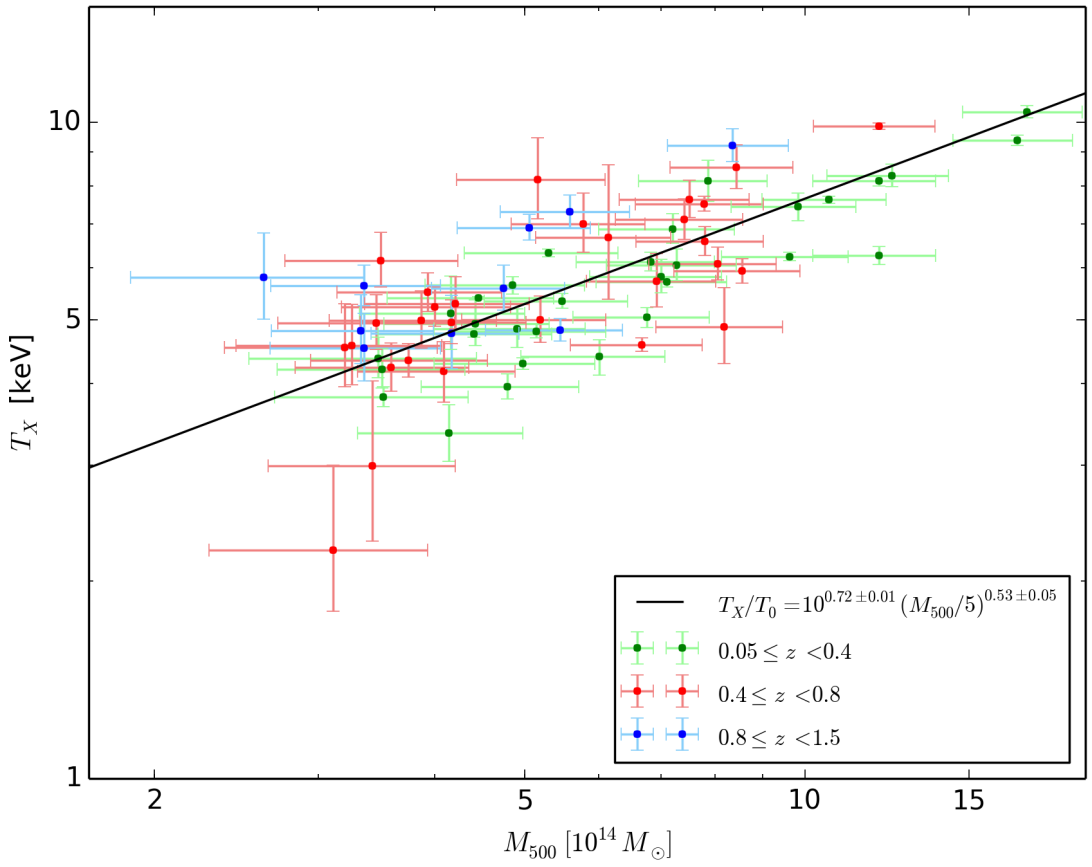

Figure 6.5: T_X-λ Scaling Relation from XCS and SPT, straight line indicates the MCMC fit of equation 6.7.

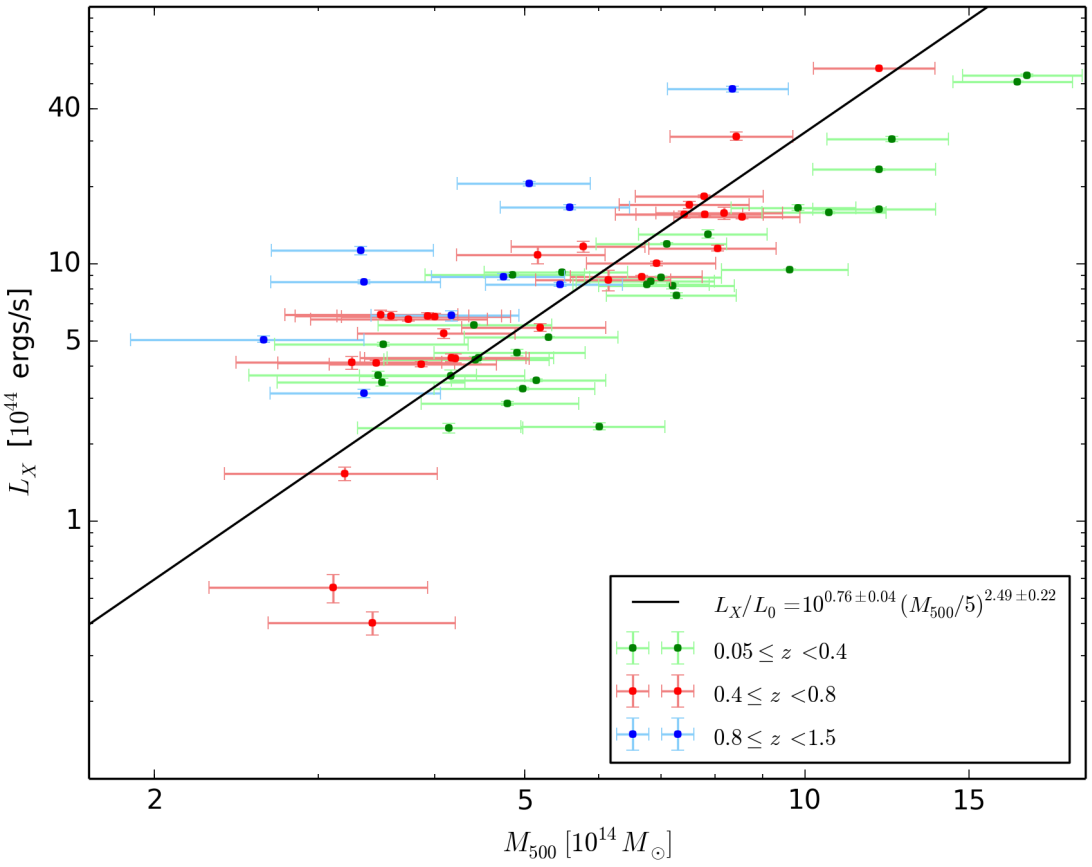

Figure 6.6: L_X-λ Scaling Relation from XCS and SPT, straight line indicates the MCMC fit of equation 6.9.

6.5 Planck

6.5.1 Planck: Catalog Description

The all-sky Planck catalog (Planck Collaboration et al., 2013) contains 1 653 of clusters and cluster candidates spanning a redshift range of $0.01 < z < 0.97$. Only 66% (1 094) of the clusters are accompanied by redshift information. Of those 1 094 clusters, 380 are inside XMM-Newton observations. Of those, 344 clusters are within 1.5 h^{-1}Mpc of an XCS extended source. All 344 were passed to XCS3P-v3, resulting in $T_{\rm X}$ values with relative errors of less than $< 30\%$ for 314.

6.5.2 Planck: SZ to X-ray Scaling Relations

Planck provides a mass estimation $M_{\rm SZ}$ which assumes hydrostatic equilibrium and uses the best-fit $Y - M$ scaling relation of Arnaud et al., 2010 as a prior. Not included in the $M_{\rm SZ}$ uncertainties are the statistical errors on the scaling relation, the intrinsic scatter in the $Y - M$ relation, or systematic errors in data selection for the $Y - M$ scaling relation fit (Planck Collaboration et al., 2013).

The model used to fit the $T_{\rm X} - M_{SZ}$ scaling relation is given in Equation 6.7. From the MCMC fit, the scaling relation is (Figure 6.7):

$$\log\left(\frac{T_{\rm X}}{T_0}\right) = (0.77 \pm 0.01) + (0.62 \pm 0.02)\log\left(\frac{M_{SZ}}{M_0}\right), \tag{6.11}$$

where $T_0 = 1$keV and $M_{SZ} = 5.0 \times 10^{14} M_{\odot}$.

The model used to fit the $L_{\rm X} - M_{SZ}$ relation is given by Equation 6.9. Figure 6.8 shows the data and the best fit relation, which has the form:

$$\log\left(\frac{L_{\rm X}}{L_0}\right) = (0.04 \pm 0.02) + (2.93 \pm 0.05)\log\left(\frac{M_{500}}{M_0}\right), \tag{6.12}$$

where $L_0 = 7.8 \times 10^{44}$ergs/s and $M_0 = 5.6 \times 10^{14} M_{\odot}$.

6.5.3 Planck and SPT Discussion

The SZ to X-ray scaling relations for Planck appear to have lower scatter than for SPT, but this is only a qualitative interpretation and might only be due to the fact that the Planck sample contains 4 times more clusters. Bootstrapping a similar (to SPT) sized sample would provide a fairer comparison. That said, there are some significant outliers in the Planck case, and these are worthy of individual investigation to determine if these correspond to issues with the XMM data (or if there are problems with the Planck identifications and/or masses).

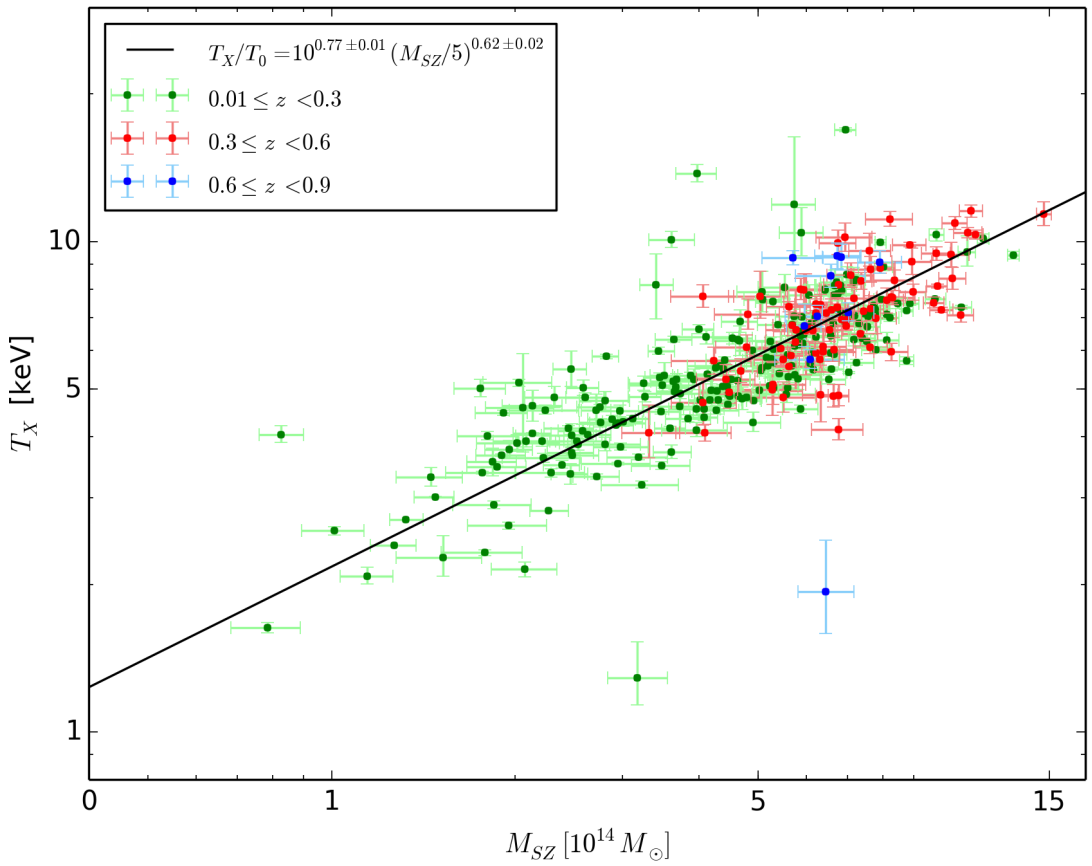

Figure 6.7: T_X-λ Scaling Relation from XCS and Planck, straight line indicates the MCMC fit of equation 6.7.

For both SZ samples, we have carried out tests like those in Section 5.2.1 to see if the scaling relation fits are dependent on the limits set on relative error (in either mass or T_X). Unlike the XCS-RM (SDSS DR8) case, but similar to the XCS-RM (DES Y1) case (Figure 5.4), changes in the relative error filter did not impact the scaling relations. This suggests that the errors on the mass are well determined.

6.6 Conclusions and Future Work

6.6.1 Conclusions

- The XCS3P-v3 methodology described in this work (see Chapter 4) has been tested on cluster catalogs different from redMaPPer.
- The resulting scaling relations between observables are acceptable and they describe a clear correlation between mass proxy observables.

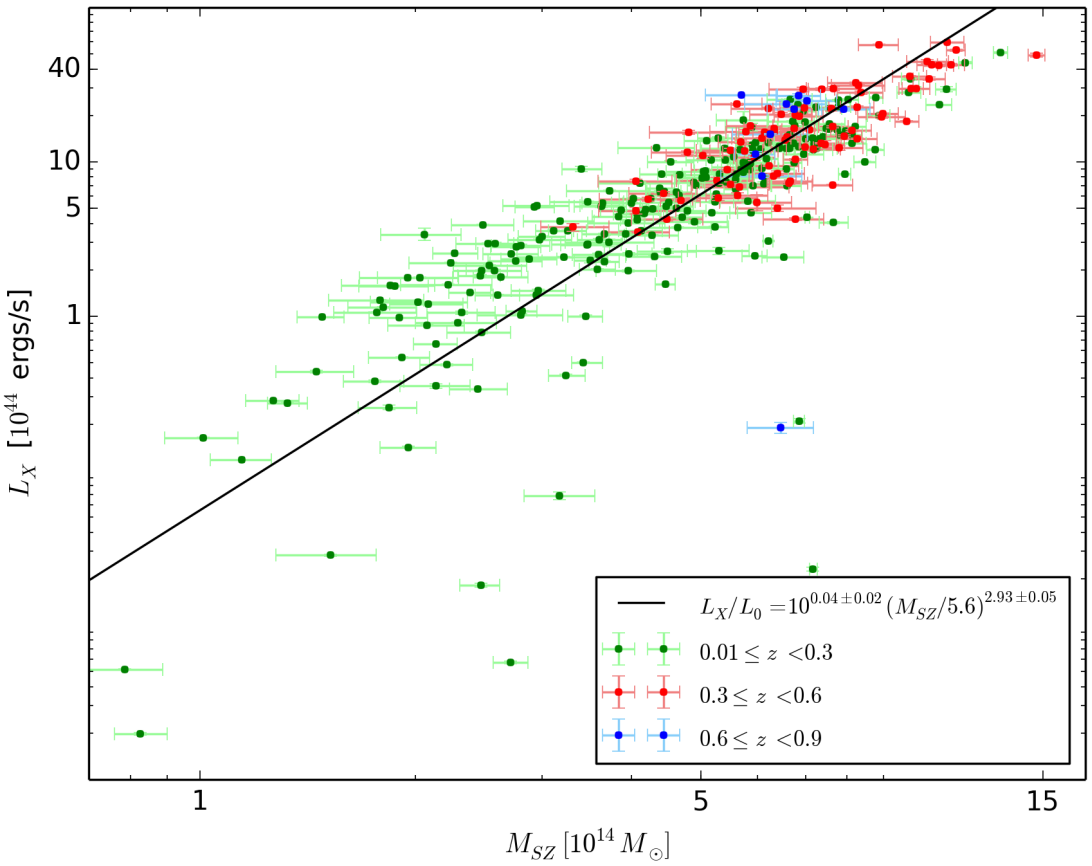

Figure 6.8: L_X-λ Scaling Relation from XCS and Planck, straight line indicates the MCMC fit of equation 6.9.

- The selection criteria were also tested on this set of catalogs, confirming its functionality.

- If the analysis is applied on catalogs that do not define errors on its observable, then the final sample will be noisy at low richness (see Figures 6.1,6.2,6.3,6.4).

- Comparisons between the scaling relations are not trivial since the procedure to derive richness and mass are not the same on each survey.

6.6.2 Future Work

- An outlier analysis is needed for each scaling relation obtained in this chapter.

- It is possible to calibrate observables obtained in the same wavelength, this is needed to make comparisons between the scaling relations.

- Images from both X-ray and optical or microwave, must to be analyzed to define a final sample and remove bad cluster matches.

Chapter 7

Conclusions

In this work we obtained optical to X-ray scaling relations, between the XMM Cluster Survey and the redMaPPer cluster catalog. Galaxy clusters are the largest gravitational bound objects in the universe, composed by 90% dark energy, 9% intracluster medium and 1% galaxies. The evolution of total mass in clusters allows us to understand the evolution of the total mass of the universe. However, total mass is not a direct observable, then mass tracers at X-ray (X-ray temperature, X-ray luminosity, gas mass), at millimeter (SZ decrement) and at the optical (richness), can be used to deduce the total mass of a cluster.

There are several scaling relation on the literature, these relate observables from different wavelength with the total mass of the cluster. It is important to understand and characterize the intrinsic scatter before considering the use of any scaling relation to constrain Cosmology.

In Chapter 3, we presented the $SF1$ algorithm to find RM clusters inside the XMM footprint. For clusters within XMM, we run the $CM1$ algorithm to match RM clusters to extended XCS sources within 1.5 h^{-1}Mpc and/or $3'$. A first filter is applied observing the X-ray observations to remove bad candidates, and classify the remaining matches as *good* or *likely*.

Chapter 4 introduces third generation of the XCS Post Processing Pipeline (XCS3P-v3). The changes implemented include: an improved method to mask the emission from extended sources near the source of interest; the introduction of the coefficient of variation as a criteria to diagnose if the iteration to R_{500} is unstable; and the correction on upper and lower luminosity errors, a test was carried out to ensure that the luminosity errors were comparable with the more conventional `cflux` approach.

XCS3P-v3 has been compared to XCS3P-v1 and XCS3P-v2 via an application to the cluster sample used in Hilton et al., 2012 where the $L_X - T_X$ scaling relation was obtained through XCS3P-v1. Rooney, 2015 found the same scaling relation using XCS3P-v2. The results from XCS3P-v3 and XCS3P-v2 show a significantly different redshift evolution to XCS3P-v1. XCS3P-v3 produces reliable L_X and T_X that are used later to find optical to X-ray scaling relations.

In Chapter 5 we obtain the optical to X-ray scaling relations from XCS and the redMaPPEr (SDSS, DES Y1) catalogs. These results represent the most comprehensive examination of the $T_X - \lambda$ and $L_X - \lambda$ relations for optical clusters to date. The slopes and normalizations are consistent between the samples. Compared with the previous published works Rykoff and Rozo, 2014; Rykoff et al., 2016, this joined sample presented in this thesis (XCS-RM (SDSS+DES Y1)) is not just considerably larger but also the intrinsic scatter on the scaling relation is smaller. The XCS-RM (SDSS+DES Y1) consists of 327 unique clusters with X-ray and optical follow up. This work demonstrates that there is a strong correlation between X-ray and optical properties of RM selected clusters. My work confirms that it is possible to connect the optical properties to the underlying mass. In turn this then supports the premise that catalogues of optically selected clusters can be used to measure cosmological parameters. As expected, there is more scatter in the $L_X - \lambda$ relation compared to $T_X - \lambda$.

Additional results in this chapter include the analysis on RM common clusters from SDSS and DES Y1, showing that it is possible to combine RM samples generated from different photometric data sets.

Finally in Chapter 6 we made a simple analysis of two optical (CAMIRA and GMBCG) and two millimeter (SPT and Planck), to validate the XCS3P-v3 and the process to obtain scaling relation (see Chapter 5). In addition, the $SF1$ and $CM1$ were also applied on these cluster catalogs to define matches with XCS. For the optical catalogs, the $T_X - \lambda$ and $L_X - \lambda$ relations were obtained assuming self similar evolution and using an MCMC approach (described in 4.4.2), notice that the richness parameter λ is defined differently on each catalog. Results show a clear correlation between optical and X-ray observables, and between SZ and X-ray observables. Both Optical catalogs do not report errors in the richness estimation, this has an impact on the final fitting as no relative error filter can be applied like in the analysis with RM.

7.1 Results Interpretations

7.1.1 $T_{\rm X} - \lambda$ scaling relation

The scaling relations found in this work relate X-ray observables ($T_{\rm X}$, $L_{\rm X}$) with the optical (richness). In order to compare our results with the predictions of the self-similar model (see Section 1.3), we need the scale of λ with the total mass of a cluster. Efforts have been done by the XCS team to obtain cluster masses using only X-ray data. Using CLMASS (Nulsen, Powell and Vikhlinin, 2010) it is possible to obtain the total mass of a cluster based on the conditions of hydrostatic equilibrium and spherical symmetry. First results were obtained but those are not yet reliable as they reproduce results only for large and massive clusters.

Saro et al., 2017 obtained the optical to SZE scaling relations for DES optically selected clusters within the SPT-SZ survey. Amoung the relations, they obtained the $\lambda - M_{500}$ relation. The optically selection was made using the redMaPPer algorithm, thus the λ parameter is the same as in this thesis. The result reported by the DES-SPT team for the mentioned scaling relation is:

$$\ln \lambda = A_\lambda + B_\lambda \ln \left(\frac{M_{500}}{3 \times 10^{14} \mathrm{h}^{-1} \mathrm{M}_\odot} \right) + C_\lambda \ln \left(\frac{E(z)}{E(z=0.6)} \right), \tag{7.1}$$

where $A_\lambda = 66.1^{+6.3}_{-5.9}$, $B_\lambda = 1.14^{+0.21}_{-0.18}$ and $C_\lambda = 0.73^{+0.77}_{-0.75}$. Equation 7.1 together with the results reported in this thesis for the $T_{\rm x} - \lambda$ (see Table 5.6) make possible to obtain a $T_{\rm x} - M_{500}$ relation through the richness λ as a common parameter. Combining the equations we can write

$$\ln T_{\rm X} = A_x + B_x \ln \left(\frac{M_{500}}{M_0} \right) + C_x \ln \left(\frac{E(z)}{E_0} \right), \tag{7.2}$$

where A_x,B_x and C_x are different to the parameters defined in Equation 7.1. The parameter of interest is B_x which is defined as $B_x \equiv \alpha \times B_\lambda$, α is taken from Equation 5.13. From Chapter 5, we know that the value of α for the combined sample (SDSS+DES Y1) is $\alpha = 0.59 \pm 0.02$. Thus,

$$B_x = \alpha \times B_\lambda = 0.59 \times 1.14 = 0.6726^{+0.23}_{-0.21}. \tag{7.3}$$

From the self-similar model, we know the value of the slope on the $M - T_{\rm X}$ relation (see Equation 1.21) is 2/3. We can conclude that our results agrees with the self-similar model within one sigma. It is important to notice that it was not expected to reproduce the values predicted by the self-similar model, because our samples were not selected considering the assumptions of that model (such as hydrodynamic equilibrium and spherical symmetry).

It is possible to compare our results with numerical simulations such as the The Cluster-EAGLE project (Barnes et al., 2017), where 30 clusters are constructed using cosmological hydrodinamical simulations. Their work reports the global properties of each cluster, such as the estimated mass, gas, stellar and black hole masses, X-ray and SZ properties as well. The $T_{\rm X} - M_{500}$ scaling relation obtained from these 30 simulated clusters has the form:

$$T_{\rm X} = 10^{A} \left(\frac{M_{500}}{4 \times 10^{14} {\rm h}^{-1} {\rm M}_{\odot}} \right)^{\alpha}, \tag{7.4}$$

where the value of α depends on the type of sample being $\alpha = 0.47^{+0.07}_{-0.02}$ for the full sample, $\alpha = 0.56^{+0.02}_{-0.03}$ for relaxed clusters and $\alpha = 0.42^{+0.09}_{-0.02}$ for unrelaxed clusters.
Compared with our results, there is more similarity with the relaxed clusters on the simulation, but the other reported values are still within two sigma.

7.1.2 $L_{\rm X} - \lambda$ scaling relation

Using again the results from Saro et al., 2017, we can relate the scaling relation obtained in Section 5.5 to obtain the $L_{\rm X} - M$ relation and then compare it with the self-similar model. The relation has the form:

$$\ln L_{\rm X} = A_x + B_x \ln \left(\frac{M_{500}}{M_0} \right) + C_x \ln \left(\frac{E(z)}{E_0} \right), \tag{7.5}$$

where the parameters of interest are B_x and C_x, the first is defined as:

$$B_x = \alpha \times B_\lambda, \tag{7.6}$$

here, α is taken from the results shown in Table 5.8, for the $L_{\rm X} - \lambda$ scaling relation. B_λ is the value obtained by the SPT team on Equation 7.1. Taking the value of α from the joined sample ($\alpha = 2.02 \pm 0.07$) it is possible to calulate

$$B_x = \alpha \times B_\lambda = (2.02 \times 1.14) = 2.30^{+0.28}_{-0.25}. \tag{7.7}$$

The other parameter of interest is C_x, which is defined as:

$$C_x = (\alpha \times C_\lambda) + 1, \tag{7.8}$$

for the joined sample, C_x is

$$C_x = (\alpha \times C_\lambda) + 1 = 2.47^{+0.84}_{-0.82}. \tag{7.9}$$

The $L_{\rm x} - M$ scaling relation has the form:

$$L_{\rm x} \propto M_{500}^{(2.30^{+0.28}_{-0.25})} E(z)^{(2.47^{+0.84}_{-0.82})}. \tag{7.10}$$

It is possible to compare Equation 7.10 with the prediction from the self-similar model (see Equation 1.28), the exponent of $E(z)$ agrees with the self-similar prediction but the coefficient of the mass is significantly higher than expected. This result supports the idea that the XCS-RM samples defined in this thesis have clusters that do not agree with the assumptions made by the self-similar model.

We also compared the $L_{\rm x} - M$ scaling relation with the results from the Cluster Eagle project (Barnes et al., 2017). The $L_{\rm x} - M$ scaling relation obtained from their sample of 30 simulated clusters is:

$$L_{\rm X} = 10^{A} \left(\frac{M_{500}}{4 \times 10^{14} {\rm h}^{-1} {\rm M}_{\odot}} \right)^{\alpha}, \tag{7.11}$$

where α takes different values, for the full sample $\alpha = 1.33^{+0.13}_{-0.08}$, for the relaxed sample $\alpha = 1.59^{+0.21}_{-0.08}$ and for the unrelaxed sample is $1.36^{+0.12}_{-0.15}$. All these results agree within one sigma with the predictions of the self-similar model, but not with the results obtained in this thesis.

7.1.3 $T_{\rm X} - L_{\rm X}$ scaling relation

It is possible to compare directly the results of the $T_{\rm X} - L_{\rm X}$ scaling relation obtained in this thesis (see Section 5.6) with the self-similar model. Table 5.9 shows the constraints for each sample, in the other hand, the self-similar model (see Equation 1.27) predicts a slope equal to 2. The results obtained in this thesis for the slope vary from 3.58 to 3.69, all of them are significantly far from the self-similar prediction. Several independent observational studies have shown that the $T_{\rm X} - L_{\rm X}$ scaling relation does not scale self-similarly, the slope is closer to 3 than to the predicted value of 2. Allen, Evrard and Mantz, 2011 reported a slope of 2.44 ± 0.03. Pratt et al., 2009 found it is 3.35 ± 0.35 from a sample of 31 nearby clusters selected with no bias towards any particular morphology type. Mantz et al., 2016 reported a slope of 2.12 ± 0.03 for a sample carefully selected composed completely of relaxed clusters.

There is evidence then that a selection of relaxed clusters is needed to reproduce the self-similar predictions.

Bibliography

Abbott, T. et al. (2016a). "Cosmology from cosmic shear with Dark Energy Survey Science Verification data". In: *Physical Review D* 94.2, p. 022001. arXiv: 1507.05552.

Abbott, T. et al. (2016b). "The Dark Energy Survey: More than dark energy - an overview". In: *Monthly Notices of the Royal Astronomical Society* 460.2, pp. 1270–1299. arXiv: 1601.00329.

Abell, George O, Jr. Corwin, Harold G. and Ronald P Olowin (1989). "A catalog of rich clusters of galaxies". In: *The Astrophysical Journal Supplement Series* 70, p. 1.

Ade, P. A. R. et al. (2016). "Planck 2015 results". In: *Astronomy & Astrophysics* 594, A13. arXiv: 1502.01589.

Aihara, Hiroaki et al. (2011). "the Eighth Data Release of the Sloan Digital Sky Survey: First Data From Sdss-Iii". In: *The Astrophysical Journal Supplement Series* 193.2, p. 29. arXiv: 1101.1559.

Akritas, Michael G. and Matthew A. Bershady (1996). "Linear Regression for Astronomical Data with Measurement Errors and Intrinsic Scatter". In: *The Astrophysical Journal* 470, p. 706. arXiv: arXiv:1011.1669v3.

Alam, Shadab et al. (2016). "The clustering of galaxies in the completed SDSS-III Baryon Oscillation Spectroscopic Survey: cosmological analysis of the DR12 galaxy sample". In: *Mon. Not. R. Astron. Soc* 000, pp. 1–38. arXiv: 1607.03144.

Allen, S. W. et al. (2004). "Constraints on dark energy from Chandra observations of the largest relaxed galaxy clusters". In: *Monthly Notices of the Royal Astronomical Society* 353.2, pp. 457–467. arXiv: 0405340 [astro-ph].

Allen, S. W. et al. (2008). "Improved constraints on dark energy from Chandra X-ray observations of the largest relaxed galaxy clusters". In: *Monthly Notices of the Royal Astronomical Society* 383.3, pp. 879–896. arXiv: 0706.0033.

Allen, Steven W, August E Evrard and A. Mantz (2011). "Cosmological Parameters from Observations of Galaxy Clusters". In: *Annual Review of Astronomy and Astrophysics*.

Annual Review of Astronomy and Astrophysics 49.1, pp. 409–470. arXiv: 1103.4829 [astro-ph.CO].

Allen, S.W., R.W. Schmidt and A.C. Fabian (2001). "The X-ray virial relations for relaxed lensing clusters observed with Chandra". In: *Monthly Notices of the Royal Astronomical Society* 328.3, pp. L37–L41.

Arnaud, K. A. (1996). "XSPEC: The First Ten Years". In: *Astronomical Data Analysis Software and Systems V* 101, p. 17. arXiv: arXiv:1011.1669v3.

Arnaud, M., E. Pointecouteau and G. W. Pratt (2005). "The structural and scaling properties of nearby galaxy clusters. II. The M-T relation". In: *Astronomy and Astrophysics* 441, pp. 893–903. arXiv: 0502210 [astro-ph].

Arnaud, M. et al. (2010). "The universal galaxy cluster pressure profile from a representative sample of nearby systems (REXCESS) and the Y SZ – M 500 relation". In: *Astronomy and Astrophysics* 517.Icm, A92. arXiv: arXiv:0910.1234v1.

Bai, Yu et al. (2015). "AN UPDATED ULTRAVIOLET CATALOG OF GALEX NEARBY GALAXIES". In: *The Astrophysical Journal Supplement Series* 220.1, p. 6.

Barnes, David J. et al. (2017). "The Cluster-EAGLE project: global properties of simulated clusters with resolved galaxies". In: 20.July, pp. 1–20. arXiv: 1703.10907.

Bleem, L. E. et al. (2015). "GALAXY CLUSTERS DISCOVERED VIA THE SUNYAEV-ZEL'DOVICH EFFECT IN THE 2500-SQUARE-DEGREE SPT-SZ SURVEY". In: *The Astrophysical Journal Supplement Series* 216.2, p. 27. arXiv: 1409.0850.

Böhringer, H, P. Schuecker and L. Guzzo (2004). "The ROSAT-ESO Flux Limited X-ray (REFLEX) Galaxy cluster survey. V. The cluster catalogue". In: *arXiv preprint astro-ph/ ...* 383, pp. 367–383. arXiv: 0405546v1 [arXiv:astro-ph].

Bohringer, H. et al. (2000). "The Northern ROSAT AllSky (NORAS) Galaxy Cluster Survey. I. XRay Properties of Clusters Detected as Extended XRay Sources". In: *The Astrophysical Journal Supplement Series* 129.2, pp. 435–474. arXiv: 0003219 [astro-ph].

Bonvin, V et al. (2017). "H0LiCOW – V. New COSMOGRAIL time delays of HE 04351223: H 0 to 3.8 per cent precision from strong lensing in a flat ΛCDM model". In: *Monthly Notices of the Royal Astronomical Society* 465.4, pp. 4914–4930. arXiv: 1607.01790v1.

Borgani, S et al. (2004). "X-ray properties of galaxy clusters and groups from a cosmological hydrodynamical simulation". In: *Monthly Notices of the Royal Astronomical Society* 348.3, pp. 1078–1096.

Borgani, Stefano (2006). "Cosmology with clusters of galaxies". In: *Lecture notes in Physics, Springer* 138.1-3, pp. 16–20. arXiv: 0605575 [astro-ph].

Brinkmam, A, H Aarts and A J Den Boggende (1998). "The Reflection Grating Spectrometer on board XMM". In: *Proceedings of the First XMM Workshop: Science with XMM*.

Brinkmann, W., E. Ferrero and M. Gliozzi (2002). "XMM-Newton observation of the BAL Quasar PHL 5200:" in: *Astronomy & Astrophysics* 385.3, pp. L31–L35.

Cash, J. R. (1974). "The numerical solution of systems of stiff ordinary differential equations". In: *Mathematical Proceedings of the Cambridge Philosophical Society* 76.02, p. 443.

Clowe, Douglas et al. (2006). "A Direct Empirical Proof of the Existence of Dark Matter". In: *The Astrophysical Journal* 648.2, pp. L109–L113. arXiv: 0608407 [astro-ph].

Crain, Robert A. et al. (2007). "The baryon fraction of CDM haloes". In: *Monthly Notices of the Royal Astronomical Society* 377.1, pp. 41–49. arXiv: 0610602 [astro-ph].

Den Herder, J W et al. (2001). "The reflection grating spectrometer on board XMM-Newton". In: *Astronomy and Astrophysics* 365.1, pp. L7–L17.

Dickey, J and F Lockman (1990). "H I IN THE GALAXY". In: *ANNU. REV. ASTRON. ASTROPHYS* 28, pp. 215–61.

Drake, Stephen A (2004). "X-Ray Data Archives Early X-ray Observatories". In: *X-Ray and Radio Connections*.

Flaugher, B. et al. (2015). "the Dark Energy Camera". In: *The Astronomical Journal* 150.5, p. 150. arXiv: 1504.02900 [astro-ph.IM].

Freeman, P. E. et al. (2002). "A WaveletBased Algorithm for the Spatial Analysis of Poisson Data". In: *The Astrophysical Journal Supplement Series* 138.1, pp. 185–218. arXiv: 0108429 [astro-ph].

Frieman, Joshua A, Michael S. Turner and Dragan Huterer (2008). "Dark Energy and the Accelerating Universe". In: *Annual Review of Astronomy and Astrophysics* 46.1, pp. 385–432. arXiv: 0803.0982.

Giodini, S. et al. (2013). "Scaling relations for galaxy clusters: properties and evolution". In: *Space Science Reviews* 177.1-4, pp. 247–282. arXiv: 1305.3286.

Gunn, J. E. et al. (1998). "The Sloan Digital Sky Survey Photometric Camera". In: *The Astronomical Journal* 116.6, pp. 3040–3081. arXiv: 9809085 [astro-ph].

Gunn, James E. et al. (2006). "The 2.5 m Telescope of the Sloan Digital Sky Survey". In: *The Astronomical Journal* 131.4, pp. 2332–2359. arXiv: 0602326 [astro-ph].

Hao, Jiangang et al. (2010). "A GMBCG Galaxy Cluster Catalog of 55,424 Rich Clusters from SDSS DR7". In: *The Astrophysical Journal Supplement Series* 191.2, pp. 254–274. arXiv: 1010.5503.

Hilton, Matt et al. (2012). "The XMM Cluster Survey: evidence for energy injection at high redshift from evolution of the X-ray luminosity-temperature relation". In: *Monthly Notices of the Royal Astronomical Society* 424.3, pp. 2086–2096. arXiv: 1205.5570.

James, F and M Roos (1975). "Minuit - a system for function minimization and analysis of the parameter errors and correlations". In: *Computer Physics Communications* 10.6, pp. 343–367.

Jansen, F. et al. (2001). "XMM-Newton observatory". In: *Astronomy and Astrophysics* 365.1, pp. L1–L6. arXiv: arXiv:0901.0974v2.

Jiang, Linhua et al. (2014). "THE SLOAN DIGITAL SKY SURVEY STRIPE 82 IMAGING DATA: DEPTH-OPTIMIZED CO-ADDS OVER 300 deg 2 IN FIVE FILTERS". In: *The Astrophysical Journal Supplement Series* 213.1, p. 12. arXiv: 1405.7382.

Joye, W A et al. (2003). "New Features of SAOImage DS9". In: *Astronomical Data Analysis Software and Systems XII* 295, p. 489.

Kaiser, Nick (1986). "Evolution and clustering of rich clusters". In: *Monthly Notices of the Royal Astronomical Society* 222.2, pp. 323–345.

Koester, B. P. et al. (2007). "A MaxBCG Catalog of 13,823 Galaxy Clusters from the Sloan Digital Sky Survey". In: *The Astrophysical Journal* 660.1, pp. 239–255. arXiv: 0701265 [astro-ph].

Koopmans, Author L H, D B Owen and J I Rosenblatt (1964). "Confidence Intervals for the Coefficient of Variation for the Normal and Log Normal Distributions". In: *Biometrika* 51.1, pp. 25–32.

Kravtsov, Andrey V. and Stefano Borgani (2012). "Formation of Galaxy Clusters". In: *Annual Review of Astronomy and Astrophysics* 50.1, pp. 353–409. arXiv: 1205.5556.

Lloyd-Davies, E. J. et al. (2011). "The XMM Cluster Survey: X-ray analysis methodology". In: *Monthly Notices of the Royal Astronomical Society* 418.1, pp. 14–53. arXiv: 1010.0677.

Loewenstein, Michael (2003). "Chemical Composition of the Intracluster Medium". In: *Origin and Evolution of the Elements*, p. 422. arXiv: 0310557 [astro-ph].

Mantz, A., S. W. Allen and D. Rapetti (2010). "The observed growth of massive galaxy clusters - IV. Robust constraints on neutrino properties". In: *Monthly Notices of the Royal Astronomical Society* 406.3, pp. 1805–1814. arXiv: 0911.1788 [astro-ph.CO].

Mantz, A. B. et al. (2014a). "Cosmology and astrophysics from relaxed galaxy clusters - II. Cosmological constraints". In: *Monthly Notices of the Royal Astronomical Society* 440.3, pp. 2077–2098. arXiv: 1402.6212.

Mantz, Adam B. et al. (2014b). "Weighing the giants - IV. cosmology and neutrino mass". In: *Monthly Notices of the Royal Astronomical Society* 446.3, pp. 2205–2225. arXiv: 1407.4516.

Mantz, Adam B. et al. (2016). "Weighing the giants– V. Galaxy cluster scaling relations". In: *Monthly Notices of the Royal Astronomical Society* 463.4, pp. 3582–3603. arXiv: 1606.03407.

Mason, K. O. et al. (2001). "The XMM-Newton optical/UV monitor telescope". In: *Astronomy and Astrophysics* 365.1, pp. L36–L44. arXiv: 0011216 [astro-ph].

Mehrtens, N et al. (2012). "The XMM Cluster Survey: Optical analysis methodology and the first data release". In: *Monthly Notices of the Royal Astronomical Society* 423.2, pp. 1024–1052.

Melchior, P et al. (2016). "Weak-lensing mass calibration of redMaPPer galaxy clusters in Dark Energy Survey Science Verification data". In: *Monthly Notices of the Royal Astronomical Society* 22.24, pp. 1–22. arXiv: 1610.06890.

Metropolis, Nicholas et al. (1953). "Equation of state calculations by fast computing machines". In: *Journal Chemical Physics* 21.6, pp. 1087–1092. arXiv: 5744249209.

Mewe, R, J.˜R. Lemen and G.˜H.˜J. van den Oord (1986). "Calculated X-radiation from optically thin plasmas. VI - Improved calculations for continuum emission and approximation formulae for nonrelativistic average Gaunt factors". In: *aaps* 65, pp. 511–536.

Mitchell, R. J. et al. (1979). "The X-ray spectra of clusters of galaxies and their relationship to other cluster properties". In: *Monthly Notices of the Royal Astronomical Society* 189.2, pp. 329–361.

Morrison, R and D. McCammon (1983). "Interstellar photoelectric absorption cross sections, 0.03-10 keV". In: *The Astrophysical Journal* 270, p. 119.

Mushotzky, R F (1984). "X-Ray Emission from Clusters of Galaxies". In: *Physica Scripta* T7, pp. 157–162.

Navarro, J. F., C. S. Frenk and S. D. M. White (1995). "Simulations of X-ray clusters". In: *Monthly Notices of the Royal Astronomical Society* 275.3, pp. 720–740.

Nulsen, P. E. J., S. L. Powell and A. Vikhlinin (2010). "Model-Independent X-Ray Mass Determinations". In: *ApJ* 722.1, pp. 55–64. arXiv: 1008.2393.

Oguri, Masamune (2014). "A cluster finding algorithm based on the multiband identification of red sequence galaxies". In: *Monthly Notices of the Royal Astronomical Society* 444.1, pp. 147–161. arXiv: 1407.4693 [astro-ph.CO].

Planck Collaboration et al. (2013). "Planck 2013 results. XXIX. Planck catalogue of Sunyaev-Zeldovich sources". In: *Astronomy & Astrophysics* 571, A29. arXiv: 1303.5089.

Pratt, G. W. et al. (2009). "Galaxy cluster X-ray luminosity scaling relations from a representative local sample (REXCESS)". In: *Astronomy and Astrophysics* 498.2, pp. 361–378. arXiv: 0809.3784.

Press, William H and Paul Schechter (1974). "Formation of Galaxies and Clusters of Galaxies by Self-Similar Gravitational Condensation". In: *The Astrophysical Journal* 187, p. 425. arXiv: 9809069v1 [arXiv:gr-qc].

Reichert, a et al. (2011). "Observational constraints on the redshift evolution of X-ray scaling relations of galaxy clusters out to z ˜ 1.5". In: *Astronomy & Astrophysics* 535, A4. arXiv: 1109.3708.

Robitaille, T. and E. Bressert (2012). "APLpy: Astronomical Plotting Library in Python". In: *Astrophysics Source Code Library*.

Robitaille, Thomas P. et al. (2013). "Astropy: A community Python package for astronomy". In: *Astronomy & Astrophysics* 558, A33. arXiv: 1307.6212.

Romer, A Kathy et al. (1999). "A Serendipitous Galaxy Cluster Survey with XMM: Expected Catalogue Properties and Scientific Applications". In: 1, pp. 594–608. arXiv: 9911499 [astro-ph].

Rooney, Philip J. (2015). "The XMM Cluster Survey : A New Cluster Catalogue and Applications ." PhD thesis. University of Sussex.

Rozo, E. et al. (2015). "RedMaPPer - IV. Photometric membership identification of red cluster galaxies with 1 per cent precision". In: *Monthly Notices of the Royal Astronomical Society* 453.1, pp. 38–52. arXiv: 1410.1193.

Rozo, Eduardo, Alexey Vikhlinin and Surhud More (2012). "The Ysz–Yx Scaling Relation as Determined from Planck and Chandra". In: *The Astrophysical Journal* 760.1, p. 67. arXiv: 1202.2150.

Rozo, Eduardo et al. (2012). "A Comparative Study of Local Galaxy Clusters: I. Derived X-ray Observables". In: *Monthly Notices of the Royal Astronomical Society* 438.1, pp. 49–61. arXiv: 1204.6301.

Rozo, Eduardo et al. (2014). "redMaPPer III: A Detailed Comparison of the Planck 2013 and SDSS DR8 RedMaPPer Cluster Catalogs". In: *Monthly Notices of the Royal Astronomical Society* 450.1, pp. 592–605. arXiv: 1401.7716.

Rykoff, E. S. and E. Rozo (2014). "redMaPPer II: X-RAY AND SZ PERFORMANCE BENCHMARKS FOR THE SDSS CATALOG". In: *The Astrophysical Journal* 783.2, p. 80. arXiv: 1303.3373.

Rykoff, E. S. et al. (2008). "Measuring the Mean and Scatter of the XRay Luminosity–Optical Richness Relation for maxBCG Galaxy Clusters". In: *The Astrophysical Journal* 675.2, pp. 1106–1124. arXiv: 0709.1158.

Rykoff, E. S. et al. (2012). "Robust Optical Richness Estimation With Reduced Scatter". In: *The Astrophysical Journal* 746.2, p. 178.

Rykoff, E. S. et al. (2013). "redMaPPer I: Algorithm and SDSS DR8 Catalog". In: *The Astrophysical Journal* 785.2, p. 104. arXiv: 1303.3562.

Rykoff, E. S. et al. (2016). "THE REDMAPPER GALAXY CLUSTER CATALOG FROM DES SCIENCE VERIFICATION DATA". In: *The Astrophysical Journal Supplement Series* 224.1, p. 1. arXiv: 1601.00621.

Salpeter, Edwin E. (1955). "The Luminosity Function and Stellar Evolution." In: *The Astrophysical Journal* 121, p. 161.

Sarazin, Craig L. (1986). "X-ray emission from clusters of galaxies". In: *Reviews of Modern Physics* 58.1, pp. 1–115.

Saro, A. et al. (2017). "Optical–SZE scaling relations for DES optically selected clusters within the SPT-SZ Survey". In: *Monthly Notices of the Royal Astronomical Society* 468.3, pp. 3347–3360. arXiv: 1605.08770.

Schellenberger, G. et al. (2015). "XMM-Newton and Chandra cross-calibration using HIFLUGCS galaxy clusters". In: *Astronomy & Astrophysics* 575. arXiv: 1404.7130.

Stott, J. P. et al. (2009). "The evolution of the red sequence slope in massive galaxy clusters". In: *Monthly Notices of the Royal Astronomical Society* 394.4, pp. 2098–2108. arXiv: 0901.1227.

Strüder, L. et al. (2001). "The European Photon Imaging Camera on XMM-Newton: The pn-CCD camera". In: *Astronomy & Astrophysics* 365.1, pp. L18–L26.

Sunyaev, R. A. and Ya B. Zeldovich (1970). "Small-scale fluctuations of relic radiation". In: *Astrophysics and Space Science* 7.1, pp. 3–19. arXiv: arXiv:1011.1669v3.

Takada, Masahiro (2010). "Subaru Hyper Suprime-Cam project". In: *AIP Conference Proceedings* 1279, pp. 120–127.

Taylor, Mark B (2005). "TOPCAT & STIL: Starlink Table / VOTable Processing Software". In: *Astronomical Data Analysis Software and Systems XIV - ASP Conference Series* 347, pp. 29–33.

The Dark Energy Survey Collaboration (2005). "The Dark Energy Survey". In: *Journal of Physics: Conference Series* 259, p. 012080. arXiv: 0510346 [astro-ph].

Turner, M. J. L., A. Abbey and M. Arnaud (2000). "The European Photon Imaging Camera on XMM-Newton: The MOS Cameras". In: *Oncogene* 14.2, pp. 223–31. arXiv: 0011498 [astro-ph].

Vikhlinin, A et al. (2009). "CHANDRA CLUSTER COSMOLOGY PROJECT III: COSMOLOGICAL PARAMETER CONSTRAINTS". In: *The Astrophysical Journal* 692.2, pp. 1060–1074. arXiv: 0812.2720 [astro-ph].

Visvanathan, N. and A. Sandage (1977). "The color-absolute magnitude relation for E and S0 galaxies. I - Calibration and tests for universality using Virgo and eight other nearby clusters". In: *The Astrophysical Journal* 216, p. 214.

Voges, Wolfgang et al. (1999). "The ROSAT All-Sky Survey Bright Source Catalogue". In: *Astronomy and Astrophysics, v.349, p.389-405 (1999)* 349, pp. 389–405. arXiv: 9909315 [astro-ph].

Voit, G Mark (2005). "Tracing cosmic evolution with clusters of galaxies". In: *Reviews of Modern Physics* 77.1, pp. 207–258. arXiv: 0410173 [astro-ph].

Wright, E. L. (2006). "A Cosmology Calculator for the World Wide Web". In: *Publications of the Astronomical Society of the Pacific* 118, pp. 1711–1715. arXiv: 0609593 [astro-ph].

York, Donald G. et al. (2000). "The Sloan Digital Sky Survey: Technical Summary". In: *The Astronomical Journal* 120.3, pp. 1579–1587. arXiv: 0006396 [astro-ph].

Zwicky, F (1933a). "Die Rotverschiebung von extragalaktischen Nebeln". In: *Helvetica Physica Acta* 6, pp. 110–127.

— (1933b). "How far do cosmic rays travel?" In: *Physical Review* 43.2, pp. 147–148.

Appendix A

Finding Sources inside XMM-Newton

This is a Python code used in this thesis to find redMaPPer objects inside XMM-Newton observations. It project the cluser world coordinate into pixel coordinates inside the observation. This program was made due the errors on the XMM central coordinates found on mosaic observations. Also the XMM Science Archive webpage is very limited in the number of clusters to crossmatch.

```
from kapteyn import wcs
from matplotlib import pyplot as plt
import numpy
import pyfits
import math
import csv
import sys



number = pyfits.open('to_mastercode.fits')
number_data = number[1].data
aux = number_data.field('aux')
obs_name = number_data.field('fits')
xapa = number_data.field('xapa')
```

```
for counter in range(int(sys.argv[1]),len(aux)):
    print('On ObsID no ='+str(counter))
    hdulist_XMM = pyfits.open('/lustre/scratch/astro/pr83/'+aux[counter]
    +'images/'+obs_name[counter])
    Obs_ID = hdulist_XMM[0].header['OBS_ID']
    print('image   '+str(counter)+'   yo!'+'----'+str(obs_name[counter]))
    xeje = hdulist_XMM[0].header['NAXIS1']
    yeje = hdulist_XMM[0].header['NAXIS2']
    ra_xmm = hdulist_XMM[0].header['RA_PNT']
    dec_xmm = hdulist_XMM[0].header['DEC_PNT']
    hdulist_RM = pyfits.open('redmapper_dr8_v6.3.1_lgt5.fit')
    rm_data = hdulist_RM[1].data
    rm_ra = rm_data.field('RA')
    rm_dec = rm_data.field('DEC')
    corner_coordinate = (xeje,yeje)
    origin_coordinate = (0,0)
    XMM_scidata = hdulist_XMM[0].data

    header = hdulist_XMM[0].header
    proj = wcs.Projection(header)

    world_edge = proj.toworld(corner_coordinate)
    world_origin = proj.toworld(origin_coordinate)

    ra_i = world_edge[0]
    dec_i = world_edge[1]

    ra_f = world_origin[0]
    dec_f = world_origin[1]



    lowmask = rm_data.field('RA') < ra_f
    low_ra_rm = rm_data[lowmask]
```

```
highmask = low_ra_rm.field('RA') > ra_i
new_rm_ra = low_ra_rm[highmask]

lowmaskdec = new_rm_ra.field('DEC') < dec_i
low_dec_rm = new_rm_ra[lowmaskdec]
highmaskdec = low_dec_rm.field('DEC') > dec_f
new_rm_data = low_dec_rm[highmaskdec]

for source in range(0,len(new_rm_data.field('RA'))):
    rm_coordinates = (new_rm_data.field('RA'), new_rm_data.field('DEC'))
    one_rm_coordinate = (rm_coordinates[0][source], rm_coordinates[1][source])
    rm_pixel_coordinates = proj.topixel(one_rm_coordinate)
    ra_pix = rm_pixel_coordinates[0]
    dec_pix = rm_pixel_coordinates[1]

    radius = math.sqrt((ra_pix-256)**2+(dec_pix-256)**2)
    ra_rm_w = new_rm_data.field('RA')[source]
    dec_rm_w = new_rm_data.field('DEC')[source]
    rad_w = math.sqrt((ra_rm_w-ra_xmm)**2+(dec_rm_w-dec_xmm)**2)

    ind = new_rm_data.field('MEM_MATCH_ID')[source]
    r_n = new_rm_data.field('RA')[source]
    d_n = new_rm_data.field('DEC')[source]
    lambda_c = new_rm_data.field('LAMBDA_CHISQ')[source]
    red = new_rm_data.field('Z_LAMBDA')[source]


    if radius < 250:
        if rad_w < 0.28:
            x1 = int(ra_pix)-5
            y1 = int(dec_pix)-5
            x2 = int(ra_pix)+5
            y2 = int(dec_pix)+5
```

```
prom = 0.0
total = 0.0
for i in range(x1,x2+1):
    for j in range(y1,y2+1):

        prom = XMM_scidata[i, j]
        total = total +  prom
if total > 40:

#if XMM_scidata[ra_pix, dec_pix] != 0.0:

     v = open('./xapa/'+str(xapa[counter]),'a')
     v.write('image ; circle('+str(ra_pix)+','+str(dec_pix)+',14)
     # color=cyan'+'\n')
     u = open('sources_xcs_full1.csv','a')
     u.write(str(ind)+','+str(r_n)+
     ','+str(d_n)+','+str(ra_pix)+','
     +str(dec_pix)+','+str(lambda_c)+','
     +str(red)+','+str(obs_name[counter])+','
     +str(xapa[counter])+'\n')
```

Appendix B

Crossmatch Code

This is a Python program to make a crossmath between XCS and redMaPPer cluster positions, considering redshift information and a defined Cosmology. In this case, redshifts are coming from redMaPPer and the cosmology is ΛCDM with $H_0 = 70$, $\Omega_m = 0.3$ and $\Omega_\Lambda = 0.7$.
The code use a searching radius of 1.5 h^{-1}Mpc.

```
import sys
from math import *
import pyfits
import math
import aplpy

from astropy.cosmology import FlatLambdaCDM
cosmo = FlatLambdaCDM(H0=70, Om0=0.3)



counter = 0
names = pyfits.open('Planck_inXMM_unique.fits')
names_data = names[1].data

xcs_1 = pyfits.open('DR_25_05_16_ext_cts50.fits')
xcs_data = xcs_1[1].data

xcs_name = xcs_data.field('xcsNAme')
RA_XCS = xcs_data.field('RA_rad')
```

```
DEC_XCS = xcs_data.field('DEC_rad')
counts = xcs_data.field('softCts')
xcs_id = xcs_data.field('xcs_ID')



RA_rm = names_data.field('RA_rad')
DEC_rm = names_data.field('DEC_rad')
red =  names_data.field('Z')
lambdac = names_data.field('MSZ')
id_rm = names_data.field('id')




u = open('crossmatch_1.5Mpc_XCS_Planckv2.csv','a')
u.write('xcsName'+','+'Planck ID'+','+'z'+','+'separation'+','+'Angle21'+','+
'softCts'+','+'DL_Mpc'+','+'MSZ'+','+'XCS_ID'+','+
'U_ID'+'\n')


v = open('crossmatch_1.5Mpc_XCS_Planckv3.csv','a')
v.write('xcsName'+','+'PlanckID'+','+'z'+','+'separation'+','
+'Angle21'+','+'softCts'+','+'DL_Mpc'+','
+'MSZ'+','+'XCS_ID'+','+'U_ID'+'\n')

for counter in range(0,len(red)):
    print('in ='+str(counter))
    z=red[counter]    # redshift
    H0 = 70.00 # Hubble constant
    WM = 0.30 # Omega(matter)
    WV = 0.70 # Omega(vacuum) or lambda

    WR = 0.        # Omega(radiation)
```

```
WK = 0.        # Omega curvaturve = 1-Omega(total)
c = 299792.458 # velocity of light in km/sec
Tyr = 977.8    # coefficent for converting 1/H into Gyr
DTT = 0.5      # time from z to now in units of 1/H0
DTT_Gyr = 0.0  # value of DTT in Gyr
age = 0.5      # age of Universe in units of 1/H0
age_Gyr = 0.0  # value of age in Gyr
zage = 0.1     # age of Universe at redshift z in units of 1/H0
zage_Gyr = 0.0 # value of zage in Gyr
DCMR = 0.0     # comoving radial distance in units of c/H0
DCMR_Mpc = 0.0
DCMR_Gyr = 0.0
DA = 0.0       # angular size distance
DA_Mpc = 0.0
DA_Gyr = 0.0
kpc_DA = 0.0
DL = 0.0       # luminosity distance
DL_Mpc = 0.0
DL_Gyr = 0.0   # DL in units of billions of light years
V_Gpc = 0.0
a = 1.0        # 1/(1+z), the scale factor of the Universe
az = 0.5       # 1/(1+z(object))

h = H0/100.
WR = 4.165E-5/(h*h)   # includes 3 massless neutrino species, T0 = 2.72528
WK = 1-WM-WR-WV
az = 1.0/(1+1.0*z)
age = 0.
n=1000         # number of points in integrals
for i in range(n):
    a = az*(i+0.5)/n
    adot = sqrt(WK+(WM/a)+(WR/(a*a))+(WV*a*a))
    age = age + 1./adot
```

```
    zage = az*age/n
    zage_Gyr = (Tyr/H0)*zage
    DTT = 0.0
    DCMR = 0.0

# do integral over a=1/(1+z) from az to 1 in n steps, midpoint rule
    for i in range(n):
        a = az+(1-az)*(i+0.5)/n
        adot = sqrt(WK+(WM/a)+(WR/(a*a))+(WV*a*a))
        DTT = DTT + 1./adot
        DCMR = DCMR + 1./(a*adot)

    DTT = (1.-az)*DTT/n
    DCMR = (1.-az)*DCMR/n
    age = DTT+zage
    age_Gyr = age*(Tyr/H0)
    DTT_Gyr = (Tyr/H0)*DTT
    DCMR_Gyr = (Tyr/H0)*DCMR
    DCMR_Mpc = (c/H0)*DCMR

# tangential comoving distance

    ratio = 1.00
    x = sqrt(abs(WK))*DCMR
    if x > 0.1:
        if WK > 0:
            ratio =  0.5*(exp(x)-exp(-x))/x
        else:
            ratio = sin(x)/x
    else:
        y = x*x
    #    if WK < 0: y = -y
    #        ratio = 1. + y/6. + y*y/120.
    DCMT = ratio*DCMR
```

```
    DA = az*DCMT
    DA_Mpc = (c/H0)*DA
    kpc_DA = DA_Mpc/206.264806
    DA_Gyr = (Tyr/H0)*DA
    DL = DA/(az*az)
    DL_Mpc = (c/H0)*DL
    DL_Gyr = (Tyr/H0)*DL

# comoving volume computation


    ratio = 1.00
    x = sqrt(abs(WK))*DCMR
    if x > 0.1:
        if WK > 0:
            ratio = (0.125*(exp(2.*x)-exp(-2.*x))-x/2.)/(x*x*x/3.)
        else:
            ratio = (x/2. - sin(2.*x)/4.)/(x*x*x/3.)
    else:
        y = x*x
    #    if WK < 0: y = -y
    #        ratio = 1. + y/5. + (2./105.)*y*y
    VCM = ratio*DCMR*DCMR*DCMR/3.
    V_Gpc = 4.*pi*((0.001*c/H0)**3)*VCM

    ang = cosmo.arcsec_per_kpc_proper(red[counter])
    ang21 = ang.value
    angtol = ang21 * 1000/60


    for sub in range(0,len(RA_XCS)):
        angle = math.sqrt(math.pow((RA_rm[counter]-RA_XCS[sub])
        *math.cos(DEC_rm[counter]),2)+math.pow(DEC_rm[counter]
        -DEC_XCS[sub],2))
```

```
distance = DL_Mpc*(1/((1+red[counter])**2)) *
angle
auw = 1/((1+red[counter])**2)
angle21 = angtol * distance    # separation in arcmin according to z
if distance <= 1.5:
    u = open('crossmatch_1.5Mpc_XCS_Planckv2.csv','a')
    u.write(str(xcs_name[sub])+','+str(id_rm[counter])+
    ','+str(red[counter])+','+str(distance)+','
    +str(angle21)+','+str(counts[sub])+','+str(DL_Mpc)
    +','+str(lambdac[counter])+','+str(xcs_id[sub])+','
    +str(id_rm[counter])+'_'+str(xcs_id[sub])+'\n')
    if angle21 <= 3.0:
        v = open('crossmatch_1.5Mpc_XCS_Planckv3.csv','a')
        v.write(str(xcs_name[sub])+','+str(id_rm[counter])
        +','+str(red[counter])+','+str(distance)+','
        +str(angle21)+','+str(counts[sub])+','+
        str(DL_Mpc)+','+str(lambdac[counter])+','+
        str(xcs_id[sub])+','+str(id_rm[counter])+'_'
        +str(xcs_id[sub])+'\n')
```

Appendix C

Rejected candidates though eyeball identification

The sample of rejected clusters from both X-ray and optical eye ball check is presented in the next webpage https://astronomy.sussex.ac.uk/~ab615/zselected/rejected_objects.html.

Appendix D

The XCS-RM (SDSS+DES Y1) Cluster Catalog

The catalog of clusters defined in Section 5.3 containing **327** clusters can be obtained from https://astronomy.sussex.ac.uk/~ab615/xcs_rm_sdss+desy1.fits. The relevant columns are described bellow:

- **xcsName**: Cluster XCS name made with the sexagesimal cluster position.
- **RA**: Right Ascension in degrees.
- **DEC**: Declination in degrees.
- **softCts**: Background subtracted source counts in the X-ray soft band.
- **TxR500**: X-ray Temperature measured on a R_{500} aperture, it is given in keV.
- **TxR500_l**: X-ray Temperature 1σ lower value, it is given in keV.
- **TxR500_u**: X-ray Temperature 1σ upper value, it is given in keV.
- **LxR500**: Bolometric luminosity measured on a R_{500} aperture, it is given in $10^{44} ergs/s$.
- **LxR500_l**: Bolometric Luminosity 1σ lower value, it is given in $10^{44} ergs/s$.
- **LxR500_u**: Bolometric Luminosity 1σ upper value, it is given in $10^{44} ergs/s$.
- **MemMatchID**: ID number for each redMaPPer cluster, SDSS and DES Y1 assign different and individual identification numbers to each cluster.
- **LAMBDA_CHISQ**: RedMaPPer optical Richness.
- **LAMBDA_CHISQ_E**: RedMaPPer optical Richness error.

- **Z_LAMBDA**: RedMaPPer photometric redshift.

- **Catalog**: Flag of the RM input catalog (SDSS or DES Y1).